U.PORTO

DOUTORAMENTO

CIÊNCIAS BIOMÉDICAS

A robust study on the Ataxin-3 fibrillization pathway for the discovery of new inhibitory compounds

Francisco Rosário de Figueiredo

D

2022

U.PORTO

Francisco Rosário de Figueiredo .A robust study on the Ataxin-3 fibrillization pathway for the discovery of new inhibitory compounds

D.ICBAS **2022**

A robust study on the Ataxin-3 fibrillization pathway for the discovery of new inhibitory compounds

Francisco Rosário de Figueiredo

INSTITUTO DE CIÊNCIAS BIOMÉDICAS ABEL SALAZAR

Francisco Rosário de Figueiredo

A robust study on the Ataxin-3 fibrillization pathway for the discovery of new inhibitory compounds

Tese de Candidatura ao grau de Doutor em Ciências Biomédicas submetida ao Instituto de Ciências Biomédicas de Abel Salazar da Universidade do Porto

Orientador: Sandra de Macedo Ribeiro

Categoria: Investigadora Principal

Afiliação: IBMC – Instituto de Biologia Molecular e Celular e i3S – Instituto de Investigação e Inovação em Saúde, Universidade do Porto

Co-orientador: Paulo Jorge Ferreira

Categoria: Professor Catedrático

Afiliação: IST - Instituto Superior Técnico e INL - International Iberian Nanotechnology Laboratory

Co-orientador: Maria Alexandra Oliveira da Silva

Categoria: Junior Researcher

Afiliação: IBMC – Instituto de Biologia Molecular e Celular e i3S – Instituto de Investigação e Inovação em Saúde, Universidade do Porto

Co-orientador/Tutor: Luis Miguel Gales Pereira Pinto

Categoria: Professor Associado

Afiliação: ICBAS – Instituto de Ciências Biomédicas Abel Salazar, IBMC – Instituto de Biologia Molecular e Celular e i3S – Instituto de Investigação e Inovação em Saúde, Universidade do Porto

Declaração de Honra

Declaro que a presente tese é de minha autoria e não foi utilizada previamente noutro curso ou unidade curricular, desta ou de outra instituição. As referências a outros autores (afirmações, ideias, pensamentos) respeitam escrupulosamente as regras da atribuição, e encontram-se devidamente indicadas no texto e nas referências bibliográficas, de acordo com as normas de referenciação. Tenho consciência de que a prática de plágio e auto-plágio constitui um ilícito académico.

À minha família

Author Statement

This work was funded by Fundação para a Ciência e a Tecnologia through PhD fellowship SFRH/BD/133009/2017.

This work was funded by PhasAGE (European Union Horizon 2020, Grant Agreement ID 952334), Fundação para a Ciência e Tecnologia: POCI-01-0145-FEDER-031173, Fundação para a Ciência e Tecnologia: POCI-01-0145-FEDER-029056, Fundação para a Ciência e Tecnologia: POCI-01-0145-FEDER-007274 and EMBO Scientific Exchange Grant 9109.

Figure 7 from Chapter 1 and both Figure 1 and 3A from Chapter 3, were taken with permission from Satoh *et al.* 2014 "Mode of substrate recognition by the Josephin domain of ataxin-3, which has an endo-type deubiquitinase activity" FEBS letters; Iadanza *et al.* 2018 "A new era for understanding amyloid structures and disease" Nature Reviews Molecular Cell Biology; Turk and Baumeister 2020 "The promise and the challenges of cryo-electron tomography" FEBS letters, respectively. If necessary authorizations of image usage will be provided upon request. All other images and schemes were created with BioRender.

The work included in this thesis was totally or partially executed by the candidate, in close cooperation/co-authorships with supervisors and other researchers. In detail Chapters 1, 2, 3, 4 and 5 were written by the candidate with revisions from the other authors and the supervising team. For Chapters 2, 3 and 4 all methodology, software usage, analysis, investigation, data curation and original writing was performed by the candidate with revisions from the supervising team.

This thesis includes one article published in a peer-reviewed international journal. This article was integrated within the thesis as Chapter 2 - *Development of a robust assay to monitor ataxin-3 amyloid fibril assembly.* This published work has a CC BY licence. It is open access and therefore has the permission to be published as part of this thesis.

Figueiredo, F.; Lopes-Marques, M.; Almeida, B.; Matscheko, N.; Martins, P.M.; Silva, A.; Macedo-Ribeiro, S. Development of a robust assay to monitor ataxin-3 amyloid fibril assembly. Cells 2022, 11, 1969. https://doi.org/10.3390/cells11121969

A provisional patent request was made for the compounds studied in Chapter 4 for their usage in MJD therapy.


IBMC
INSTITUTO DE BIOLOGIA MOLECULAR E CELULAR
INSTITUTE FOR MOLECULAR AND CELL BIOLOGY


INSTITUTO DE INVESTIGAÇÃO
E INOVAÇÃO EM SAÚDE
UNIVERSIDADE DO PORTO


U.PORTO


UNIVERSITY OF HELSINKI


INTERNATIONAL IBERIAN
NANOTECHNOLOGY
LABORATORY


ICBAS | INSTITUTO DE CIÊNCIAS BIOMÉDICAS ABEL SALAZAR
SCHOOL OF MEDICINE AND
BIOMEDICAL SCIENCES


FCT
Fundação para a Ciência e a Tecnologia
MINISTÉRIO DA CIÊNCIA, TECNOLOGIA E ENSINO SUPERIOR


PhasAGE


EMBO

Agradecimentos

Todo o trabalho apresentado aqui só foi possível de ser realizado por ter tido ao meu lado uma equipa espetacular como esta. Sem ela, este trabalho não seria possível. Assim, gostaria de deixar aqui os meus melhores agradecimentos:

À Sandra Macedo Ribeiro, por me ter concedido esta oportunidade e por ter acreditado em mim. Por todo o apoio, incentivo e liberdade científica que me proporcionou ao mesmo tempo que me orientou por todos os desafios que surgiram.

Ao Paulo Ferreira, pelo desafio que me lançou em fazer-me aventurar por um Doutoramento. Por todos os debates científicos que me levaram até aqui. Por me ter dado acesso a novas ferramentas e oportunidades.

À Alexandra Silva, a minha “Xana”. Por toda a ajuda e orientação proporcionada ao longo destes anos todos, ao mesmo tempo que me permitiu criar uma relação de amizade que transcendeu ao Doutoramento.

Ao Luis Gales por toda a ajuda e disponibilidade.

Ao Gonçalo por ter sido o meu mentor durante o primeiro ano, e por ter continuado até hoje. Apesar da distância, sempre me ajudou e certificou que estava no caminho certo.

A todos os membros e ex-membros do BSF e MS, à Joaninha, Zsuzsa, Inês, Maria, Ritz, M&M, Pedro Martins, Pedro Pereira, Jorge, JAM, Martyna, Oleg, Saulé, Cláudia, Sára e Vitor. Por toda a ajuda! Pelas palavras, pela orientação, pelas imagens e revisões, pelos nachos e pizzas, pelos lanches de quinta-feira e por todas as novas histórias que agora tenho para contar. A todos vós, muito obrigado.

Ao INL por me ter proporcionado o acesso a máquinas de microscopia electrónica de topo e únicas em Portugal e em particular ao Oliver por me ter ajudado a iniciar no mundo do cryo-EM, pelas ajudas, reuniões e feedback proporcionado que nos ajudaram a chegar a bom caminho.

Ao Pedro Brites e ao meu colega e muito amigo Tiago Silva. Por um novo mundo de oportunidades que me proporcionaram.

To Sarah Butcher and everyone from her group and to the cryo-EM facility. Thank you very much for the opportunity and to treat me so well.

A todas as plataformas científicas do IBMC/i3S e do INL e aos seus membros por toda a disponibilidade e vontade em ajudar-me e em certificar que tinha todas as ferramentas necessárias para atingir os meus objetivos.

A todos os meus amigos, dentro e fora do mundo científico. Aos meus companheiros e de piscina. Obrigado a todos vós pelas palavras e gestos. Pelas viagens e concertos e tudo o resto que me servia de lufada de ar fresco para repor energias.

À minha família. Que sempre me apoiou e prestou ajuda. Que me acudiu sempre que precisei e que esteve sempre lá, mesmo quando eu não estive. Obrigado Mãe, Pai e Luis.

A elas. À Vera e as Marias! Às miúdas da minha vida. A minha âncora, o meu farol, meu abrigo, meu tudo! A Ti que foste sempre a primeira a dizer “vai”. A vocês a quem dedico o este trabalho e sem vocês eu não seria o que sou hoje. O meu muito e eterno obrigado.

Index

Abbreviations List

AD	Alzheimer's Disease
ALS	Amyotrophic Lateral Sclerosis
APS	Ammonium Persulfate
ASOs	Antisense Oligonucleotides
Atx3	Ataxin-3
BBB	Blood-Brain Barrier
cDNA	Complementary Deoxyribonucleic Acid
CMC	Critical Micellar Concentration
CRISPR	Clustered Regularly Interspaced Short Palindromic Repeats
Cryo-EM	Cryogenic Electron Microscopy
Cryo-ET	Cryogenic Electron Tomography
DLS	Dynamic Light Scattering
DMSO	Dimethyl Sulfoxide
DNA	Deoxyribonucleic Acid
DNAse	Deoxyribonuclease
DNS	Diffuse Nuclear Staining
DRPLA	Dentatorubralpallidoluysian Atrophy
DTT	Dithiothreitol
EDTA	Ethylenediamine Tetraacetic Acid
GCS	Granular Cytoplasmic Staining
HD	Huntington's Disease
HEPES	4-(2-Hydroxyethyl)-1-Piperazineethanesulfonic Acid
HMW	High Molecular Weight
IMAC	Immobilized Metal Affinity Chromatography
IPTG	Isopropyl β-D-1-Thiogalactopyranoside
JD	Josephin Domain
K_D	Dissociation Constants
K_{on}	Association Constants
LB	Luria Broth
LLPS	Liquid-Liquid Phase Separation

miRNA	Micro Ribonucleic Acid
MJD	Machado-Joseph Disease
NB	Nanobody
NMR	Nuclear Magnetic Resonance
NNI	Neuronal Nuclear Inclusions
OD	Optical Density
Pd	Polydispersity
PDB	Protein Data Bank
PEG	Polyethylene Glycol
PMSF	Phenylmethylsulfonyl Fluoride
PolyQ	Polyglutamine
PolyUb	Polyubiquitin
QBP1	PolyQ Binding Peptide 1
R_H	Hydrodynamic Radius
RNA	Ribonucleic Acid
RNAi	Ribonucleic Acid Interference
RNAse	Ribonuclease
ROS	Reactive Oxygen Species
RPM	Revolutions Per Minute
RT	Room Temperature
SBMA	Spinobulbar Muscular Atrophy
SCA	Spinorecebellar Ataxia
SCA1	Spinocerebellar Ataxia Type 1
SCA3	Spinorecebellar Ataxia Type 3
SDS	Sodium Dodecyl Sulfate
SDS-PAGE	Sodium Dodecyl Sulfate Polyacrylamide Gel Electrophoresis
SEC	Size Exclusion Chromatography
SH3	SRC Homology Domain
shRNA	Short Hairpin Ribonucleic Acid
siRNA	Small Interference Ribonucleic Acid
SPA	Single Particle Analysis
TBS	Tris-Buffered Saline

TEM	Transmission Electron Microscopy
TEMED	Thermo Scientific Tetramethylethylenediamine
TEV	Tobacco Etch Virus
ThT	Thioflavin-T
UBB	Polyubiquitin
UIM	Ubiquitin Interactive Motif
VHH	Variable Domain of Heavy Chain or Nanobody

Abstract

Machado-Joseph disease (MJD) also known as Spinocerebellar Ataxia Type 3 is an inherited neurodegenerative disorder of late onset. MJD is linked to the expansion of the polyglutamine (polyQ) tract in the ataxin-3 protein (Atx3). Although MJD was discovered more than 30 years ago, the correlation between polyQ expansion and the pathology of the disease is not completely understood. It is accepted that Atx3 can undergo a multistep amyloid assembly and that the hallmark of MJD is the presence of nuclear inclusions in patient's brain. These nuclear inclusions are rich in the mutant and expanded Atx3 and display predominant β-sheet structure. However, identifying which are the toxic species is still controversial.

Here we fully describe in detail a robust Thioflavin-T protocol to study Atx3 aggregation *in vitro* and highlight the major parameters that should be taken in consideration when studying Atx3 aggregation. We demonstrate how this protocol can be used in a high-throughput screening assay for the pursuit of a novel Atx3 aggregation inhibitor. A commercially available chemical library of more than 1200 compounds was quickly screened using the described ThT assay and 28 new possible candidates of Atx3 aggregation were found. Four different compounds were selected for further evaluation, using several different techniques. By combining transmission electron microscopy, size exclusion chromatography and dynamic light scattering we characterize how this compounds interfere in non-expanded and expanded Atx3 aggregation. The robustness of *in vitro* data allowed us to start our own *in cell* and *in vivo* experiments that are still ongoing.

At the same time, we improved a transmission electron microscopy negative staining protocol that allowed us to identify the different species that are formed during Atx3 aggregation. This was an important key to grant us access to state-of-the art cryo-Electron Microscopy equipment. Together with our University of Helsinki collaborators, we applied cryo-electron tomography in the study of non-expanded and expanded fibrils. Simultaneously, we also used Atx3-binding chaperones that can stabilize and compromise Atx3 aggregation, where we expect to identify intermediate oligomeric species.

Structural studies are fundamental to uncover and identify the ultrastructural features of self-assembled Atx3 species that are formed along the aggregation pathway. And this could be the first step to understand the toxicity of Atx3 in MJD.

Resumo

A doença de Machado-Joseph (MJD) também é conhecida por Ataxia Espinocerebelosa do Tipo 3 é uma doença neuro degenerativa hereditária de inicio tardio. A MJD está associada à expansão da região das polyglutaminas (polyQ) da proteína Ataxina-3 (Atx3). Apesar da MJD ter sido descoberta há mais de 30 anos, a correlação entre a expansão das polyQ e da patologia da doença ainda não está totalmente esclarecida. Está cientificamente aceite que a Atx3 consegue sofrer uma agregação amiloide em vários passos e que uma característica dos pacientes de MJD é a presença de inclusões neuronais nos seus cérebros. Estas inclusões são muito ricas em Atx3 expandida que demonstra uma estrutura predominante de *β-sheet*. Apesar disto, a identificação das espécies tóxicas na doença de MJD é ainda um tópico de muito controverso.

Neste trabalho descrevemos com detalhe um robusto protocolo de Tioflavina-T (ThT) para o estudo da agregação da Atx3 *in vitro* e destacamos os principais parâmetros que devem ser considerados ao estudar a agregação da Atx3. Demonstramos também como este protocolo pode ser utilizado numa triagem de alto rendimento na procura de um novo inibidor de agregação de Atx3. Uma biblioteca com mais de 1200 compostos diferentes foi rapidamente rastreada utilizando o protocolo ThT descrito e 28 possíveis novos inibidores da agregação da Atx3 foram identificados. Destes, quatro foram selecionados para uma avaliação mais profunda utilizando diferentes técnicas. Ao combinar microscopia eletrónica de transmissão com cromatografia de exclusão por tamanho e dispersão de luz dinâmica conseguimos caracterizar como estes compostos interferem na agregação da Atx3 expandida e não-expandida. A robustez dos nossos resultados *in vitro* permitiu-nos começar os nossos próprios ensaios *in cell* e *in vivo* que se encontram neste momento a serem realizados.

Ao mesmo tempo, melhoramos um protocolo de contraste negativo para microscopia eletrónica que nos permitiu identificar diferentes espécies de agregados que são formados durante a agregação da Atx3. Isto foi um passo muito importante para nos permitir obter acesso e financiamento para utilizarmos equipamento criomicroscopia eletrónica. Juntamente com os nossos colaboradores da Universidade de Helsínquia, aplicamos criotomografia eletrónica para estudar as fibras amiloides de Atx3 expandida e não-expandida. Simultaneamente, também utilizamos chaperones que se ligam à Atx3, conseguindo-a estabilizar e afetar a sua agregação. Com esta técnica esperamos conseguir identificar espécies oligoméricas intermédias.

Estudos estruturais são fundamentais para descobrir e identificar as características da ultraestrutura das espécies de Atx3 que se formam durante o processo de agregação. Estes resultados podem ser os primeiros passos para se perceber a toxicidade da Atx3 na MJD.

Chapter 1 - General Introduction

1.1 Polyglutamine diseases

Polyglutamine (polyQ) diseases are a group of rare disorders characterized by an abnormal trinucleotide CAG repeat expansion in the coding region of genes (Lieberman, Shakkottai, & Albin, 2019). The expanded CAG repeat is translated into an expanded polyQ tract in the resulting protein (Minakawa & Nagai, 2021). Expansion of glutamine repeats in disease-causing genes was described in nine inherited neurodegenerative disorders: Spinobulbar Muscular Atrophy (SBMA), Huntington's Disease (HD), Dentatorubralpallidoluysian Atrophy (DRPLA) and Spinorecebellar Ataxias (SCAs) 1, 2, 3, 6, 7 and 17 (Table 1). In addition, other diseases resulting from different trinucleotides repeat expansions have been also identified, such as Oculopharyngeal Muscular Dystrophy, Myotonic Type 1, Fragile X-Associated Tremor Ataxia Syndrome, Friedreich Ataxia, among others (Almeida, Fernandes, Abreu, & Macedo-Ribeiro, 2013).

Table 1 – Summary of polyQ repeat expansions diseases. [Adapted from Lieberman et al. (2019) and Almeida et al. (2013)]

Disease	Locus; gene	Protein	Normal polyQ tract length	Pathogenic polyQ tract	Normal function
SBMA	Xq11-q12; *AR*	Androgen receptor	6 - 36	38 – 70	Transcription factor
HD	4p16.3; *HTT*	Huntingtin	6 - 35	36 – 121	Likely scaffold protein
DRPLA	12p13; *ATN1*	Atrophin-1	3 - 38	49 – 88	Transcription corepressor
SCA1	6p23; *ATXN1*	Ataxin-1	6 - 34	39 – 88	Likely gene expression
SCA2	12q24; *ATXN2*	Ataxin-2	14 - 31	32 – 77	RNA metabolism
SCA3	14q24; *ATXN3*	Ataxin-3	12 - 40	55 – 86	Deubiquitinase
SCA6	19p13; *CACNA1A*	Cav2.1	4 - 18	21 – 33	Calcium channel
SCA7	3p21-p12; *ATXN7*	Ataxin-7	7 - 18	38 – 200	SAGA complex
SCA17	6p27; *TBP*	TATA-binding protein	12 43	45 – 63	Transcription factor

Abbreviations: SBMA - Spinobulbar Muscular Atrophy; HD – Huntington's Disease; DRPLA - Dentatorubralpallidoluysian Atrophy; SCA – Spinocerebellar Ataxia.

A feature common to all polyQ diseases is the pathogenic repeat expansion, which affects unrelated proteins with different functions (Table 1). Furthermore, polyQ diseases have a threshold phenomenon, meaning that once a certain number of trinucleotide repeats is reached, a complete or partial penetrance of disease is present in patients. However, the number of repeats associated with disease phenotype is distinct for each disease (Table 1). All polyQ diseases are neurodegenerative disorders with midlife onset of disease and a slowly progressive phenotype (Blum, Schwendeman, & Shaham, 2013). Pathogenic expanded proteins are ubiquitously expressed in different cell types and tissues of the human body but display a selective propensity to cause degeneration in neural tissue (Blum et al., 2013) through a progressive neuronal loss in certain regions of the brain or spinal cord that is specific for each disease (Seidel, Siswanto, et al., 2012). Patients suffering from polyQ diseases exhibit distinct motor and cognitive impairment and psychiatric alterations in accordance with the disease. The age of onset exhibits an inversely genotype-phenotype correlation in polyQ diseases, meaning that longer repeat tracts generally cause earlier onset disease (França Jr et al., 2012; Maciel et al., 1995). Another common hallmark of polyQ diseases is the presence of cytoplasmic and nuclear inclusions containing the pathogenic protein in the cells from affected regions of the brain or spinal cord (Lieberman et al., 2019). PolyQ proteins are also linked to the formation of β-sheet amyloid-like inclusions similar to those present in protein misfolding disorders. In these inclusions, additional proteins and macromolecules can be found such as ubiquitin and ubiquitin-binding proteins, proteasome components, chaperones, and transcriptional coregulators (Almeida et al., 2013; Lieberman et al., 2019; Minakawa & Nagai, 2021).

1.2 Machado-Joseph disease

Spinocerebellar Ataxia Type 3 (SCA3) or Machado-Joseph disease (MJD) is the most common autosomal dominant ataxia worldwide (Maria do Carmo Costa, 2020; Klockgether, Mariotti, & Paulson, 2019). MJD was first described by Coutinho and Andrade (1978) but previous studies had already described it as different diseases such as “Machado disease” (Nakano, Dawson, & Spence, 1972), “Nigrospino-dentatal degeneration” (Woods & Schaumburg, 1972), “Joseph disease” (Rosenberg, Nyhan, Bay, & Shore, 1976) or “Azorean disease of the nervous system” (Romanul, Fowler, Radvany, Feldman, & Feingold, 1977). Due to the high variability in clinical symptoms, the authors (Coutinho & Andrade, 1978) proposed that the above-mentioned disorders were in fact variations of the same disease. Although gait and limb ataxia are the main

clinical features of MJD, it is normally accompanied by other symptoms (Henry L. Paulson, 2007). Since there is a vast clinical presentation of MJD symptoms, four different subtypes of MJD were proposed (Coutinho & Andrade, 1978; Lima & Coutinho, 1980; Henry L. Paulson, 2007; Riess, Rüb, Pastore, Bauer, & Schöls, 2008; Rosenberg, 1992) according to the main symptoms presented by the patients (Table 2). Type 1 MJD is characterized by an early onset (before 20 years) and is the more aggressive form of MJD as it also progresses more quickly. Type 2 MJD is the most common type with an intermediate age of onset between 20 and 50 years. Type 3 MJD manifests later in life (age of onset > 40 years) and type 4 MJD is the rarest form of disease characterized by the parkinsonism symptoms together with other clinical features. Other common symptoms to all the subtypes can be present such as weight loss, restless legs syndrome and mild cognitive and behavioural problems (Maria do Carmo Costa & Paulson, 2012; Henry L. Paulson, 2007; Riess et al., 2008).

Table 2 – MJD subtypes and symptoms. Clinical features for the different MJD subtypes [Adapted from Maria do Carmo Costa and Paulson (2012)].

MJD Subtype	Symptoms
Type 1	• Ataxia; • Pyramidal signs: rigidity and spasticity (abnormal muscle tightness due to prolonged muscle contraction); • Extrapyramidal signs: bradykinesia (slowness of movement) and dystonia (involuntary muscle contraction).
Type 2	• Ataxia; • Progressive external ophthalmoplegia (paralysis or weakness of the eye muscles); • Pyramidal signs.
Type 3	• Ataxia; • Peripheral signs: motor neuronopathy (affecting motor nerves) and muscle atrophy.
Type 4	• Parkinsonism.

The brain pathology of MJD is severe affecting multiple neuronal systems. MJD patients display atrophy of the cerebellum and brainstem (Da Silva, Teixeira-Castro, & Maciel, 2019) as demonstrated by magnetic resonance imaging and macroscopic brain inspections (Seidel, Siswanto, et al., 2012). Microscopic analysis from post-mortem patients' brains also revealed neuronal loss in the cerebral cortex, basal ganglia,

thalamus, midbrain, pons, medulla oblongata and cerebellum (Seidel, Siswanto, et al., 2012) (Figure 1).

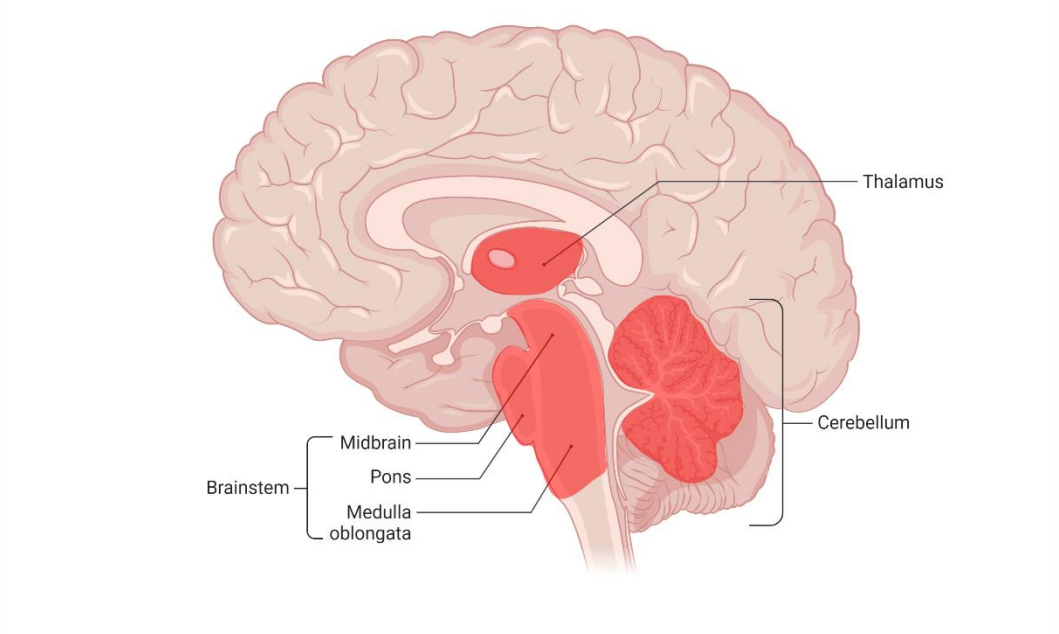

Figure 1 - Distribution of local neuronal loss in the brain of MJD/SCA3 patients. [Adapted from Seidel, Siswanto, et al. (2012)].

MJD is linked to the polyQ expansion of a variable size polyQ segment in Ataxin-3 (Atx3) protein (Table 1). Generally, when the Atx3 polyQ tract expands more than 60 repeats MJD symptoms appear (Henry L. Paulson, 2007), although some patients may present an incomplete penetrance if the threshold is above 45 repeats (Padiath, Srivastava, Roy, Jain, & Brahmachari, 2005). Atx3 protein is a multidomain protein with an N-terminal globular domain, called Josephin-Domain (JD), and a C-terminal low complexity region which includes the polyQ tract and two or three Ubiquitin Interactive Motifs (UIMs) (figure 2). The number of UIMs depends on the splice variant with the 3

UIM Atx3 being the predominant isoform found in brain cells (Harris, Dodelzon, Gong, Gonzalez-Alegre, & Paulson, 2010).

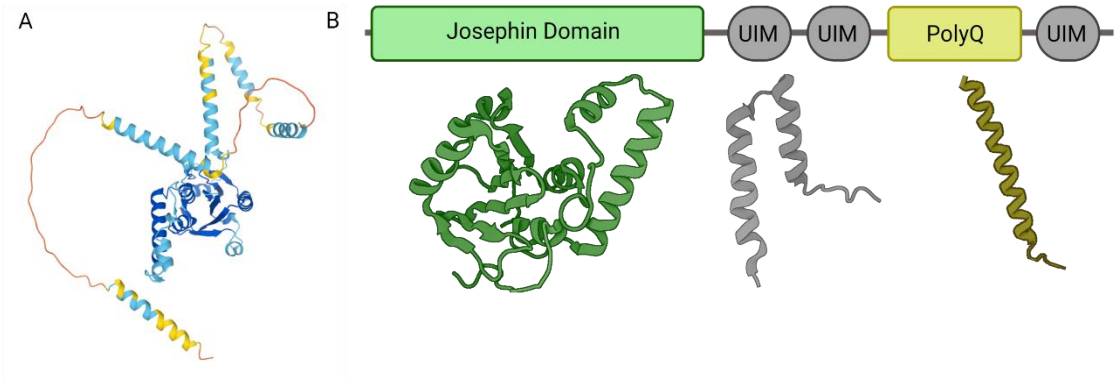

Figure 2 – Ataxin-3 is a multidomain protein with globular and intrinsically disordered domains. (A) AlphaFold (Jumper et al., 2021; Varadi et al., 2022) structure prediction of human Ataxin-3 (Uniprot P54252), with prediction model confidence of very high (dark blue), confident (light blue), low (yellow) and very low (orange). **(B)** Schematic representation of the structure of Ataxin-3, isoform UIM3 (Uniprot P54252-2) composed by the Josephin domain (green) and a flexible tail containing three ubiquitin interaction motifs (UIM) (grey) and the expandable polyQ stretch (yellow). Bellow the scheme are cartoon representations of JD, half-closed conformation of the mobile hairpin (PDB accession code 2dos), the UIM1-2 (PDB accession code 2klz) and the polyQ tract (PDB accession code 4wth).

Atx3 is a deubiquitinase and participates in the protein quality control pathway (Maria do Carmo Costa & Paulson, 2012). This complicated network is responsible for: assisting the folding of new formed proteins; making sure that proteins are generated in its right time and place; preventing protein misfolding and aggregation; avoiding accumulation of damaged or dysfunctional proteins, among others (Ciechanover & Kwon, 2017; Da Silva et al., 2019). In order to achieve this, it uses several molecular mechanisms such as ubiquitin-protease system, autophagy-lysosome system, unfolded protein response, SUMOylation and NEDDylation (Maejima, 2020) of which many proteins and molecular chaperones are essential for ensuing proteostasis and for the correct function of the protein quality control pathway. Atx3 function is associated to the regulation, stability or activity of other proteins (Maria do Carmo Costa & Paulson, 2012) it can interact with more than twenty different proteins with distinct functions such as signal transduction, cell quality control and transcriptional regulation (Almeida et al., 2013; Maria do Carmo Costa, 2020). However, for reasons that are not completely clear, this complex regulatory system becomes malfunctional with ageing, a feature linked with symptom development in several age-related neurodegenerative disorders such HD,

Alzheimer's disease (AD), Parkinson's disease (PD), Prion disease and Amyotrophic Lateral Sclerosis (ALS) (Ciechanover & Kwon, 2017; Liu et al., 2021).

1.3 Ataxin-3 aggregation in Machado-Joseph disease

1.3.1 *In vivo* studies

Protein aggregation and the presence of protein aggregates are a hallmark of polyQ diseases (Seidel et al., 2017). In these aggregates, it is common to find the disease-causing protein along with other proteins such as transcription factors, proteasome subunits, ubiquitin-like proteins, heat shock proteins and other polyQ proteins (Maria do Carmo Costa & Paulson, 2012; Henry L Paulson, 1999). There are several types of aggregates described in polyQ diseases, but the most common in MJD are the neuronal nuclear inclusions (NNI), granular cytoplasmic staining (GCS), diffuse granular nuclear aggregates (DNS, diffuse nuclear staining) and condensed aggregates in the axon (Seidel, Meister, et al., 2012; Seidel et al., 2017). Based on the analysis of post-mortem MJD brains, an aggregation model associated with pathology was proposed: GCS and DNS represent early stages of aggregation, since are rarely marked for p62 protein, a selective autophagy receptor that recognizes ubiquitinated proteins targeting the aggregates for degradation into autophagic vesicles (Seidel, Meister, et al., 2012). The appearance of NNI is an advanced stage of aggregation, since p62 protein and proteasomal stress markers such as polyubiquitins (polyUb) are commonly found in these structures, an indication of compromised ubiquitin proteasome systems. The last step of aggregation is characterized by the up-regulation of the HSP70 chaperone family, which are involved in the protein quality control system and are capable of refolding proteins in NNI. (Seidel, Meister, et al., 2012; Seidel et al., 2017). Protein aggregates evolve from GCS to DNS and then to NNI. In support of this model is the fact that there is no combination of GCS + NNI present and the p62 staining is clearly preferential to NNI (Seidel, Meister, et al., 2012; Seidel et al., 2017). NNI are not the best marker of MJD pathology since there are reports of their presence also in unaffected areas of the brain (Rüb et al., 2006; Yamada, Tan, Inenaga, Tsuji, & Takahashi, 2004), and the thalamic neurodegeneration occurs independently of the detection of NNI (Rüb et al., 2006). These contradictory findings suggest a non-correlation between the distribution of NNI and neurodegeneration, suggesting that NNI does not have a direct role in the fate (survival or death) of an affected neuron (Maria do Carmo Costa & Paulson, 2012; Rüb et al., 2006). It is possible that NNI could have more than one function including a

protective one, as they could act as a reservoir of pathogenic expanded protein (Seidel et al., 2017). Different types of aggregates exist in the MJD patient's brain and each type of aggregate accumulates specific cellular material (Seidel, Meister, et al., 2012; Seidel, Siswanto, et al., 2012; Seidel et al., 2017). This implies that Atx3 could interact with a large amount of different proteins and potentially trigger several interconnected pathogenic cascades in MJD (Maria do Carmo Costa & Paulson, 2012).

Studies on the molecular composition of these aggregates and their structures would allow us to uncover the correlation between the neurodegeneration and its role in disease progression and possibly other aspects of MJD. It is important to consider that all these studies were based on post-mortem analysis, after a fully penetrance of the disease. In late stages of the disease, the brains of MJD patients are significantly lighter than the brains without any neurological or psychiatric disease (Maria do Carmo Costa & Paulson, 2012) meaning that a big neuronal loss is present in these patients. Considering that all post-mortem findings are made in the surviving cells, the interpretation of the results should be made with caution.

1.3.2 *In vitro* studies

In vitro studies showed that the expansion of the polyQ region to pathological ranges promoted the formation of insoluble β-sheet rich fibrils positive for Congo-red staining (Bevivino & Loll, 2001). Later it was demonstrated that normal non-expanded Atx3 could also form fibrillar insoluble structures when destabilized by denaturation agents (Chow, Paulson, & Bottomley, 2004). The JD alone could also form insoluble fibrils (Masino et al., 2004) in partially destabilizing conditions suggesting that other regions besides the polyQ tract had a role in Atx3 aggregation and fibril formation. Gales et al. (2005) demonstrated that JD and non-expanded Atx3 could aggregate and form fibrillar structures in near-physiological conditions. A combination of limited proteolysis and mass spectrometry studies helped uncover the aggregation-prone region of the JD that formed the protofibrils core (Ellisdon, Thomas, & Bottomley, 2006; Masino, Nicastro, Calder, Vendruscolo, & Pastore, 2011; Scarff et al., 2013). The currently accepted model for Atx3 aggregation consists of a two-step process (Ellisdon et al., 2006). The first step is JD dependent and is common to both expanded and non-expanded Atx3, leading to the formation of fibrils that are not SDS-resistant (Figure 3). A second step, exclusive to the expanded pathological Atx3, is mediated by the expanded polyQ segment and leads to the assembly of mature and SDS-resistant Atx3 fibrils (Figure 3). The protein structures formed in the first step of Atx3 aggregation are detected with A11, OC and

Atx3 1H9 antibodies (Figure 3). Antibody A11 is specific for several toxic amyloid and amyloid-like oligomers and Antibody OC is specific for amyloid fibrils (Glabe & Kayed, 2006; Kayed et al., 2003).

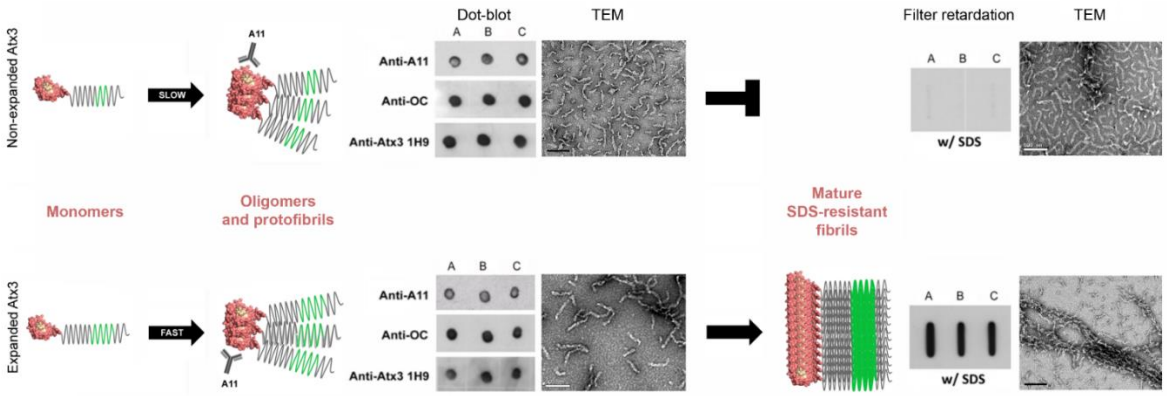

Figure 3 – The two-step model of Atx3 aggregation. The first step of Atx3 self-assembly, common to "normal" and polyQ expanded Atx3, is seeded by the aggregation-prone JD segment. A second step, exclusively dependent on the polyQ expansion, leads to the generation of mature and SDS-resistant Atx3 fibril. The first step of aggregation forms oligomers that are recognized by the A11 antibody, which recognizes some oligomeric species. When analysed by dot-blot assay, the first step of Atx3 aggregation, both expanded and non-expanded samples are positive for A11, OC and 1H9 (anti-Atx3 antibody) antibodies. Filter retardation assay shows SDS-resistant fibrils in expanded Atx3 stained with 1H9 antibody. A, B and C are replicas. [Adapted from Silva, de Almeida, and Macedo-Ribeiro (2018)].

Although JD has a crucial role in Atx3 aggregation, other studies showed that the flexible region, which includes UIM1 and UIM2, also contributes to the Atx3 aggregation without altering its structure or stability. (Invernizzi, Lambrughi, Regonesi, Tortora, & Papaleo, 2013; Santambrogio et al., 2012). It was proposed that UIM1 and UIM2 interact through intermolecular electrostatic interactions (Invernizzi et al., 2013), thus increasing the local concentration of JD and promoting aggregation in the absence of the polyQ region. Silva et al. (2017) using Dynamic Light Scattering (DLS) complemented with Transmission Electron Microscopy (TEM) and Size Exclusion Chromatography (SEC) proposed a mechanism for non-expanded Atx3 self-assembly and estimated the rate constants of the elementary steps of this process. The authors also showed that, *in vitro*, in the beginning of Atx3 aggregation, the most common monomeric species have an average radius of 1.7 nm that then develop into (proto)fibrils that reach an average size of 91 nm at the end of the fibrillization process (Silva et al., 2017). This multi-step aggregation seeded by aggregation-prone regions outside the polyQ region is not exclusive to Atx3/MJD, and it is also observed in other polyQ disorders such as SCA1, SMBA and HD (Figure 4) (Asencio-Hernández et al., 2014; de Chiara, Menon, Dal Piaz, Calder, & Pastore, 2005; Oppong et al., 2017; Thakur et al., 2009).

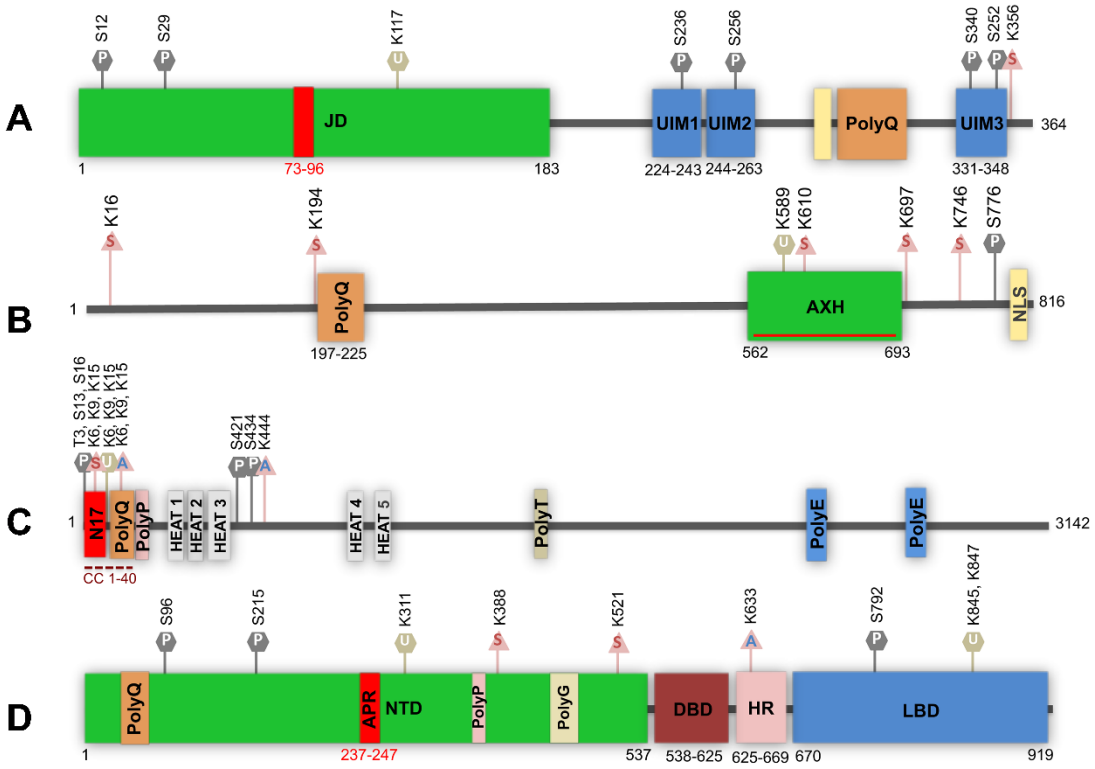

Figure 4 – Schematic representation of polyQ proteins with aggregation prone regions outside the polyQ region. In red are marked the Aggregation Prone Regions (APR) of **(A)** Ataxin-3, **(B)** Ataxin-1, **(C)** Huntingtin and **(D)** Androgen Receptor proteins. [Adapted from Silva et al. (2018)].

Aggregation of proteins containing polyQ regions and other subunits that can influence the aggregation process, implies a self-assembly multistep mechanism for these proteins, which can be regulated by multiple factors, including post-translational modifications and the presence of interacting proteins or other molecules. For most of the diseases linked with protein aggregation, the mechanisms underlying cell-specific death and degeneration are still unknown. The biochemical studies to explore in a stepwise manner the influence of various factors, which can be cell-specific, on Atx3 aggregation are critical to understand their role for disease-related and cell-specific death. This subject is explored in detail in the Chapter 2.

1.4 Ataxin-3 aggregation and toxicity

Protein aggregation into amyloid structures is a very dynamic phenomenon, and between the monomeric protein and the amyloid fibrils, there are several intermediate

physical states in which proteins could be, such as monomers, dimers, tetramers, non-β oligomers, nanofibrils, amyloid fibrils, clustered amyloid fibrils and plaque formation (Wetzel, 2020). The process of amyloid fibril formation is summarized in Figure 5 which shows how a monomeric protein assembles into amyloid fibrils by a generic nucleation and growth mechanism (Iadanza, Jackson, Hewitt, Ranson, & Radford, 2018), which can be divided into three major steps: nucleation phase, an elongation phase and stationary phase (Figure 5). This is a very dynamic process where native proteins can be in equilibrium with their unfolded and/or partially folded state. The first step of assembly (nucleation step) is the formation of an altered conformer or oligomer, which are transient and often heterogeneous, for which determining their structure is technically challenging (Glabe, 2006). Then these oligomers can continue to associate and form higher-order species which are precursors for amyloid fibrils (on-pathway) or dead-end assemblies that will not form amyloid fibrils (off-pathway) (Ferrone, 1999). Although off-pathway oligomers do not form amyloid fibrils, they might be toxic and have a pertinent role in the disease (Iadanza et al., 2018). These on-pathway oligomers continue to assemble further into high-order oligomers, where one or more can make a fibril nucleus, which by rapidly recruiting other monomers can polymerize into the amyloid fibrils (Ferrone, 1999; Iadanza et al., 2018). Fibrils will continue recruiting monomers into their ends - this exponential growth corresponds to the elongation phase (Figure 5). When a β-strand fragments, this generates two new fibril ends that can continue to recruit monomers. At the same time, another process such as secondary nucleation can occur, in which the oligomer formation is catalysed by the surface of a pre-existing fibril (Ferrone, 1999; Linse, 2017), hence increasing the rate of fibril formation. When almost all monomer is depleted because it was used to form fibrillar material, the aggregation process enters a plateau, the stationary phase (Figure 5). The mechanism and elementary kinetic rate constants of the different steps leading to protein aggregation may be estimated from physical models, some of which are available online (F. Cohen & Kelly, 2003; Oosawa & Asakura, 1975; Sárkány, Rocha, Damas, Macedo-Ribeiro, & Martins, 2019; Xue, Homans, & Radford, 2008).

Recently, several studies have shown that pathological fibrillization could be preceded by a Liquid-Liquid Phase Separation (LLPS) of the pathogenic protein (Burke, Janke, Rhine, & Fawzi, 2015; Molliex et al., 2015; Patel et al., 2015; Peskett et al., 2018). Briefly, proteins can form non-membrane bound structures that behave like liquid droplets and can flow, fuse and maintain spherical shape after fusion (Hyman, Weber, & Jülicher, 2014). Because these droplets increase local protein concentration, LLPS of pathological proteins increases the propensity to form amyloid-like fibrils (Molliex et al.,

2015). This phenomenon was already described for proteins that are involved in different neurodegenerative diseases such as AD, ALS, Frontotemporal Dementia, Inclusion Body Myopathy and HD (Burke et al., 2015; Molliex et al., 2015; Patel et al., 2015; Peskett et al., 2018; Wen et al., 2021). Using yeast cells expressing huntingtin exon1 Peskett et al. (2018) showed that, the liquid-like assemblies could convert into solid-like assemblies with fibrillar structures. Recently, Murakami et al. (2021) showed that non-expanded Atx3 could undergo LLPS in the presence of polyethylene glycol (PEG), which mimics intracellular crowding. Since this is a recent subject, more studies on the mechanism of LLPS and the subsequent aggregation process are still needed.

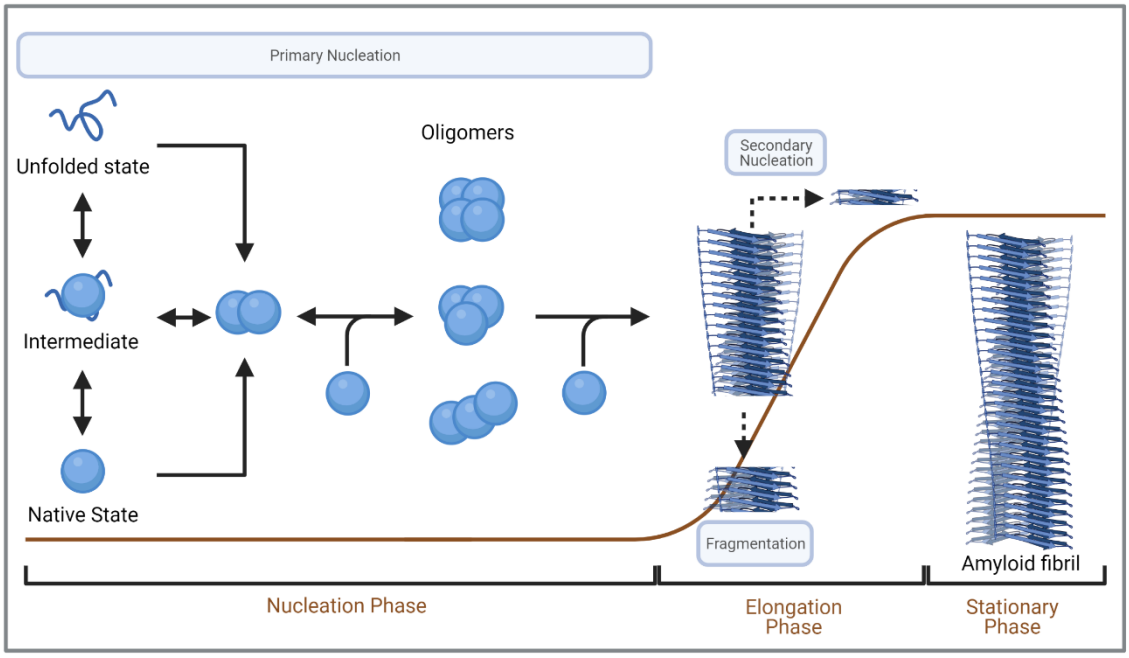

Figure 5 - Schematic representation of amyloid fibril formation. Native proteins are in equilibrium with their less-structured, partially folded and/or unfolded state. One of these states initiates amyloid fibril formation by assembling into oligomer species which will continue to aggregate and form a fibril nucleus. This rapid process will continue by recruiting more monomeric protein and then nucleate assembly into amyloid fibrils. This process occurs in the nucleation phase also called the lag time of assembly. As fibrils continue growing, they can fragment (which generates more fibril ends that can elongate) or can seed more fibril formation by secondary nucleation. This elongation is made in exponential growth (brown line) and it is called the elongation phase and continues until almost all monomeric protein was converted into a fibrillar form where it reaches the stationary phase. [Adapted from Iadanza et al. (2018)].

In vitro, aggregation kinetics can be measured by using the dye Thioflavin-T (ThT), which binds to β-sheet present in amyloid fibrils (S. Cohen et al., 2013; Groenning et al., 2007) and generates an enhanced fluorescence signal. ThT is not the only available staining dye for amyloid structures, Congo Red, Thioflavin-S, Congo Corinth, Benzopurpurin, Vital Red, Trypan Blue, Amidoblack 10B, Biebrich Searlet WS, Aniline

Blue WS and Acid Fuchsin are other dyes that can also be used (Yakupova, Bobyleva, Vikhlyantsev, & Bobylev, 2019). ThT is widely used to investigate amyloid formation *in vitro*, however, it is not the best reporter to study intermediate oligomeric species that are formed during aggregation, although it can bind to some of them (Gade Malmos et al., 2017; Yakupova et al., 2019). ThT kinetics can be used to study how different additives (drugs, solutions, molecular chaperones, small molecules, detergents or synthetic membranes and even protein mutations) can interfere with protein aggregation and even identifying the type of aggregation modulator (Iadanza et al., 2018; Sárkány et al., 2019). In Chapter 2 and Chapter 4, ThT assay is used to evaluate how Atx3 aggregation is affected in the presence of different additives.

Protein aggregation or protein propensity to aggregate can also be predicted using several different protein aggregation predictors. Currently there are more than 30 different computational methods to evaluate aggregation like: TANGO (Fernandez-Escamilla, Rousseau, Schymkowitz, & Serrano, 2004), Beta-strand Contiguity (Zibaee, Makin, Goedert, & Serpell, 2007), PASTA (Walsh, Seno, Tosatto, & Trovato, 2014), AmyloGram (Burdukiewicz et al., 2017) and AggreRATE-Pred (Rawat, Prabakaran, Kumar, & Gromiha, 2020). These algorithms analyse different protein parameters like, β-strand formation, amyloidogenic regions, overall aggregation, energy and β-sheet conformation. Most of these predictors are web-based and their input is the protein sequence and/or Protein Data Bank (PDB) file.

Studies of several diseases involving proteins with the ability to form amyloid fibrils, proposed that oligomeric intermediates formed during aggregation were the major toxic species. Some examples are, HD and other polyQ diseases (Henry L. Paulson, 2007; Wetzel, 2020), PD (Winner et al., 2011), AD (Benilova, Karran, & De Strooper, 2012; Karpinar et al., 2009) and ALS (Sangwan et al., 2017). A major theory supporting these findings, suggests that toxicity from this oligomeric species arise from their misfolded nature, since they display in their surface chemical groups that normally are not exposed to the cellular environment (Knowles, Vendruscolo, & Dobson, 2014). These groups have a hydrophobic nature and inappropriately interact with cellular components, causing toxicity by affecting proteasomal degradation, impairment of autophagy, perturbation of mitochondrial function, production of reactive oxygen species (ROS), sequestration of other proteins and disruption of membranes (including from mitochondria, endoplasmic reticulum, lysosomes and plasma membrane) (Iadanza et al., 2018; Knowles et al., 2014). For instance, in AD, patients with severe cognitive decline do not correlate with the plaque formation, suggesting that pre-amyloid aggregates are the cause of the disease (Glabe, 2006; Glabe & Kayed, 2006; Winner et

al., 2011). *In vitro* studies corroborated the cytotoxic capabilities of oligomers and how can they disrupt membranes (Evangelisti et al., 2016; Serra-Batiste et al., 2016). This was backed up with studies using proteins that are not associated with amyloidosis, like SRC Homology 3 (SH3) domain and HypF, which showed that oligomers formed from these two proteins are highly cytotoxic (Baglioni et al., 2006; Bucciantini et al., 2002). However, is important to note that a study from Fusco et al. (2017) with different α-synuclein oligomers revealed that not all oligomers are toxic and Karamanos et al. (2019) showed that oligomers from a truncated variant of human β2-microglobulin are also not cytotoxic.

The correlation between protein aggregation and toxicity it is not clearly understood and this uncertainty is also applied for the polyQ proteins. *In situ* experiments using a yeast model for HD showed that huntingtin polyQ expansion promotes alterations in mitochondria and lipid droplet morphology (Gruber et al., 2018). This study showed that huntingtin fibrils interact and deform cellular membranes, suggesting that fibrils could be disease-relevant and not just inert end-stage products of aggregation (Gruber et al., 2018; Tipping, van Oosten-Hawle, Hewitt, & Radford, 2015). Drombosky et al. (2018) engineered a huntingtin exon1 analogue with a short polyQ tract, well below the pathogenic threshold, that quickly formed amyloid fibrils and caused HD-like toxicity in rat neurons and *Drosophila*. Their extensive study showed that huntingtin exon1 toxicity is associated with the aggregation propensity and not to the polyQ tract extension. This same conclusion was also corroborated with other *in vitro* and *Drosophila* experiments where strong HD-like toxicity is generated from huntingtin exon1 molecule with a polyQ tract bellow the pathological threshold (Wetzel, 2020). Although different studies imply that amyloid-like aggregates are the toxic entities in HD, they do not address their ultrastructure. Several *in vitro* studies using polyQ peptides showed that the aggregation process occurred without the formation of β-sheet-rich intermediates (Chen, Ferrone, & Wetzel, 2002), the polyQ aggregation was a highly specific process correlated with the molecular structure of product, meaning that not all polyQ aggregates presented Congo red birefringence (Chen, Berthelier, Hamilton, O'Nuallai, & Wetzel, 2002) and when using polyQ peptides with different lengths, those which were bigger than 37 residues had higher chances to spontaneously form ordered amyloid-like aggregates, in comparison with 15-20 residues polyQ peptides (Chen, Berthelier, Yang, & Wetzel, 2001). More recently Ruggeri et al. (2016) explored the morphological, mechanical and structural properties of a single oligomeric and fibrillar huntingtin exon1 species. By combining different high-resolution methodologies, they showed that cross-β sheet structure smoothness, stiffness and content increased proportionally with the polyQ length.

Although most of the polyQ studies are performed using huntingtin, a study from Amigoni et al. (2019) showed that methacycline reduced toxicity in an MJD *Caenorhabditis elegans* model. Methacycline specifically binds to oligomers of the JD and it does not alter Atx3 aggregation kinetics nor changes the secondary structure of final aggregates, instead increases the solubility of the aggregated species (Amigoni et al., 2019).

The original findings on amyloid fibrils were associated as the causative agent of disease (Glenner, Terry, Harada, Isersky, & Page, 1971) but now they are more associated with end-stage products of aggregation (Tipping et al., 2015). Because protein aggregation is dynamic process, several different protein aggregates co-exist at the same time. There is a heterogeneous population of protein aggregates, which makes the task of identifying which are the toxic species a great challenge, currently unsolved. With the advances in new technologies, such as cryo-Electron Microscopy (cryo-EM), combined with other biophysical measurements scientists will in the future uncover which amyloid aggregation pathway, which intermediates structures and/or fibril structures are responsible for the disease. Cryo-EM also was used to show that *in vitro* amyloid fibrils are sometimes, structurally different from the ones extracted from tissues of patients or animals, such as serum amyloid A (Bansal et al., 2021), heparin-induced tau filaments (Zhang et al., 2019), amyloid-β (Kollmer et al., 2019) and α-synuclein (Schweighauser et al., 2020). *In situ* studies using cryo-EM on intracellular inclusions will certainly reveal which fibril/amyloid structures correlates with disease phenotype and how the cellular function is disrupted. More studies that would reveal details and structures of oligomeric and fibrillar species are important to understand why different species have different toxicities.

1.5 Structures of polyQ proteins

The determination of the three-dimensional structure of the polyQ proteins is the first step to understand the role of the polyQ segment on protein structure and the impact of polyQ expansion on the structure and function of the carrier proteins. Together with the mechanistic information on the aggregation pathways, information about the structures of polyQ-containing proteins could provide valuable clues for structure-based design of anti-aggregation molecules. Protein structures can be experimentally determined by X-ray crystallography, solid-state or solution Nuclear Magnetic Resonance (NMR), and more recently by “new” state of the art cryo-EM. The coordinates for all experimentally determined three-dimensional structures of proteins are deposited

at the PDB. Currently, there are more than 200.000 structure depositions from which, around 165.000 were obtained by X-ray crystallography, 14.000 by NMR and 11.000 by EM (source: www.wwpdb.org). Since there are millions of known proteins but only a fraction of them have their structure available, scientists developed protein structure predictors, such as AlphaFold (Jumper et al., 2021), RoseTTAFold (Baek et al., 2021) or Amber (Case et al., 2008). This allow scientists to predict 3D protein structure, like Atx3 (Figure 2A) based on its amino acid sequence.

Scientists are studying the structure of polyQ proteins and in the last few years' new insights have been found, but unfortunately much is still missing. Determining the structure of polyQ regions has been a challenge since they appear to be very unstable (Totzeck, Andrade-Navarro, & Mier, 2017). Studies suggest that polyQ regions have predominantly a random coil conformation, but there are also evidences for the presence of a β-sheet and helical structure (Masino, 2004; Papaleo & Invernizzi, 2011; Totzeck et al., 2017). There is no consensus in regard to the structure of polyQ itself, since some authors propose that both pathogenic and non-pathogenic polyQ structure is largely the same (Klein et al., 2007) while other authors claim that here is a change in the secondary structure (Davies et al., 2008). However, there is a clear agreement that their aggregates are highly rich in β-sheet (Poirier, Jiang, & Ross, 2005). In PDB it is possible to find the structure of the antigen-binding domain from three different anti-polyQ antibodies, 1C2 (entry 4JJ5), MW1 (PDB entry 2OTW) and 3B5H10 (PDB entry 4DCQ) that were used to probe the conformation of polyQ. Klein et al. (2013) showed that in fact these three different antibodies interact similarly with polyQ of various lengths and therefore they do not recognise a mutant-specific and toxic polyQ conformation. An important study from Urbanek et al. (2020) showed that both polyQ flanking regions in huntingtin exon1 have a structural effect. Protein probably uses these flexibility and versatility of polyQ region to perform its biological functions without aggregate or exert toxicity. This study also shows that observations made from isolated polyQ regions should also be interpreted with caution, and authors encourage to always include polyQ flanking regions in biophysical studies (Urbanek et al., 2020).

In regard to polyQ proteins, they are unstructured, flexible and very difficult to crystallize (Totzeck et al., 2017) and until now, no single complete polyQ protein structure was deposited in PDB, which the structure determied by X-ray crystallization. Computational analysis by Totzeck et al. (2017) to PDB data base, showed that the secondary structure in polyQ proximity is predominantly random coil or helix and these regions are often not solved in 3D structures. There are a few solved domains of polyQ-containing proteins available at PDB, such as AXH domain from Ataxin-1 (PDB entry

1AO8), 16 peptides from Ataxin-2 in complex with PABPC1 (PDB entry 3KTR), zinc finger domain from Ataxin-7 (PDB entry 2KKR), IQ domain from Cav2.1 (PDB entry 3BXK), AF2 and FXXLF motifs from AR protein (PDB entry 1XOW) and the TATA-binding core domain (PDB entry 1CDW).

Although there is no available a 3D structure for complete Atx3 protein at the moment, Nicastro et al. (2005) determined for the first time the structure of Atx3 JD using solution NMR (Figure 6A - Nicastro et al. (2005)). In this study, the authors show that JD consists of two subdomains separated by a cleft. The N-terminal subdomain includes four α-helices and the C-terminal contains a six-stranded antiparallel β-sheet. JD has a relatively rigid structure with a flexible helical hairpin formed by α_1 and α_2, extending from the core structure (Nicastro et al., 2005). In the same year, Mao and colleagues deposited in PDB another structure of Atx3 JD (Figure 6B) also determined by solution NMR. The results are similar to the previous study: JD adopts an α/β fold with a six-stranded antiparallel β-sheet flanked on both sites with seven α-helices (Mao et al., 2005). There are two clear conformational changes, in the α_2 helices (Figure 6) because of protein flexibility associated with Atx3 deubiquitinating activity (Mao et al., 2005; Nicastro et al., 2005).

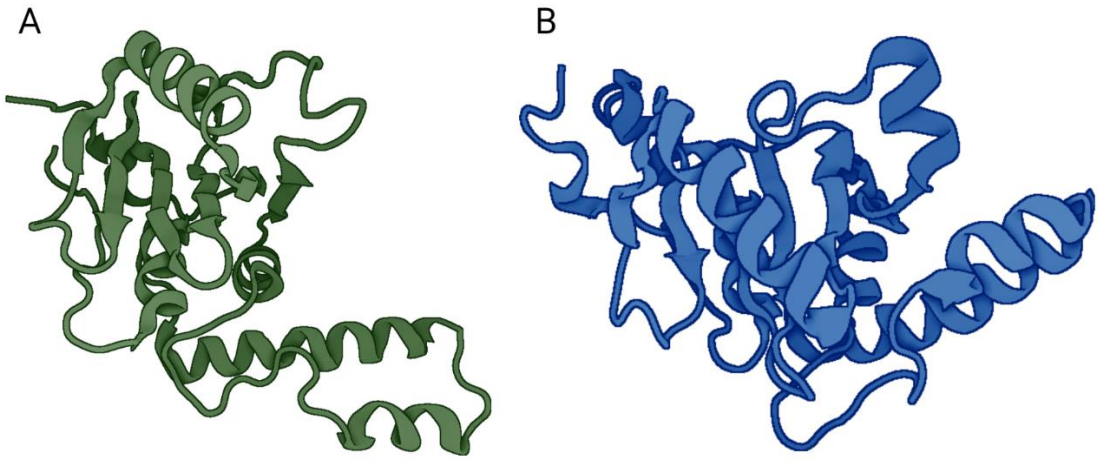

Figure 6 – Solution structure of the Josephin Domain of Atx3. Cartoon representations of JD from Atx3. **(A)** PDB entry 1YZB from Nicastro et al. (2005). **(B)** PDB entry 2AGA from Mao et al. (2005).

Later, with the work of Satoh et al. (2014) focused on the deubiquitinase activity of Atx3, used solution NMR to determine another NMR structure form JD. In that structure, there are core similarities with the previous ones, although the α_2-α_3 that make the extended helical arm had structural differences (Figure 7). Authors suggest that these differences could arise from the different experimental conditions since slightly different

temperatures were used and the pH varied in the three studies. Flexibility of this region was proposed to be critical for the recognition mode of specific substrates by JD (Mao et al., 2005; Nicastro et al., 2005; Satoh et al., 2014). Hence, JD could alternate between closed (Figure 7B, Mao et al. (2005)), half-open (Figure 7C, Nicastro et al. (2005)), open and half-closed (Figure 7D and 7A respectively, Satoh et al. (2014)). These three studies confirmed that JD possesses a highly flexible extended helical arm in dynamic equilibrium between open and closed states that could be important for substrate recognition (Mao et al., 2005; Nicastro et al., 2005; Satoh et al., 2014).

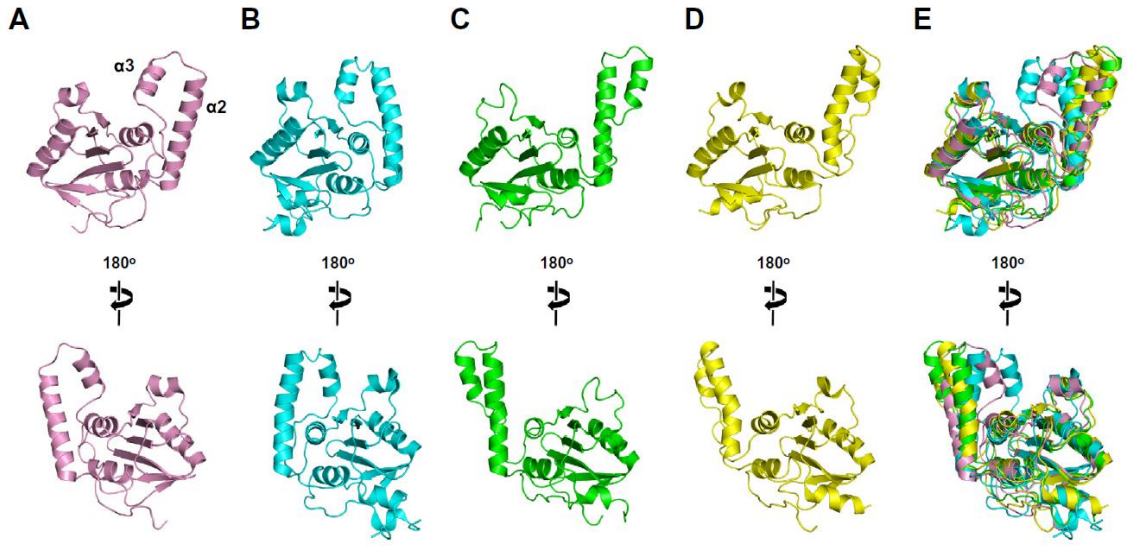

Figure 7 – Comparison of the solution structures of the Josephin Domain of Atx3. Cartoon representations of JD from Atx3. **(A)** Half-closed (pink, PDB entry 2DOS), **(B)** Closed (cyan, PDB entry 2AGA), **(C)** Half-Open (green, PDB entry 1YZB), **(D)** Open (yellow, PDB entry 2JRI), **(E)** their superimposed models. [The image was taken with permission from Satoh et al. (2014)].

The structure of the tandem UIM domain of Atx3 in complex with ubiquitin (PDB entry 2KLZ) was also determined using solution NMR. In that structure, it is possible to observe that both UIM1 and UIM2 consist of two α-helices and a flexible linker (Figure 2B) (Song et al., 2010). More recently, Zhemkov, Kulminskaya, Bezprozvanny, and Kim (2016) obtained a 2.2 Å resolution from two different crystal forms of the C-terminal tails of Atx3 in fusion with maltose binding protein. The structure of the Atx3 C-terminal region, which includes 13 glutamine residues adopted both random coil and α-helical conformation in the crystal structures (PDB entry 4WTH).

Regarding huntingtin and its domains, there are several entries in PDB of its N-terminal residues (PDB entries 2LD2, 2LD0, 4RAV and 3LRH), but a study from Guo et al. (2018) using a cryo-EM approach, showed for the first time the structure of a full-length polyQ-containing protein at 4 Å resolution in complex with the HAP40 protein, a

known huntingtin interactor involved in endocytosis. This later was improved by Harding et al. (2021) where they combined cryo-EM, Small-Angle X-ray Scattering and Cross-Linking Mass Spectrometry to obtain the structures of both wild type and mutant huntingtin. Although this study did not resolve all flexible and disordered regions (~25% of huntingtin-HAP40 complex), they were able to show a 2.6 Å resolution structure, revealing that the polyQ expansion in mutant huntingtin has a greater conformational heterogeneity than that of the wild type protein (Harding et al., 2021). This study confirmed the existence of a central cavity that is formed by the folding of N- and C-terminal huntingtin regions and how these structural characteristics are affected by polyQ expansion (Vijayvargia et al., 2016).

These findings are a clear example on how structural studies have shown the protein's architecture and provided foundation for the functional and drug development studies that target huntingtin and other polyQ proteins. This latter study also showed the structural consequences of the huntingtin polyQ expansion. This was possible by the development/improvement of new technologies such as cryo-EM, coupling the pet protein with a known interactor and complementing several biophysical studies at the same time. Except for huntingtin, no other full length polyQ protein structure is available at the moment. Our work proposed to tackle this, by combining Atx3 with a chaperone that stabilizes Atx3 and prevents its aggregation, at the same time that we applied a cryo-EM approach to obtain a high-resolution structure. Another objective from our work is to use cryo-EM in a time-course analysis to obtain structural information on the oligomers and fibrils that are formed during the Atx3 aggregation pathway for both normal and mutant protein.

1.6 Therapies for Machado-Joseph disease

The hallmark of MJD and other polyQ diseases are the inclusion bodies that found in *post-mortem* patient's brains (McGowan et al., 2000; Henry L Paulson et al., 1997; Seidel, Meister, et al., 2012; Seidel et al., 2017). These inclusion bodies consist mostly in proteins with expanded polyQ tract, although at the moment there is no unanimity in the role of these inclusions in disease. Some authors claim that they are unspecific or characteristic for a particular disease or that they have a protective role since functioning as a reservoir of mutant protein (Da Silva et al., 2019; Minakawa & Nagai, 2021). The role of Atx3 aggregation in the MJD pathogenesis is still unclear, but it is accepted that mutant and toxic Atx3 misfolds, resulting in the deposition of insoluble intracellular aggregates that sequester critical protein quality control machinery, thus

contributing to neuronal stress and death (Da Silva et al., 2019; McLoughlin, Moore, & Paulson, 2020; Henry L Paulson, Shakkottai, Clark, & Orr, 2017). This is likely true for other polyQ diseases (McLoughlin et al., 2020; Henry L. Paulson, 2007). To increase even further the complexity of identifying the toxic species in MJD, Li, Yu, Teng, and Bonini (2008), using a *Drosophila* model, showed compelling evidence that CAG repeat RNAs had a toxic effect. Without fully understanding the clearly complex mechanism of toxicity of MJD and other polyQ diseases, the development of any therapeutic agents should be made with caution to assure the most efficient and safe therapy possible.

In the last years, there has been important advances in the field towards the search for a new therapy for MJD, using cutting-edge approaches in a multi-complex tissue that is the brain. Different types of therapeutics are being developed for this multi-level system, since there are numerous possible approaches: molecular approaches for DNA or RNA therapies that could prevent protein aggregation or promote protein degradation; targeting mutant proteins by promoting proteostasis or transcriptional dysregulation; targeting abnormal protein-protein interactions; pharmacological approaches to correct neuronal and neurotransmission defects, cell dysfunction, levels of hormones and/or trophic factors and calcium homeostasis (Maria do Carmo Costa, 2020; Da Silva et al., 2019; Duarte-Silva & Maciel, 2018; Minakawa & Nagai, 2021; Neves-Carvalho, Duarte-Silva, Teixeira-Castro, & Maciel, 2020).

Although the genetic cause involved in MJD and other polyQ diseases was already identified 30 years ago, allowing for extensive research and progress towards understanding the pathogenesis of polyQ diseases, no effective treatment is available to mitigate or even reduce the severe impact of these highly incapacitating and fatal disorders (Klockgether et al., 2019). To this date, all the pharmacological and non-pharmacological treatments available for MJD are purely symptom-related, aiming to improve neurological symptoms and enhance patients' quality of life (Da Silva et al., 2019; Duarte-Silva & Maciel, 2018). The current pharmacological treatments used for MJD are tailored for each patient taking into consideration each symptom and other comorbidities present (Table 3) (Da Silva et al., 2019; Saute & Jardim, 2018). Treatment response is also variable and needs to be continuously monitored and adjusted when required (Da Silva et al., 2019). At the same time, non-pharmacological treatments are recommended such as exercise/physical therapy (to increase muscle strength and maintain independence), mobility aids like canes, crutches, walkers, wheelchairs and others (to allow independent activity and avoid social isolation), speech therapy (for the treatment of speech impairments and difficulty in swallowing), occupational therapy (to counteract depressive symptoms) and lifestyle and home adaptations (to preserve a

sense of independence in patients) (Da Silva et al., 2019; Duarte-Silva & Maciel, 2018; Neves-Carvalho et al., 2020).

Table 3 – List of available symptomatic pharmacological treatments for MJD. [Adapted from Da Silva et al. (2019); Saute and Jardim (2018)].

Symptom	**Pharmacological Treatment**
Ataxia	Varenicline (recommended to improve gait)
Spasticity	Botulinum toxin administration and/or complementary pharmacological therapies: phenol blocks, baclofen, benzodiazepines or gabapentin
Dystonia	Trihexyphenidyl, baclofen, tetrabenazine, dopaminergic drugs or botulinum toxin (for focal dystonia)
Muscle Cramps	Mexiletine or carbamazepine
Parkinsonism	Levodopa or dopaminergic agonists
Ophthalmological Symptoms	Gabapentin or baclofen
Vestibular Dysfunction	Antihistamines, benzodiazepines and/or antiemetic drugs
Chronic Pain	Depending on the characteristics of pain, the most common are: anti-inflammatory, opioid drugs, tricyclic antidepressants, carbamazepine, pregabalin or gabapentin
Autonomic Bladder Dysfunction	Antimuscarinic drugs depend on the comorbidities of each patient
Sleep Disturbances	Benzodiazepines for improving sleep quality and modafinil for daytime fatigue
Depression	Antidepressant drugs

Peptides and other chemical compounds were already explored for their potential therapeutic effect on polyQ diseases. One great example is the PolyQ Binding Peptide 1 (QBP1), which was identified in a peptide library and exhibited a preferential affinity for expanded polyQ tract (Nagai et al., 2000). The addition or overexpression of QBP1 in COS-7 cultured cells (Nagai et al., 2007; Nagai et al., 2000; Takahashi et al., 2007) and in *Drosophila* models of polyQ diseases (Nagai et al., 2003) significantly suppressed the formation of polyQ inclusions and polyQ-induced cell death. Intranasal administration of QBP1 mixed with chitosan, significantly increased QBP1 concentration in rodents' brains and improved motor coordination and explorative behaviour (Yang et al., 2018). Although it is important to note that QBP1 does not stop Atx3 aggregation but it blocks the formation of mature fibrils of the polyQ-expanded protein (Knight, Karamanos, Radford, & Ashcroft, 2018). Chlorzoxazone-baclofen, tested for SCA1 treatment, showed that the ideal drug concentrations for triggering target cells and improving motor performance are low and do not compromise cerebellar function (Bushart, Huang, Man, Morrison, & Shakkottai, 2021). Another study using a screening of FDA-approved compounds

identified three distinct compounds - aripiprazole, salinomycin sodium and AM251 - as promising therapies to reduce the soluble Atx3 levels in certain regions of MJD mouse brain (Maria do Carmo Costa et al., 2016). Although the use of AM251 reduced mutant Atx3-mediated toxicity in MJD flies, aripiprazole was identified as a potential therapeutic agent for MJD, because it reduced levels of what authors suggest to be oligomeric forms of mutant Atx3 in *in vitro*, *ex vivo* and *in vivo* assays (Maria do Carmo Costa et al., 2016). These are just a few examples of drugs tested *in vitro* and *in vivo* that revealed promising results for the future treatment of polyQ diseases. In addition, it is very important to access their impact on patient symptoms and also characterize possible side effects, since some compounds could also target other biological processes that are universal to cell homeostasis (Da Silva et al., 2019; Duarte-Silva & Maciel, 2018).

Another promising innovative therapy for MJD could be the development of DNA-targeted strategies to specifically target the pathogenic mutations (Maria do Carmo Costa, 2020; Neves-Carvalho et al., 2020). Techniques such as clustered regularly interspaced short palindromic repeats (CRISPR)/Cas9, zinc-finger nucleases or transcription activator-like effector nucleases could potentially have a future therapeutic application. Ouyang et al. (2018) applied for the first time the CRISPR/Cas9 mediated deletion of the expanded polyQ-encoding region of *ATXN3* gene in induced pluripotent stem cells derived from MJD patients to genetically delete the expanded polyQ-encoding region. Gene silencing therapies with strategies that target RNA are also being developed (Kourkouta et al., 2019; Martier et al., 2019; McLoughlin et al., 2018; Nobrega, Codesso, Mendonca, & Pereira de Almeida, 2019). This can be achieved by using interference RNA (RNAi) agents - short hairpin RNA (shRNA), small interference RNA (siRNA) and microRNA (miRNA) - or using antisense oligonucleotides (ASOs) that could target the polyQ mutation or a single nucleotide polymorphism or target both mutant and wild-type alleles (Maria do Carmo Costa, 2020; Ghosh & Tabrizi, 2017; Neves-Carvalho et al., 2020). Recently, two independent studies using ASOs strategies targeting *ATXN3* transcripts (Kourkouta et al., 2019) or the CAG repeats (McLoughlin et al., 2018) showed the ability to reduce mutant Atx3 in MJD mouse models. The latter two promising studies are in an advanced stage of development and show a high probability of achieving disease-modifying therapies for MJD (Maria do Carmo Costa, 2020; Kourkouta et al., 2019; McLoughlin et al., 2018; Neves-Carvalho et al., 2020). A ASO that targets *HTT* transcript for the treatment of HD is currently in phase 3 clinical trials with great preclinical results (McLoughlin et al., 2020). Naphthyridine-azaquinolone is a compound that specifically binds to slipped-CAG DNA intermediates of expansion mutations in HD mice models (Nakamori et al., 2020) which might constitute an innovative approach to reduce

mutant huntingtin aggregates in HD mouse striatum due to its selectivity for CAG hairpins with >30 CAG repeats (Nakamori et al., 2020) and is another example of RNA targeted therapy.

Consistent with the lack of effective treatment for MJD, at least 15 interventional studies with MJD patients failed to provide a robust impact on patients (Maria do Carmo Costa, 2020; Da Silva et al., 2019; Saute & Jardim, 2018). There are three ongoing interventional studies for SCAs that also include MJD patients: one with the drug troriluzole (NCT03701399), a second one with umbilical cord mesenchymal stem cell therapy (NCT03378414), and a more recent with BIIB132, a ASO that targets Atx3 pre-mRNA (NCT05160558). Biohaven Pharmaceuticals, Inc. is the company that is responsible for the phase 3 clinical trial involving troriluzole which recently issued an update stating that MJD patients that have been administered troriluzole "*showed a numerical treatment benefit and minimal disease progression over the study period*" compared to the placebo group. Patients in this study who were able to walk without assistance also had a greater numerical treatment benefit. Although, overall SCA patients in this study did not benefited from troriluzole treatment, MJD patients - which accounted for 41% of the study population - did, and Biohaven Pharmaceuticals, Inc is planning to engage with the FDA to move this program forward. Troriluzole is a chemical that modulates glutamate, an excitatory neurotransmitter.

Although the apparent success of troriluzole, there is a low success rate of clinical trials and this could be explained by the lack of preclinical studies (Duarte-Silva & Maciel, 2018; Neves-Carvalho et al., 2020). Most of the drugs used in SCA clinical trials had not been tested preclinically (Neves-Carvalho et al., 2020). Future clinical trials should rely on a solid research background focused on the innovative drug with sufficient and reproducible preclinical data to support the viability and efficacy of the treatment (Maria do Carmo Costa, 2020; Da Silva et al., 2019; Duarte-Silva & Maciel, 2018). The link between clinical trials and preclinical studies can be achieved with extensive *in vitro* research and access to several animal models of SCAs including MJD models. A number of factors like the importance of identifying and targeting all the toxic species, drug off-target and distribution combined with possible side effects will make the appearance of a new therapy a major challenge. Ideally the best treatment for MJD should aim to silence expression of the mutant genes or remove/correct the toxic polyQ sequence which probably eliminate the cause of the disease. The usages of ASOs is a promising step toward gene therapy and is already approved for treatment of spinal muscular atrophy (Chiriboga, 2017) showing a very safety profile while being extremely efficient (McLoughlin et al., 2020).

1.7 Objectives

MJD is an autosomal dominant neurodegenerative disorder caused by an abnormal glutamine expansion in the Atx3 protein that triggers a complex aggregation process. The link between Atx3 aggregation and cell toxicity is not completely identified supporting the need for a thorough structural characterization of Atx3 amyloid structures and the identification of the molecular mechanisms governing its self-assembly. This work aimed to contribute to the structural characterization of the Atx3 aggregation process and to find novel modulators for this process. The specific goals were:

1) Establishment of a standardized and reproducible protocol for studying the Atx3 aggregating *in vitro* (Chapter 2);
2) Investigation of the structural and morphological characteristics of Atx3 oligomers and fibrils along the aggregation pathway (Chapter 3) using an improved TEM-based method complemented with the cryo-EM technique;
3) Characterization of morphological changes in Atx3 oligomers/fibrils induced by Atx3-interacting nanobodies (Chapter 3);
4) Screening of novel compounds with an inhibitory effect on Atx3 aggregation (Chapter 4) complemented with *in vitro* and *in vivo* characterization.

1.8 References

Almeida, B., Fernandes, S., Abreu, I. A., & Macedo-Ribeiro, S. (2013). Trinucleotide repeats: a structural perspective. *Frontiers in neurology, 4*, 76.

Amigoni, L., Airoldi, C., Natalello, A., Romeo, M., Diomede, L., Tortora, P., & Regonesi, M. E. (2019). Methacycline displays a strong efficacy in reducing toxicity in a SCA3 Caenorhabditis elegans model. *Biochimica et Biophysica Acta (BBA) - General Subjects, 1863*(2), 279-290.

Asencio-Hernández, J., Ruhlmann, C., McEwen, A., Eberling, P., Nominé, Y., Céraline, J., . . . Delsuc, M. A. (2014). Reversible amyloid fiber formation in the N terminus of androgen receptor. *Chembiochem, 15*(16), 2370-2373.

Baek, M., DiMaio, F., Anishchenko, I., Dauparas, J., Ovchinnikov, S., Lee, G. R., . . . Schaeffer, R. D. (2021). Accurate prediction of protein structures and interactions using a three-track neural network. *Science, 373*(6557), 871-876.

Baglioni, S., Casamenti, F., Bucciantini, M., Luheshi, L. M., Taddei, N., Chiti, F., . . . Stefani, M. (2006). Prefibrillar amyloid aggregates could be generic toxins in higher organisms. *Journal of Neuroscience, 26*(31), 8160-8167.

Bansal, A., Schmidt, M., Rennegarbe, M., Haupt, C., Liberta, F., Stecher, S., . . . Fändrich, M. (2021). AA amyloid fibrils from diseased tissue are structurally different from in vitro formed SAA fibrils. *Nature communications, 12*(1), 1-9.

Benilova, I., Karran, E., & De Strooper, B. (2012). The toxic Aβ oligomer and Alzheimer's disease: an emperor in need of clothes. *Nature neuroscience, 15*(3), 349-357.

Bevivino, A., & Loll, P. (2001). An expanded glutamine repeat destabilizes native ataxin-3 structure and mediates formation of parallel β-fibrils. *Proceedings of the National Academy of sciences, 98*(21), 11955-11960.

Blum, E., Schwendeman, A., & Shaham, S. (2013). PolyQ disease: misfiring of a developmental cell death program? *Trends in cell biology, 23*(4), 168-174.

Bucciantini, M., Giannoni, E., Chiti, F., Baroni, F., Formigli, L., Zurdo, J., . . . Stefani, M. (2002). Inherent toxicity of aggregates implies a common mechanism for protein misfolding diseases. *Nature, 416*(6880), 507-511.

Burdukiewicz, M., Sobczyk, P., Rödiger, S., Duda-Madej, A., Mackiewicz, P., & Kotulska, M. (2017). Amyloidogenic motifs revealed by n-gram analysis. *Scientific reports, 7*(1), 1-10.

Burke, K., Janke, A., Rhine, C., & Fawzi, N. (2015). Residue-by-residue view of in vitro FUS granules that bind the C-terminal domain of RNA polymerase II. *Molecular cell, 60*(2), 231-241.

Bushart, D., Huang, H., Man, L. u., Morrison, L., & Shakkottai, V. (2021). A Chlorzoxazone-Baclofen Combination Improves Cerebellar Impairment in Spinocerebellar Ataxia Type 1. *Movement Disorders, 36*(3), 622-631. doi:10.1002/mds.28355

Case, D., Darden, T., Cheatham, T., Simmerling, C., Wang, J., Duke, R., . . . Zhang, W. (2008). *Amber 10*. Retrieved from

Chen, S., Berthelier, V., Hamilton, J. B., O'Nuallai, B., & Wetzel, R. (2002). Amyloid-like features of polyglutamine aggregates and their assembly kinetics. *Biochemistry, 41*(23), 7391-7399.

Chen, S., Berthelier, V., Yang, W., & Wetzel, R. (2001). Polyglutamine aggregation behavior in vitro supports a recruitment mechanism of cytotoxicity. *Journal of molecular biology, 311*(1), 173-182. doi:10.1006/jmbi.2001.4850

Chen, S., Ferrone, F. A., & Wetzel, R. (2002). Huntington's disease age-of-onset linked to polyglutamine aggregation nucleation. *Proceedings of the National Academy of sciences, 99*(18), 11884-11889.

Chiriboga, C. (2017). Nusinersen for the treatment of spinal muscular atrophy. *Expert review of neurotherapeutics, 17*(10), 955-962.

Chow, M., Paulson, H. L., & Bottomley, S. (2004). Destabilization of a non-pathological variant of ataxin-3 results in fibrillogenesis via a partially folded intermediate: a model for misfolding in polyglutamine disease. *Journal of molecular biology, 335*(1), 333-341.

Ciechanover, A., & Kwon, Y. T. (2017). Protein quality control by molecular chaperones in neurodegeneration. *Frontiers in neuroscience, 11*, 185.

Cohen, F., & Kelly, J. (2003). Therapeutic approaches to protein-misfolding diseases. *Nature, 426*(6968), 905-909.

Cohen, S., Linse, S., Luheshi, L., Hellstrand, E., White, D., Rajah, L., . . . Knowles, T. (2013). Proliferation of amyloid-β42 aggregates occurs through a secondary nucleation mechanism. *Proceedings of the National Academy of sciences, 110*(24), 9758-9763.

Costa, M. d. C. (2020). Recent therapeutic prospects for Machado-Joseph disease. *Current Opinion in Neurology, 33*(4), 519-526. doi:10.1097/WCO.0000000000000832

Costa, M. d. C., Ashraf, N., Fischer, S., Yang, Y., Schapka, E., Joshi, G., . . . Paulson, H. L. (2016). Unbiased screen identifies aripiprazole as a modulator of abundance of the polyglutamine disease protein, ataxin-3. *Brain, 139*(11), 2891-2908. doi:10.1093/brain/aww228

Costa, M. d. C., & Paulson, H. L. (2012). Toward understanding Machado–Joseph disease. *Progress in neurobiology, 97*(2), 239-257.

Coutinho, P., & Andrade, C. (1978). Autosomal dominant system degeneration in Portuguese families of the Azores Islands: a new genetic disorder involving cerebellar, pyramidal, extrapyramidal and spinal cord motor functions. *Neurology, 28*(7), 703-703.

Da Silva, J. D., Teixeira-Castro, A., & Maciel, P. (2019). From Pathogenesis to Novel Therapeutics for Spinocerebellar Ataxia Type 3: Evading Potholes on the Way to Translation. *Neurotherapeutics, 16*(4), 1009-1031. doi:10.1007/s13311-019-00798-1

Davies, P., Watt, K., Kelly, S. M., Clark, C., Price, N. C., & McEwan, I. J. (2008). Consequences of poly-glutamine repeat length for the conformation and folding of the androgen receptor amino-terminal domain. *Journal of Molecular Endocrinology, 41*(5), 301-314.

de Chiara, C., Menon, R. P., Dal Piaz, F., Calder, L., & Pastore, A. (2005). Polyglutamine is not all: the functional role of the AXH domain in the ataxin-1 protein. *Journal of molecular biology, 354*(4), 883-893.

Drombosky, K., Rode, S., Kodali, R., Jacob, T. C., Palladino, M., & Wetzel, R. (2018). Mutational analysis implicates the amyloid fibril as the toxic entity in Huntington's disease. *Neurobiology of disease, 120*, 126-138.

Duarte-Silva, S., & Maciel, P. (2018). Pharmacological Therapies for Machado-Joseph Disease. *Advances in Experimental Medicine and Biology, 1049*, 369-394. doi:10.1007/978-3-319-71779-1_19

Ellisdon, A. M., Thomas, B., & Bottomley, S. P. (2006). The two-stage pathway of ataxin-3 fibrillogenesis involves a polyglutamine-independent step. *Journal of Biological Chemistry, 281*(25), 16888-16896.

Evangelisti, E., Cascella, R., Becatti, M., Marrazza, G., Dobson, C. M., Chiti, F., . . . Cecchi, C. (2016). Binding affinity of amyloid oligomers to cellular membranes is a generic indicator of cellular dysfunction in protein misfolding diseases. *Scientific reports, 6*(1), 1-14.

Fernandez-Escamilla, A.-M., Rousseau, F., Schymkowitz, J., & Serrano, L. (2004). Prediction of sequence-dependent and mutational effects on the aggregation of peptides and proteins. *Nature biotechnology, 22*(10), 1302-1306.

Ferrone, F. (1999). Analysis of protein aggregation kinetics. In *Methods in Enzymology* (Vol. 309, pp. 256-274): Elsevier.

França Jr, M., Emmel, V., D'Abreu, A., Maurer-Morelli, C. V., Secolin, R., Bonadia, L., . . . Saraiva-Pereira, M. L. (2012). Normal ATXN3 allele but not CHIP polymorphisms modulates age at onset in Machado–Joseph disease. *Frontiers in neurology, 3*, 164.

Fusco, G., Chen, S. W., Williamson, P. T., Cascella, R., Perni, M., Jarvis, J. A., . . . Cremades, N. (2017). Structural basis of membrane disruption and cellular toxicity by α-synuclein oligomers. *Science, 358*(6369), 1440-1443.

Gade Malmos, K., Blancas-Mejia, L. M., Weber, B., Buchner, J., Ramirez-Alvarado, M., Naiki, H., & Otzen, D. (2017). ThT 101: a primer on the use of thioflavin T to investigate amyloid formation. *Amyloid, 24*(1), 1-16.

Gales, L., Cortes, L., Almeida, C., Melo, C. V., Costa, M. d. C., Maciel, P., . . . Macedo-Ribeiro, S. (2005). Towards a structural understanding of the fibrillization pathway in Machado-Joseph's disease: trapping early oligomers of non-expanded ataxin-3. *Journal of molecular biology, 353*(3), 642-654.

Ghosh, R., & Tabrizi, S. (2017). Gene suppression approaches to neurodegeneration. *Alzheimer's Research & Therapy, 9*(1), 82. doi:10.1186/s13195-017-0307-1

Glabe, C. G. (2006). Common mechanisms of amyloid oligomer pathogenesis in degenerative disease. *Neurobiology of aging, 27*(4), 570-575.

Glabe, C. G., & Kayed, R. (2006). Common structure and toxic function of amyloid oligomers implies a common mechanism of pathogenesis. *Neurology, 66*(1 suppl 1), S74-S78.

Glenner, G., Terry, W., Harada, M., Isersky, C., & Page, D. L. (1971). Amyloid fibril proteins: proof of homology with immunoglobulin light chains by sequence analyses. *Science, 172*(3988), 1150-1151.

Groenning, M., Olsen, L., van de Weert, M., Flink, J. M., Frokjaer, S., & Jørgensen, F. S. (2007). Study on the binding of Thioflavin T to β-sheet-rich and non-β-sheet cavities. *Journal of Structural Biology, 158*(3), 358-369.

Gruber, A., Hornburg, D., Antonin, M., Krahmer, N., Collado, J., Schaffer, M., . . . Fernandez-Busnadiego, R. (2018). Molecular and structural architecture of polyQ aggregates in yeast. *PNAS, 115*(15), E3446-E3453. doi:10.1073/pnas.1717978115

Guo, Q., Huang, B., Cheng, J., Seefelder, M., Engler, T., Pfeifer, G., . . . Maurer, M. (2018). The cryo-electron microscopy structure of huntingtin. *Nature, 555*(7694), 117-120.

Harding, R., Deme, J., Hevler, J., Tamara, S., Lemak, A., Cantle, J., . . . Arrowsmith, C. (2021). Huntingtin structure is orchestrated by HAP40 and shows a polyglutamine expansion-specific interaction with exon 1. *Communications Biology, 4*(1), 1374. doi:10.1038/s42003-021-02895-4

Harris, G. M., Dodelzon, K., Gong, L., Gonzalez-Alegre, P., & Paulson, H. L. (2010). Splice isoforms of the polyglutamine disease protein ataxin-3 exhibit similar enzymatic yet different aggregation properties. *PLoS One, 5*(10), e13695.

Hyman, A. A., Weber, C. A., & Jülicher, F. (2014). Liquid-liquid phase separation in biology. *Annual review of cell and developmental biology, 30*, 39-58.

Iadanza, M. G., Jackson, M. P., Hewitt, E. W., Ranson, N. A., & Radford, S. E. (2018). A new era for understanding amyloid structures and disease. *Nature Reviews Molecular Cell Biology, 19*(12), 755-773.

Invernizzi, G., Lambrughi, M., Regonesi, M. E., Tortora, P., & Papaleo, E. (2013). The conformational ensemble of the disordered and aggregation-protective 182–291 region of ataxin-3. *Biochimica et Biophysica Acta (BBA)-General Subjects, 1830*(11), 5236-5247.

Jumper, J., Evans, R., Pritzel, A., Green, T., Figurnov, M., Ronneberger, O., . . . Potapenko, A. (2021). Highly accurate protein structure prediction with AlphaFold. *Nature, 596*(7873), 583-589.

Karamanos, T. K., Jackson, M. P., Calabrese, A. N., Goodchild, S. C., Cawood, E. E., Thompson, G. S., . . . Radford, S. E. (2019). Structural mapping of oligomeric intermediates in an amyloid assembly pathway. *Elife, 8*, e46574.

Karpinar, D. P., Balija, M. B. G., Kügler, S., Opazo, F., Rezaei-Ghaleh, N., Wender, N., . . . Heise, H. (2009). Pre-fibrillar α-synuclein variants with impaired β-structure increase neurotoxicity in Parkinson's disease models. *The EMBO journal, 28*(20), 3256-3268.

Kayed, R., Head, E., Thompson, J. L., McIntire, T. M., Milton, S. C., Cotman, C. W., & Glabe, C. G. (2003). Common structure of soluble amyloid oligomers implies common mechanism of pathogenesis. *Science, 300*(5618), 486-489.

Klein, F. A., Pastore, A., Masino, L., Zeder-Lutz, G., Nierengarten, H., Oulad-Abdelghani, M., . . . Trottier, Y. (2007). Pathogenic and non-pathogenic polyglutamine tracts have similar structural properties: towards a length-dependent toxicity gradient. *Journal of molecular biology, 371*(1), 235-244.

Klein, F. A., Zeder-Lutz, G., Cousido-Siah, A., Mitschler, A., Katz, A., Eberling, P., . . . Trottier, Y. (2013). Linear and extended: a common polyglutamine conformation recognized by the three antibodies MW1, 1C2 and 3B5H10. *Human molecular genetics, 22*(20), 4215-4223.

Klockgether, T., Mariotti, C., & Paulson, H. L. (2019). Spinocerebellar ataxia. *Nature Reviews Disease Primers, 5*(1), 24. doi:10.1038/s41572-019-0074-3

Knight, P., Karamanos, T. K., Radford, S. E., & Ashcroft, A. E. (2018). Identification of a novel site of interaction between ataxin-3 and the amyloid aggregation inhibitor polyglutamine binding peptide 1. *European Journal of Mass Spectrometry, 24*(1), 129-140. doi:10.1177/1469066717729298

Knowles, T. P., Vendruscolo, M., & Dobson, C. M. (2014). The amyloid state and its association with protein misfolding diseases. *Nature Reviews Molecular Cell Biology, 15*(6), 384-396.

Kollmer, M., Close, W., Funk, L., Rasmussen, J., Bsoul, A., Schierhorn, A., . . . Fändrich, M. (2019). Cryo-EM structure and polymorphism of Aβ amyloid fibrils purified from Alzheimer's brain tissue. *Nature communications, 10*(1), 1-8.

Kourkouta, E., Weij, R., Gonzalez-Barriga, A., Mulder, M., Verheul, R., Bosgra, S., . . . Datson, N. (2019). Suppression of Mutant Protein Expression in SCA3 and SCA1 Mice Using a CAG Repeat-Targeting Antisense Oligonucleotide. *Molecular Therapy Nucleic Acids, 17*, 601-614. doi:10.1016/j.omtn.2019.07.004

Li, L.-B., Yu, Z., Teng, X., & Bonini, N. M. (2008). RNA toxicity is a component of ataxin-3 degeneration in Drosophila. *Nature, 453*(7198), 1107-1111.

Lieberman, A., Shakkottai, V., & Albin, R. (2019). Polyglutamine Repeats in Neurodegenerative Diseases. *Annual Review of Pathology: Mechanisms of Disease, 14*, 1-27. doi:10.1146/annurev-pathmechdis-012418-012857

Lima, L., & Coutinho, P. (1980). Clinical criteria for diagnosis of Machado-Joseph disease: report of a non-Azorean Portuguese family. *Neurology, 30*(3), 319-319.

Linse, S. (2017). Monomer-dependent secondary nucleation in amyloid formation. *Biophysical reviews, 9*(4), 329-338.

Liu, Y., Ding, R., Xu, Z., Xue, Y., Zhang, D., Zhang, Y., . . . Li, X. (2021). Roles and Mechanisms of the Protein Quality Control System in Alzheimer's Disease. *International Journal of Molecular Sciences, 23*(1), 345.

Maciel, P., Gaspar, C., DeStefano, A. L., Silveira, I., Coutinho, P., Radvany, J., . . . Loureiro, J. E. (1995). Correlation between CAG repeat length and clinical features in Machado-Joseph disease. *American journal of human genetics, 57*(1), 54.

Maejima, Y. (2020). The critical roles of protein quality control systems in the pathogenesis of heart failure. *Journal of Cardiology, 75*(3), 219-227.

Mao, Y., Senic-Matuglia, F., Di Fiore, P. P., Polo, S., Hodsdon, M. E., & De Camilli, P. (2005). Deubiquitinating function of ataxin-3: insights from the solution structure of the Josephin domain. *Proceedings of the National Academy of sciences, 102*(36), 12700-12705.

Martier, R., Sogorb-Gonzalez, M., Stricker-Shaver, J., Hübener-Schmid, J., Keskin, S., Klima, J., . . . Ellederova, Z. (2019). Development of an AAV-based microRNA gene therapy to treat Machado-Joseph disease. *Molecular Therapy-Methods & Clinical Development, 15*, 343-358.

Masino, L. (2004). Polyglutamine and neurodegeneration: structural aspects. *Protein & Peptide Letters, 11*(3), 239-248.

Masino, L., Nicastro, G., Calder, L., Vendruscolo, M., & Pastore, A. (2011). Functional interactions as a survival strategy against abnormal aggregation. *The FASEB journal, 25*(1), 45-54.

Masino, L., Nicastro, G., Menon, R. P., Dal Piaz, F., Calder, L., & Pastore, A. (2004). Characterization of the structure and the amyloidogenic properties of the Josephin domain of the polyglutamine-containing protein ataxin-3. *Journal of molecular biology, 344*(4), 1021-1035.

McGowan, D., van Roon-Mom, W., Holloway, H., Bates, G., Mangiarini, L., Cooper, G., . . . Snell, R. (2000). Amyloid-like inclusions in Huntington's disease. *Neuroscience, 100*(4), 677-680.

McLoughlin, H. S., Moore, L. R., Chopra, R., Komlo, R., McKenzie, M., Blumenstein, K., . . . Paulson, H. L. (2018). Oligonucleotide therapy mitigates disease in spinocerebellar ataxia type 3 mice. *Annals of Neurology, 84*(1), 64-77. doi:10.1002/ana.25264

McLoughlin, H. S., Moore, L. R., & Paulson, H. L. (2020). Pathogenesis of SCA3 and implications for other polyglutamine diseases. *Neurobiology of disease, 134*, 104635.

Minakawa, E., & Nagai, Y. (2021). Protein Aggregation Inhibitors as Disease-Modifying Therapies for Polyglutamine Diseases. *Frontiers in neuroscience, 15*, 621996. doi:10.3389/fnins.2021.621996

Molliex, A., Temirov, J., Lee, J., Coughlin, M., Kanagaraj, A. P., Kim, H. J., . . . Taylor, J. P. (2015). Phase separation by low complexity domains promotes stress granule assembly and drives pathological fibrillization. *Cell, 163*(1), 123-133.

Murakami, K., Kajimoto, S., Shibata, D., Kuroi, K., Fujii, F., & Nakabayashi, T. (2021). Observation of liquid–liquid phase separation of ataxin-3 and quantitative evaluation of its concentration in a single droplet using Raman microscopy. *Chemical science, 12*(21), 7411-7418.

Nagai, Y., Fujikake, N., Ohno, K., Higashiyama, H., Popiel, H., Rahadian, J., . . . Toda, T. (2003). Prevention of polyglutamine oligomerization and neurodegeneration by the peptide inhibitor QBP1 in Drosophila. *Human molecular genetics, 12*(11), 1253-1259. doi:10.1093/hmg/ddg144

Nagai, Y., Inui, T., Popiel, A., Fujikake, N., Hasegawa, K., Urade, Y., . . . Toda, T. (2007). A toxic monomeric conformer of the polyglutamine protein. *Nature structural & molecular biology, 14*(4), 332-340. doi:10.1038/nsmb1215

Nagai, Y., Tucker, T., Ren, H., Kenan, D. J., Henderson, B. S., Keene, J. D., . . . Burke, J. R. (2000). Inhibition of polyglutamine protein aggregation and cell death by novel peptides identified by phage display screening. *Journal of Biological Chemistry, 275*(14), 10437-10442. doi:10.1074/jbc.275.14.10437

Nakamori, M., Panigrahi, G., Lanni, S., Gall-Duncan, T., Hayakawa, H., Tanaka, H., . . . Pearson, C. (2020). A slipped-CAG DNA-binding small molecule induces trinucleotide-repeat contractions in vivo. *Nature genetics, 52*(2), 146-159. doi:10.1038/s41588-019-0575-8

Nakano, K. K., Dawson, D. M., & Spence, A. (1972). Machado disease: a hereditary ataxia in Portuguese emigrants to Massachusetts. *Neurology, 22*(1), 49-49.

Neves-Carvalho, A., Duarte-Silva, S., Teixeira-Castro, A., & Maciel, P. (2020). Polyglutamine spinocerebellar ataxias: emerging therapeutic targets. *Expert Opinion on Therapeutic Targets, 24*(11), 1099-1119. doi:10.1080/14728222.2020.1827394

Nicastro, G., Menon, R. P., Masino, L., Knowles, P. P., McDonald, N. Q., & Pastore, A. (2005). The solution structure of the Josephin domain of ataxin-3: structural determinants for molecular recognition. *Proceedings of the National Academy of sciences, 102*(30), 10493-10498.

Nobrega, C., Codesso, J. M., Mendonca, L., & Pereira de Almeida, L. (2019). RNA interference therapy for Machado–Joseph disease: long-term safety profile of lentiviral vectors encoding short hairpin RNAs targeting mutant ataxin-3. *Human gene therapy, 30*(7), 841-854.

Oosawa, F., & Asakura, S. (1975). *Thermodynamics of the Polymerization of Protein*: Academic Press.

Oppong, E., Stier, G., Gaal, M., Seeger, R., Stoeck, M., Delsuc, M.-A., . . . Kieffer, B. (2017). An Amyloidogenic Sequence at the N-Terminus of the Androgen Receptor Impacts Polyglutamine Aggregation. *Biomolecules, 7*(2), 44.

Ouyang, S., Xie, Y., Xiong, Z., Yang, Y., Xian, Y., Ou, Z., . . . Sun, X. (2018). CRISPR/Cas9-Targeted Deletion of Polyglutamine in Spinocerebellar Ataxia Type 3-Derived Induced Pluripotent Stem Cells. *Stem Cells and Development, 27*(11), 756-770. doi:10.1089/scd.2017.0209

Padiath, Q., Srivastava, A., Roy, S., Jain, S., & Brahmachari, S. K. (2005). Identification of a novel 45 repeat unstable allele associated with a disease phenotype at the MJD1/SCA3 locus. *American Journal of Medical Genetics Part B, 133B*(1), 124-126. doi:10.1002/ajmg.b.30088

Papaleo, E., & Invernizzi, G. (2011). Conformational diseases: structural studies of aggregation of polyglutamine proteins. *Current computer-aided drug design, 7*(1), 23-43.

Patel, A., Lee, H. O., Jawerth, L., Maharana, S., Jahnel, M., Hein, M. Y., . . . Franzmann, T. M. (2015). A liquid-to-solid phase transition of the ALS protein FUS accelerated by disease mutation. *Cell, 162*(5), 1066-1077.

Paulson, H. L. (1999). Protein fate in neurodegenerative proteinopathies: polyglutamine diseases join the (mis) fold. *The American Journal of Human Genetics, 64*(2), 339-345.

Paulson, H. L. (2007). Dominantly inherited ataxias: lessons learned from Machado-Joseph disease/spinocerebellar ataxia type 3. *Seminars in Neurology, 27*(2), 133-142. doi:10.1055/s-2007-971172

Paulson, H. L., Perez, M., Trottier, Y., Trojanowski, J., Subramony, S., Das, S., . . . Pittman, R. (1997). Intranuclear inclusions of expanded polyglutamine protein in spinocerebellar ataxia type 3. *Neuron, 19*(2), 333-344.

Paulson, H. L., Shakkottai, V. G., Clark, H. B., & Orr, H. T. (2017). Polyglutamine spinocerebellar ataxias—from genes to potential treatments. *Nature Reviews Neuroscience, 18*(10), 613-626.

Peskett, T. R., Rau, F., O'Driscoll, J., Patani, R., Lowe, A. R., & Saibil, H. R. (2018). A liquid to solid phase transition underlying pathological huntingtin exon1 aggregation. *Molecular cell, 70*(4), 588-601. e586.

Poirier, M. A., Jiang, H., & Ross, C. A. (2005). A structure-based analysis of huntingtin mutant polyglutamine aggregation and toxicity: evidence for a compact beta-sheet structure. *Human molecular genetics, 14*(6), 765-774.

Rawat, P., Prabakaran, R., Kumar, S., & Gromiha, M. M. (2020). AggreRATE-Pred: a mathematical model for the prediction of change in aggregation rate upon point mutation. *Bioinformatics, 36*(5), 1439-1444.

Riess, O., Rüb, U., Pastore, A., Bauer, P., & Schöls, L. (2008). SCA3: neurological features, pathogenesis and animal models. *The Cerebellum, 7*(2), 125-137.

Romanul, F. C., Fowler, H. L., Radvany, J., Feldman, R. G., & Feingold, M. (1977). Azorean disease of the nervous system. *New England Journal of Medicine, 296*(26), 1505-1508.

Rosenberg, R. N. (1992). Machado-Joseph disease: an autosomal dominant motor system degeneration. *Movement Disorders Journal, 7*(3), 193-203.

Rosenberg, R. N., Nyhan, W., Bay, C., & Shore, P. (1976). Autosomal dominant striatonigral degeneration. A clinical, pathologic, and biochemical study of a new genetic disorder. *Neurology, 26*(8), 703-714. doi:10.1212/wnl.26.8.703

Rüb, U., De Vos, R. A., Brunt, E. R., Sebestény, T., Schöls, L., Auburger, G., . . . Seidel, K. (2006). Spinocerebellar ataxia type 3 (SCA3): thalamic neurodegeneration occurs independently from thalamic ataxin-3 immunopositive neuronal intranuclear inclusions. *Brain pathology, 16*(3), 218-227.

Ruggeri, F., Vieweg, S., Cendrowska, U., Longo, G., Chiki, A., Lashuel, H., & Dietler, G. (2016). Nanoscale studies link amyloid maturity with polyglutamine diseases onset. *Scientific reports, 6*, 31155. doi:10.1038/srep31155

Sangwan, S., Zhao, A., Adams, K. L., Jayson, C. K., Sawaya, M. R., Guenther, E. L., . . . Soriaga, A. B. (2017). Atomic structure of a toxic, oligomeric segment of SOD1 linked to amyotrophic lateral sclerosis (ALS). *Proceedings of the National Academy of sciences, 114*(33), 8770-8775.

Santambrogio, C., Frana, A. M., Natalello, A., Papaleo, E., Regonesi, M. E., Doglia, S. M., . . . Grandori, R. (2012). The role of the central flexible region on the aggregation and conformational properties of human ataxin-3. *The FEBS journal, 279*(3), 451-463.

Sárkány, Z., Rocha, F., Damas, A. M., Macedo-Ribeiro, S., & Martins, P. M. (2019). Chemical Kinetic Strategies for High-Throughput Screening of Protein Aggregation Modulators. *Chemistry: An Asian Journal, 14*(4), 500-508.

Satoh, T., Sumiyoshi, A., Yagi-Utsumi, M., Sakata, E., Sasakawa, H., Kurimoto, E., . . . Kato, K. (2014). Mode of substrate recognition by the Josephin domain of ataxin-3, which has an endo-type deubiquitinase activity. *FEBS letters, 588*(23), 4422-4430.

Saute, J., & Jardim, L. (2018). Planning Future Clinical Trials for Machado-Joseph Disease. *Advances in Experimental Medicine and Biology, 1049*, 321-348. doi:10.1007/978-3-319-71779-1_17

Scarff, C. A., Sicorello, A., Tomé, R. J., Macedo-Ribeiro, S., Ashcroft, A. E., & Radford, S. E. (2013). A tale of a tail: Structural insights into the conformational properties of the polyglutamine protein ataxin-3. *International Journal of Mass Spectrometry, 345*, 63-70.

Schweighauser, M., Shi, Y., Tarutani, A., Kametani, F., Murzin, A. G., Ghetti, B., . . . Hasegawa, K. (2020). Structures of α-synuclein filaments from multiple system atrophy. *Nature, 585*(7825), 464-469.

Seidel, K., Meister, M., Dugbartey, G. J., Zijlstra, M. P., Vinet, J., Brunt, E. R., . . . den Dunnen, W. (2012). Cellular protein quality control and the evolution of aggregates in spinocerebellar ataxia type 3 (SCA3). *Neuropathology and applied neurobiology, 38*(6), 548-558. doi:10.1111/j.1365-2990.2011.01220.x

Seidel, K., Siswanto, S., Brunt, E. R., den Dunnen, W., Korf, H.-W., & Rub, U. (2012). Brain pathology of spinocerebellar ataxias. *Acta Neuropathologica, 124*(1), 1-21. doi:10.1007/s00401-012-1000-x

Seidel, K., Siswanto, S., Fredrich, M., Bouzrou, M., den Dunnen, W., Ozerden, I., . . . Rub, U. (2017). On the distribution of intranuclear and cytoplasmic aggregates in the brainstem of patients with spinocerebellar ataxia type 2 and 3. *Brain pathology, 27*(3), 345-355. doi:10.1111/bpa.12412

Serra-Batiste, M., Ninot-Pedrosa, M., Bayoumi, M., Gairí, M., Maglia, G., & Carulla, N. (2016). Aβ42 assembles into specific β-barrel pore-forming oligomers in membrane-mimicking environments. *Proceedings of the National Academy of sciences, 113*(39), 10866-10871.

Silva, A., Almeida, B., Fraga, J. S., Taboada, P., Martins, P. M., & Macedo-Ribeiro, S. (2017). Distribution of Amyloid-Like and Oligomeric Species from Protein Aggregation Kinetics. *Angewandte Chemie International Edition, 56*(45), 14042-14045.

Silva, A., de Almeida, A. V., & Macedo-Ribeiro, S. (2018). Polyglutamine expansion diseases: More than simple repeats. *Journal of Structural Biology, 201*(2), 139-154. doi:10.1016/j.jsb.2017.09.006

Song, A.-X., Zhou, C.-J., Peng, Y., Gao, X.-C., Zhou, Z.-R., Fu, Q.-S., . . . Hu, H.-Y. (2010). Structural transformation of the tandem ubiquitin-interacting motifs in ataxin-3 and their cooperative interactions with ubiquitin chains. *PLoS One, 5*(10), e13202.

Takahashi, Y., Okamoto, Y., Popiel, A., Fujikake, N., Toda, T., Kinjo, M., & Nagai, Y. (2007). Detection of polyglutamine protein oligomers in cells by fluorescence correlation spectroscopy. *Journal of Biological Chemistry, 282*(33), 24039-24048. doi:10.1074/jbc.M704789200

Thakur, A. K., Jayaraman, M., Mishra, R., Thakur, M., Chellgren, V. M., L Byeon, I.-J., . . . Conway, J. F. (2009). Polyglutamine disruption of the huntingtin exon 1 N terminus triggers a complex aggregation mechanism. *Nature structural & molecular biology, 16*(4), 380-389.

Tipping, K. W., van Oosten-Hawle, P., Hewitt, E. W., & Radford, S. E. (2015). Amyloid fibres: inert end-stage aggregates or key players in disease? *Trends in biochemical sciences, 40*(12), 719-727.

Totzeck, F., Andrade-Navarro, M. A., & Mier, P. (2017). The protein structure context of polyQ regions. *PLoS One, 12*(1), e0170801.

Urbanek, A., Popovic, M., Morató, A., Estaña, A., Elena-Real, C. A., Mier, P., . . . Andrade-Navarro, M. A. (2020). Flanking regions determine the structure of the poly-glutamine in huntingtin through mechanisms common among glutamine-rich human proteins. *Structure, 28*(7), 733-746. e735.

Varadi, M., Anyango, S., Deshpande, M., Nair, S., Natassia, C., Yordanova, G., . . . Laydon, A. (2022). AlphaFold Protein Structure Database: Massively expanding the structural coverage of protein-sequence space with high-accuracy models. *Nucleic acids research, 50*(D1), D439-D444.

Vijayvargia, R., Epand, R., Leitner, A., Jung, T.-Y., Shin, B., Jung, R., . . . Seong, I. S. (2016). Huntingtin's spherical solenoid structure enables polyglutamine tract-dependent modulation of its structure and function. *Elife, 5*, e11184. doi:10.7554/eLife.11184

Walsh, I., Seno, F., Tosatto, S. C., & Trovato, A. (2014). PASTA 2.0: an improved server for protein aggregation prediction. *Nucleic acids research, 42*(W1), W301-W307.

Wen, J., Hong, L., Krainer, G., Yao, Q.-Q., Knowles, T. P., Wu, S., & Perrett, S. (2021). Conformational expansion of tau in condensates promotes irreversible aggregation. *Journal of the American Chemical Society, 143*(33), 13056-13064.

Wetzel, R. (2020). Exploding the Repeat Length Paradigm while Exploring Amyloid Toxicity in Huntington's Disease. *Accounts of Chemical Research, 53*(10), 2347-2357. doi:10.1021/acs.accounts.0c00450

Winner, B., Jappelli, R., Maji, S. K., Desplats, P. A., Boyer, L., Aigner, S., . . . Campioni, S. (2011). In vivo demonstration that α-synuclein oligomers are toxic. *Proceedings of the National Academy of sciences, 108*(10), 4194-4199.

Woods, B. T., & Schaumburg, H. H. (1972). Nigro-spino-dentatal degeneration with nuclear ophthalmoplegia: a unique and partially treatable clinico-pathological entity. *Journal of the neurological sciences, 17*(2), 149-166.

Xue, W.-F., Homans, S. W., & Radford, S. E. (2008). Systematic analysis of nucleation-dependent polymerization reveals new insights into the mechanism of amyloid self-assembly. *Proceedings of the National Academy of sciences, 105*(26), 8926-8931.

Yakupova, E. I., Bobyleva, L. G., Vikhlyantsev, I. M., & Bobylev, A. G. (2019). Congo Red and amyloids: history and relationship. *Bioscience reports, 39*(1).

Yamada, M., Tan, C., Inenaga, C., Tsuji, S., & Takahashi, H. (2004). Sharing of polyglutamine localization by the neuronal nucleus and cytoplasm in CAG-repeat diseases. *Neuropathology and applied neurobiology, 30*(6), 665-675.

Yang, M., Zhang, Q., Wang, Q., Sørensen, K. K., Boesen, J. T., Ma, S. Y., . . . Chan, H. Y. E. (2018). Brain-targeting delivery of two peptidylic inhibitors for their combination therapy in transgenic polyglutamine disease mice via intranasal administration. *Molecular Pharmaceutics, 15*(12), 5781-5792.

Zhang, W., Falcon, B., Murzin, A. G., Fan, J., Crowther, R. A., Goedert, M., & Scheres, S. H. (2019). Heparin-induced tau filaments are polymorphic and differ from those in Alzheimer's and Pick's diseases. *Elife, 8*, e43584.

Zhemkov, V. A., Kulminskaya, A. A., Bezprozvanny, I. B., & Kim, M. (2016). The 2.2-Angstrom resolution crystal structure of the carboxy-terminal region of ataxin-3. *FEBS open bio, 6*(3), 168-178.

Zibaee, S., Makin, O. S., Goedert, M., & Serpell, L. C. (2007). A simple algorithm locates β-strands in the amyloid fibril core of α-synuclein, Aβ, and tau using the amino acid sequence alone. *Protein Science, 16*(5), 906-918.

Chapter 2 - A Robust Assay to Monitor Ataxin-3 Amyloid Fibril Assembly

Francisco Figueiredo, Mónica Lopes-Marques, Bruno Almeida, Nena Matscheko, Pedro Martins, Alexandra Silva, Sandra Macedo-Ribeiro

Site-directed mutagenesis was performed by Bruno Almeida; switchSENSE assays were performed by Nena Matscheko; Filter retardation assays, native gels and thermal shift assays were performed by Alexandra Silva

Article

A Robust Assay to Monitor Ataxin-3 Amyloid Fibril Assembly

Francisco Figueiredo [1,2,3,4], Mónica Lopes-Marques [1,2,5], Bruno Almeida [6,7], Nena Matscheko [8], Pedro M. Martins [1,2], Alexandra Silva [1,2,*] and Sandra Macedo-Ribeiro [1,2,*]

[1] Instituto de Investigação e Inovação em Saúde (i3S), Universidade do Porto, Porto, Portugal; francisco.figueiredo@ibmc.up.pt (F.F.); mmarques@i3s.up.pt (M.L.-M.); pmartins@ibmc.up.pt (P.M.M.)
[2] Instituto de Biologia Molecular e Celular (IBMC), Universidade do Porto, Porto, Portugal
[3] International Iberian Nanotechnology Laboratory (INL), Braga, Portugal
[4] Instituto de Ciências Biomédicas Abel Salazar (ICBAS), Universidade do Porto, Porto, Portugal
[5] Department of Biology, Faculty of Sciences, University of Porto, Porto, Portugal
[6] Life and Health Sciences Research Institute (ICVS), School of Medicine, University of Minho, Braga, Portugal; brunoalmeida@med.uminho.pt
[7] ICVS/3B's—PT Government Associate Laboratory Braga, Portugal
[8] Dynamic Biosensors GmbH, Martinsried, Germany; matscheko@dynamic-biosensors.com
* Correspondence: a.silva@ibmc.up.pt (A.S.); sribeiro@ibmc.up.pt (S.M.-R.)

Abstract: Spinocerebellar ataxia type 3 (SCA3) is caused by the expansion of a glutamine repeat in the protein ataxin-3, which is deposited as intracellular aggregates in affected brain regions. Despite the controversial role of ataxin-3 amyloid structures in SCA3 pathology, the identification of molecules with the capacity to prevent aberrant self-assembly and stabilize functional conformation(s) of ataxin-3 is a key to the development of therapeutic solutions. Amyloid-specific kinetic assays are routinely used to measure rates of protein self-assembly in vitro and are employed during screening for fibrillation inhibitors. The high tendency of ataxin-3 to assemble into oligomeric structures implies that minor changes in experimental conditions can modify ataxin-3 amyloid assembly kinetics. Here, we determine the self-association rates of ataxin-3 and present a detailed study of the aggregation of normal and pathogenic ataxin-3, highlighting the experimental conditions that should be considered when implementing and validating ataxin-3 amyloid progress curves in different settings and in the presence of ataxin-3 interactors. This assay provides a unique and robust platform to screen for modulators of the first steps of ataxin-3 aggregation—a starting point for further studies with cell and animal models of SCA3.

Keywords: thioflavin-T; polyglutamine expansion; reproducibility; ubiquitin; self-association rates; equilibrium dissociation constant; switchSENSE

Citation: Figueiredo, F.; Lopes-Marques, M.; Almeida, B.; Matscheko, N.; Martins, P.M.; Silva, A.; Macedo-Ribeiro, S. A Robust Assay to Monitor Ataxin-3 Amyloid Fibril Assembly. *Cells* **2022**, *11*, 1969. https://doi.org/10.3390/cells11121969

Academic Editor: Takahiro Seki

Received: 10 May 2022
Accepted: 16 June 2022
Published: 19 June 2022

1. Introduction

Ataxin-3 is a modular protein that contains a globular Josephin domain and a flexible C-terminal tail, which includes two or three

ubiquitin interaction motifs (UIMs) and a polyglutamine (polyQ) stretch. Expansion of the polyQ tract above a threshold of 45–55 residues leads to ataxin-3 self-assembly and triggers spinocerebellar ataxia type 3 (SCA3), also known as Machado–Joseph disease, a highly incapacitating autosomal-dominant neurodegenerative disorder. Deposition of amyloid-like fibrillar aggregates containing the mutant polyQ-expanded protein in neurons represents a characteristic hallmark of SCA3 and of other polyQ expansion diseases [1,2]. Although the precise neurotoxic culprit is widely debated, protein aggregation is a major contributing factor to the underlying neurodegeneration, as pathogenic ataxin-3 has been shown to accumulate in intracellular deposits in affected brain regions, such as the cerebellum, brain stem, and spinal cord [3,4]. This perception is strengthened by the observation that increasing the length of the polyQ tract enhances protein aggregation propensity in vitro, in correlation with an upsurge in disease severity [5–7]. Despite nearly 30 years of intensive research, which started with the identification of the causative gene and continued with the discovery of ataxin-3 function(s) and its aggregation mechanisms, SCA3 remains an incurable disease with an urgent need for disease-modifying therapies [8]. Several strategies have been employed to therapeutically target polyglutamine disorders based on the prevention of the misfolding and aggregation of proteins containing expanded polyglutamine tracts (reviewed by Minakawa and Nagai [9]). Given the morphological heterogeneity of the aggregates and the transient nature of the aggregation intermediates, identifying protein aggregation inhibitors with neuroprotective properties is a challenge and requires a thorough knowledge of the self-assembly pathways of the target proteins.

Previous studies have shown that ataxin-3 assembly into amyloid fibrils follows a multi-step pathway involving multiple domains and at least two well-defined aggregation steps. The first step is mediated by an aggregation-prone region located in the Josephin domain [10–13]. This aggregation-prone region (^{73}GFFSIQVISNALKVWGLELILFNS^{96}) leads to the formation of sodium dodecyl sulfate (SDS)-soluble protofibrils both in non-expanded and expanded ataxin-3. The second step, leading to the formation of large, stable, and SDS-resistant amyloid-like fibrils, is polyQ-dependent and exclusive to expanded ataxin-3 [11,14,15]. The complexity of the ataxin-3 aggregation pathway renders the characterization of the self-assembly mechanisms and its modulation by point mutations, interacting partners, or aggregation inhibitors particularly challenging. We have noticed that small changes in buffer conditions significantly modify ataxin-3 aggregation kinetics in vitro, altering both the oligomerization processes and the balance between ordered fibrillar structures and amorphous aggregation. In this context, studying ataxin-3 aggregation mechanisms in vitro under controlled experimental conditions can provide instrumental information to evaluate how different factors and molecules modulate its assembly into ordered fibrillar structures—a starting point for further studies with cell and animal models of SCA3.

Robust and reproducible in vitro aggregation assays are necessary to explore ataxin-3 self-assembly and screen for aggregation inhibitors that could lead to the development of disease-modifying therapies for SCA3 [16]. Here, we present detailed assays developed to monitor the aggregation of wild-type (Atx3 13Q) and polyQ-expanded ataxin-3 (Atx3 77Q) using a miniaturized thioflavin-T (ThT) assay in combination with transmission electron microscopy (TEM) visualization to characterize aggregate morphology [17]. Using this optimized assay, we evaluated the impact of a broad range of conditions on ataxin-3 aggregation in vitro, including ionic strength, pH, the presence of detergents, and molecular crowders. Furthermore, we show how ataxin-3-interacting peptides and proteins, such as polyQ binding peptide 1 (QBP1) and linear ubiquitin chains (previously reported to modulate ataxin-3 aggregation [18–23]), modify ataxin-3 amyloid assembly and how these correlate with changes in fibril morphology.

2. Materials and Methods

2.1. Expression Plasmids

The plasmid constructs used in this work are listed in Table 1. Sequence details are provided in the Supplementary Materials. The cDNAs coding for human normal (13Q) and polyQ-expanded (77Q) ataxin-3 (Atxn3) (isoform 2, UniProt accession: P54252-2) with three ubiquitin interaction motifs (UIMs) were cloned into the pDEST17 Gateway vector (Life Technologies) as previously described [10]. The plasmids were further modified to introduce a tobacco etch virus (TEV) protease cleavage site downstream of the hexahistidine tag [11]. To prepare the constructs with codons optimized for improved expression of repeated polyQ sequences in E. coli, two synthetic constructs (Supplementary Table S1) were designed and purchased from GenScript (USA) and inserted between the restriction sites Ppu10I and BsrGI of the original ATXN3 gene sequence cloned in pDEST17. Site-directed mutagenesis (Supplementary Table S1) performed with the QuikChange II Site-Directed Mutagenesis Kit (Agilent Technologies) was used to produce Atx3 13Q I77K Q78K W87K and Atx3 77Q R388G variants (Single Nucleotide Polymorphism Database locus accession code: rs12895357, UniProt VAR_013689). The plasmid for the expression of untagged Homo sapiens polyubiquitin with 3 ubiquitin repeats in tandem (pET23a-HsUBB) was a gift from Prof. Jorge Azevedo [23] (Addgene plasmid #69562).

Table 1. Summary of the constructs used in the present work and adopted nomenclature. For sequence details, see Supplementary Table S1.

Construct Name	Protein Expressed	Original Reference	Addgene ID
Atx3 JD	Ataxin-3 Josephin Domain	[10,11]	184247
Atx3 D1	Ataxin-3 JD + UIM1-2	[22]	184246
Atx3 13Q	Ataxin-3 (13Q) with a glycine residue after the polyQ tract	This work	184248
Atx3 13Q I77K Q78Q W87K	Ataxin-3 (13Q) with a triple mutation on ubiquitin-binding site 2	This work	185908

Atx3 77Q	PolyQ-expanded ataxin-3 (77Q) with an arginine residue after the polyQ tract (UniProt natural variant VAR_013689)	[15]	184249
Atx3 77Q R388G	PolyQ-expanded ataxin-3 (77Q) with a glycine residueafter the polyQ tract	This work	184251
HsUBB	*Homo sapiens* linear tri-ubiquitin chain	[23]	69562

2.2. Ataxin-3 Expression and Purification

Ataxin-3 variants and truncated constructs were expressed and purified as previously described [10] with minor modifications. Briefly, *E. coli* BL21(DE3)-SI cells (Life Technologies) were transformed with pDEST17 plasmids carrying the various ataxin-3 variants and truncated constructs and plated on LB Agar without NaCl (LBON) plates supplemented with 100 μg mL^{-1} ampicillin. A pre-inoculum was prepared with 4-5 isolated colonies in 150 mL LBON medium supplemented with 100 μg mL^{-1} ampicillin, and cells were grown overnight at 37 °C, 180 rpm. The folllowing day, 10 mL of pre-inoculum was added to 500 mL of LBON medium supplemented with 100 μg mL^{-1} ampicillin and 0.4 % (*w*/*v*) glucose and grown at 37 °C, 180 rpm, until the OD_{600nm} reached 0.8. The culture was then cooled to 30 °C and protein expression was induced with 300 mM NaCl. After 3 h of expression, the cells were harvested by centrifugation and resuspended in buffer A (20 mM sodium phosphate pH 7.5, 500 mM NaCl, 2.5 % (*v*/*v*) glycerol, 20 mM imidazole) containing 100 μg L^{-1} lysozyme.

For ataxin-3 purification, the cells were disrupted by gentle stirring for 1 h on ice in the presence of 0.02 mg mL^{-1} DNase, 0.02 mg mL^{-1} RNase, 1 mM $MgCl_2$, and 1 mM phenylmethylsulfonyl fluoride (PMSF—from a 1 M stock solution in ethanol). The supernatant obtained after centrifugation was loaded onto a Ni^{2+}-charged IMAC HiTrap column (GE Healthcare Life Sciences) pre-equilibrated in buffer A and eluted with a series of imidazole steps (50 mM, 250 mM, and 500 mM). EDTA was added to a final concentration of 1 mM to eluted fractions containing ataxin-3 to reduce proteolytic cleavage. The 250 mM imidazole fraction was applied to a HiPrep 26/60 Sephacryl S-300 HR column (GE Healthcare Life Sciences) pre-equilibrated in protein storage buffer (20 mM sodium phosphate pH 7.5, 150 mM NaCl, 5% (*v*/*v*) glycerol, 2 mM EDTA, 1 mM DTT). After SDS–PAGE analysis, fractions from this column corresponding to pure ataxin-3 isoforms were pooled and concentrated in an Amicon Ultra-15 centrifugal filter unit (10 kDa, Millipore) to 10–20 mg mL^{-1}, frozen in liquid nitrogen, and stored at −80 °C. Protein concentration was determined by measuring the absorbance at 280 nm using the protein's extinction coefficients, as detailed in Supplementary Table S2.

Immediately before each aggregation assay, purified ataxin-3 aliquots were applied to a Superose 12 10/300 GL column (GE Healthcare Life Sciences) pre-equilibrated in aggregation buffer (20 mM sodium phosphate pH 7.5, 150 mM NaCl, 1 mM DTT or 20 mM HEPES pH 7.5, 150 mM NaCl, 1 mM DTT) and 0.4 mL fractions were collected. Protein elution was monitored at 280 nm, and the protein concentration of the fraction corresponding to monomeric protein was determined from the absorbance at 280 nm (Supplementary Table S2).

2.3. HsUBB Expression and Purification

Homo sapiens polyubiquitin containing 3 ubiquitin units (HsUBB) was expressed and purified as previously described [23] with minor modifications. Briefly, *E. coli* BL21 (DE3) cells (Life Technologies) were transformed with pET23a-HsUBB and plated on LB Agar medium supplemented with 100 μg mL^{-1} ampicillin. A pre-inoculum was prepared from 4–5 isolated colonies in LB medium supplemented with 100 μg mL^{-1} ampicillin and grown overnight at 37 °C, 180 rpm. The pre-inoculum was added to LB medium supplemented with 100 μg mL^{-1} ampicillin and grown at 37 °C, 180 rpm, until the OD_{600nm} reached 0.8. HsUBB expression was induced with 0.5 mM IPTG for 3 h at 37 °C. The cells were harvested by centrifugation and resuspended in 50 mM Tris–HCl pH 8.5, 1 mM EDTA, 0.5 mM DTT, 0.25 mg mL^{-1} PMSF. Cells were lysed by sonication and the lysate was clarified by centrifugation (34,957 g, 45 min, 4 °C—Sorvall ST 40R—Rotor JA25.50). The cell lysate was applied to a 6 mL Resource Q ion-exchange column (GE Healthcare Life Sciences) and the flow-through was concentrated and injected onto a Superdex 75 (GE Healthcare Life Sciences) column equilibrated in 50 mM Tris–HCl pH 8.5, 150 mM NaCl, 10 % (*v*/*v*) glycerol, 1 mM DTT. The peak corresponding to pure HsUBB was concentrated in an Amicon Ultra-15 centrifugal filter unit (10 kDa, Millipore) and stored at −80 °C. The protein concentration was determined by measuring the absorbance at 280 nm using an extinction coefficient of 5,960 $M^{-1}cm^{-1}$. Before the aggregation assay with ataxin-3, HsUBB was repurified as described in Subsection 2.2 with a Superose 12 10/300 GL column (GE Healthcare Life Sciences) pre-equilibrated with the ataxin-3 aggregation buffer.

2.4. Thioflavin-T Aggregation Assay

Ataxin-3 amyloid formation was monitored by following the increase in ThT fluorescence at 480 nm (440 nm excitation) on a fluorimeter. For this study, two different fluorimeters were used: the FluoDia T70 microplate fluorimeter (Photon Technology International) using Thermowell 96-Well Polycarbonate PCR Microplates (Costar) and the CHAMELEON V (HIDEX) plate reader using 384-well microplates (low flange, black, flat bottom, polystyrene; Corning). Samples (50 μL) of 5 μM ataxin-3 in aggregation buffer containing 30 μM ThT and different concentrations of the tested compounds (as detailed below), were incubated at 37 °C, and ThT fluorescence was measured every 30 min for 60 h. To prevent evaporation, each well was covered with 20 μL paraffin oil.

2.5. Transmission Electron Microscopy

For visualization of protein fibrils/aggregates by TEM, endpoint protein samples used in the ThT assay were diluted five-fold in water and adsorbed onto glow-discharged, carbon-coated films supported on 300-mesh nickel grids and negatively stained with 1% (*w*/*v*) uranyl acetate using a protocol adapted from Rames and collaborators [24]. Grids were visualized using a JEM-1400 (JEOL) TEM at an accelerating voltage of 80 kV.

2.6. Filter Retardation Assay

To detect Atx3 77Q mature SDS-resistant fibrils, samples (5 μL) collected from each well at the endpoint of the ThT aggregation assay were diluted in 200 μL of TBS (50 mM Tris–HCl pH 7.5, 150 mM NaCl) supplemented with 2 % (*w*/*v*) SDS and boiled for 5 min. Using a Bio-Dot® SF microfiltration apparatus (Bio-Rad), the samples were filtered through a cellulose acetate membrane (0.2 μm, Whatman) pre-equilibrated in TBS, and the membrane was washed twice with TBS supplemented with 0.1 % (*w*/*v*) SDS. Next, the membrane was removed from the apparatus and blocked with TBS supplemented with 5% (*w*/*v*) non-fat dry milk for 1 h at room temperature (RT). The Atx3 77Q mature SDS-resistant fibrils retained in the membrane were probed with monoclonal mouse anti-Atx3 clone 1H9 (Millipore) antibody 1:10,000 overnight at 4 °C, incubated with anti-mouse antibody 1:10,000 for 1 h at RT, and detected using Amersham ECL Prime Western blotting chemiluminescent detection reagent (Cityva).

2.7. Native Gel Assay

Samples of 40 μM Atx3 13Q or Atx3 77Q were incubated with HsUBB at different molar ratios (1:0.5; 1:1; 1:2 and 1:3) in 20 mM HEPES pH 7.5, 150 mM NaCl, 5% (*v*/*v*) glycerol, 2 mM EDTA, 1 mM DTT, for 1 h on ice. Proteins were loaded and separated in an 8% native polyacrylamide gel electrophoresis (PAGE) gel (240 mM Tris–HCl pH 9.5, 8 % (*v*/*v*) acrylamide, 0.1% (*w*/*v*) APS, 0.1% (*v*/*v*) TEMED), in a Mini-PROTEAN Tetra cell (Bio-Rad) at 100 V, and stained by incubation with BlueSafe (NZYTech).

2.8. Ataxin-3 13Q and Ataxin-3 JD Oligomerization Kinetics Measured via switchSENSE

Measurements were set up in the switchBUILD software with "His-tag capture" as the immobilization method and performed in static measurement mode on a DRX device on MPC-48-2-R1 biochips (both Dynamic Biosensors GmbH (DBS)). The system was primed with running buffer (phosphate-buffered saline (PBS) pH 7.5, 1 mM TCEP) and the biochip was functionalized with 200 nM NTA3-functionalized cNL-B48 DNA (His-tag capture kit, order number CK-TN-1-B48, DBS) in hybridization buffer (10 mM sodium phosphate pH 7.4, 40 mM NaCl, 0.05% (*v*/*v*) Tween 20, 50 μM EDTA, 50 μM EGTA) for 10 min. The NTA3 group was stripped and activated by injection of EDTA and loading solution. Capture of 500 nM His-tagged Atx3 13Q or the Atx3 JD domain, diluted in running buffer and stored at 10 °C in the autosampler until automatic pickup, was performed for 2 min at a flow rate of 20 μL min^{-1} at 37 °C. Association of Atx3 13Q or Atx3 JD domain diluted in running buffer to indicated concentrations, as well as subsequent dissociation in running buffer, was performed at 37 °C, 100 and 50 μL min^{-1}, respectively. Samples were measured in consecutive rounds with increasing analyte concentrations and NTA regeneration in between. Data were analysed with the switchANALYSIS software kinetics tool. Data were normalized to the baseline of the association, Atx3 13Q data were referenced with a 0 M run, and global mono-exponential fits were calculated by least-squares residual determination.

3. Results

3.1. Development of a Miniaturized Ataxin-3 Aggregation Assay

Ataxin-3 self-assembly has a complex mechanism, with oligomeric and amyloid pathways taking place simultaneously [17,25]. The high tendency of ataxin-3 to assemble into high-molecular weight oligomeric structures [10], concomitantly with the occurrence of two parallel ataxin-3 oligomerisation pathways on- and off-route to the formation of amyloid fibrils, implies that a tight control of the multiple variables and aggregation buffer components is critical to the development of reproducible assays to monitor protein aggregation [16]. We have previously established a miniaturized assay to follow the amyloid assembly of Atx3 13Q [16,17]. In that assay, freshly re-purified Atx3 13Q (5 μM) was incubated at 37 °C in phosphate buffer and amyloid formation was monitored by ThT binding in a final volume of 50 μL. Under those previously established conditions, the lag phase of aggregation was longer than 20 h and often varied between 30 and 40 h [17]. The long lag phase of ataxin-3 amyloid assembly in phosphate buffer, combined with the molecular stochasticity of the primary nucleation, accounts for the large variations in the lag phase duration that we observed during the aggregation assays under these conditions. In contrast, the lag phase for Atx3 13Q aggregation was decreased by ~20 h when sodium phosphate (as in [16,17]) was replaced with HEPES in the aggregation solution (Figure 1A). The aggregation assay using HEPES buffer was very robust, as shown by the high reproducibility observed in 192 replicates setup in a 386-well plate using 3 μM Atx3 13Q (Supplementary Figure S1), suggesting that this assay can be used for medium- and high-throughput screening for ataxin-3 aggregation inhibitors.

Next, we evaluated the behaviour of ataxin-3 variants and truncated constructs (Figure 1B) in aggregation solutions buffered with HEPES. The purified proteins (Supplementary Figure S2), stored at −80 °C, were thawed and re-purified by size exclusion chromatography in the selected buffer before the aggregation assay (Figure 1D). This step is critical to remove the glycerol used in the ataxin-3 storage buffer, which has a strong effect on the aggregation kinetics (see below), and to eliminate putative aggregates formed during freezing/thawing, which could modify the nucleation process and compromise assay reproducibility. A complete protocol including all the steps for ataxin-3 production and aggregation analysis is presented in the Supplementary Materials. One relevant factor to ensure high-quality protein is the utilization of codon-optimized nucleotide sequences to express ataxin-3 with various polyQ tract sizes, particularly important for producing high-purity Atx3 77Q. Our results showed that ataxin-3 self-assembles into amyloid-like structures with fibrillar morphology independently of the polyQ tract (Figure 1E,H), similar to what had been previously observed in phosphate-buffered aggregation solutions [17]. In addition, SDS–PAGE analysis of ataxin-3 at the endpoint of aggregation (~60 h, 37 °C) showed that no relevant protein degradation occurred under the established assay conditions (Figure 1F).

Previous data showed that both Atx3 77Q and Atx3 13Q aggregate, with the globular JD playing a central role in the first steps of ataxin-3 self-assembly [10,13,26,27]. To quantify Atx3 JD and Atx3 13Q self-association kinetics, we used electrically switchable nanolever (switchSENSE) technology [28,29]. SwitchSENSE is a biophysical characterization method ideally suited to kinetic binding analysis of challenging molecules, such as aggregation-prone proteins. The low surface density of the immobilized protein of interest allows a controlled induction of the oligomerization processes upon analyte injection in the liquid phase. The nanolevers were functionalized with 500 nM Atx3 13Q or JD and binding of unlabeled JD or Atx3 13Q to the surface-tethered proteins allowed the measurement of JD and Atx3 13Q self-association kinetics. The association and dissociation curves were measured for analyte concentrations between 3.75 and 15 μM. The equilibrium dissociation constants (K_D) for Atx3 13Q and JD self-association (Figure 1G) were in the μM range, in good agreement with the K_D of 4.6 μM estimated from our biophysical model for Atx3 13Q aggregation [17]. Although the association rate constants (k_{on}) were similar for both constructs, the isolated JD dissociated faster, showing that the C-terminal tail of ataxin-3 stabilizes its self-association, in good agreement with the differences observed in the ThT aggregation kinetics (Figure 1E).

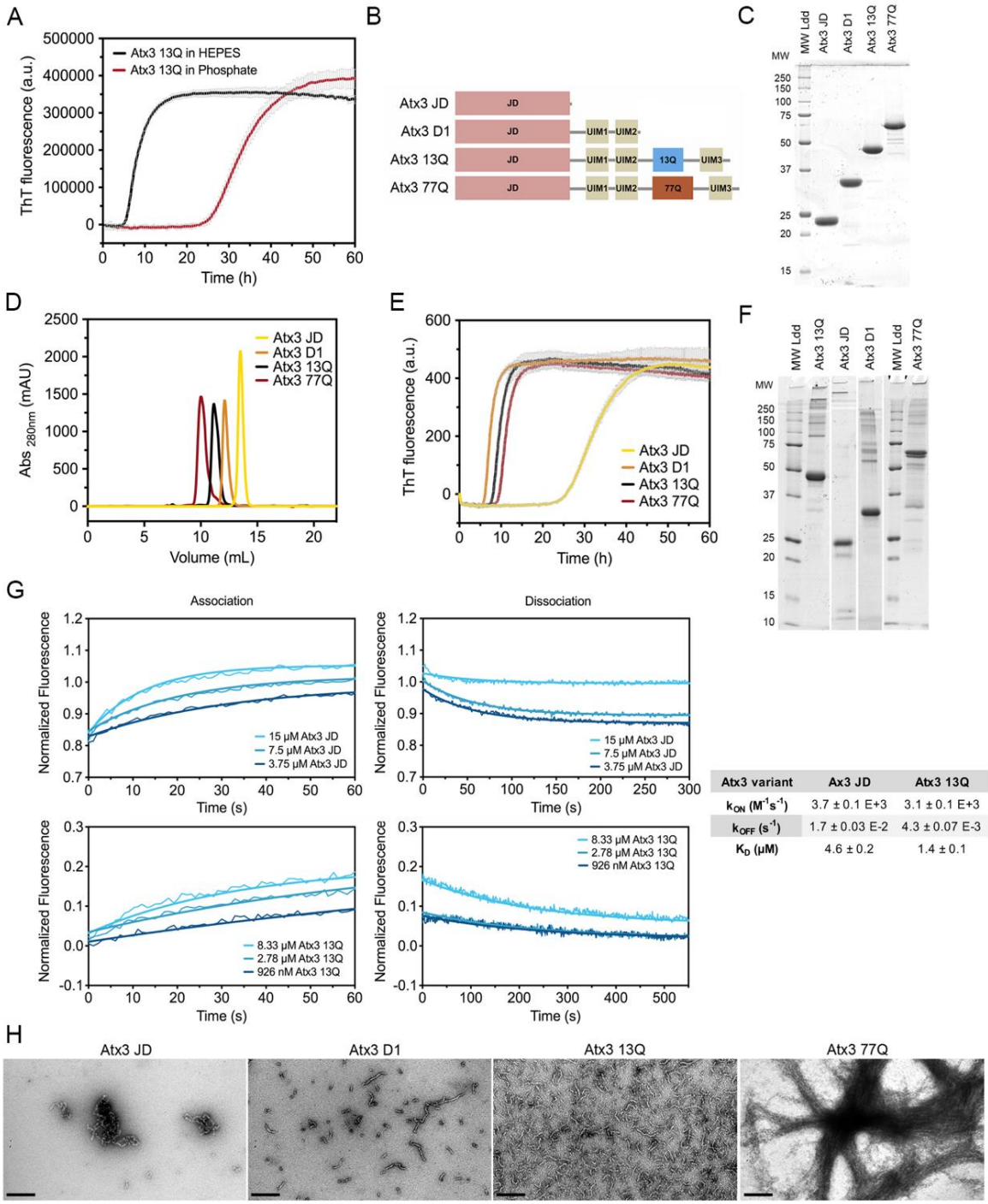

Atx3 variant	Ax3 JD	Atx3 13Q
k_{ON} ($M^{-1}s^{-1}$)	3.7 ± 0.1 E+3	3.1 ± 0.1 E+3
k_{OFF} (s^{-1})	1.7 ± 0.03 E-2	4.3 ± 0.07 E-3
K_D (μM)	4.6 ± 0.2	1.4 ± 0.1

Figure 1. Ataxin-3 amyloid assembly assay. (**A**) ThT assay performed to monitor the formation of Atx3 13Q amyloid species in two distinct buffers, HEPES vs. phosphate buffer. Curves represent the means and standard deviations of five replicates for each condition (FluoDia T70 plate reader). (**B**) Schematic representation of the ataxin-3 constructs used in this work. (**C**) SDS–PAGE of freshly thawed ataxin-3 constructs prior to re-purification. (**D**) Size exclusion chromatography of re-purified ataxin-3 isoforms, where no aggregates are detectable. (**E**) ThT assay performed to measure the formation of amyloid species for different ataxin-3 constructs in HEPES buffer. Curves represent the means and standard deviations of five replicates for each condition (CHAMELEON vs. plate reader). (**F**) SDS–PAGE of ataxin-3 constructs at the end of the ThT aggregation assay. (**G**) Self-assembly kinetics of Atx3 JD and Atx3 13Q determined using

switchSENSE technology and derived rate and equilibrium constants. (**H**) TEM images after negative staining of endpoint samples (60 h, 37 °C) of all ataxin-3 constructs. Scale bars correspond to 200 nm.

Interestingly, the truncated variant lacking the polyQ segment and the C-terminal UIM3 (Atx3 D1) had the same amyloid assembly kinetics as the full-length ataxin-3, highlighting the relevance of the region bridging the JD and the polyQ for self-assembly into amyloid-like fibrils [18,30]. In contrast to previously published data [15,31], the aggregation kinetics for the non-expanded Atx3 13Q and disease-related Atx3 77Q fully overlapped. This result was obtained consistently when the proteins were freshly re-purified, immediately before the aggregation assays. This step removes minute amounts of aggregated species, most frequently contaminating freshly thawed Atx3 77Q monomeric fractions (Supplementary Figure S2C,D), which might act as nucleation seeds and accelerate aggregation of pathogenic ataxin-3 in vitro. Analysis of the fibril morphologies by negative staining transmission electron microscopy (TEM; Figure 1H) showed that only Atx3 77Q assembled into mature fibrillar agglomerates [27], a process that apparently does not interfere with the maximum ThT signal (Figure 1E). This indicates that monitoring ataxin-3 aggregation by ThT binding kinetics only reflects the first aggregation step that is reliant on JD self-assembly. This assay may be used to evaluate the effects of mutations or compare the modulatory roles of various buffer components and ataxin-3-interacting molecules on ataxin-3 early aggregation processes, as shown below.

3.2. Analysis of the Aggregation Kinetics of Natural Ataxin-3 Variants

An intragenic polymorphism in the Atxn3 gene (rs12895357, UniProt variant VAR_013689) was observed in the population, with one variant containing a GGG codon, translated to glycine downstream of the CAG repeats, and another variant containing a CGG codon, translated to arginine. This polymorphic position was used to study SCA3 haplotype and origins [32–34]. Taking into consideration the data available in the 1000 Genomes Project, Phase 3 [35], which gathered genomic information from 4,973 healthy individuals, the variant containing the glycine residue after the polyQ repeat was prevalent in all populations (Supplementary Figure S3). The variant containing arginine at the equivalent position was also found in all populations, being more prevalent in the East Asian population and was originally linked with repeat expansion in Japanese SCA3 patients [36].

Our Atx3 13Q construct contains a glycine residue after the polyQ sequence, while the Atx3 77Q construct has an arginine in the equivalent position (Supplementary Table S2). We compared the aggregation kinetics of Atx3 77Q and Atx3 77Q R388G (Figure 2) to evaluate the potential impact on the nature of the residue at this position upon expanded ataxin-3 aggregation. The results showed that the presence of a glycine or an arginine immediately after the polyQ tract did not alter the ThT fluorescence curves (Figure 2A), as they monitored the first step of ataxin-3 aggregation. Additionally, no differences were observed in the Atx3 77Q or Atx3

77Q R388G fibril morphologies (Figure 2B), both of which matured into SDS-resistant fibrillar clusters (Figure 2C). Therefore, we decided to use our original Atx3 77Q construct to explore the influence of various buffer components on ataxin-3 aggregation kinetics.

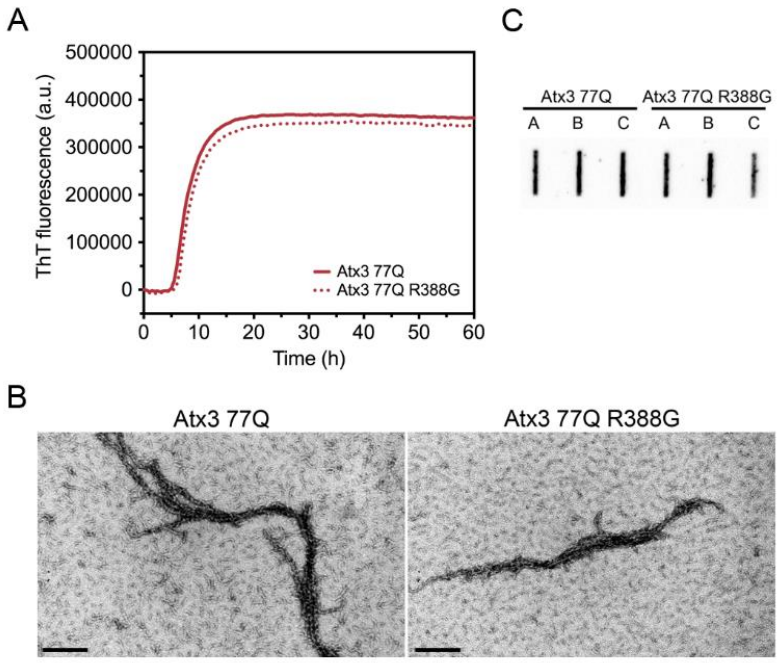

Figure 2. Effect of ataxin-3 variant rs12895357 on aggregation kinetics. (**A**) ThT assay performed to measure the formation of amyloid-like species in Atx3 77Q and Atx3 77Q R388G. Curves represent the means and standard deviations of five replicates for each condition (FluoDia T70 plate reader). (**B**) TEM images after negative staining of endpoint samples (60 h, 37 °C) of both ataxin-3 variants. Scale bars correspond to 200 nm. (**C**) Filter retardation assay monitored by immunostaining with mouse anti-ataxin-3 1H9 of aggregation endpoints (60 h, 37 °C) from Atx3 77Q and Atx3 77Q R388G. A, B, and C are replicates.

3.3. The Influence of the Buffer Components on Ataxin-3 Aggregation

Several studies have shown the impact of ionic strength on the aggregation propensity of various amyloid-forming proteins [37–43]. To evaluate the influence of ionic strength on ataxin-3 self-assembly, we monitored the effect of varying the NaCl concentration between 50 and 300 mM on the aggregation kinetics. In the selected buffer conditions, varying the NaCl concentration had no major effect on the formation of ThT-positive amyloid-like species for both expanded and non-expanded ataxin-3 (Figure 3A,B). However, large variability in the maximum ThT fluorescence in the different replicates was noted for the non-expanded Atx3 13Q in the presence of 300 mM NaCl (Figure 3A). This variability possibly resulted from the presence of air bubbles in this particular experiment, as replicates of this assay did not show a reduction of ThT signal (Supplementary Figure S4). No relevant differences were found in the morphology of the fibrils at the endpoint of the ThT aggregation assay (~60 h) as observed by TEM analysis (Figure 3C). Similarly, no differences in ataxin-3

aggregation kinetics were observed when the pH of the HEPES buffer was varied between 7.0 and 8.5 (Supplementary Figure S5).

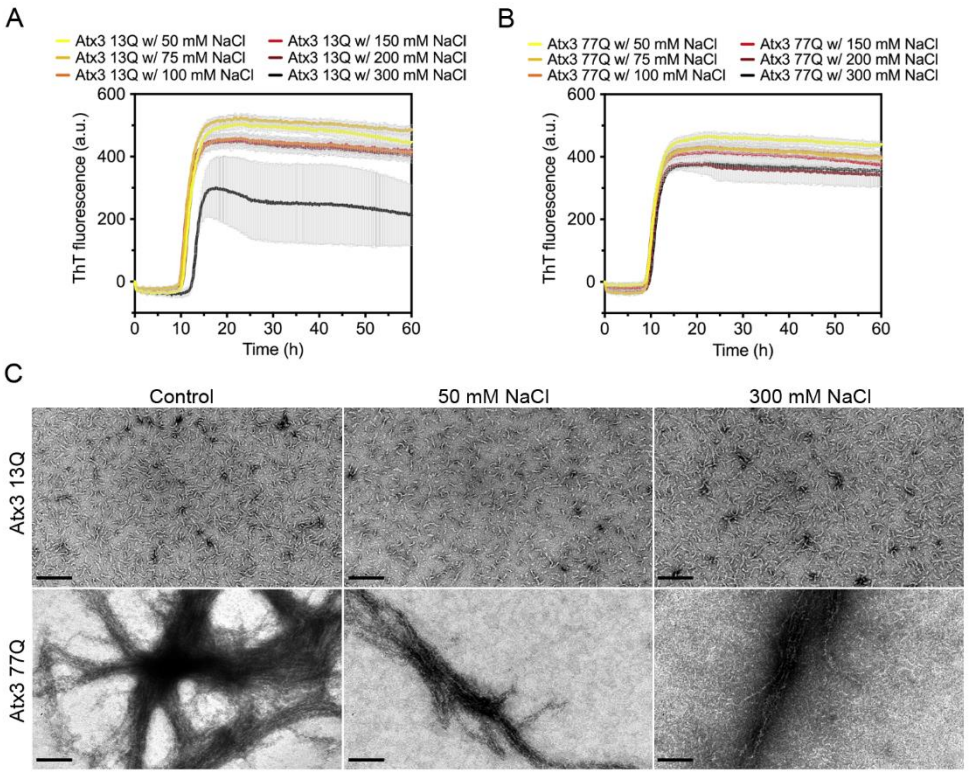

Figure 3. Effect of NaCl on ataxin-3 aggregation kinetics. ThT assay performed to measure the formation of amyloid-like species in (**A**) Atx3 13Q and (**B**) Atx3 77Q in the presence of 50, 75, 100, 150 (control), 200, and 300 mM NaCl. Curves represent the means and standard deviations of five replicates for each condition (CHAMELEON vs. plate reader). (**C**) TEM images after negative staining of ThT assay endpoint samples (60 h, 37 °C) of Atx3 13Q and Atx3 77Q in the presence of 150 (control), 50, and 300 mM NaCl. Scale bars correspond to 200 nm.

We next tested the effect of glycerol on ataxin-3 aggregation. Glycerol is frequently used to prevent protein aggregation [44,45] and was added to the ataxin-3 purification and storage buffers [10,16,17]. We evaluated the effect of varying the glycerol concentration on ataxin-3 aggregation (Figure 4). In the presence of 0.5 % or 1 % (*v*/*v*) glycerol, the aggregation lag-phase was elongated, both for polyQ-expanded and non-expanded ataxin-3 (Figure 4A,B). The presence of 5% (*v*/*v*) glycerol increased the aggregation lag-phase and diminished the maximum ThT fluorescence for both ataxin-3 variants (Figure 4A, B). Accordingly, the morphological analysis of the endpoint samples by TEM showed a clear decrease in the size and number of Atx3 13Q protofibrils and Atx3 77Q mature fibrils in the presence of 5% (*v*/*v*) glycerol (Figure 4C).

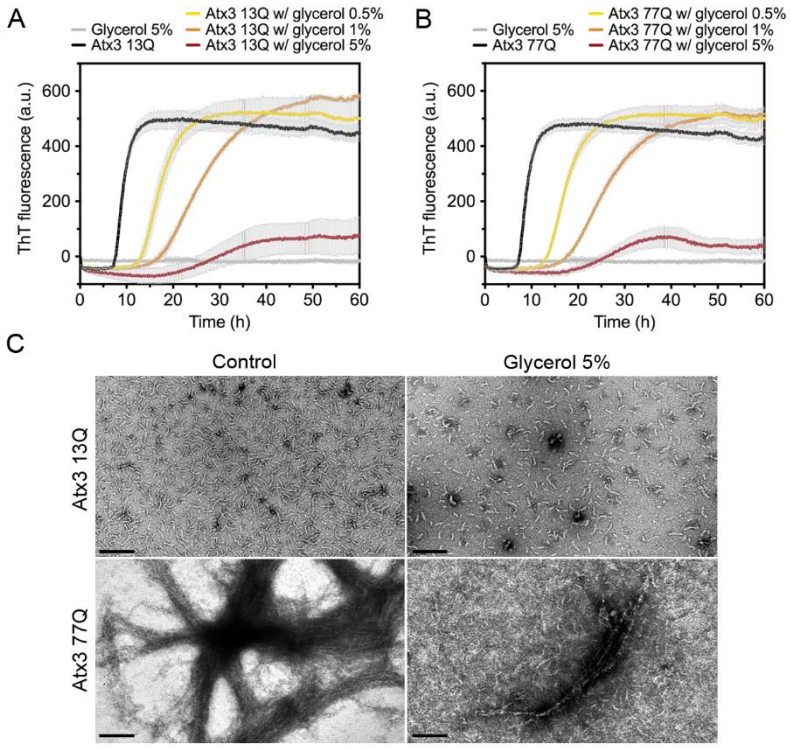

Figure 4. Effect of glycerol on ataxin-3 aggregation kinetics. ThT assay performed to measure the formation of amyloid-like species in (**A**) Atx3 13Q and (**B**) Atx3 77Q in the presence of 0.5, 1, and 5% (*v*/*v*) glycerol. Curves represent the means and standard deviations of five replicates for each condition (CHAMELEON vs. plate reader). (**C**) TEM images after negative staining of ThT assay endpoint samples (60 h, 37 °C) of Atx3 13Q and Atx3 77Q in the absence (control) and in the presence of 5% (*v*/*v*) glycerol. Scale bars correspond to 200 nm.

The effects of other widely used buffer additives, such as (i) the chelating agent ethylenediamine tetraacetic acid (EDTA), (ii) the protease inhibitor phenylmethylsulfonyl fluoride (PMSF), (iii) the preservative sodium azide, and (iv) the solvents ethanol and dimethyl sulfoxide (DMSO), were also tested. All the conditions tested had no significant effect on the aggregation kinetics of both Atx3 13Q (Supplementary Figure S6A,C) or Atx3 77Q (Supplementary Figure S6B,D).

3.4. The Influence of Detergents on Ataxin-3 Aggregation

Detergents can be used to perturb hydrophobic protein–protein interactions and prevent unwanted protein aggregation. To evaluate the effect of detergents on ataxin-3 aggregation, we tested SDS and the milder biological detergents Triton X-100 and Tween 20.

SDS had an immediate effect on ThT fluorescence, suggesting that in the assay conditions this surfactant completely abrogated ataxin-3 aggregation (Figure 5A,D). A possible fluorescence quenching effect was observed in the presence of 1mM or 5mM SDS, where the ThT signal decreased to values below the initial zero. This effect was not as evident when SDS was added to ThT alone. TEM analysis detected no protofibrils or mature fibrils at the

endpoint of Atx3 13Q or Atx3 77Q aggregation in the presence of SDS (Figure 5G). Previous studies had shown that 5mM SDS enhanced the α-helical content of the JD, stabilizing ataxin-3 and interfering with both JD-mediated and polyQ expansion-triggered aggregation steps [46]. In contrast to our results, these previous studies found that 1mM SDS increased ataxin-3 aggregation, using an assay with 6-fold higher ataxin-3 concentrations. We hypothesize that the higher SDS:ataxin-3 ratio in our assay might explain the divergent results observed with 1 mM SDS and that the anti-amyloid assembly effects of SDS might have been caused by specific interactions with ataxin-3 that prevented early fibril assembly events.

The effect of Triton X-100 and Tween 20 on ataxin-3 aggregation was evaluated using five different concentrations (0.15, 0.3, 0.8, 1, and 5 mM). Both detergents led to a sharp increase in the ThT signal at the onset of ataxin-3 aggregation (Figure 5B,C,E,F). As increasing concentrations of Triton X-100 (Figure 5B,E) or Tween 20 (Figure 5C,F) were used, the maximum value of ThT fluorescence decreased. Ataxin-3 aggregation curves in the presence of 5 mM Triton X-100 or Tween 20 showed lower ThT fluorescence values, which may suggest a strong anti-aggregation effect. The critical micellar concentrations (CMCs) of Triton X-100 and Tween 20 in water are ~0.2 mM and ~0.06 mM, respectively. Although these values may vary with the specific buffer conditions and temperature, the decrease in ataxin-3 aggregation with the increasing concentration of these non-ionic detergents could be correlated with ataxin-3 stabilization by interaction with the detergent micelles. However, a fluorescence quenching effect was observed when 5 mM Tween 20 or 5 mM Triton X-100 were added to ThT alone (Figure 5B,C,E,F), suggesting that the aggregation inhibition effects are likely artefactual [47]. TEM analysis at the endpoint of aggregation also revealed that the number and size of Atx3 13Q protofibrils were similar to those in the control condition (Figure 5G). Atx3 77Q was also able to form mature fibrils in the presence of these detergents (Figure 5G).

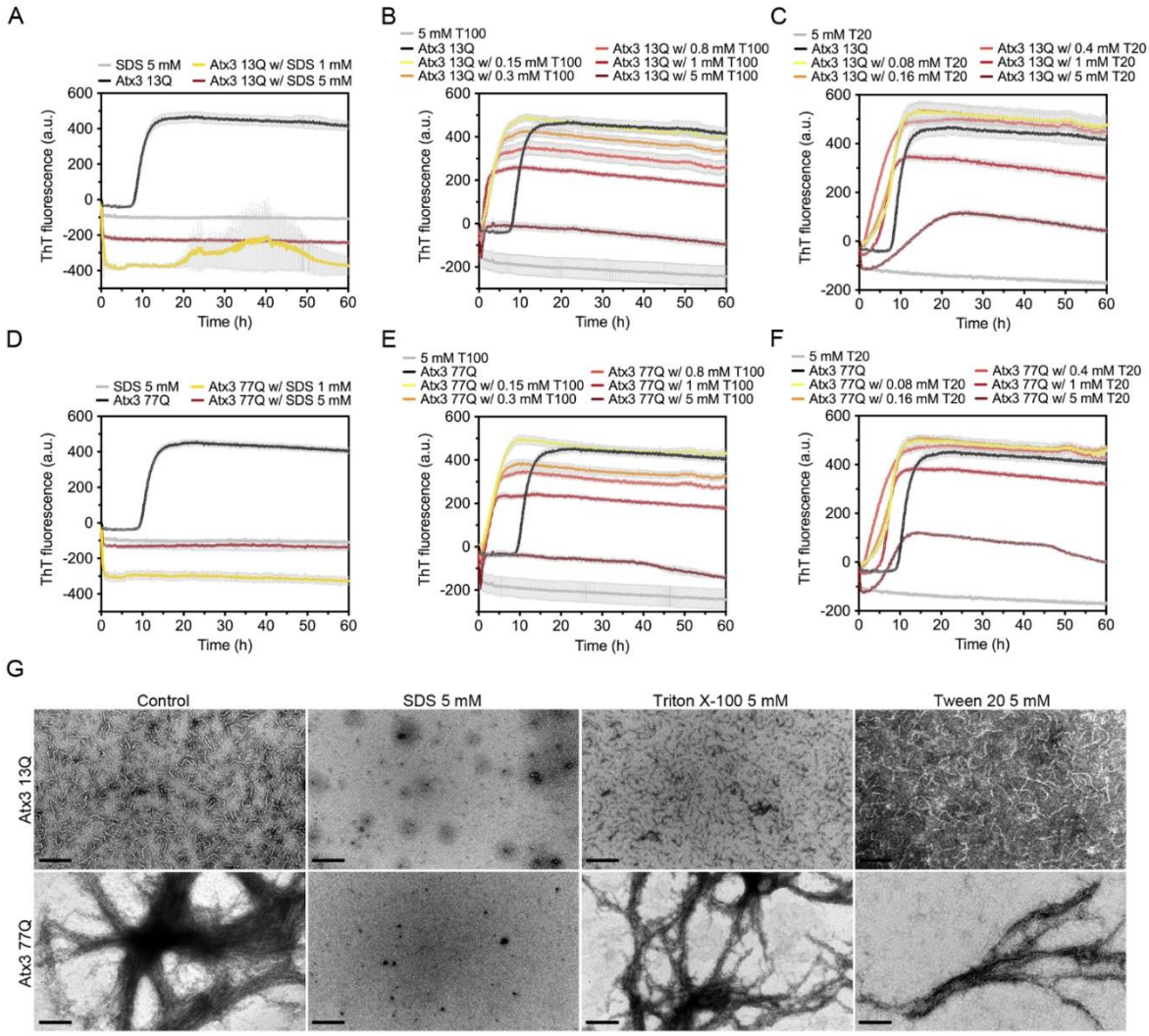

Figure 5. Effect of SDS, Triton X-100, and Tween 20 on ataxin-3 aggregation kinetics. ThT assay to measure the formation of amyloid-like species in (**A**–**C**) Atx3 13Q and (**D**–**F**) Atx3 77Q in the presence of different concentrations of SDS, Triton X-100 (T100), and Tween 20 (T20). Curves represent the means and standard deviations of five replicates for each condition (CHAMELEON vs. plate reader). (**G**) TEM images after negative staining of ThT assay endpoint samples (60 h, 37 °C) of Atx3 13Q and Atx3 77Q in the presence of 5 mM SDS, Triton X-100, or Tween 20, in comparison with the control condition in the absence of these additives. Scale bars correspond to 200 nm.

3.5. The Influence of Molecular Crowders on Ataxin-3 Aggregation

Molecular crowders are widely used in aggregation assays to mimic the high macromolecular concentrations within biological cells and predict the effects on protein aggregation [48]. For this reason, we studied the effect of well-known molecular crowders, such as dextran and polyethylene glycol (PEG), on the aggregation profiles of ataxin-3 (Figure 6).

We tested the effect of 10 and 20% (*w*/*v*) dextran, a commonly used crowding agent [48], on ataxin-3 aggregation. Dextran shortened the duration of the lag-phase and decreased the maximum ThT fluorescence values of both ataxin-3 variants (Figure

6A,D). The effect of 20% (*w*/*v*) dextran was more pronounced on Atx3 77Q (Figure 6D), resulting in an inhibition of ataxin-3 amyloid-like aggregation, which was consistent with the absence of long mature fibrils (Figure 6G). Nevertheless, minor amounts of short protofibrils (Atx3 13Q) and amorphous aggregates (Atx3 77Q) were still observed (Figure 6G).

The addition of PEG 5,000 or PEG 10,000 to ataxin-3 aggregation assays resulted in a concentration-dependent reduction of the maximum ThT fluorescence (Figure 6B,C,E,F), suggesting that PEG was able to interfere with the formation of ataxin-3 amyloid-like structures. However, the addition of 20% (*w*/*v*) PEG 5,000 or PEG 10,000 inhibited the ataxin-3 aggregation process of both non-expanded and polyQ-expanded ataxin-3, as suggested by the absence of ThT fluorescence (Figure 6B,C,E,F). This effect was confirmed by the absence of fibrillar amyloid-like structures as observed by TEM (Figure 6G).

These results showed that dextran, PEG 5,000, and PEG 10,000 were strong inhibitors of ataxin-3 amyloid assembly acting on the first stage of the aggregation pathway and consequently inhibiting the formation of Atx3 13Q protofibrils and mature Atx3 77Q fibrils.

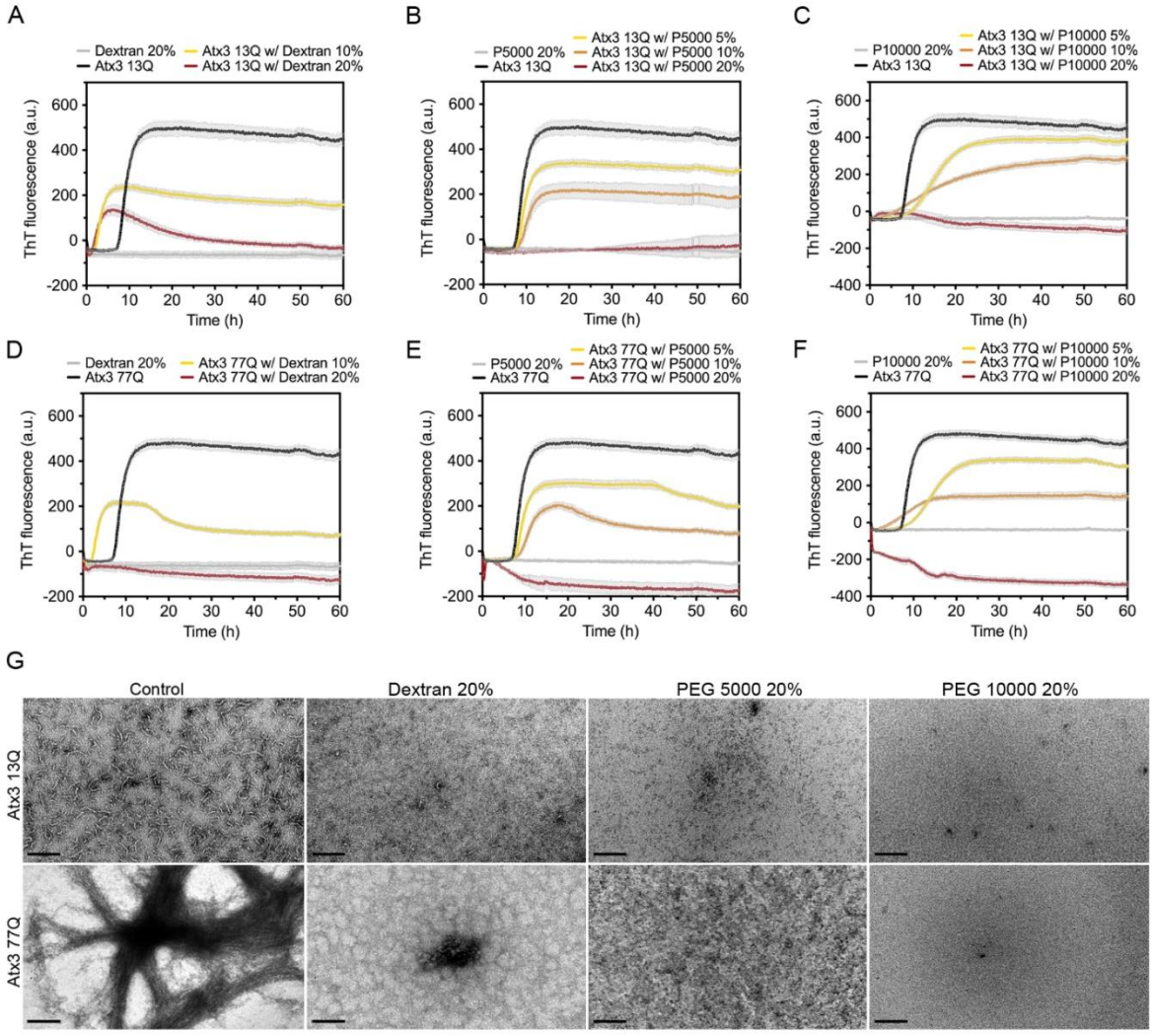

Figure 6. Effects of dextran, PEG 5,000, and PEG 10,000 on ataxin-3 aggregation kinetics. ThT assay performed to measure the formation of amyloid-like species in (**A**–**C**) Atx3 13Q and (**D**–**F**) Atx3 77Q in the presence of different concentrations of dextran, PEG 5,000, and PEG 10,000. Curves represent the means and standard deviations of five replicates for each condition (CHAMELEON vs. plate reader). (**G**) TEM images after negative staining of endpoint samples (60 h, 37 °C) of Atx3 13Q and Atx3 77Q in the presence of Dextran, PEG 5,000 (P5000), and PEG 10,000 (P10,000), compared to the control condition in the absence of additives. Scale bars correspond to 200 nm.

3.6. The Influence of Ataxin-3 Interactors on Ataxin-3 Aggregation

Several studies have reported the interaction of ataxin-3 with ubiquitin and polyubiquitin chains [49–53]. Two ubiquitin binding sites have been identified in the JD, one of them overlapping with the aggregation-prone sequence, and the addition of ubiquitin has also been reported to decrease JD aggregation [54]. In agreement with this, mutation of the second ubiquitin binding site of ataxin-3, coincident with the aggregation-prone segment in the JD, affected the first JD-mediated aggregation step (Supplementary Figure S7). We evaluated the interaction of Atx3 13Q and Atx3 77Q with a linear tri-ubiquitin chain (HsUBB) by native gel electrophoresis and the results suggested that both variants interact weakly with HsUBB (Figure 7A). A ThT aggregation assay of Atx3 13Q and Atx3 77Q in the presence of different molar ratios of HsUBB (1:2 and 1:5) showed that HsUBB did not change the aggregation kinetics of non-expanded ataxin-3 but had a slight impact on the maximum ThT fluorescence of Atx3 77Q (Figure 7B,C). At the highest concentration used, HsUBB reduced the number of Atx3 13Q protofibrils and the overall size of Atx3 77Q mature fibrils, as evaluated by TEM (Figure 7D). Analysis of the final products of Atx3 77Q aggregation by filter retardation assay revealed a slight decrease in the amount of Atx3 77Q SDS-resistant mature fibrils at the molar ratio of 1:5 (Figure 7E), suggesting a role for this linear ubiquitin chain in the modulation of pathogenic ataxin-3 aggregation.

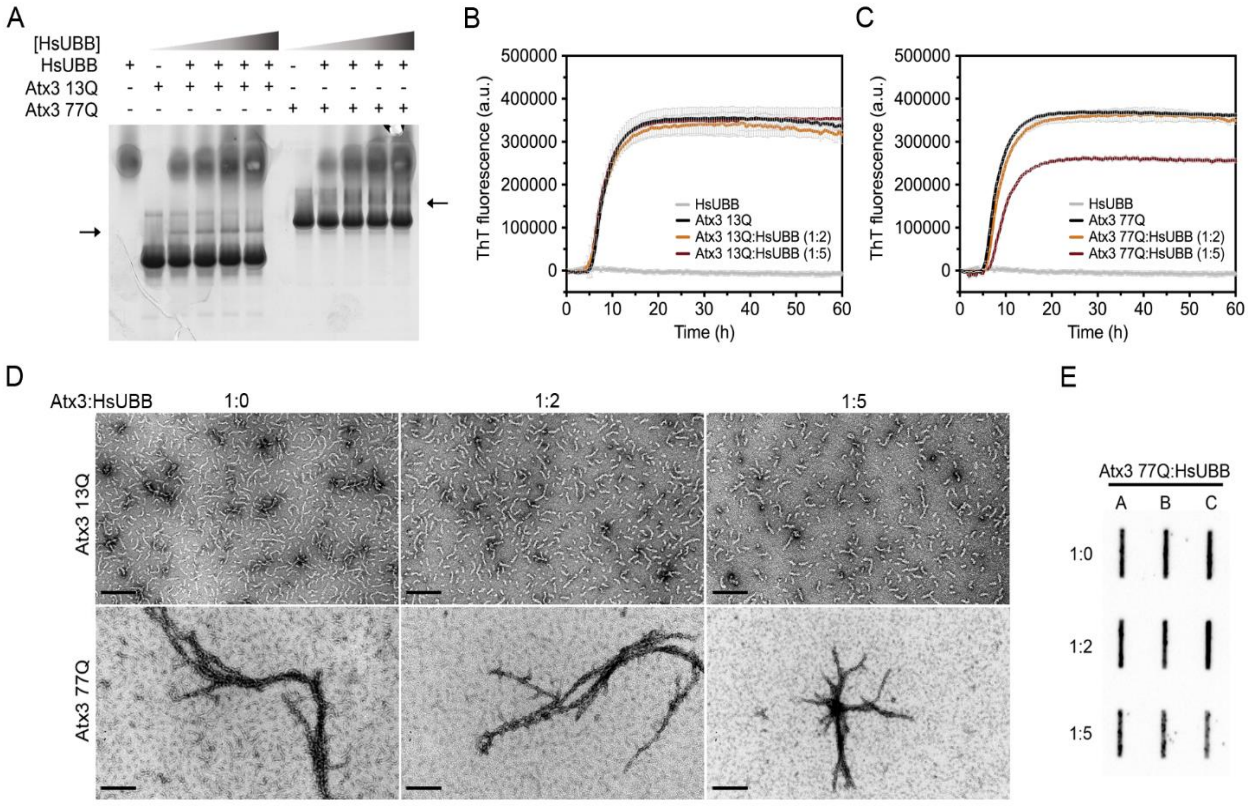

Figure 7. Effect of HsUBB on ataxin-3 aggregation kinetics. (**A**) Native gel electrophoresis of Atx3 13Q and Atx3 77Q with different ratios of ataxin-3:HsUBB, suggesting a weak interaction between ataxin-3 and tri-ubiquitin. ThT assay performed to measure the formation of amyloid-like species of (**B**) Atx3 13Q and (**C**) Atx3 77Q in the presence of 10 and 25 μM HsUBB. Curves represent the means and standard deviations of five replicates for each condition (FluoDia T70 plate reader). HsUBB was re-purified by size exclusion chromatography in ataxin-3 aggregation buffer prior to the aggregation assay. (**D**) TEM images after negative staining of endpoint samples (60 h, 37 °C) of Atx3 13Q and Atx3 77Q in the presence of different concentrations of HsUBB. Scale bars correspond to 200 nm. (**E**) Filter retardation assay of aggregation endpoint samples (60 h, 37 °C) from the Atx3 77Q aggregation assay in the presence of HsUBB. A, B, and C are replicates.

The polyglutamine-binding peptide 1 (QBP1) is an 11-residue sequence that has been shown to inhibit the formation of mature SDS-resistant fibrils of polyQ-expanded ataxin-3 [15,18]. QBP1 binds to monomeric ataxin-3, between the JD domain and the UIM1 (residues 182–221), inhibiting the polyQ-dependent aggregation stage [18]. As expected, in our experiments, QBP1 did not prevent the formation of ataxin-3 protofibrils (Figure 8). For all QBP1:ataxin-3 molar ratios tested, we obtained coincident ThT aggregation curves for both ataxin-3 variants (Figure 8A,B). Samples of Atx3 13Q and Atx3 77Q in the presence of QBP1 at a molar ratio of 1:10 (ataxin-3:QBP1) were collected and analysed by TEM (Figure 8C). The results confirmed that the presence of QBP1 did not prevent the formation of Atx3 13Q protofibrils but that it did abolish the maturation of the Atx3 77Q fibrils (Figure 8C), as previously described [18].

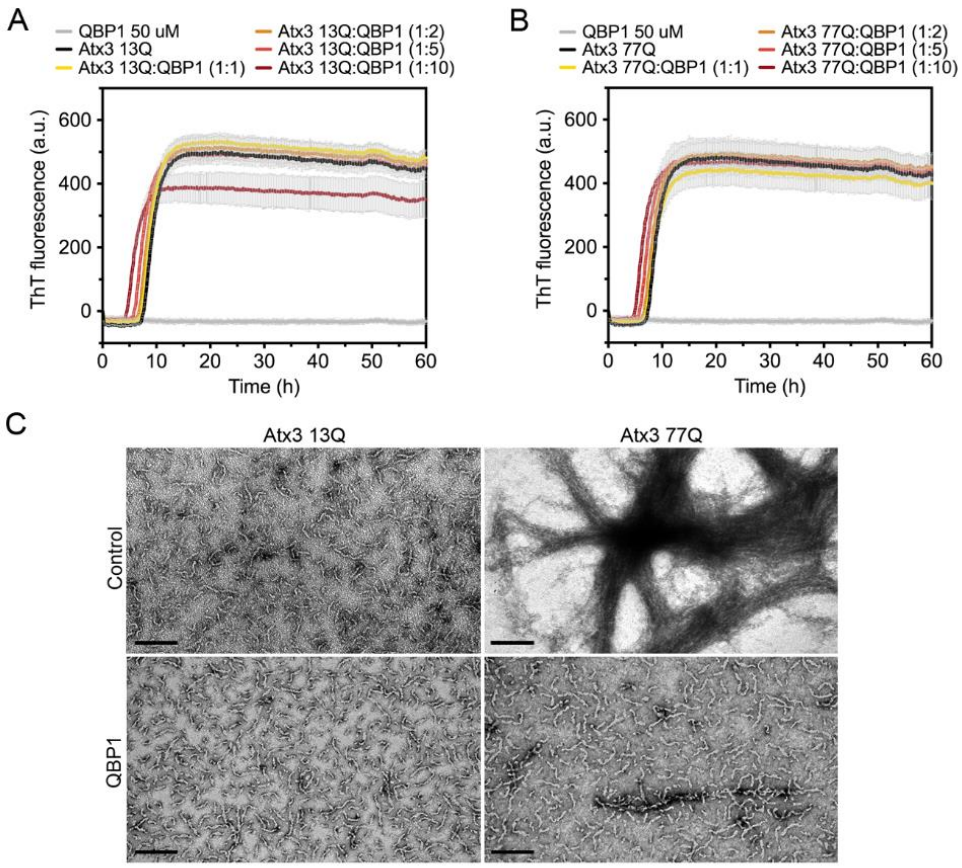

Figure 8. Effect of QBP1 on ataxin-3 aggregation kinetics and fibril maturation. ThT assay performed to measure the formation of amyloid-like species of (**A**) Atx3 13Q and (**B**) Atx3 77Q in the presence of 5, 10, 25, and 50 μM QBP1 in ataxin-3 aggregation buffer. Curves represent the means and standard deviations of five replicates for each condition (CHAMELEON vs. plate reader). (**C**) TEM images after negative staining of endpoint samples (60 h, 37 °C) of Atx3 13Q and Atx3 77Q in the presence of QBP1 at a molar ratio of 1:10 (ataxin-3:QBP1). Scale bars correspond to 200 nm.

4. Discussion

Several studies have shown that both normal and polyQ-expanded ataxin-3 are able to self-assemble into amyloid-like fibrils in vitro, opening new routes to study how various molecules modulate self-association and to discover anti-aggregation agents. Here, we present an optimized and robust assay to study the effect of distinct factors on the first step of ataxin-3 aggregation in vitro, following the guidelines that ensure assay reproducibility [16,55]. This assay requires low concentrations of protein (5 μM) and can be used to study both normal and polyQ-expanded ataxin-3. To ensure high reproducibility, ataxin-3 and/or its interacting partners are always re-purified by size-exclusion chromatography in the selected aggregation buffer immediately before setting up the aggregation assay. A detailed protocol for ataxin-3 production and aggregation studies is also included as ancillary information, along with the relevant data concerning the sequences of all the ataxin-3 constructs used in this work. Using this approach, we investigated

how several external factors can affect protein aggregation in vitro and assessed the aggregation behaviour of ataxin-3 variants commonly found in the human population.

4.1. The Relevance of the Buffer System for Ataxin-3 Aggregation

Phosphate is considered a biologically relevant buffer, frequently used for studying amyloid formation in vitro. Our results show that the buffer system used in the self-assembly assays has an important impact on ThT-monitored ataxin-3 amyloid formation, as previously seen for Aβ(1–40) [56]. In particular, replacing sodium phosphate with HEPES induced an 80% reduction in the duration of the lag phase of the ataxin-3 amyloid progress curves and increased assay reproducibility, without affecting the morphology of the endpoint fibrils visualized by TEM. It is unclear why the two buffer ions significantly alter the lag phase, but this could be the result of weak interactions with unique ataxin-3 sequence motifs triggering or stabilizing the rate-limiting assembly of the first aggregation nuclei. This is an interesting question worth exploring in future research.

4.2. The Role of Additives in Ataxin-3 Aggregation

In our assay conditions, varying the NaCl concentration between 50 and 200 mM, or the pH between 7.0 and 8.5, did not strongly affect ataxin-3 amyloid assembly nor the morphology of the endpoint fibrils. In contrast, glycerol, an additive regularly used in ataxin-3 purification, had a major role in decreasing ataxin-3 fibril assembly, even at concentrations as low as 0.5% (*v*/*v*). Therefore, the presence of glycerol is an important parameter to define when designing the aggregation protocol. In contrast, EDTA (2-5 mM), PMSF (1 mM), sodium azide (0.05% (*w*/*v*)), ethanol (1% (*v*/*v*), and DMSO (0.05% (*v*/*v*)) did not affect the ataxin-3 amyloid progress curves.

4.3. The Effect of Detergents on Ataxin-3 Aggregation Monitored by ThT

The behaviour of the ThT curves for ataxin-3 amyloid assembly in the presence of anionic and non-ionic detergents is worth discussing in detail. Although ThT is an amyloid-specific dye commonly used to monitor amyloid formation kinetics in real time, particular care should be taken in the interpretation of the experimental results [16,57]. When SDS, Triton X-100, and Tween 20 were included in the aggregation assay, a decrease in the fluorescence signal of ThT was observed with increasing concentrations of the detergents. However, a sharp decrease in ThT fluorescence, observed in the control experiments without ataxin-3, suggested that these results should be interpreted with caution and confirmed by complementary techniques. In fact, TEM analysis showed that the anionic detergent SDS was able to abolish ataxin-3 assembly into amyloid fibrils, but the non-ionic detergents did not affect ataxin-3 amyloid formation.

4.4. Molecular Crowders and Ataxin-3 Aggregation

The intracellular environment is very complex. To mimic its complexity and study how crowding could impact ataxin-3 aggregation, we used different crowding agents. It is known that the effect of crowders on amyloid proteins varies with the concentration and type of crowder used [48,58–60]. Recently, it has been shown that huntingtin aggregation was affected by the presence of dextran, Ficoll, and PEG 20,000 increasing the heterogeneity of the huntingtin non-fibrillar aggregate species formed [58]. All the crowding agents tested (dextran, PEG 5,000, and PEG 10,000) decreased the ThT signal in a concentration-dependent manner and abolished ataxin-3 fibril formation, as confirmed by TEM analysis. Macromolecular crowders are generally associated with a solubility-decreasing effect caused by the exclusion of protein molecules from the physical volume occupied by the crowding agents [61]. Nevertheless, when macromolecular crowders establish attractive interactions with the protein, solubility-enhancing effects may prevail over volume exclusion [62]. Since the studied crowding agents thermodynamically and kinetically inhibited ataxin-3 aggregation, we conclude that the enthalpic effects prevailed over the entropic ones.

4.5. The Effect of Ataxin-3-Interacting Proteins in Amyloid Assembly

Ataxin-3 is a deubiquitinase that preferentially cleaves K63-linked chains of four or more ubiquitin moieties [53,63]. Previous studies have shown that the surface areas involved in ubiquitin binding include the aggregation-prone regions in JD and that incubation with monomeric ubiquitin delayed its aggregation [49,54]. Since it had been suggested that native protein interactions may deter the self-assembly of aggregation-prone proteins [64], we tested the effect of HsUBB, a linear tri-ubiquitin chain whose structure is a close mimic of the extended conformation adopted by K63-linked ubiquitin chains [65], on ataxin-3 aggregation. Our results showed that in the tested experimental conditions, HsUBB does not interfere with ataxin-3 amyloid fibril assembly. However, for Atx3 77Q, a decrease in the maximum ThT fluorescence was observed at the highest molar ratio (1:5), suggesting that this may be an avenue of research worth pursuing.

QBP1 is an 11-residue peptide that can inhibit polyQ aggregation both in vitro and in vivo [18–21]. QBP1 is very efficient at inhibiting the formation of mature SDS-resistant fibrils without interfering with the first step of ataxin-3 aggregation. Our studies corroborated this and allowed us to verify that ThT binding curves are a good tool for evaluating modulators of the JD-mediated step of ataxin-3 aggregation, although TEM and filter retardation analysis should be complementarily used to monitor the expanded polyQ-dependent aggregation step.

5. Conclusions

In conclusion, we have developed a standard optimized assay to study the first step of ataxin-3 aggregation. We showed that small amounts of additives, in particular glycerol, can affect the aggregation process and that different control experiments are

required to identify what type of effect is revealed by ThT fluorescence analysis. Further, the relevance of complementary studies to monitor fibril morphology by negative staining electron microscopy to obtain an integrated view of the effect of different molecules on amyloid fibril assembly and maturation has been highlighted. Several independent studies have shown that individuals with the same number of glutamine repeats have different ages of disease onset and varying symptoms [66–71]. These studies emphasize that polyQ expansion is not the only factor underlying the development of SCA3 and that other physiological and external factors play a role in the manifestation of the disease. This optimized aggregation assay can be used to study the effect of various modulators of disease progression on ataxin-3 self-assembly and to discover new ataxin-3 aggregation inhibitors for future therapy development.

Supplementary Materials: The following supporting information can be downloaded at: www.mdpi.com/xxx/s1, Figure S1: Repeatability of ataxin-3 aggregation assay in HEPES buffer; Figure S2: Purification and thermal shift assay of different Ataxin-3 constructs; Figure S3: Distribution of variant rs12895357 in a healthy population; Figure S4: Effect of 300 mM NaCl on ataxin-3 aggregation kinetics; Figure S5: Effect of pH on ataxin-3 aggregation kinetics; Figure S6: Different aggregation buffer components do not affect ataxin-3 aggregation kinetics; Figure S7: Effect of mutating the second ubiquitin binding site of the JD on ataxin-3 aggregation kinetics; Table S1: Nucleotide sequences of primers and synthetic genes used in this work; Table S2: Amino acid sequences of proteins and peptides used in the aggregation assays; Table S3: List of reagents used in this work, with brand name and catalogue references.

Author Contributions: Conceptualization, A.S. and S.M.-R.; methodology, F.F., A.S., B.A., and N.M.; software, F.F., N.M., and A.S.; validation, P.M.M., A.S., and S.M.-R.; formal analysis, F.F., N.M., P.M.M., A.S., and S.M.-R.; investigation, F.F. and A.S.; resources, N.M. and S.M.-R.; data curation, F.F. and A.S.; writing—original draft preparation, F.F.; writing—review and editing, F.F., M.L.-M., B.A., N.M., P.M.M., A.S., and S.M.-R.; supervision, A.S. and S.M.-R.; project administration, S.M.-R.; funding acquisition, A.S. and S.M.-R. All authors have read and agreed to the published version of the manuscript.

Funding: This study was supported by FEDER funds through the COMPETE 2020—Operacional Programme for Competitiveness and Internationalisation (POCI), Portugal 2020; Portuguese funds through FCT in the framework of the projects "PQTools: Molecular tools for Machado-Joseph Disease" (POCI-01-0145-FEDER-031173), "NAPPIT-MJD:Nuclear ataxin-3 protein-protein interactions as therapeutic targets in Machado-Joseph disease" (POCI-01-0145-FEDER-029056), "AggreGATE: Targeting diffusible oligomers of alpha-synuclein and ataxin-3: a drug repurposing opportunity for the treatment of neurodegenerative diseases" (POCI-01-0145-FEDER-031323), and "Institute for Research and Innovation in Health Sciences" (POCI-01-0145-FEDER-007274); the European Union's Horizon 2020 Research and Innovation programme under grant agreement ID 952334 "PhasAGE". The work was also supported by a research grant from National Ataxia Foundation to A.S. F.F. is the recipient of an FCT PhD fellowship (SFRH/BD/133009/2017). The funders had no role in the design, collection, analysis or interpretation of the data, or in the writing of the manuscript.

Institutional Review Board Statement: Not applicable.

Informed Consent Statement: Not applicable.

Data Availability Statement: The datasets generated and/or analyzed during the current study are available from the corresponding authors upon request. All plasmids used in this work are deposited at Addgene.

Acknowledgments: We acknowledge the support of the i3S Scientific Platforms HEMS (member of the national infrastructure PPBI—Portuguese Platform of Bioimaging (PPBI-POCI-01-0145-FEDER-022122)) and Biochemical and Biophysical Technologies for the use of their facilities and equipment. We acknowledge Bastian Groitl and Daisylea de Souza Paiva for support with the switchSENSE technology, and Matthew Merski and Pedro J. B. Pereira for careful revision of the manuscript.

Conflicts of Interest: The authors declare no conflict of interest.

References

1. McGowan, D.; van Roon-Mom, W.; Holloway, H.; Bates, G.; Mangiarini, L.; Cooper, G.; Faull, R.; Snell, R. Amyloid-like inclusions in Huntington's disease. *Neuroscience* **2000**, *100*, 677-680.

2. Paulson, H.L.; Perez, M.; Trottier, Y.; Trojanowski, J.; Subramony, S.; Das, S.; Vig, P.; Mandel, J.-L.; Fischbeck, K.; Pittman, R. Intranuclear inclusions of expanded polyglutamine protein in spinocerebellar ataxia type 3. *Neuron* **1997**, *19*, 333-344.

3. Seidel, K.; Meister, M.; Dugbartey, G.J.; Zijlstra, M.P.; Vinet, J.; Brunt, E.R.; van Leeuwen, F.W.; Rub, U.; Kampinga, H.H.; den Dunnen, W.F. Cellular protein quality control and the evolution of aggregates in spinocerebellar ataxia type 3 (SCA3). *Neuropathol Appl Neurobiol* **2012**, *38*, 548-558, doi:10.1111/j.1365-2990.2011.01220.x.

4. Seidel, K.; Siswanto, S.; Fredrich, M.; Bouzrou, M.; den Dunnen, W.F.A.; Ozerden, I.; Korf, H.W.; Melegh, B.; de Vries, J.J.; Brunt, E.R.; et al. On the distribution of intranuclear and cytoplasmic aggregates in the brainstem of patients with spinocerebellar ataxia type 2 and 3. *Brain Pathol* **2017**, *27*, 345-355, doi:10.1111/bpa.12412.

5. Chen, S.; Ferrone, F.A.; Wetzel, R. Huntington's disease age-of-onset linked to polyglutamine aggregation nucleation. *Proc Natl Acad Sci USA* **2002**, *99*, 11884-11889.

6. Maciel, P.; Gaspar, C.; DeStefano, A.L.; Silveira, I.; Coutinho, P.; Radvany, J.; Dawson, D.M.; Sudarsky, L.; Guimarães, J.; Loureiro, J.E. Correlation between CAG repeat length and clinical features in Machado-Joseph disease. *Am J Hum Genet* **1995**, *57*, 54.

7. França Jr, M.C.; Emmel, V.E.; D'Abreu, A.; Maurer-Morelli, C.V.; Secolin, R.; Bonadia, L.C.; Silva, M.S.; Nucci, A.; Jardim, L.B.; Saraiva-Pereira, M.L. Normal ATXN3 allele but not CHIP polymorphisms modulates age at onset in Machado–Joseph disease. *Front Neurol* **2012**, *3*, 164.

8. Costa, M.D.C. Recent therapeutic prospects for Machado-Joseph disease. *Curr Opin Neurol* **2020**, *33*, 519-526, doi:10.1097/WCO.0000000000000832.

9. Minakawa, E.N.; Nagai, Y. Protein Aggregation Inhibitors as Disease-Modifying Therapies for Polyglutamine Diseases. *Front Neurosci* **2021**, *15*, 621996, doi:10.3389/fnins.2021.621996.

10. Gales, L.; Cortes, L.; Almeida, C.; Melo, C.V.; do Carmo Costa, M.; Maciel, P.; Clarke, D.T.; Damas, A.M.; Macedo-Ribeiro, S. Towards a structural understanding of the fibrillization pathway in Machado-Joseph's disease: trapping early oligomers of non-expanded ataxin-3. *J Mol Biol* **2005**, *353*, 642-654.

11. Scarff, C.A.; Sicorello, A.; Tomé, R.J.; Macedo-Ribeiro, S.; Ashcroft, A.E.; Radford, S.E. A tale of a tail: Structural insights into the conformational properties of the polyglutamine protein ataxin-3. *Int J Mass Spectrom* **2013**, *345*, 63-70.

12. Masino, L.; Nicastro, G.; De Simone, A.; Calder, L.; Molloy, J.; Pastore, A. The Josephin domain determines the morphological and mechanical properties of ataxin-3 fibrils. *Biophys J* **2011**, *100*, 2033-2042.

13. Masino, L.; Nicastro, G.; Menon, R.P.; Dal Piaz, F.; Calder, L.; Pastore, A. Characterization of the structure and the amyloidogenic properties of the Josephin domain of the polyglutamine-containing protein ataxin-3. *J Mol Biol* **2004**, *344*, 1021-1035.

14. Ellisdon, A.M.; Pearce, M.C.; Bottomley, S.P. Mechanisms of ataxin-3 misfolding and fibril formation: kinetic analysis of a disease-associated polyglutamine protein. *J Mol Biol* **2007**, *368*, 595-605, doi:10.1016/j.jmb.2007.02.058.

15. Scarff, C.A.; Almeida, B.; Fraga, J.; Macedo-Ribeiro, S.; Radford, S.E.; Ashcroft, A.E. Examination of ataxin-3 (atx-3) aggregation by structural mass spectrometry techniques: a rationale for expedited aggregation upon polyglutamine (polyQ) expansion. *Mol Cell Proteomics* **2015**, *14*, 1241-1253.

16. Martins, P.M.; Navarro, S.; Silva, A.; Pinto, M.F.; Sárkány, Z.; Figueiredo, F.; Pereira, P.J.B.; Pinheiro, F.; Bednarikova, Z.; Burdukiewicz, M. MIRRAGGE–minimum information required for reproducible AGGregation experiments. *Front Mol Neurosci* **2020**, 222.

17. Silva, A.; Almeida, B.; Fraga, J.S.; Taboada, P.; Martins, P.M.; Macedo-Ribeiro, S. Distribution of Amyloid-Like and Oligomeric Species from Protein Aggregation Kinetics. *Angew Chem Int Ed* **2017**, *56*, 14042-14045.

18. Knight, P.D.; Karamanos, T.K.; Radford, S.E.; Ashcroft, A.E. Identification of a novel site of interaction between ataxin-3 and the amyloid aggregation inhibitor polyglutamine binding peptide 1. *Eur J Mass Spectrom* **2018**, *24*, 129-140, doi:10.1177/1469066717729298.

19. Armen, R.S.; Bernard, B.M.; Day, R.; Alonso, D.O.; Daggett, V. Characterization of a possible amyloidogenic precursor in glutamine-repeat neurodegenerative diseases. *Proc Natl Acad Sci USA* **2005**, *102*, 13433-13438.

20. Nagai, Y.; Tucker, T.; Ren, H.; Kenan, D.J.; Henderson, B.S.; Keene, J.D.; Strittmatter, W.J.; Burke, J.R. Inhibition of polyglutamine protein aggregation and cell death by novel peptides identified by phage display screening. *J Biol Chem* **2000**, *275*, 10437-10442, doi:10.1074/jbc.275.14.10437.

21. Tomita, K.; Popiel, H.A.; Nagai, Y.; Toda, T.; Yoshimitsu, Y.; Ohno, H.; Oishi, S.; Fujii, N. Structure-activity relationship study on polyglutamine binding peptide QBP1. *Bioorg Med Chem* **2009**, *17*, 1259-1263, doi:10.1016/j.bmc.2008.12.018.

22. Ferro, A.; Carvalho, A.L.; Teixeira-Castro, A.; Almeida, C.; Tomé, R.J.; Cortes, L.; Rodrigues, A.-J.; Logarinho, E.; Sequeiros, J.; Macedo-Ribeiro, S. NEDD8: a new ataxin-3 interactor. *Biochim Biophys Acta - Mol Cell Res* **2007**, *1773*, 1619-1627.

23. Grou, C.P.; Pinto, M.P.; Mendes, A.V.; Domingues, P.; Azevedo, J.E. The de novo synthesis of ubiquitin: identification of deubiquitinases acting on ubiquitin precursors. *Sci Rep* **2015**, *5*, 12836, doi:10.1038/srep12836.

24. Rames, M.; Yu, Y.; Ren, G. Optimized negative staining: a high-throughput protocol for examining small and asymmetric protein structure by electron microscopy. *JoVE* **2014**, e51087.

25. Silva, A.; de Almeida, A.V.; Macedo-Ribeiro, S. Polyglutamine expansion diseases: More than simple repeats. *J Struct Biol* **2018**, *201*, 139-154, doi:10.1016/j.jsb.2017.09.006.

26. Chow, M.K.; Paulson, H.L.; Bottomley, S.P. Destabilization of a non-pathological variant of ataxin-3 results in fibrillogenesis via a partially folded intermediate: a model for misfolding in polyglutamine disease. *J Mol Biol* **2004**, *335*, 333-341.

27. Ellisdon, A.M.; Thomas, B.; Bottomley, S.P. The two-stage pathway of ataxin-3 fibrillogenesis involves a polyglutamine-independent step. *J Biol Chem* **2006**, *281*, 16888-16896.

28. Knezevic, J.; Langer, A.; Hampel, P.A.; Kaiser, W.; Strasser, R.; Rant, U. Quantitation of affinity, avidity, and binding kinetics of protein analytes with a dynamically switchable biosurface. *J Am Chem Soc* **2012**, *134*, 15225-15228.

29. Müller-Landau, H.; Varela, P.F. Standard operation procedure for switchSENSE DRX systems. *Eur Biophys J* **2021**, *50*, 389-400.

30. Santambrogio, C.; Frana, A.M.; Natalello, A.; Papaleo, E.; Regonesi, M.E.; Doglia, S.M.; Tortora, P.; Invernizzi, G.; Grandori, R. The role of the central flexible region on the aggregation and conformational properties of human ataxin-3. *FEBS J* **2012**, *279*, 451-463.

31. Lupton, C.J.; Steer, D.L.; Wintrode, P.L.; Bottomley, S.P.; Hughes, V.A.; Ellisdon, A.M. Enhanced molecular mobility of ordinarily structured regions drives polyglutamine disease. *J Bioll Chem* **2015**, *290*, 24190-24200.

32. Gaspar, C.; Lopes-Cendes, I.; Hayes, S.; Goto, J.; Arvidsson, K.; Dias, A.; Silveira, I.; Maciel, P.; Coutinho, P.; Lima, M. Ancestral origins of the Machado-Joseph disease mutation: a worldwide haplotype study. *Am J Hum Genet* **2001**, *68*, 523-528.

33. Li, T.; Martins, S.; Peng, Y.; Wang, P.; Hou, X.; Chen, Z.; Wang, C.; Tang, Z.; Qiu, R.; Chen, C.; et al. Is the High Frequency of Machado-Joseph Disease in China Due to New Mutational Origins? *Front Genet* **2018**, *9*, 740, doi:10.3389/fgene.2018.00740.

34. Sharony, R.; Martins, S.; Costa, I.P.D.; Zaltzman, R.; Amorim, A.; Sequeiros, J.; Gordon, C.R. Yemenite-Jewish families with Machado-Joseph disease (MJD/SCA3) share a recent common ancestor. *Eur J Hum Genet* **2019**, *27*, 1731-1737, doi:10.1038/s41431-019-0449-7.

35. Genomes Project, C.; Auton, A.; Brooks, L.D.; Durbin, R.M.; Garrison, E.P.; Kang, H.M.; Korbel, J.O.; Marchini, J.L.; McCarthy, S.; McVean, G.A.; et al. A global reference for human genetic variation. *Nature* **2015**, *526*, 68-74, doi:10.1038/nature15393.

36. Goto, J.; Watanabe, M.; Ichikawa, Y.; Yee, S.-B.; Ihara, N.; Endo, K.; Igarashi, S.; Takiyama, Y.; Gaspar, C.; Maciel, P. Machado–Joseph disease gene products carrying different carboxyl termini. *Neurosci Res* **1997**, *28*, 373-377.

37. Flynn, J.D.; McGlinchey, R.P.; Walker, R.L., 3rd; Lee, J.C. Structural features of alpha-synuclein amyloid fibrils revealed by Raman spectroscopy. *J Biol Chem* **2018**, *293*, 767-776, doi:10.1074/jbc.M117.812388.

38. Moller, J.; Schroer, M.A.; Erlkamp, M.; Grobelny, S.; Paulus, M.; Tiemeyer, S.; Wirkert, F.J.; Tolan, M.; Winter, R. The effect of ionic strength, temperature, and pressure on the interaction potential of dense protein solutions: from nonlinear pressure response to protein crystallization. *Biophys J* **2012**, *102*, 2641-2648, doi:10.1016/j.bpj.2012.04.043.

39. Munishkina, L.A.; Henriques, J.; Uversky, V.N.; Fink, A.L. Role of protein− water interactions and electrostatics in α-synuclein fibril formation. *Biochemistry* **2004**, *43*, 3289-3300.

40. Ziaunys, M.; Sakalauskas, A.; Mikalauskaite, K.; Smirnovas, V. Polymorphism of Alpha-Synuclein Amyloid Fibrils Depends on Ionic Strength and Protein Concentration. *Int J Mol Sci* **2021**, *22*, doi:10.3390/ijms222212382.

41. Campos-Ramirez, A.; Marquez, M.; Quintanar, L.; Rojas-Ochoa, L.F. Effect of ionic strength on the aggregation kinetics of the amidated amyloid beta peptide Abeta (1-40) in aqueous solutions. *Biophys Chem* **2017**, *228*, 98-107, doi:10.1016/j.bpc.2017.05.004.

42. Abelein, A.; Jarvet, J.; Barth, A.; Graslund, A.; Danielsson, J. Ionic Strength Modulation of the Free Energy Landscape of Abeta40 Peptide Fibril Formation. *J Am Chem Soc* **2016**, *138*, 6893-6902, doi:10.1021/jacs.6b04511.

43. Marek, P.J.; Patsalo, V.; Green, D.F.; Raleigh, D.P. Ionic strength effects on amyloid formation by amylin are a complicated interplay among Debye screening, ion selectivity, and Hofmeister effects. *Biochemistry* **2012**, *51*, 8478-8490, doi:10.1021/bi300574r.

44. Gekko, K.; Timasheff, S.N. Mechanism of protein stabilization by glycerol: preferential hydration in glycerol-water mixtures. *Biochemistry* **1981**, *20*, 4667-4676.

45. Vagenende, V.; Yap, M.G.; Trout, B.L. Mechanisms of protein stabilization and prevention of protein aggregation by glycerol. *Biochemistry* **2009**, *48*, 11084-11096, doi:10.1021/bi900649t.

46. Saunders, H.M.; Hughes, V.A.; Cappai, R.; Bottomley, S.P. Conformational behavior and aggregation of ataxin-3 in SDS. *PLoS One* **2013**, *8*, e69416, doi:10.1371/journal.pone.0069416.

47. Kumar, S.; Singh, A.K.; Krishnamoorthy, G.; Swaminathan, R. Thioflavin T displays enhanced fluorescence selectively inside anionic micelles and mammalian cells. *J Fluoresc* **2008**, *18*, 1199-1205.

48. Seeliger, J.; Werkmuller, A.; Winter, R. Macromolecular crowding as a suppressor of human IAPP fibril formation and cytotoxicity. *PLoS One* **2013**, *8*, e69652, doi:10.1371/journal.pone.0069652.

49. Nicastro, G.; Masino, L.; Esposito, V.; Menon, R.P.; De Simone, A.; Fraternali, F.; Pastore, A. Josephin domain of ataxin-3 contains two distinct ubiquitin-binding sites. *Biopolymers* **2009**, *91*, 1203-1214.

50. Nicastro, G.; Menon, R.P.; Masino, L.; Knowles, P.P.; McDonald, N.Q.; Pastore, A. The solution structure of the Josephin domain of ataxin-3: structural determinants for molecular recognition. *Proc Natl Acad Sci USA* **2005**, *102*, 10493-10498.

51. Chai, Y.; Berke, S.S.; Cohen, R.E.; Paulson, H.L. Poly-ubiquitin binding by the polyglutamine disease protein ataxin-3 links its normal function to protein surveillance pathways. *J Biol Chem* **2004**, *279*, 3605-3611.

52. Nicastro, G.; Todi, S.V.; Karaca, E.; Bonvin, A.M.; Paulson, H.L.; Pastore, A. Understanding the role of the Josephin domain in the PolyUb binding and cleavage properties of ataxin-3. *PloS One* **2010**, *5*, e12430.

53. Burnett, B.; Li, F.; Pittman, R.N. The polyglutamine neurodegenerative protein ataxin-3 binds polyubiquitylated proteins and has ubiquitin protease activity. *Hum Mol Genet* **2003**, *12*, 3195-3205, doi:10.1093/hmg/ddg344.

54. Masino, L.; Nicastro, G.; Calder, L.; Vendruscolo, M.; Pastore, A. Functional interactions as a survival strategy against abnormal aggregation. *FASEB J* **2011**, *25*, 45-54.

55. Baker, M. 1,500 scientists lift the lid on reproducibility. *Nature* **2016**, *533*.

56. Garvey, M.; Tepper, K.; Haupt, C.; Knüpfer, U.; Klement, K.; Meinhardt, J.; Horn, U.; Balbach, J.; Fändrich, M. Phosphate and HEPES buffers potently affect the fibrillation and oligomerization mechanism of Alzheimer's Aβ peptide. *Biochem Biophys Res Commun* **2011**, *409*, 385-388.

57. Gade Malmos, K.; Blancas-Mejia, L.M.; Weber, B.; Buchner, J.; Ramirez-Alvarado, M.; Naiki, H.; Otzen, D. ThT 101: a primer on the use of thioflavin T to investigate amyloid formation. *Amyloid* **2017**, *24*, 1-16.

58. Groover, S.E.; Adegbuyiro, A.; Fan, C.K.; Hodges, B.L.; Beasley, M.; Taylor, K.; Stonebraker, A.R.; Siriwardhana, C.; Legleiter, J. Macromolecular crowding in solution alters huntingtin interaction and aggregation at interfaces. *Colloids Surf B Biointerfaces* **2021**, *206*, 111969, doi:10.1016/j.colsurfb.2021.111969.

59. Uversky, V.N.; Cooper, E.M.; Bower, K.S.; Li, J.; Fink, A.L. Accelerated α-synuclein fibrillation in crowded milieu. *FEBS Lett* **2002**, *515*, 99-103.

60. Fang, X.; Yousaf, M.; Huang, Q.; Yang, Y.; Wang, C. Dual effect of PEG-PE micelle over the oligomerization and fibrillation of human islet amyloid polypeptide. *Sci Rep* **2018**, *8*, 4463, doi:10.1038/s41598-018-22820-w.

61. Minton, A.P. The effect of volume occupancy upon the thermodynamic activity of proteins: some biochemical consequences. *Mol Cell Biochem* **1983**, *55*, 119-140.

62. Ferreira, C.; Pinto, M.F.; Macedo-Ribeiro, S.; Pereira, P.J.B.; Rocha, F.A.; Martins, P.M. Protein crystals as a key for deciphering macromolecular crowding effects on biological reactions. *Phys Chem Chem Phys* **2020**, *22*, 16143-16149.

63. Winborn, B.J.; Travis, S.M.; Todi, S.V.; Scaglione, K.M.; Xu, P.; Williams, A.J.; Cohen, R.E.; Peng, J.; Paulson, H.L. The deubiquitinating enzyme ataxin-3, a polyglutamine disease protein, edits Lys63 linkages in mixed linkage ubiquitin chains. *J Biol Chem* **2008**, *283*, 26436-26443, doi:10.1074/jbc.M803692200.

64. Pastore, A.; Temussi, P.A. The two faces of Janus: functional interactions and protein aggregation. *Curr Opin Struct Biol* **2012**, *22*, 30-37.

65. Weeks, S.D.; Grasty, K.C.; Hernandez-Cuebas, L.; Loll, P.J. Crystal structures of Lys-63-linked tri-and di-ubiquitin reveal a highly extended chain architecture. *Proteins Struct Funct Bioinf* **2009**, *77*, 753-759.

66. Hsieh, M.; Tsai, H.-F.; Lu, T.-M.; Yang, C.-Y.; Wu, H.-M.; Li, S.-Y. Studies of the CAG repeat in the Machado-Joseph disease gene in Taiwan. *Human Genet* **1997**, *100*, 155-162.

67. Kawaguchi, Y.; Okamoto, T.; Taniwaki, M.; Aizawa, M.; Inoue, M.; Katayama, S.; Kawakami, H.; Nakamura, S.; Nishimura, M.; Akiguchi, I. CAG expansions in a novel gene for Machado-Joseph disease at chromosome 14q32. 1. *Nature Genet* **1994**, *8*, 221-228.

68. Gu, W.; Ma, H.; Wang, K.; Jin, M.; Zhou, Y.; Liu, X.; Wang, G.; Shen, Y. The shortest expanded allele of the MJD1 gene in a Chinese MJD kindred with autonomic dysfunction. *Eur Neurol* **2004**, *52*, 107-111, doi:10.1159/000080221.

69. Padiath, Q.S.; Srivastava, A.K.; Roy, S.; Jain, S.; Brahmachari, S.K. Identification of a novel 45 repeat unstable allele associated with a disease phenotype at the MJD1/SCA3 locus. *Am J Med Genet B Neuropsychiatr Genet* **2005**, *133B*, 124-126, doi:10.1002/ajmg.b.30088.

70. Takiyama, Y.; Sakoe, K.; Nakano, I.; Nishizawa, M. Machado-Joseph disease: cerebellar ataxia and autonomic dysfunction in a patient with the shortest known expanded allele (56 CAG repeat units) of the MJD1 gene. *Neurology* **1997**, *49*, 604-606, doi:10.1212/wnl.49.2.604.

71. Van Alfen, N.; Sinke, R.J.; Zwarts, M.J.; Gabreëls-Festen, A.; Praamstra, P.; Kremer, B.P.; Horstink, M.W. Intermediate CAG repeat lengths (53, 54) for MJD/SCA3 are associated with an abnormal phenotype. *Annals Neurol* **2001**, *49*, 805-808.

Supporting Information

A Robust Assay to Monitor Ataxin-3 Amyloid Fibril Assembly

Francisco Figueiredo, Mónica Lopes-Marques, Bruno Almeida, Nena Matscheko, Pedro Martins, Alexandra Silva, Sandra Macedo-Ribeiro

S1. Primers and Plasmid Sequences

Supplementary Table S1. Nucleotide sequences of primers and synthetic genes used in this work.

Name	Sequence	Purpose
I77K_For	5´-gatgacagtggttttttctctaaacaggttataagcaatgccttg-3´	Mutagenesis of Atx3 13Q
I77K_Rev	5´- caaggcattgcttataacctgtttagagaaaaaaccact gtcatc-3´	Mutagenesis of Atx3 13Q
Q78K_For	5'-gatgacagtggttttttctctattaaggttataagcaatgccttg-3´	Mutagenesis of Atx3 13Q
Q78K_Rev	5´-caaggcattgcttataaccttaatagagaaaaaaccactgtcatc-3´	Mutagenesis of Atx3 13Q
W87K_For	5'-gcaatgccttgaaagttaagggtttagaactaatcctgttcaac-3'	Mutagenesis of Atx3 13Q
W87K_Rev	5'-gttgaacaggattagttctaaacccttaactttcaaggcattgc-3'	Mutagenesis of Atx3 13Q
R388G_For	5'-tggcctgacagatctccctgttgttgttgctgc-3'	Mutagenesis of Atx3 77Q
R388G_Rev	5'-gcagcaacaacaacagggagatctgtcaggcca-3'	Mutagenesis of Atx3 77Q
77Q_opt	5'- atgcatcgaccaaaactgattggcgaagaactggctcaactgaaagaacagcgtgtgcataagaccgacctggaacgtgtcctggaagcaaatgacggcagcggcatgctggatga agacgaagaagatctgcagcgtgccctggcactgtctcgtcaggaaattgatatggaagacgaagaagcagatctgcgtcgcgctattcagctgtcaatgcagggcagctctcgtaac atctcgcaggacatgacccagacgagcggtaccaatctgacgtctgaagaactgcgcaaacgtcgcgaagcatattttgaaaaacagcaacagaagcaacaacagcagcaacaac aacaacaacagcagcagcagcagcaacaacaacagcaacaacaacagcaacagcagcaacagcaacagcagcaacaacagcaacagcaacaacagcaacagcaac aacagcaacaacagcaacaacagcaacaacagcaacaacagcaacagcagcaacagcagcagcaacagcagcaacaacaacagagagatctgtcaggccagag ttcccatccgtgtgaacgtccggccacctcaagcggtgcactgggtagtgatctgggtgacgccatgtccgaagaagacatgctgcaggcagcagtgacgatgtccctggaaaccgtg cgtaacgacctgaaaaccgaaggcaaaaaataagacccagctttcttgtaca-3'	Synthetic sequence of codon-optimized construct for production of Atx3(77Q)

13Q_opt	5’- atgcatcgaccaaaacttattggagaagaattagcacaactaaaagagcaaagagtccataaaacagacctggaacgagtgttagaagcaaatgatggctcaggaatgttagacga agatgaggaggatttgcagagggctctggcactaagtcgccaagaaattgacatggaagatgaggaagcagatctccgcagggctattcagctaagtatgcaaggtagttccagaaa catatctcaagatatgacacagacatcaggtacaaatcttacttcagaagagcttcggaagagacgagaagcctactttgaaaaacagcagcaaaagcagcaacagcagcagcagc agcagcagcaggggacctatcaggacagagttcacatccatgtgaaaggccagccaccagttcaggagcacttgggagtgatctaggtgatgctatgagtgaagaagacatgcttc aggcagctgtgaccatgtctttagaaactgtcagaaatgatttgaaaacagaaggaaaaaaataagacccagctttcttgtaca-3’	Synthetic sequence of codon-optimized construct for production of Atx3(13Q)

Supplementary Table S2. Amino acid sequences of proteins and peptides used in the aggregation assays. Josephin Domain (Green); Aggregation-prone Region (Red); polyQ (Orange); Atx3 77Q mutants (Blue, Bold); Atx3 13Q ubiquitin binding site 2 mutants (Purple, Bold).

Name	**Sequence**	**Extinction Coefficients (M^{-1}.cm^{-1})**
Atx3 JD	MSYYHHHHHHLESTSLYKKAGWMESIFHEKQEGSLCAQHCLNNLLQGEYFSPVELSSIAHQLDEEERMRMAEGGVTSEDYRTFLQQPSGNMDDSGFFSIQVISNALKVWGLELILFNSPEYQRLRIDPINERSFICNYKEHWFTVRKLGKQWFNLNSLLTGPELISDTYLALFLAQLQQEGYSIFVVKGDLPDCEADQLLQMIR	35660
Atx3 D1	MSYYHHHHHHLENLYFQGMESIFHEKQEGSLCAQHCLNNLLQGEYFSPVELSSIAHQLDEEERMRMAEGGVTSEDYRTFLQQPSGNMDDSGFFSIQVISNALKVWGLELILFNSPEYQRLRIDPINERSFICNYKEHWFTVRKLGKQWFNLNSLLTGPELISDTYLALFLAQLQQEGYSIFVVKGDLPDCEADQLLQMIRVQQMHRPKLIGEELAQLKEQRVHKTDLERVLEANDGSGMLDEDEEDLQRALALSRQEIDMEDEEADLRRAIQLSMQGSSR	30160
Atx3 13Q	MSYYHHHHHHLENLYFQGMESIFHEKQEGSLCAQHCLNNLLQGEYFSPVELSSIAHQLDEEERMRMAEGGVTSEDYRTFLQQPSGNMDDSGFFSIQVISNALKVWGLELILFNSPEYQRLRIDPINERSFICNYKEHWFTVRKLGKQWFNLNSLLTGPELISDTYLALFLAQLQQEGYSIFVVKGDLPDCEADQLLQMIRVQQMHRPKLIGEELAQLKEQRVHKTDLERVLEANDGSGMLDEDEEDLQRALALSRQEIDMEDEEADLRRAIQLSMQGSSRNISQDMTQTSGTNLTSEELRKRREAYFEKQQQKQQQQQQQQQQGDLSGQSSHPCERPATSSGALGSDLGDAMSEEDMLQAAVTMSLETVRNDLKTEGKK	31650
Atx3 77Q	MSYYHHHHHHLENLYFQGMESIFHEKQEGSLCAQHCLNNLLQGEYFSPVELSSIAHQLDEEERMRMAEGGVTSEDYRTFLQQPSGNMDDSGFFSIQVISNALKVWGLELILFNSPEYQRLRIDPINERSFICNYKEHWFTVRKLGKQWFNLNSLLTGPELISDTYLALFLAQLQQEGYSIFVVKGDLPDCEADQLLQMIRVQQMHRPKLIGEELAQLKEQRVHKTDLERVLEANDGSGMLDEDEEDLQRALALSRQEIDMEDEEADLRRAIQLSMQGSSRNISQDMTQTSGTNLTSEELRKRREAYFEKQQQKQQQQQQQQQQQQQQQQQQQQQQQQQQQQQQQQQQQQQQQQQQQQQQQQQQQQQQQQQQQQQQQQQQQQQQQQQQQRDLSGQSSHPCERPATSSGALGSDLGDAMSEEDMLQAAVTMSLETVRNDLKTEGKK	31650
Atx3 77Q R388G	MSYYHHHHHHLENLYFQGMESIFHEKQEGSLCAQHCLNNLLQGEYFSPVELSSIAHQLDEEERMRMAEGGVTSEDYRTFLQQPSGNMDDSGFFSIQVISNALKVWGLELILFNSPEYQRLRIDPINERSFICNYKEHWFTVRKLGKQWFNLNSLLTGPELISDTYLALFLAQLQQEGYSIFVVKGDLPDCEADQLLQMIRVQQMHRPKLIGEELAQLKEQRVHKTDLERVLEANDGSGMLDEDEEDLQRALALSRQEIDMEDEEADLRRAIQLSMQGSSRNISQDMTQTSGTNLTSEELRKRREAYFEKQQQKQQQQQQQQQQQQQQQQQQQQQQQQQQQQQQQQQQQQQQQQQQQQQQQQQQQQQQQQQQQQQQQQQQQQQQQQQQQ**G**DLSGQSSHPCERPATSSGALGSDLGDAMSEEDMLQAAVTMSLETVRNDLKTEGKK	31650
Atx3 13Q I77K Q78K W87K	MSYYHHHHHHLENLYFQGMESIFHEKQEGSLCAQHCLNNLLQGEYFSPVELSSIAHQLDEEERMRMAEGGVTSEDYRTFLQQPSGNMDDSGFFS**KK**VISNALKV**K**GLELILFNSPEYQRLRIDPINERSFICNYKEHWFTVRKLGKQWFNLNSLLTGPELISDTYLALFLAQLQQEGYSIFVVKGDLPDCEADQLLQMIRVQQMHRPKLIGEELAQLKEQRVHKTDLERVLEANDGSGMLDEDEEDLQRALALSRQEIDMEDEEADLRRAIQLSMQGSSRNISQDMTQTSGTNLTSEELRKRREAYFEKQQQKQQQQQQQQQQGDLSGQSSHPCERPATSSGALGSDLGDAMSEEDMLQAAVTMSLETVRNDLKTEGKK	26150

HsUBB3	MQIFVKTLTGKTITLEVEPSDTIENVKAKIQDKEGIPPDQQRLIFAGKQLEDGRTLSDYNIQK ESTLHLVLRLRGGMQIFVKTLTGKTITLEVEPSDTIENVKAKIQDKEGIPPDQQRLIFAGKQL EDGRTLSDYNIQKESTLHLVLRLRGGMQIFVKTLTGKTITLEVEPSDTIENVKAKIQDKEGIP PDQQRLIFAGKQLEDGRTLSDYNIQKESTLHLVLRLRGGC	4470
QBP1	SNWKWWPGIFD	16500

2

S2. Step by Step Protocols

S2.1 Ataxin-3 Expression

The full list of reagents used in this work is detailed in section 4 (S4) of the Supporting Information.

1. First, the plasmid carrying the selected ataxin-3 variant was transformed in *E. coli* BL21(DE3)-SI (Life Technologies, Carlsbad, CA, USA) by adding 1 µL of selected plasmid (40-100 ng μL^{-1}) to 50 µL of competent cells in an microtube, and incubating for 30 min on ice.

2. BL21(DE3)-SI cells were heat-shocked for 45 seconds at 42 °C, followed by a 10 min incubation on ice. Next, 500 µL of LB medium without NaCl (LB_{ON}) (Formedium, UK) were added and the cells were incubated for 1 h at 37 °C, 180 rpm.

3. BL21(DE3)-SI cells were pelleted by centrifugation for 1 min at 11200 g, and the supernatant was removed. Cells were gently resuspended in 100 µL of fresh LB_{ON}.

4. The suspension was plated on a LB_{ON} plate supplemented with 100 µg mL^{-1} ampicillin and the plate incubated overnight at 37 °C.

5. Starter culture was prepared in 500 mL baffled Erlenmeyer containing 150 mL of LB_{ON} supplemented with 100 µg mL^{-1} ampicillin. Next 4/5 isolated colonies selected from the stored plate were used to inoculate the culture. The starter culture was left overnight at 37 °C, 180 rpm.

6. Culture was expanded by inoculating 20 mL of starter culture into 2 L baffled Erlenmeyer containing 500 mL of LB_{ON} supplemented with 100 µg mL^{-1} ampicillin and 0.4 % (w/v) glucose. The culture was maintained at 37 °C, 180 rpm, and OD_{600} was checked regularly.

7. When culture OD_{600nm} reached 0.8, the Erlenmeyers were cooled to 30 °C for 30 min with no shaking (1 mL sample was retrieved for SDS-PAGE analysis to monitor ataxin-3 expression before induction).

8. Protein expression was induced by adding 50 mL of induction medium (2x LB_{ON} with 3 M NaCl) to each Erlenmeyer to achieve the final concentration of 300 mM NaCl.

Protein expression was carried out at 30 °C for 3 h (180 rpm) (1 mL sample was retrieved for SDS-PAGE analysis to monitor ataxin-3 expression after induction).

9. Cells were harvested by centrifugation for 20 min at 3993 g at 4 °C. The supernatant was discarded and the cell pellet was carefully resuspended in 30 mL (30 mL per 1.5 L of cell culture) of ice-cold Buffer A (20 mM sodium phosphate pH 7.5, 500 mM NaCl, 2.5% (v/v) glycerol and 20 mM imidazole) supplemented with 100 µg L^{-1} of lysozyme. Cell suspensions were stored at -20 °C in 50 mL falcons until further use.

S2.2 Ataxin-3 Purification

1. The cell suspension was slowly thawed by placing the 50 mL falcon under tap water continuously running for 15 min. The cellular suspension was transferred to a 250 mL Erlenmeyer and the cells were disrupted by slowly stirring for 1 h on ice in the presence of lysozyme (0.02 mg mL^{-1}), DNAse (0.02 mg mL^{-1}), RNAse (0.02 mg mL^{-1}), $MgCl_2$ (1 mM) and PMSF (1 mM). After cell disruption, 10 µL of the sample was collected for SDS-PAGE analysis.

2. The cell suspension was centrifuged for 45 min at 34864 g (4 °C). The supernatant was filtered (0.45 µm protein low binding filter - Whatman Puradisc 25, ref: 6747-2504) and loaded into a Ni^{2+}-charged IMAC HiTrap column (GE Healthcare Life Sciences, ref: 17-0920-05) pre-equilibrated in 20 column volumes (CV) of Buffer A.

3. Bound proteins are eluted by applying 10 CV steps of increasing imidazole concentration (50, 250 and 500 mM imidazole in Buffer A) (Supplementary Figure S1A, B, C, D). Ataxin-3-containing fractions eluted with 250 mM imidazole were supplemented with EDTA to a final concentration of 1 mM. The collected fractions (5-10 mL) were carefully homogenised, filtered (0.22 µm protein low binding filter, Millipore, ref: SLGV033RB) and kept on ice.

4. Monomeric ataxin-3 was obtained following purification by size exclusion chromatography (SEC) using the HiPrep 20/60 Sephacryl S-300 HR column (GE Healthcare Life Sciences, ref: 17-1196-01) equilibrated in SEC buffer (20 mM sodium phosphate pH 7.5, 150 mM NaCl, 5 % (v/v) glycerol, 2 mM EDTA, 1 mM DTT) (Supplementary Figure S1A, B, C, D). The fractions (2.5 mL) corresponding to the central part of the peak of monomeric ataxin-3 were collected (Supplementary Figure S1A, B,

C, D) and kept on ice prior to concentration in a centrifugal ultrafiltration device (Amicon Ultra-15, 10 kDa, Millipore) at 4 °C. Final protein concentrations range between 10 and 20 mg mL^{-1}. The concentration was determined by measuring the absorbance at 280 nm in a Nanodrop 1000 spectrophotometer (Thermo Fisher Scientific) and using the extinction coefficients detailed in Table S1.

5. The concentrated protein was transferred into a protein-low binding microtube, centrifuged for 10 min at 16363 g, 4 °C, to remove putative aggregates, and the supernatant was transferred into a new protein-low binding microtube and the final concentration was determined by measuring the absorbance at 280 nm.

6. Purified ataxin-3 proteins were stored at -80°C in protein low-binding microtubes (Eppendorf, ref: 022431081) in 50 µL or 100 µL aliquots, following flash freezing in liquid nitrogen.

S2.3 Ataxin-3 Aggregation Assay / Thioflavin-T Aggregation Assay

1. Purified ataxin-3 aliquots were thawed on ice, centrifuged for 10 min at 16363 g, 4 °C, filtered in a low-binding protein filter (Millipore, ref: UFC30GV00) and injected on a Superose 12 10/300 GL (GE Healthcare Life Sciences, ref: 17-5173-01) column equilibrated in aggregation buffer (20 mM HEPES pH 7.5, 150 mM NaCl, 1 mM DTT or 20 mM HEPES pH 7.5, 150 mM NaCl, 1 mM DTT) (Figure 1D). Fractions (0.4 mL) corresponding to the central part of the lower molecular weight peak (Figure 1D) were collected, and the protein concentration was determined as described in step 4 of S2.2. The final concentration of protein was adjusted to 15 µM in aggregation buffer.

2. Pre-dilute the stock solution of Thioflavin-T (ThT) which is at 3.5 M in water to 500 µM in aggregation buffer.

3. Prepare a master mix of 300 µL that is enough to perform 5 replicates of 50 µL each. In this master mix, the final concentration of ataxin-3 and ThT are 5 µM and 30 µM respectively. If any compound or protein is being tested they should be added into this master mix in this step, regardless of the buffer/solvent that they are in. Pre-dilution was made in the aggregation buffer. Mix gently to avoid the formation of air bubbles.

4. Pipette 50 µL of master mix to the microplate. The 96-well microplate (Thermowell 96-Well Polycarbonate PCR Microplates, Costar, Tewkesbury, MA, USA) or 384-well microplate (low flange, black, flat bottom, polystyrene microplate, Corning,

Kennebunk, ME). Air bubbles were removed by plate centrifugation for 2 min at 306 g at RT.

5. To avoid evaporation during the aggregation assay, 20 µL of paraffin oil is added to each reaction well and then put the plate in the plate reader previously heated to 37 °C.

6. ThT fluorescence was measured at 37 °C on a HIDEX CHAMELEON V plate reader (Turku, Finland) or a FluoDia T70 microplate fluorimeter (Photon Technology International, Edison, NJ, USA) at 480 nm (440 nm excitation) every 30 min over a period of 60 h. Plates were shaken every 30 min for 3 seconds before each set of readings.

7. After 60 h, stop the assay and analyse data in Prism 9 software (GraphPad Software, San Diego, CA, USA). Data was analysed in Prism 9 software.

S2.4 Transmission Electron Microscopy Assay

This protocol was adapted from Rames *et al.*, 2014 [1].

S2.4.1 Preparation of Fresh Negative Staining Solution at 1% (w/v)

1. 1 mg Uranyl Acetate (UA) powder was added to a glass bottle containing 100 mL deionized water covered with aluminium foil to protect from light.

2. The solution was stirred overnight (ON) at RT.

3. The solution was gently filtered through a 0.2 µm filter mounted on a 20 mL syringe. Both syringe and filter were covered with aluminium foil to prevent light exposure. The filtered solution was collected in 2 mL aliquots (or less) using microtubes wrapped with aluminium foil.

4. The aliquots were frozen in liquid nitrogen after filtration and stored at -80°C until further usage.

S2.4.2 Preparation of Negative Staining Workstation and Incubation Workstation

5. A microtube of 1 % UA solution was thawed in a water at RT with the aluminium foil wrapped around the microtube to prevent exposure to light.

6. The solution was filtered using a 1 mL syringe wrapped in aluminium foil and mounted with a 0.2 µm filter. The filtered solution was collected into a new aluminium foil wrapped microtube, and placed inside a cap covered ice box waiting for usage.

7. Solution plates were made by finger pushing a long enough piece of Parafilm sheet onto the surface of an empty 200 uL tip cover plate. This generated rows of circular holes with a diameter of approximately 5 mm. 6 holes were made in each row and the 200 uL tip cover plate was placed on a surface of flattened ice inside an ice container lid, as a staining workstation.

8. For each grid, pipette a row consisting of 3 consecutive droplets of 35 µL deionized water followed by 3 consecutive droplets of 35 µL filtered UA solution. The staining workstation was covered with a lid to prevent exposure to light before staining proteins.

9. An Electron Microscopy (EM) grid incubation station was prepared by filling an empty box with ice next to a hanger that allowed the tip of the tweezer to be partially inserted into the incubation station. The tip of the tweezers will be nearby the ice surface and its tip will be covered by the lid of the incubation station.

S2.4.3 – Negative-Staining Operation

10. The thin carbon film coated EM grids were glow-discharged for 10 sec.

11. Each grid was picked up with tweezers and the tweezers were hooked into the hanger by keeping the grid at an approximately 45° tilt and close to the ice surface inside the incubation station.

12. Depending on the sample, the protein sample was diluted in water or not. 5 µl of diluted sample were deposited immediately after the dilution on the carbon side of EM grid.

13. The sample on the EM grids was incubated for 1 min inside the incubation station.

14. The excess solution was removed by quickly touching the grid edge with filter paper.

15. Afterwards, the grid was quickly placed in the first drop of pure water surface atop the Parafilm sheet and the excess water was promptly removed with filter paper.

16. Step 16 was repeated two more times by washing the EM grid on the remaining two water droplets on the Parafilm.

17. The EM grid was floated immediately on the surface of the first drop of UA solution, right after the excess water on the EM grid was removed, and then incubated for 10 sec.

18. The tweezers were cleaned by penetrating the tips 2-3 times on filter paper.

19. The excess solution on the grid was removed by contacting the grid edge with the filter paper, and then the grid was floated on the second drop of UA.

20. Steps 18 and 19 were repeated into the third droplet of UA solution and the staining station was covered for 1 min.

21. The excess solution was removed by touching the filter paper to the entire grid backside (opposite the carbon side).

22. The grid was placed onto a sheet of filter paper inside a petri dish, and the dish was partially covered with a cap to dry for at least 30 min at RT. The grids were stored in an TEM grid box for future TEM examination.

S2.5 Thermal Shift Assay Protocol

Ataxin-3 variants melting temperature was determined using the hydrophobic fluorescent dye SYPRO Orange. For each condition, 12.5 µL of SYPRO Orange 5000x (Invitrogen) diluted to 10x in ataxin-3 SEC buffer were mixed with 12.5 µL of ataxin-3 at (0.8 mg mL-1) and loaded in a white 96-well PCR plate (Bio-Rad). For all the conditions three replicates were prepared. The thermal shift assay was performed in an iCycler iQ5 Multicolor Real Time PCR detection system (Bio-Rad) running the following protocol: heating from 25 °C to 85 °C with a 30s hold time every 0.5 °C, followed by a fluorescence reading using Cy3 dye filter (excitation/emission, 545/585). Melting curves were analysed using the CFX Manager software (Bio-Rad) to calculate melting temperature (Tm) from the maximum value of the first derivative curve of the melting curve.

S3. Supporting Figures

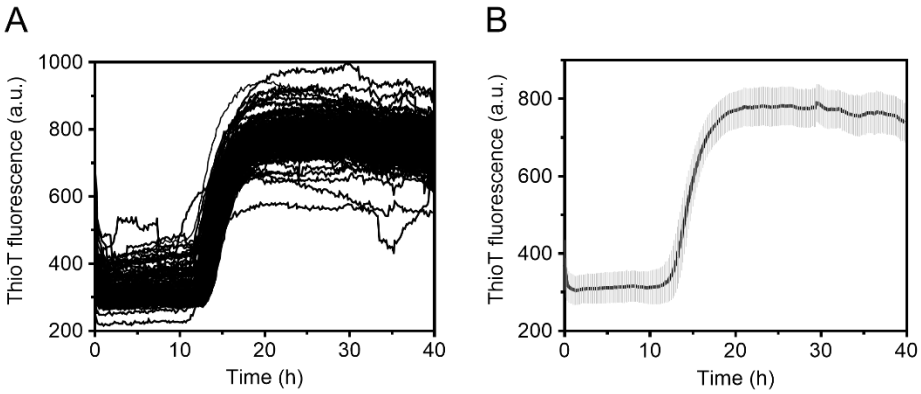

Supplementary Figure S1. Repeatability of the Atx3 13Q aggregation assay in HEPES buffer. (A) 192 replicas of Atx3 13Q (3 µM) ThT assay using the HIDEX CHAMELEON V plate reader. **(B)** Mean and standard deviation of the 192 replicates presented in (A).

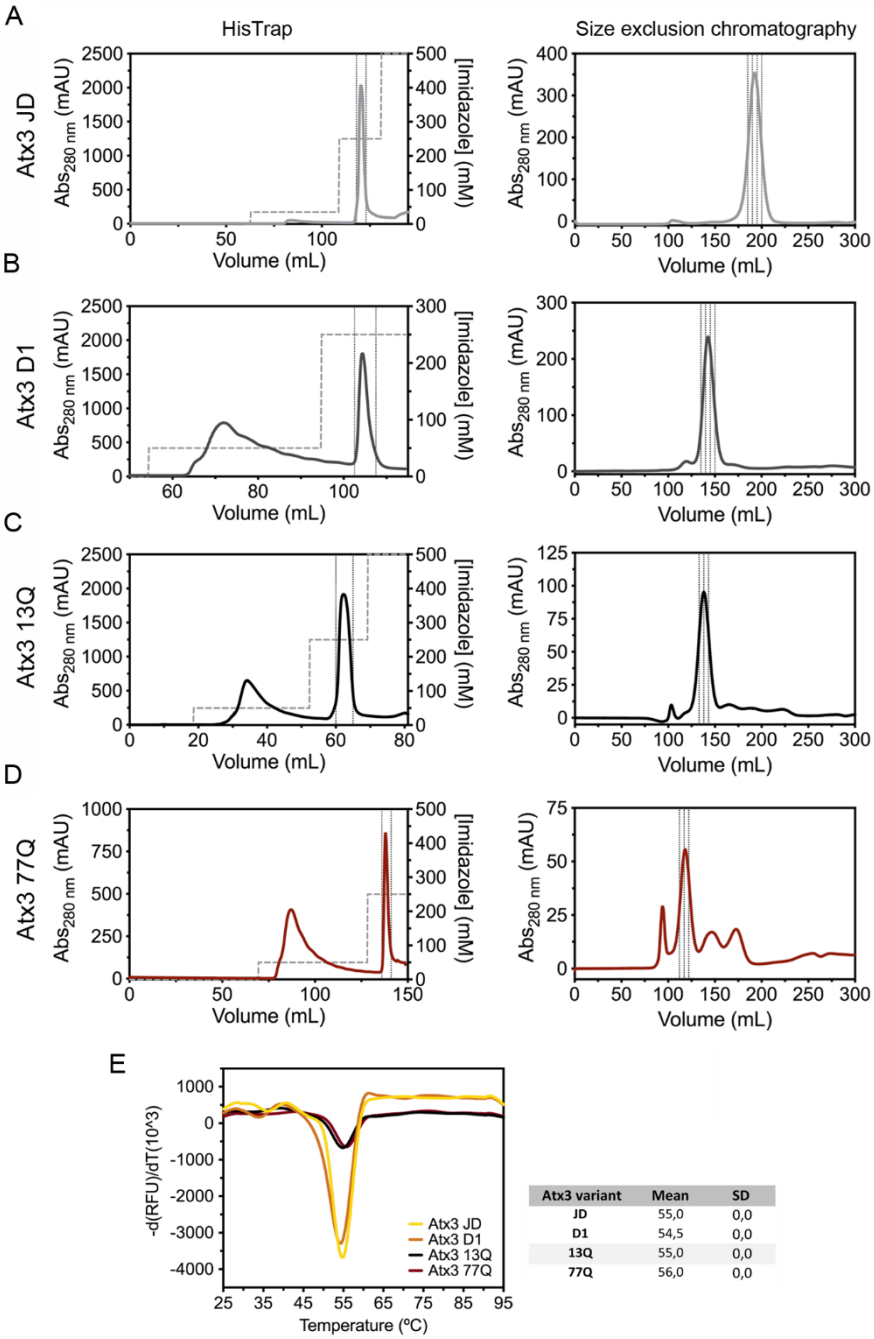

Atx3 variant	Mean	SD
JD	55,0	0,0
D1	54,5	0,0
13Q	55,0	0,0
77Q	56,0	0,0

Supplementary Figure S2. Purification and thermal shift assay of different Ataxin-3 constructs. Chromatograms showing the purification of the ataxin-3 constructs **(A)** JD, **(B)** D1, **(C)** Atx3 13Q and **(D)** Atx3 77Q by Ni^{2+}-charged IMAC HiTrap and HiPrep 20/60 Sephacryl S-300 HR column. Grey lines represent fractions selected for further purification or storage. **(E)** Thermal shift assay of Atx3 JD, Atx3 D1, Atx3 13Q and Atx3 77Q. Curves represent an average of 3 replicates per condition.

Population	Allele C	Allele G
African	0,831	0,169
American	0,816	0,184
East Asian	0,576	0,424
European	0,728	0,272
South Asian	0,663	0,337
Total	0,724	0,276

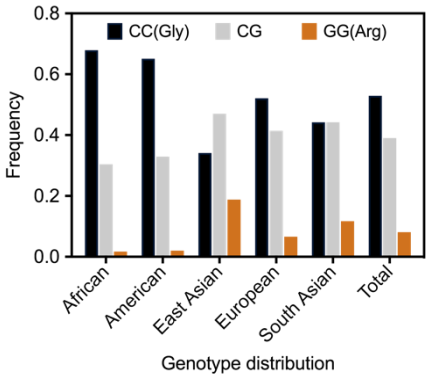

Supplementary Figure S3. Distribution of variant rs12895357 in healthy population. Data collected from the 1000 Genome project Phase 3 which aggregated genomic information from 4973 healthy individuals showed that homozygotic individuals for G306R are found in all population being more prevalent in East Asian populations.

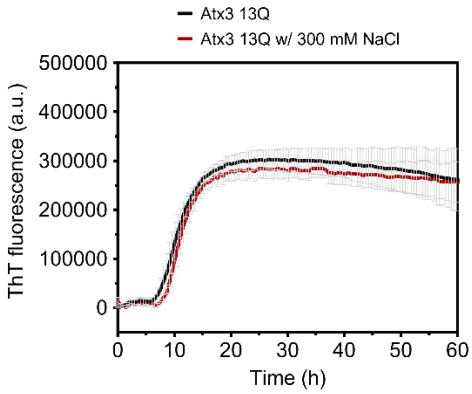

Supplementary Figure S4. Effect of 300 mM NaCl on ataxin-3 aggregation kinetics. ThT assay to measure the formation of amyloid-like species in Atx3 13Q in the presence of 300 mM of NaCl. Curves represent the mean and standard deviation of five replicates for each condition using FluoDia T70 microplate fluorimeter.

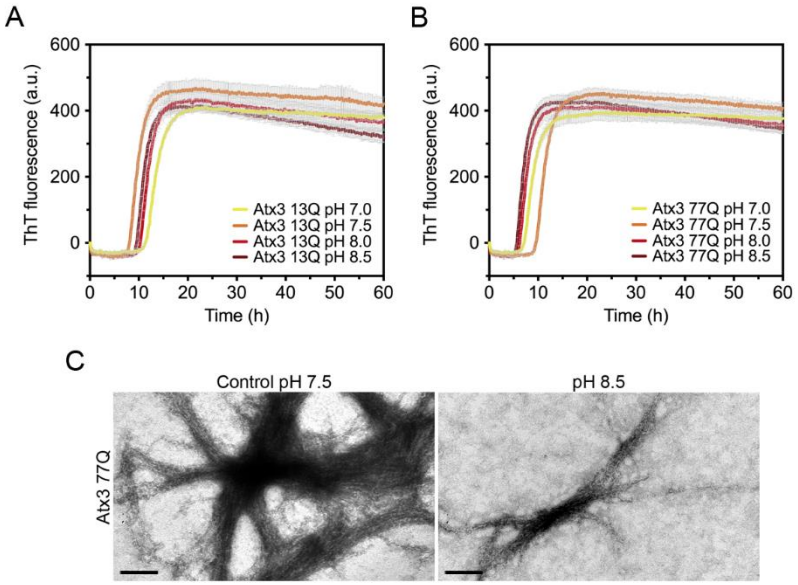

Supplementary Figure S5. Effect of pH on ataxin-3 aggregation kinetics. **(A**) Atx3 13Q and **(B)** Atx3 77Q amyloid-like formation, monitored by ThT fluorescence, at pH of 7.0, 7.5 (control), 8.0 and 8.5. Curves

represent the mean and standard deviation of five replicates for each condition using the HIDEX CHAMELEON V plate reader. **(C)** TEM images after negative staining of ThT assay endpoint samples (60 h, 37 °C) of Atx3 77Q at pH 7.5 (control) and 8.5. Scale bars correspond to 200 nm.

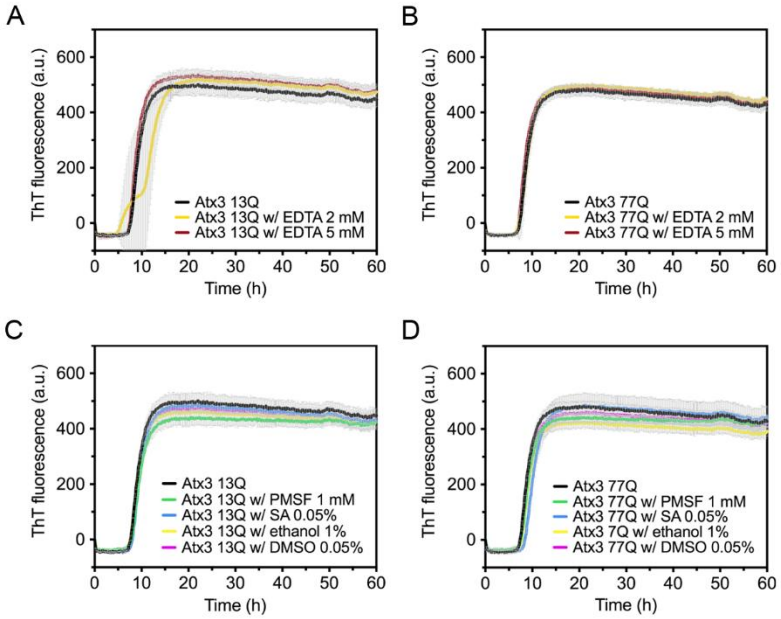

Supplementary Figure S6. Different aggregation buffer components do not affect ataxin-3 aggregation kinetics. ThT assay to measure the formation of amyloid-like species in **(A, B)** Atx3 13Q and **(C, D)** Atx3 77Q in the presence of different concentrations of EDTA, PMSF, sodium azide (SA), ethanol and DMSO. Curves represent the mean and standard deviation of five replicates for each condition using the HIDEX CHAMELEON V plate reader.

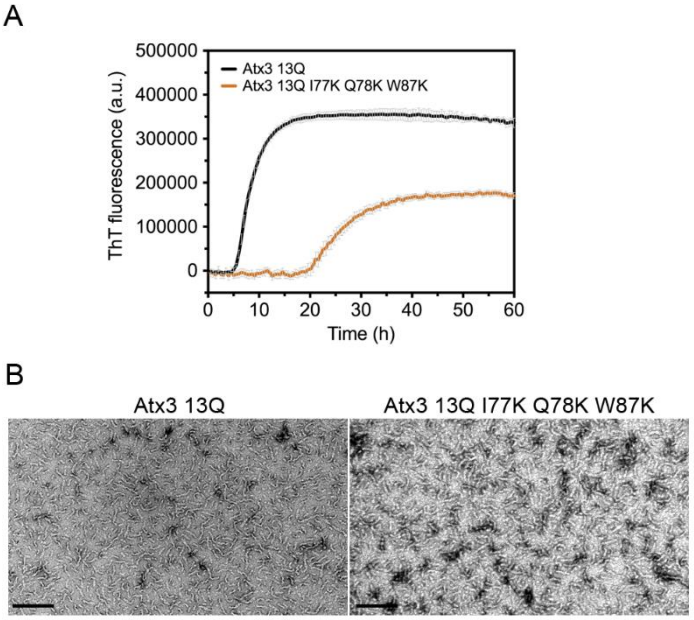

Supplementary Figure S7. Effect of mutating the second ubiquitin binding site of the JD on ataxin-3 aggregation kinetics. ThT assay to measure the formation of amyloid-like species in **(A)** Atx3 13Q and Atx3 13Q I77K Q78K W87K. Curves represent the mean and standard deviation of five replicates for each condition using a FluoDia T70 microplate fluorimeter. **(B)** TEM images after negative staining of ThT assay

endpoint samples (60 h, 37 °C) of Atx3 13Q and Atx3 13Q I77K Q78K W87K. Scale bars correspond to 200 nm.

S4. Reagents Used

Supplementary Table S4. List of reagents used in this work.

Reagent	Brand	Reference
Acrylamide	Bio-Rad	1610148
Ampicillin	Formedium	AMP100
APS (Ammonium Persulfate)	Bio-Rad	161-0700
DNase	Sigma-Aldrich	DN25-100
DTT (Dithiothreitol)	Biosynth	D-8200
EDTA (Ethylenediaminetetraacetic acid)	Merck	1.08418.0250
Glucose	Millipore	1.04074.1000
Glycerol	VWR	24388.384
Glycine	Sigma-Aldrich	G8898
HEPES (4-(2-hydroxyethyl)-1-piperazineethanesulfonic acid)	Sigma-Aldrich	H3375
Imidazole	Acro Organics	301870010
IPTG (Isopropyl β-D-1-thiogalactopyranoside)	NZYTech	MB02603
Luria Broth w/o NaCl	Formedium	LBO0102
Lysozyme	Sigma-Aldrich	62971
Magnesium chloride hexahydrate	Merck	1.05833.0250
Parafin Oil	Sigma-Aldrich	76235
PEG (Polyethyleneglycol)	Sigma-Aldrich	P2263
PMSF (Phenylmethanesulfonyl fluoride)	Sigma-Aldrich	P7626
RNase	NZYTech	MB18701
SDS (Sodium dodecyl sulfate)	Sigma-Aldrich	L3771
Sodium chloride	Merck	1.06406.1000
Sodium phosphate dibasic dihydrate	Merck	1.06580.1000
Sodium phosphate monobasic dihydrate	Merck	1.06342.1000
TEMED (tetramethylethylenediamine)	Merck	T9281
Thioflavin-T	Sigma-Aldrich	T3516
Tris-HCl	Merck	1.08382.2500
Uranyl Acetate	EMS	22400

S5. References

1. Rames, M.; Yu, Y.; Ren, G. Optimized negative staining: a high-throughput protocol for examining small and asymmetric protein structure by electron microscopy. *JoVE (Journal of Visualized Experiments)* **2014**, e51087.

Chapter 3 - Unveiling the structural details of Ataxin-3 aggregation pathway using cryo-EM

Francisco Figueiredo, Alexandra Silva, Ausra Domanska, Pasi Laurinmaki, Sarah Butcher, Sandra Macedo-Ribeiro

All nanobodies experiments were performed by Alexandra Silva

3.1 Introduction

Machado-Joseph Disease (MJD) is a rare, inherited neurodegenerative disease that affects the central nervous system and to this date, does not have a cure. All therapies available are limited to treating some of the associated symptoms (do Carmo Costa & Paulson, 2012). MJD is linked to a mutation in the *ATXN3* gene that leads to the extension of the polyglutamine (polyQ) tract of ataxin-3 (Atx3) protein (Kawaguchi et al., 1994). Atx3 protein contains an N-terminal globular Josephin Domain (JD) and a C-terminal region with two or three Ubiquitin Interacting Motifs (UIMs) and a polyQ tract. Atx3 can aggregate and form amyloid fibrils (Gales et al., 2005). This aggregation occurs in two distinct steps (Andrew M Ellisdon, Thomas, & Bottomley, 2006; Gales et al., 2005; Masino et al., 2011; Masino et al., 2004; Scarff et al., 2013). The first step is mediated by the JD and leads to the formation of SDS-soluble protofibrils, that is common to both non-expanded and expanded Atx3. The second step which is exclusive to the expanded Atx3, forms large, mature and stable amyloid-like fibrils that are SDS-resistant (A. M. Ellisdon, Pearce, & Bottomley, 2007; Scarff et al., 2015; Scarff et al., 2013). Protein aggregation into amyloid and amyloid-like fibrils is a very dynamic process that can be modulated by many factors (Iadanza, Jackson, Hewitt, Ranson, & Radford, 2018) (Discussed in Chapter 1 and Chapter 2). Therefore, several intermediate structures are formed in this process, some of which are reported to be more toxic than the amyloid and amyloid-like structures formed at the aggregation endpoint (Evangelisti et al., 2016; Glabe, 2006; Glabe & Kayed, 2006; Lashuel et al., 2002; Winner et al., 2011). Identifying Atx3 self-assembled species along the aggregation pathway and uncovering their structural features could be the first step to understand the toxicity of Atx3 in MJD.

Structural studies are of utmost importance because amyloid fibril structures are highly diverse, as seen in the examples depicted in Figure 1. Different proteins yield different fibrillar structures (Fitzpatrick et al., 2017; Sachse, Fändrich, & Grigorieff, 2008). Cryo-Electron Microscopy (cryo-EM) is a powerful tool to obtain atomic resolution of amyloid structures and study the physical properties of the fibril and its assemblies. Amyloid fibrils have a large variety of inter-monomer and inter-fibril interactions (Iadanza et al., 2018) and this could explain the phenotypic differences observed in each associated disease. Our work proposes to tackle this gap of information in MJD, since there is no known structure of Atx3 amyloid fibrils.

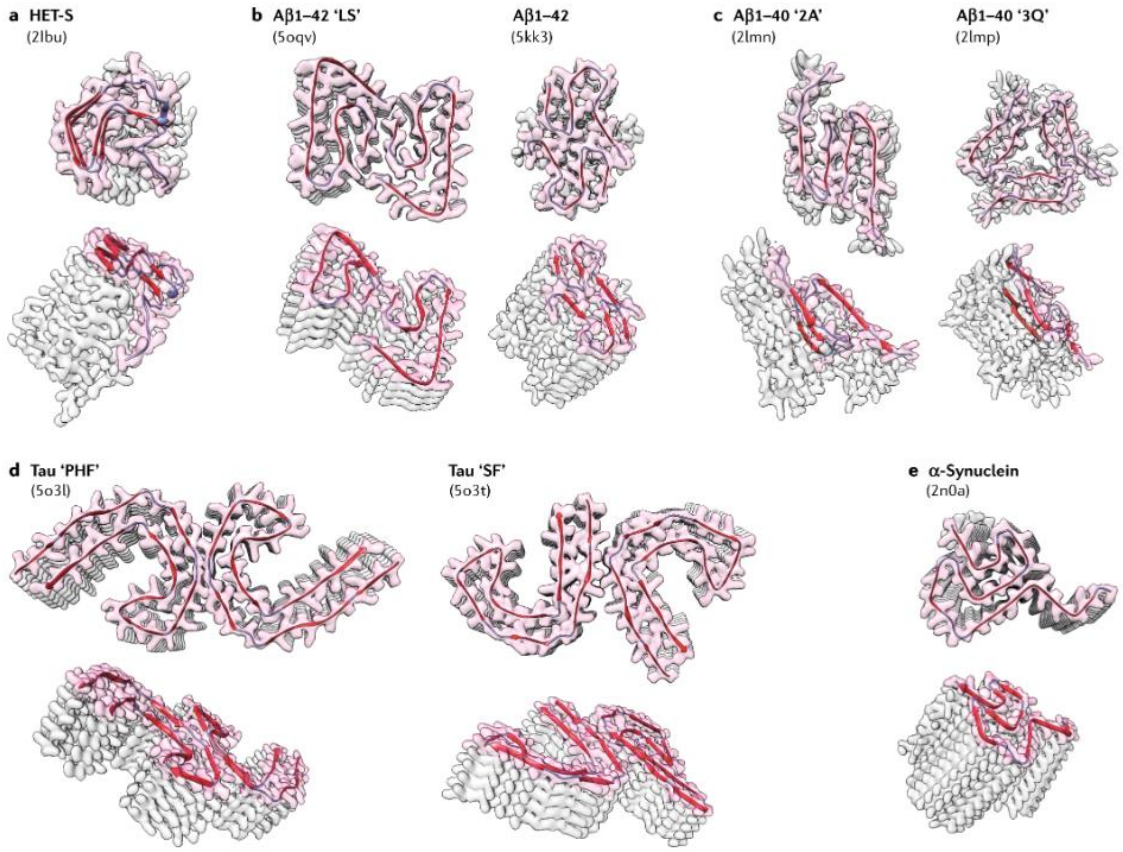

Figure 1 – Structural heterogeneity of amyloid fibrils. (A) Single filament of β-helix from HET-S (PDB entry 2lbu). **(B)** Two polymorphs of amyloid-β 42 fibrils formed under different growth conditions (PDB entry 5oqv (left) and 5kk3 (right)). **(C)** Two polymorphs of amyloid-β 40, prepared under same solution but propagated from different morphologies (2A PDB entry 2lmn (left) and 3Q PDB entry 2lmp (right)). **(D)** Two polymorphs of tau fibrils: paired helical (left – PDB entry 5o3l) and straight (right – PDB entry 5o3t). **(E)** Single filament of α-synuclein fibril (PDB entry 2n0a). The main chain of the top layer of polypeptide chain in each fibril is shown in red. [Taken with permission from Iadanza et al. (2018)].

Transmission Electron Microscopy (TEM) is a useful technique that allow us to visualize structures at a nanometre scale (Gras, Waddington, & Goldie, 2011) and with recent advances in detector technology and new/improved image processing techniques, the called Resolution Revolution, cryo-EM now is probably the mainstream tool to obtain high resolution 3D structures of macromolecules (Ravelli et al., 2020). TEM is also very versatile instrument, since it allows us to visualize monomeric samples bellow <100 kDa (Herzik, Wu, & Lander, 2019) up to big amyloid filaments (Fitzpatrick et al., 2017). One great advantage of cryo-EM is that very small amount of sample is needed. Samples that cannot be isolated in large quantities for X-ray crystallography, that are heterogeneous or form flexible complexes that do not crystallize can be used in cryo-EM (Kühlbrandt, 2014). Our first proposed objective for this work, is to characterize Atx3 aggregation by TEM in order to identify structural features of the oligomeric and

fibrillar species that are formed in the aggregation pathway of non-expanded and expanded Atx3.

The first step on this, is to evaluate how these aggregates look like under conventional TEM by negative staining. Although this technique was developed in the 1950s for staining of virus particles (Brenner & Horne, 1959) it is still the best method for a rapid assessment of sample quality before optimizing cryo conditions (Harris, 2007; Scarff, Fuller, Thompson, & Iadanza, 2018). In theory, this technique could be done in any laboratory with access to any type of TEM. Also, the small time needed for EM grid preparation allied with the high contrast provided, makes negative staining ideal for evaluation of sample purity, concentration, heterogeneity and flexibility (Thompson, Walker, Siebert, Muench, & Ranson, 2016). The principle behind negative staining technique is that the particle of interest is deposited in the EM grid and then is covered with an electron dense stain salt solution, followed by drying (Carroni & Saibil, 2016; Harris, 2007; Scarff et al., 2018). The most common negative staining solutions are uranyl acetate and uranyl formate, but others such phospho-tungstates, ammonium molybdate or lanthanide-based solutions can be used. Uranyl acetate and formate have the advantage of also having fixative properties but at the same time, they are both toxic and mildly radioactive. (Rames, Yu, & Ren, 2014; Scarff et al., 2018). These heavy metal ions that cover and surround the particle of interest have a greater ability to disperse electrons compared to the atoms present in the sample, creating a darkness around the sample allowing a higher image contrast (Harris, 2007) and protecting sample from beam damage (Rames et al., 2014). Unfortunately, negative staining biggest disadvantage is the artefacts that can be formed. These artefacts could be originated from stain-sample (buffer or molecule) interactions, general aggregation, molecular dissociation, dehydration, flattening and stacking (Rames et al., 2014; Scarff et al., 2018). It is known that phosphate buffer and high salt concentrations can form crystalline precipitates, also, reducing agents, detergents, sucrose and glycerol can affect stain quality (Burgess, Walker, Thirumurugan, Trinick, & Knight, 2004; Scarff et al., 2018).

After evaluating sample quality by negative staining, we then proceeded to the next step, cryo-EM. Cryo-EM allows for sample be preserved in a close native state, by quickly vitrifying it in liquid ethane at liquid nitrogen temperature, hence the name, “cryo-EM” (Bai, McMullan, & Scheres, 2015). Sample vitrification is the first step of the cryo-EM workflow and it is done automatically using an vitrification device (Figure 2). Commercially devices are available and consist of a chamber with controlled temperature and humidity where sample (<5 µL volume) is deposited into the EM grid. To start this procedure, normally EM grids are glow discharged prior to sample

deposition. This increases the hydrophilicity of the carbon coated grid, granting a more even sample distribution (Dubochet, Ducommun, Zollinger, & Kellenberger, 1971). Then, the sample is applied to the grid and the grid is blotted with filter paper to remove excess sample and form an aqueous film where sample is located. This is a very critical step where glow discharge of the grid, sample deposition, air-water interfaces, temperature and humidity could influence sample/grid quality (Ravelli et al., 2020). After blotting, the tweezers that holds the EM grid, quickly plunges it in a liquid ethane bath that is liquid nitrogen cold (around -180 ºC). At this temperature, water forms a noncrystalline solid called amorphous or vitreous ice (Dubochet et al., 1971) where fully preserved samples could be imaged in a native and hydrated environment (Koning et al., 2022).

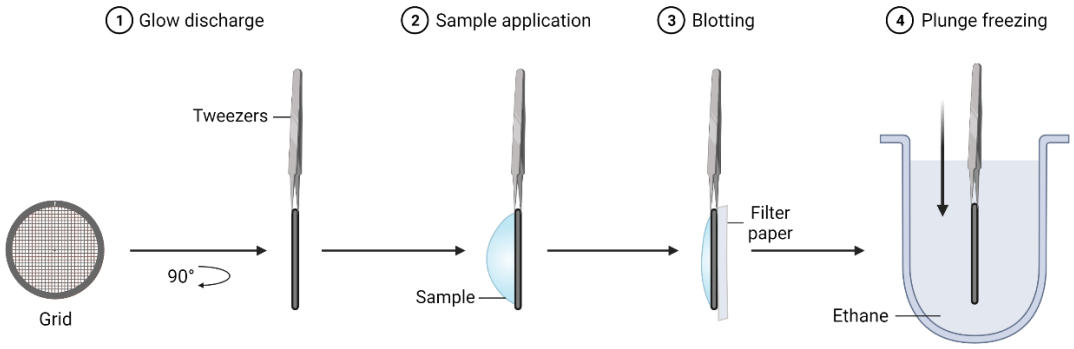

Figure 2 – Cryo-EM plunge freezing protocol. These are the four main steps to prepare a cryo-EM grid.

Because sample is in native state, with no contrast agents added to solution and it is sensitive to electron damage, image acquisition must be done in low dose conditions (Carroni & Saibil, 2016). After data acquisition, analysis is done in a Single Particle Analysis (SPA) approach, where particle reconstruction can be obtained by using different powerful algorithms that require appropriate computational resources. These algorithms, use the several thousand projection images of isolated particles, to average them into a 3D structure (Bai, Fernandez, McMullan, & Scheres, 2013).

Results from negative staining followed by preliminary results from cryo-EM showed that Atx3 fibrils appear to be flexible assemblies. This took us to apply a cryo-Electron Tomography (cryo-ET) approach to further investigate their structure instead of a SPA. In our case, cryo-ET sample preparation is the same as for SPA, the difference is in how the data sets are acquired. Instead of acquiring several random images, tomograms are acquired. A tomogram is a group of images collected through a set of defined tilts (Figure 3A). Tomograms can be acquired in different ways, depending on sample sensitivity (Turk & Baumeister, 2020). In our experiments, we used a dose-

symmetric approach (Figure 3B). This consists on starting the data collection at low angles and moving to the highest tilt in both directions simultaneously (Hagen, Wan, & Briggs, 2017), in our scheme, we did a ±60º tilt series with a 2º tilt step making tilt angle acquisition like: 0º, +2º, -2º, -4º, +4º, +6º, -6º, -8º (…). The advantages of this method of acquisition is that by starting collection a low angles where the path for the electrons is the shortest, there is a maximization of the amount of high resolution information, minimizes alignment jumps of the TEM and the accumulated electron dose is smoothly distributed through the tilt series (Hagen et al., 2017).

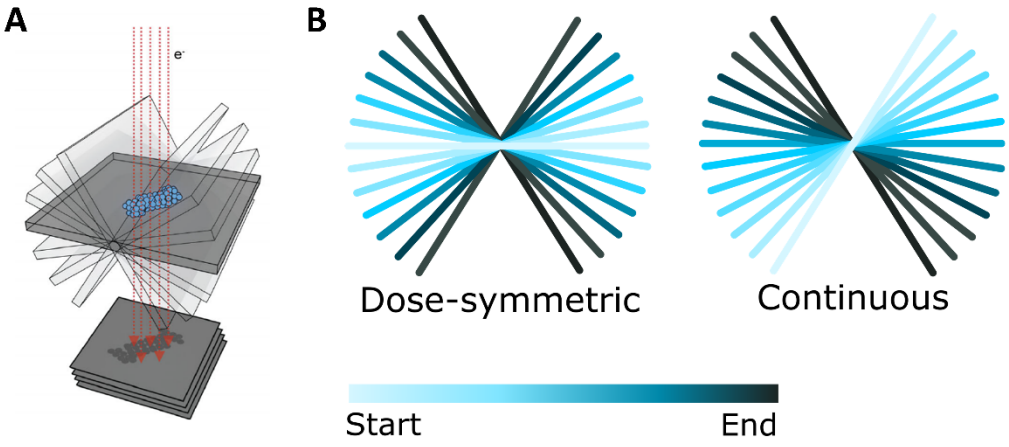

Figure 3 – Cryo-Electron Tomography data acquisition method. (A) Example of how a tomogram is acquired. **(B)** Differences schemes of how a tomogram could be acquired. [(A) Taken from Turk and Baumeister (2020) and (B) Adapted from Hutchings and Zanetti (2018)]**.**

To achieve the proposed objectives, we developed an improved negative staining protocol that allowed us to fast screen samples, while obtaining consistently good TEM images of our structures of interest. We then applied and obtained funding through Instruct-ERIC platform and the European Molecular Biology Organization (EMBO) to establish a new collaboration with Sarah Butcher's laboratory from the University of Helsinki, Finland to perform the cryo-EM studies. While there, I had the opportunity to visit CryoSol facilities (https://cryosol-world.com) in the Netherlands where we prepared some samples for cryo-EM using the new state-of-the-art VitroJet equipment that does not require blotting of the grid and quickly vitrifies samples by a cold jet prior to plunging EM grid in liquid ethane (Ravelli et al., 2020).

To complement the study of Atx3 fibrillization by cryo-EM, we were also interested in observing how Atx3 aggregates are affected in the presence of a Atx3-binding

chaperone. In this case, we tested Atx3-binding Nanobodies (NB) that were developed and are currently being studied in our lab.

In this work, we were able to develop a negative staining protocol to study Atx3 fibrillization, apply a cryo-EM time-course analysis where we successful obtained several tomograms of non-expanded and expanded Atx3 protofibrils and mature and SDS-resistant fibrils and acquired several data sets of Atx3:NB samples. Data analysis is still ongoing and for future perspectives, we expect to obtain a structure from Atx3 non-expanded and expanded fibrils and at the same time Atx3:NB complexes.

3.2 Materials and methods

Protein expression and purification, Thioflavin-T aggregation kinetics and TEM protocol were described in Chapters 2 and 4.

3.2.1 Cryo-EM sample preparation

Aggregation assays were performed using 5 µM of both non-expanded (Atx3 13Q) and expanded (Atx3 77Q) Atx3, alone or in combination with NB05 at a final concentration of 25 µM (1:5 ratio, Atx3:NB). Briefly, incubations were performed in aggregation buffer (20 mM HEPES pH 7.5, 150 mM NaCl, 1mM DTT) for 96 hours at 37 ºC in a 200 µL volume, without shaking. 10 µL samples were collected at different time points, (0, 43 and 96 hours) for cryo-EM analysis. To these aliquots, gold fiducial markers were added, in a final concentration of 150 mM. 3 µL sample with fiducials were applied to a glow-discharged 300 mesh copper Quantifoil R 1.2/1.3 grid. Grids were back blotted for 1.5 seconds with filter paper to remove the excess sample and flash-frozen in liquid ethane with Leica vitrification robot EM GP (Leica) at Instruct-ERIC Center Finland at the University of Helsinki and stored in liquid nitrogen until cryo-EM analysis.

A second experiment was prepared in the same conditions as described above to be performed in Maastricht University, Netherlands using CryoSol Vitrojet equipment. Pre-clipped grids were plasma cleaned for 90 seconds at 2.2 mA at 0.35 mbar; 0,1 nL of sample was then applied to the grids and immediately flash-frozen and stored in liquid nitrogen. Samples were shipped to the University of Helsinki, Finland for visualization.

In all, 200 kV data acquisition was carried out at the Instruct-ERIC Center Finland at the University of Helsinki, Finland. The frozen-hydrated grids were loaded into an FEI TALOS Artica electron microscope operated at 200 kV. More than 500 movies were

acquired with Falcon 3EC direct electron detector at a nominal magnification of x150000 giving a pixel size of 0.97 Å per pixel. The total electron dose was approximately 30 electrons per $Å^2$ fractionated into 30 frames. MotionCor2 (X. Li et al., 2013) was used to produce a single micrograph from aligned and averaged movie frames.

3.2.2 Tilt series collection

We collected at least seven tilt series of each Atx3 variant per time point using SerialEM software (Mastronarde, 2005) in a dose symmetric mode on an FEI TALOS Artica electron microscope operated at 200 kV and equipped with a Falcon 3EC direct electron detector, from -60º to +60º in 2º increments, at 5 µm target under focus, 4.1 Å/pixel sampling size, with a cumulative dose of ~80 electrons per $Å^2$.

3.2.3 Tomographic reconstruction

All Atx3 fibrils and protofibers tilt series were binned by 2x and initially aligned and reconstructed into tomograms with IMOD software (Kremer, Mastronarde, & McIntosh, 1996).

3.3 Results

3.3.1 Optimization of negative staining technique

Negative staining is a technique developed in the late 1950s (Brenner & Horne, 1959) and it is an easy, straightforward and qualitative way to increase specimen contrast and evaluate sample quality by TEM. However, inherent to this technique is the formation of artefacts whether from drying the sample, crystals formed from the staining reagent or from the reaction from the staining reagent with sample/sample buffer. The basic protocol used before, which is visually described in Figure 4 consisted in applying 5 µL sample (diluted 5x in water) into a TEM grid for one minute, blot the grid with a piece of paper, apply 5 µL of 1 % (w/v) uranly acetate for 30 seconds and blot the grid with another piece of paper. There was no glow discharge of the grid prior to use and all this procedure was done at room temperature.

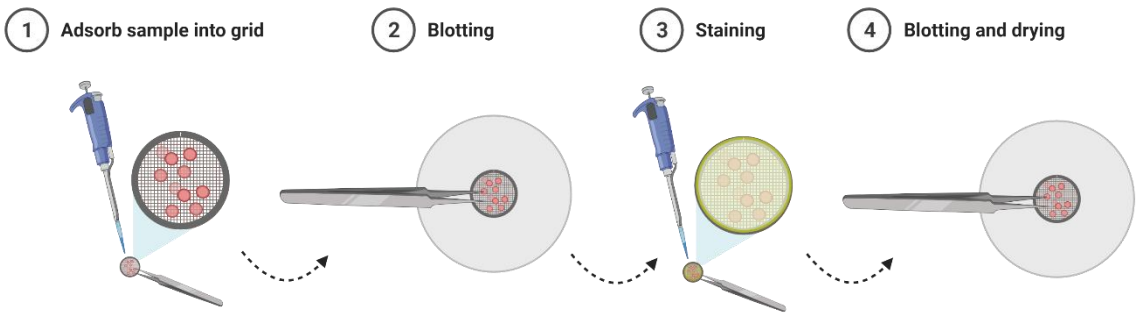

Figure 4 – Previous negative staining protocol. This consisted in four quick steps: apply sample to the grid for 1 minute, blot the back of the grid to remove excess of sample, apply the staining agent (1 % (w/v) of urany acetate) for 30 seconds and then blot and dry the grid.

This simple method allowed us to visualize Atx3 samples. However, since background noise was always present in negative staining images from Atx3 samples (Figure 5) and one of the objectives of the study was to identify structures formed during Atx3 fibrillization pathway, doubts emerged as it was not obvious if the observed structures were artefacts/background noise or possible Atx3 oligomeric species.

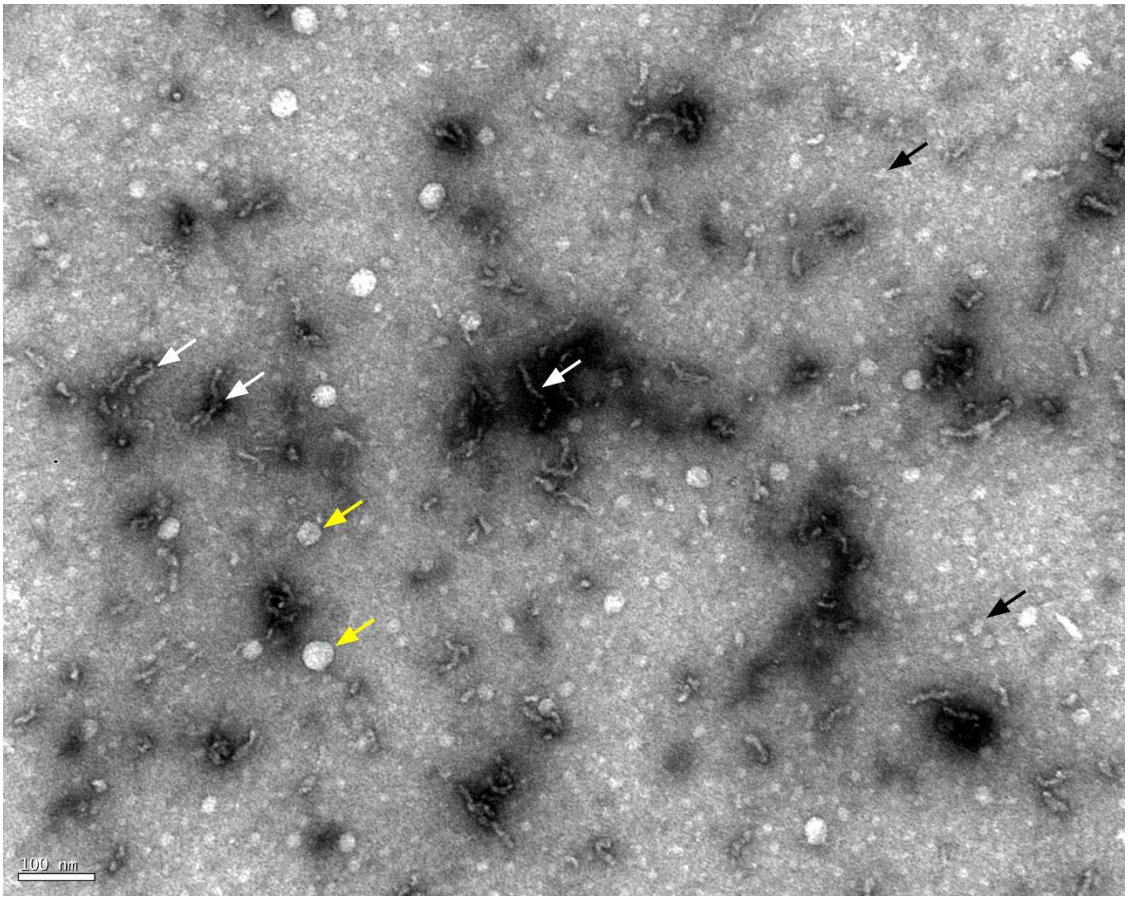

Figure 5 – Artefacts present in TEM image of negatively stained Atx3 sample in Phosphate buffer. TEM image after negative staining of aggregation endpoint (60 hours, 37 ºC) of Atx3 13Q

sample in Phosphate buffer. White arrow: Atx3 13Q protofiber; Black and yellow arrow: possible staining artefacts. Scale bar 100 nm.

In Figure 5 it is possible to observe several common artefacts. The white arrows highlight the Atx3 13Q protofibers. However, the black arrows report on structures that could be Atx3 13Q oligomeric species or possible artefacts. The same applies to the yellow arrow, where a not so electron-dense spherical structure is being observed.

We changed the aggregation buffer from sodium phosphate buffer to HEPES (detailed discussion in Chapter 2) and this improved background noise. However, the sample distribution on grid was not optimal (Figure 6). Atx3 13Q protofibers are well visible and detailed (Figure 6 – white arrow), but there were still some uncertainties about other structures visible (Figure 6 – black arrow). An improvement to the technique was necessary to boost image quality and sample quantity in order to better understand what was being observed in TEM.

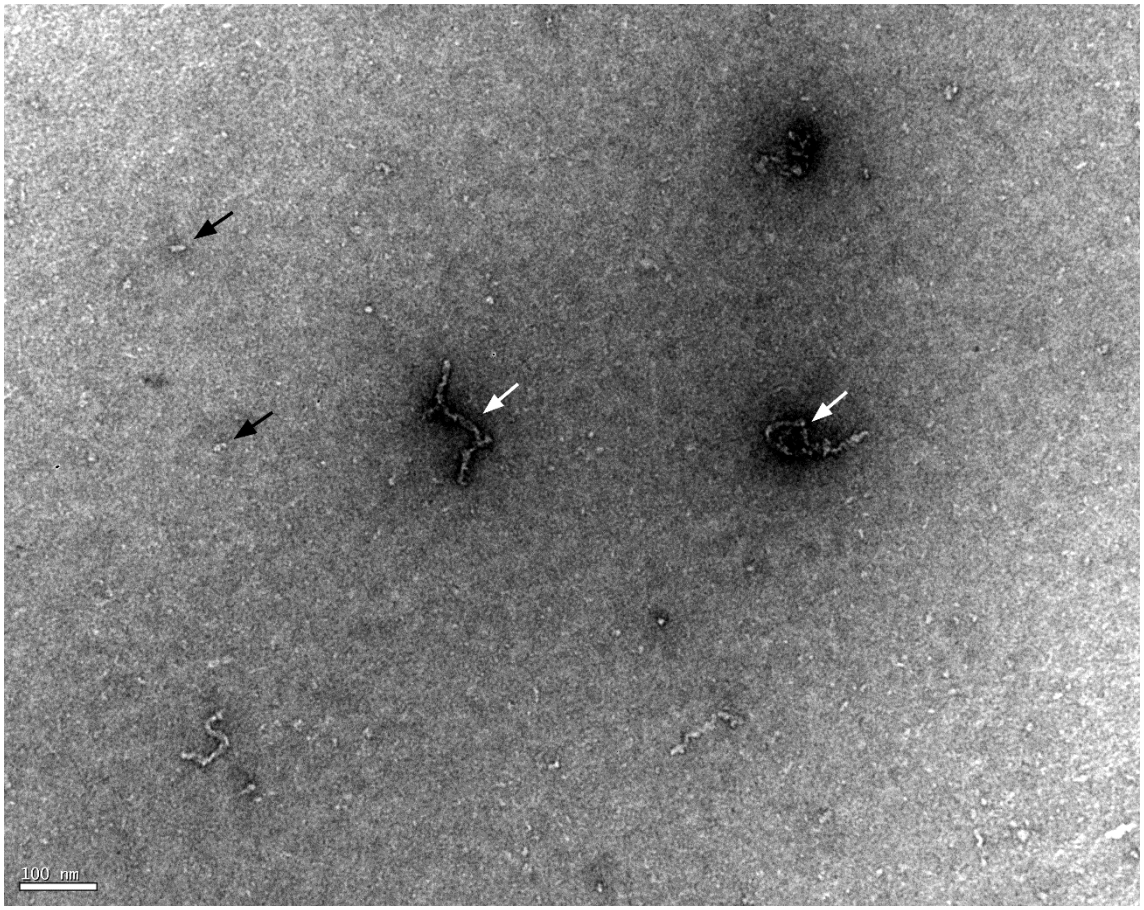

Figure 6 - Artefacts present in TEM image of negatively stained Atx3 sample in HEPES buffer. TEM image after negative staining of aggregation endpoint (60 hours, 37 ºC) of Atx3 13Q sample in HEPES buffer. White arrow: Atx3 13Q protofiber; Black: possible staining artefacts. Scale bar 100 nm.

The best result was obtained by applying a protocol adapted from Rames et al. (2014) that is completely described in Chapter 2 and which critical steps are detailed in Figure 7. Two different staining agents were tested, uranyl acetate and uranyl formate. The three main differences between this method and the previously used one, were the glow discharge of the TEM grid before use, three consecutive washes with water before being applied the staining agent and performing all steps over ice to avoid evaporation and/or any possible protein degradation.

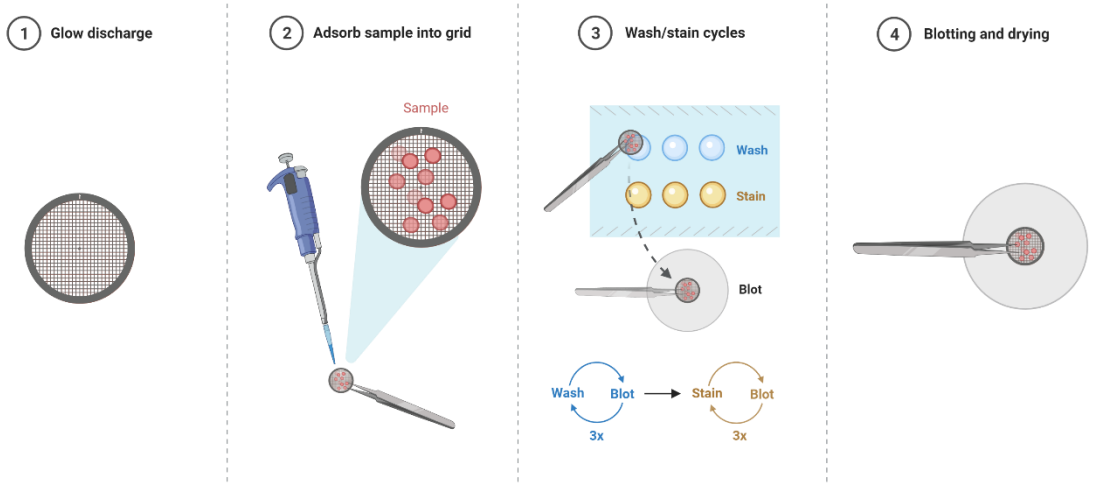

Figure 7 – Improved negative staining protocol adapted from Rames et al. (2014). First the EM grid is glow discharged, only then it is applied Atx3 sample for 1 minute over ice, followed by three consecutive washes in water and three washes in staining reagent, all washing steps are performed over ice. Then grid is blotted and dried prior to TEM analysis.

As seen in Figure 8, this method consistently yielded a good particle distribution throughout the grid and the background staining was more homogeneous. This method also showed that there were no significant differences between using uranyl acetate (Figure 8A) and uranly formate (Figure 8B) in our samples. Therefore, we decided to continue using uranyl acetate in our negative staining protocol. This method also showed very good results in the staining mature Atx3 fibrils from the expanded Atx3 77Q (Figure 9).

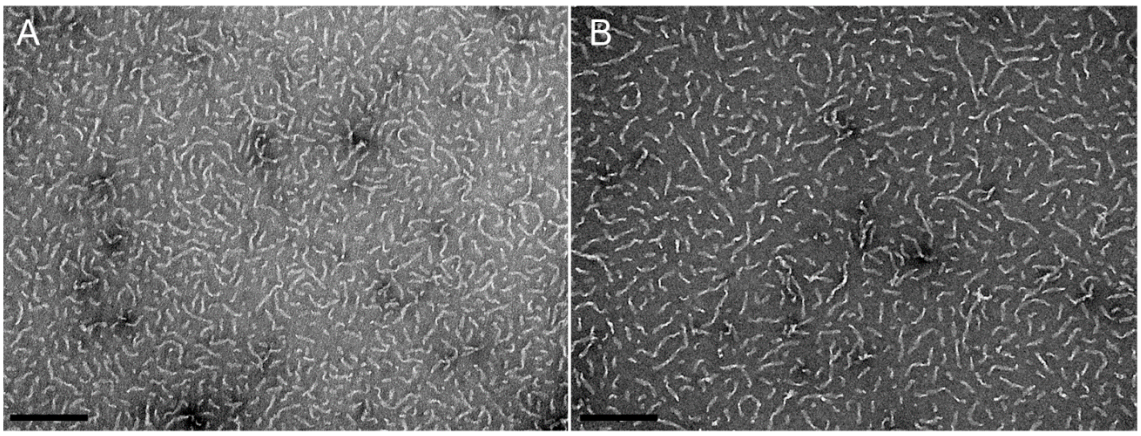

Figure 8 – New negative staining protocol in Atx3 13Q endpoint aggregation samples. TEM image after negative staining with **(A)** uranyl acetate and **(B)** uranyl formate of aggregation endpoint (60 hours, 37 ºC) of Atx3 13Q sample in HEPES buffer. Scale bar 100 nm.

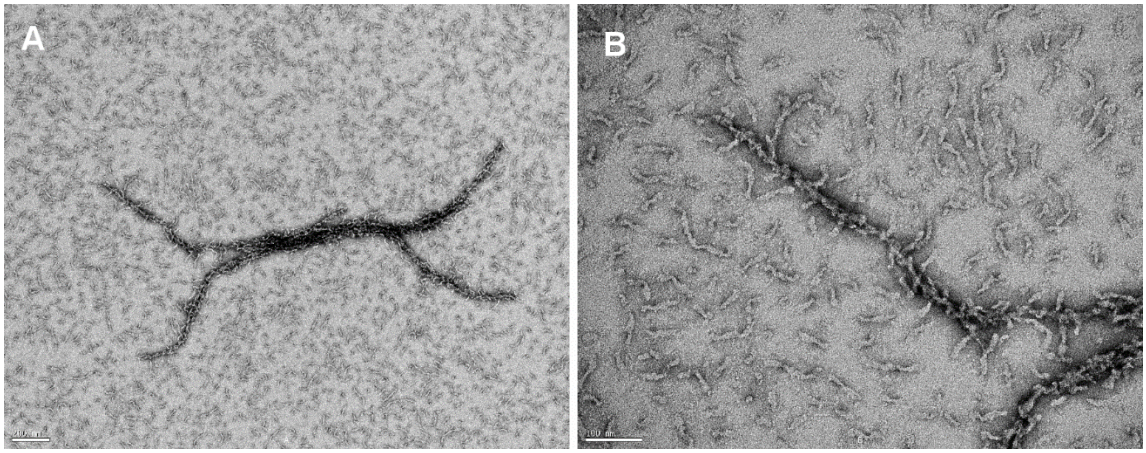

Figure 9 - New negative staining protocol in Atx3 77Q endpoint aggregation samples. TEM image after negative staining with uranyl acetate of aggregation endpoint (96 hours, 37 ºC) of **(A)** Atx3 77Q in HEPES buffer. **(B)** Zoom in detail of Atx3 77Q fibril. Scale bar 100 nm

3.3.2 First cryo-EM assay

After successfully obtaining good negative staining images of our Atx3 samples, we obtained funding from EMBO and Instruct-ERIC platform to perform cryo-EM on our samples in Sarah Butcher's laboratory in Helsinki University, Finland. Our first assay consisted of an Atx3 13Q sample that was tested to confirm that techniques could be reproduced in the host lab. Protein re-purification by size-exclusion chromatography was done as described in Chapter 2 and the protein was incubated at 37 ºC for 96 hours. After 96 hours of incubation, the protein was prepared for cryo-EM. Sample aggregation was measured by ThT fluorescence (data not shown). Due to the unavailability of a conventional TEM, there was no possibility to observe sample quality by negative staining before cryo-EM. In this assay was tested a concentration of 150 mM fiducials

markers which consist of gold nanoparticles, with 10 nm diameter that are needed for the tilt alignment in case of a tomography approach.

Two different types of TEM grids were tested, Quantifoil R1.2/1.3 on 300 copper mesh grids and Quantifoil Multi A on 400 copper mesh grids. There are two differences in these grids, the mesh size and the holes in the Quantifoil™ support foil. Mesh is the number of squares per inch and it is illustrated in Figure 10. Cryo-EM grids need a support film that hold the sample, and there are several commercially available supports films. We used Quantifoil™ and tested two different hole types: R1.2/1.3, with several holes with a diameter of approximately 1.3 µm and MultiA, where holes have multi shape (from round to elliptical) and multi sizes (from 1 to 8 µm).

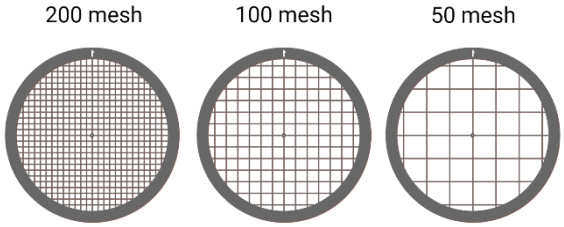

Figure 10 – Differences in mesh size of EM grids. Mesh is the number of squares per inch, higher the mesh, smaller are the squares in the grid.

The first results were very promising since Atx3 13Q fibrils could be easily observed (Figure 11). Normal ice contamination is also visible from the preparation/manipulation of the grids and fiducial markers were in a good concentration.

A small data set of images was acquired and it was done automatically by the cryo-EM. This can be done because, cryo-EM can detect patterns and correctly identifies the holes in the grid and the holes in the Quantifoil™. However, since Quantifoil MultiA has a mixed pattern of both hole size and shape, cryo-EM managing software struggled to select the correct areas where it should acquire images in these grids. At the same time, the 400 mesh (with smaller grid squares) would generate a problem for tomogram acquisition since in higher tilts, grid bars could interfere with image collection. With this outcome, we decided to use only the 300 copper mesh grids with Quantifoil R1.2/1.3.

Two sample concentrations were used, no dilution (5 µM) and 1:1 dilution (2.5 µM) and the undiluted sample had a better sample distribution on the grid, therefore, all grid preparations made onwards, were made using undiluted sample (5 µM).

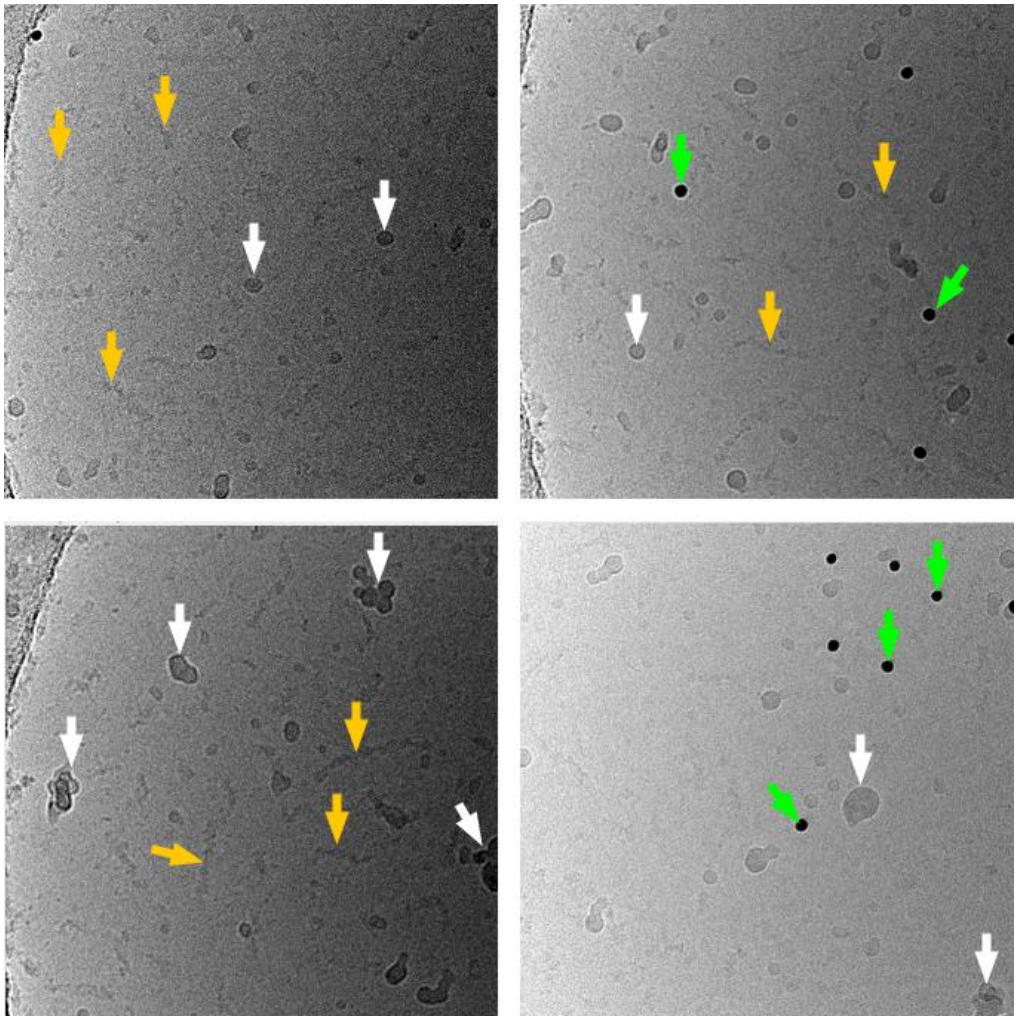

Figure 11 – Cryo-EM of Atx3 13Q endpoint aggregation samples. Cryo-EM images of aggregation endpoint (96 hours, 37 ºC) of 5 µM Atx3 13Q sample in HEPES buffer. Yellow arrow: Atx3 13Q protofibrils. White arrow: Ice contamination. Green arrow: Gold fiducial.

For the first time we were able to visualize Atx3 13Q fibrils by cryo-EM. The shape is similar to the one observed by negative staining and, as expected, sample heterogeneity is observed. Several different fibril sizes and bent structures can be observed in Figure 11. This small data set was analysed by SPA in order for me to obtain training in data processing techniques and to gather if any structural feature could be observed from this data. Using a box size of 500 pixel size (485 Å) we manually selected 200 particles – 200 fibril fragments – and applied a 2D classification using RELION – 2D classification algorithm (Scheres, 2012) and results are detailed in Figure 12.

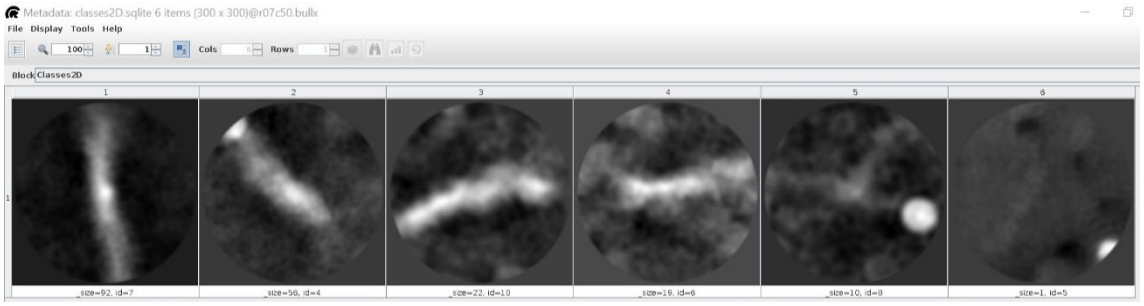

Figure 12 – 2D classification of selected particles. Classification of experimental SPA dataset using RELION – 2D (Scheres, 2012). No good classes were obtained.

2D classification is useful to enhance signal-to-noise ratio, group similar particles and discard invalid particles or contaminants. However, the high structural heterogeneity of the Atx3 fibrils challenges a successful SPA approach, and together with our collaborators we chose to continue the study of Atx3 fibrils using a cryo-ET approach.

3.3.3 Cryo-electron tomography approach

Repeating the same methodology described in 3.3.2, an assay with Atx3 13Q and Atx3 77Q was set up. Sample from both Atx3 isoforms was collected in three different time points: 0, 43 and 96 hours.

At the start of the Atx3 aggregation process (0 hours), no structures/aggregates can be observed, confirming that protein is monomeric. Since protein is smaller than 50 kDa, it is not visible by cryo-EM (Figure 13). After 43 hours of aggregation at 37 ºC, protein aggregates are visible in both Atx3 samples, different sizes of aggregates are observable but protein is mostly in a fibrillar form (Figure 13). After 96 hours of aggregation, fibrils in the Atx3 13Q sample are longer than those observed at 46 hours and a significant heterogeneity is still observed. In the Atx3 77Q sample, mature fibrillar clusters, only observed in the expanded form of Atx3, are present (Figure 13).

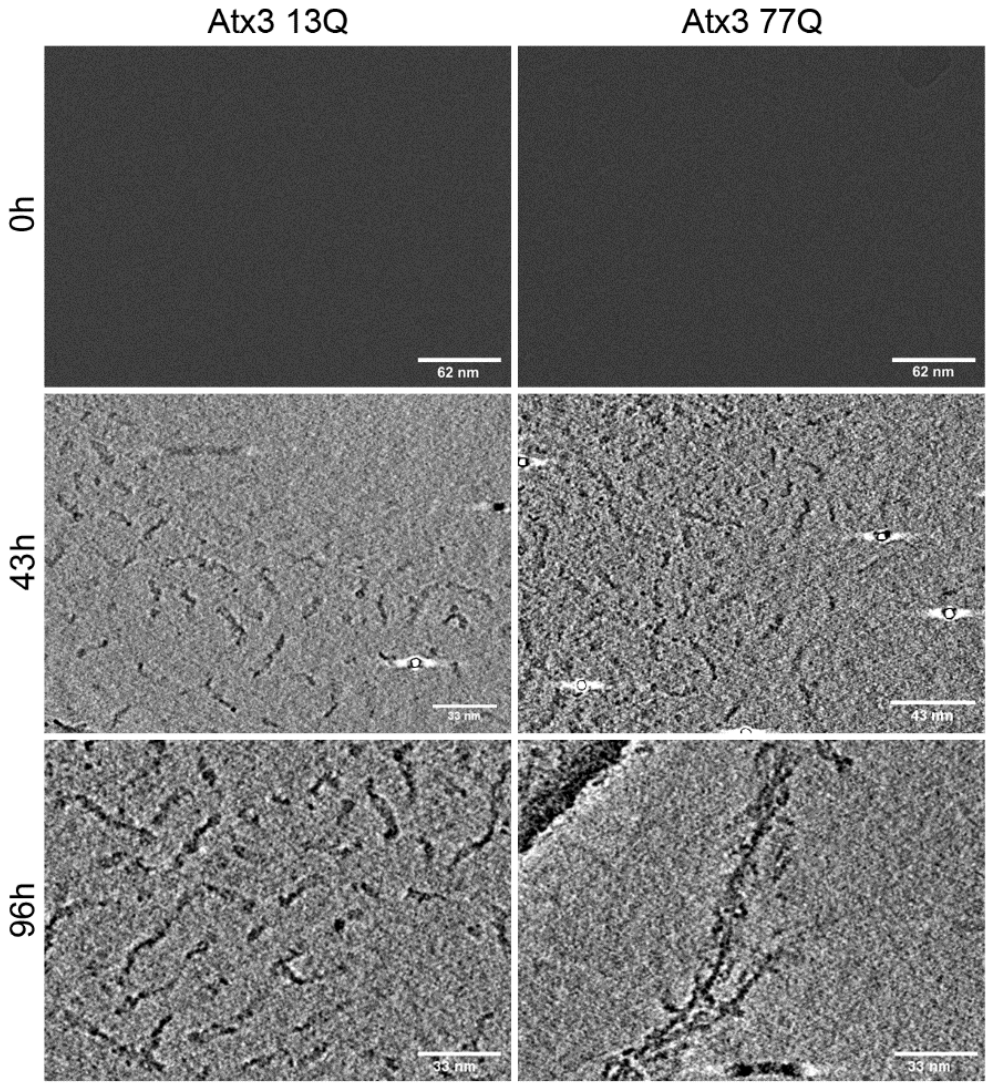

Figure 13 – Ataxin-3 13Q and 77Q reconstructed tomograms from a time course aggregation assay. Slice parallel to the xy plane through a representative 2x downsampled cryo-Electron Tomograms of aggregated Atx3 13Q and Atx3 77Q at 0, 48 and 96 hours of aggregation.

3.3.4 VitroJet sample preparation

The study of NBs and how they influence Atx3 aggregation were not a primary objective of this study. The usage of NBs as modulators of Atx3 aggregation could have two possibly outcomes. The first and major one is from the therapeutic point of view, since some NBs can inhibit Atx3 aggregation. The second is that they bind and stabilize Atx3, which could be useful to obtain a ultrastructure of the Atx3:NB complex. A similar approach to what was used to solve huntingtin ultrastructure (Guo et al., 2018; Harding et al., 2021).

As observed in Figure 14, by using a Thioflavin-T assay NB05 can alter aggregation of both non-expanded and expanded Atx3 (Figure 14A). Although there is an increase in fluorescence, meaning that aggregation was still occurring, TEM analysis

showed that NB05 prevented the formation of mature SDS-resistant fibrils (Figure 14B). This was confirmed by filter retardation assay (Figure 14C).

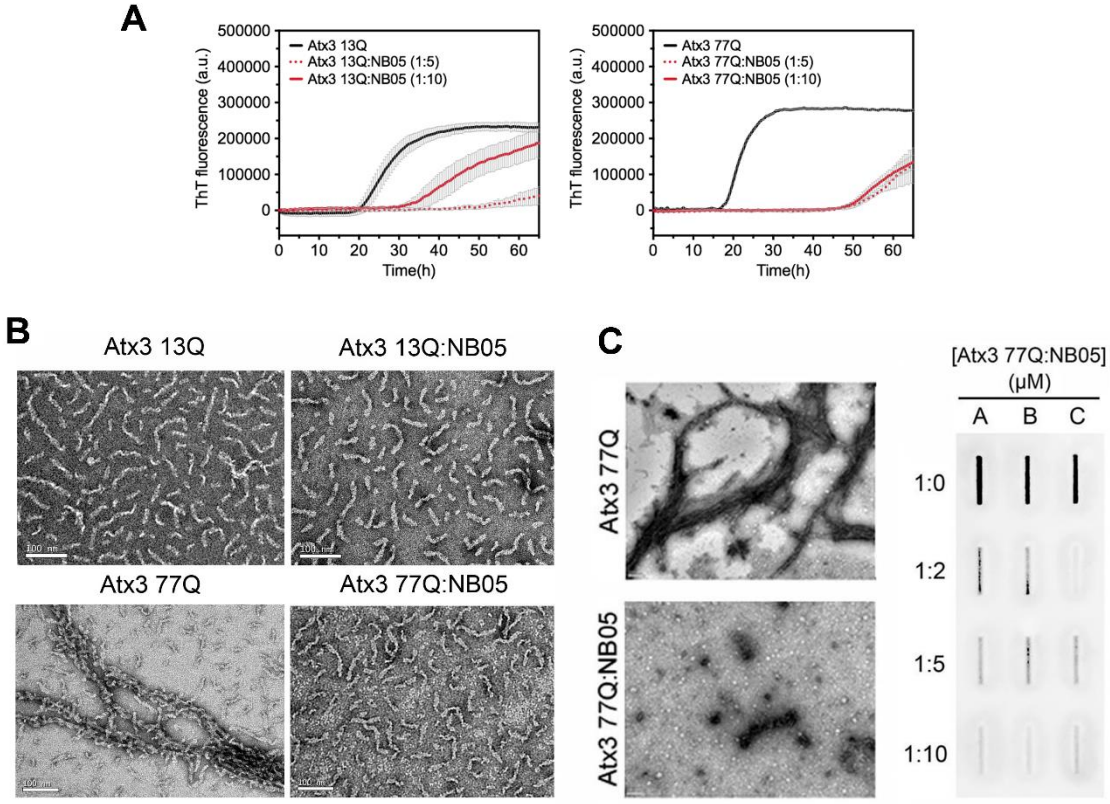

Figure 14 – Effect of NB05 on Atx3 aggregation kinetics. (A) ThT assay to measure the formation of amyloid-like species in Atx3 13Q and Atx3 77Q in the presence of 25 and 50 μM of NB05. Curves represent the mean and standard deviation of five replicates of each condition. **(B)** TEM images after negative staining of end point samples (70 h, 37 ºC) of both Atx3 isoforms with NB05 (1:5). Scale bar 100 nm. **(C)** Filter retardation assay monitored by immunostaining with mouse anti-Atx3 1H9 of aggregation end points (60 h, 37 ºC) from Atx3 77Q in the presence of NB05. A, B and C are replicates.

VitroJet allows users to pin printing samples on a TEM grid, which provides a more efficient sample deposition on the grid. Each TEM grid is individually glow discharged right before sample deposition. After sample deposition, the grid is rapidly vitrified by jets of cryogen followed by submersion into a cryogen bath (Ravelli et al., 2020). For this new technique, a new aggregation assay of Atx3 was prepared and samples were vitrified at Maastricht University, Maastricht, Netherlands.

As expected, NB05 was able to alter Atx3 aggregation (Figure 15) and no observable fibrils are seen in this sample. Therefore, these samples were treated for SPA and large data sets were collected. In Figure 15 we can see two example images from Atx3 13Q with NB05 (96 hours at 37 ºC) data sets. These images were already

aligned and corrected. Currently several automatic particle picking algorithms were used, like Xmipp3 (De la Rosa-Trevín et al., 2013) and sphire-CRYOLO (Wagner et al., 2019) using different box sizes, but unfortunately no good 2D classification was obtained. Currently we are testing cryoSPARC (Punjani, Rubinstein, Fleet, & Brubaker, 2017) in hope to get a better outcome.

Figure 15 – Effects of NB05 in Atx3 13Q aggregation. Cryo-EM images of assay endpoint (96 h, 37 ºC) of Atx3 13Q in the presence of NB05 (1:5 ratio). Sample vitrification was obtained by using VitroJet technology.

3.4 Discussion

To visualize the morphologies of the aggregated species formed along the Atx3 aggregation pathway, we have optimized a negative staining method that allow us to study Atx3 aggregation by TEM. For the first time we visualized Atx3 protofibrils and SDS-resistant fibrils by cryo-EM. We also obtained preliminary cryo-EM data on the morphological changes induced by a Atx3-binding nanobody on Atx3 fibrils.

The first challenge was to obtain a clear TEM image of Atx3 aggregation samples, mostly by changing the sample buffer. It is known that uranyl acetate should not be used in samples diluted in phosphate buffer (Harris, 2007) because it induces precipitation and deposition of phosphate salts in the specimen/grid. We were able to tackle this problem by: changing Atx3 aggregation buffer from phosphate buffer to HEPES buffer and introducing three washing steps between sample deposition and applying the staining agent. Although changing the buffer alone helped clear most of the background noise (Figure 6), sample deposition was suboptimal. This was greatly improved by glow discharge of the TEM grid, which increases the hydrophilicity of the carbon coated grid (Dubochet et al., 1971) ensuring a more even sample distribution (Figure 8). Next, we tested several compounds routinely used for negative staining: uranyl acetate, uranyl formate, phosphotungstic acid and NanoVan™ (a vanadium based commercial solution). In our tests, both phosphotungstic acid and NanoVan™ did not yield good quality images for our Atx3 samples but both uranyl acetate and uranyl formate worked very well (Figure 8). Since uranyl acetate and uranyl formate have fine grain sizes (4 – 5 Å) as compared to phospho-tungstates (8 – 9 Å) (Scarff et al., 2018), have lower pH and possess fixative properties this could be the explanation why they worked better in our samples. Since both contrast agents worked very well with Atx3 samples and uranyl acetate is stable for many months after preparation, in contrast to uranyl formate, we decided to favour the utilization of uranyl acetate in our negative staining protocols. Despite the versatility of negative staining, not all biological samples can be visualized using this technique. Samples can collapse or disassemble when adsorbed, cannot be dried on the grid, can flatten on the grid or induced preferred orientation on the support film (Rames et al., 2014; Scarff et al., 2018). Negative staining is a valuable tool and should be always performed prior to cryo-EM analysis and its outcome is highly sample dependent. Therefore, the best approach is trial and error than following a fixed protocol.

After visualizing with great detail fibrils from non-expanded and expanded Atx3 forms using negative staining, we were able to perform a time-course analysis by cryo-EM. The structures of several amyloid fibrils have been determined by Cryo-EM at

resolutions ranging between 25 Å (Jimenez et al., 1999) and 3.2 Å (Fitzpatrick et al., 2017). Some examples are the SRC Homology Domain (SH3) (Jimenez et al., 1999), the prion protein (Tattum et al., 2006), amyloid-β 1-40 (Sachse et al., 2008), α-synuclein (Y. Li et al., 2018), mutant huntingtin exon1 and polyQ aggregates (Galaz-Montoya, Shahmoradian, Shen, Frydman, & Chiu, 2021) and *ex vivo* tau (Fitzpatrick et al., 2017), where the large structural diversity of amyloid structures is evident. However, most of them have a repetitive pattern of its structural feature, the cross-β fold (Iadanza et al., 2018). Although we expect Atx3 fibrils to have similar cross-β fold, these fibrils are twisted and fold themselves, a challenge to identify repetitive patterns and apply more straight forward algorithms for particle selection and averaging. A SPA of these structures did not reveal apparent repetitive motifs, therefore, we changed our approach to cryo-ET for the analysis of Atx3 fibril structures.

Cryo-ET is a robust technique to obtain the structures of large flexible macromolecular complexes (Turk & Baumeister, 2020). It is greatly used in *in situ* context but also to study small objects such as virus, amyloid fibrils, nuclear pore complexes, vesicles and flagellar motors (Chang et al., 2020; Galaz-Montoya et al., 2021; Grunewald et al., 2003; Mattei, Glass, Hagen, Kräusslich, & Briggs, 2016; Schur et al., 2016; Turk & Baumeister, 2020; Wan et al., 2017). We collected several cryo-ET images at different time points of Atx3 aggregation for both non-expanded and expanded variants. To this point we were only able to align and mount the tomograms, but the next steps to build a model of the fibril structures from the tomograms are ongoing. Afterwards, we will apply subtomogram averaging, that consists of extracting subtomograms from the tomogram, which will then be aligned and averaged to obtain a higher 3D resolution structure (Briggs, 2013) a similar approach used by Galaz-Montoya et al. (2021) to obtain topological insights of mutant huntingtin exon1 and polyQ aggregates.

Interestingly, our cryo-EM data of Atx3 samples in the presence of nanobodies confirmed that no fibrillar structures were formed (Figure 15), and for these samples data sets for SPA were collected. Data analysis is still ongoing but from these data sets we expect to obtain a structure of the Ax3:NB05 complex. Since the presence of nanobodies disrupts protein aggregation, this could be innovative information on alternative oligomeric species formed during the Atx3 aggregation pathway in the presence of this nanobody.

Further work will be tomogram reconstruction and subtomogram averaging for both non-expanded and expanded Atx3 fibrils and SPA of both non-expanded and expanded Atx3 in the presence of NB05.

3.5 References

Bai, X.-c., Fernandez, I. S., McMullan, G., & Scheres, S. H. (2013). Ribosome structures to near-atomic resolution from thirty thousand cryo-EM particles. *Elife, 2*, e00461.

Bai, X.-C., McMullan, G., & Scheres, S. H. (2015). How cryo-EM is revolutionizing structural biology. *Trends in biochemical sciences, 40*(1), 49-57.

Brenner, S., & Horne, R. (1959). A negative staining method for high resolution electron microscopy of viruses. *Biochimica et biophysica acta, 34*, 103-110.

Briggs, J. A. (2013). Structural biology in situ—the potential of subtomogram averaging. *Current opinion in structural biology, 23*(2), 261-267.

Burgess, S. A., Walker, M. L., Thirumurugan, K., Trinick, J., & Knight, P. J. (2004). Use of negative stain and single-particle image processing to explore dynamic properties of flexible macromolecules. *Journal of Structural Biology, 147*(3), 247-258.

Carroni, M., & Saibil, H. R. (2016). Cryo electron microscopy to determine the structure of macromolecular complexes. *Methods, 95*, 78-85.

Chang, Y., Zhang, K., Carroll, B. L., Zhao, X., Charon, N. W., Norris, S. J., . . . Liu, J. (2020). Molecular mechanism for rotational switching of the bacterial flagellar motor. *Nature structural & molecular biology, 27*(11), 1041-1047.

De la Rosa-Trevín, J., Otón, J., Marabini, R., Zaldívar, A., Vargas, J., Carazo, J., & Sorzano, C. (2013). Xmipp 3.0: an improved software suite for image processing in electron microscopy. *Journal of Structural Biology, 184*(2), 321-328.

do Carmo Costa, M., & Paulson, H. L. (2012). Toward understanding Machado–Joseph disease. *Progress in neurobiology, 97*(2), 239-257.

Dubochet, J., Ducommun, M., Zollinger, M., & Kellenberger, E. (1971). A new preparation method for dark-field electron microscopy of biomacromolecules. *Journal of ultrastructure research, 35*(1-2), 147-167.

Ellisdon, A. M., Pearce, M. C., & Bottomley, S. P. (2007). Mechanisms of ataxin-3 misfolding and fibril formation: kinetic analysis of a disease-associated polyglutamine protein. *J Mol Biol, 368*(2), 595-605. doi:10.1016/j.jmb.2007.02.058

Ellisdon, A. M., Thomas, B., & Bottomley, S. P. (2006). The two-stage pathway of ataxin-3 fibrillogenesis involves a polyglutamine-independent step. *Journal of Biological Chemistry, 281*(25), 16888-16896.

Evangelisti, E., Cascella, R., Becatti, M., Marrazza, G., Dobson, C. M., Chiti, F., . . . Cecchi, C. (2016). Binding affinity of amyloid oligomers to cellular membranes is a generic indicator of cellular dysfunction in protein misfolding diseases. *Scientific reports, 6*(1), 1-14.

Fitzpatrick, A. W., Falcon, B., He, S., Murzin, A. G., Murshudov, G., Garringer, H. J., . . . Scheres, S. H. (2017). Cryo-EM structures of tau filaments from Alzheimer's disease. *Nature, 547*(7662), 185-190.

Galaz-Montoya, J. G., Shahmoradian, S. H., Shen, K., Frydman, J., & Chiu, W. (2021). Cryo-electron tomography provides topological insights into mutant huntingtin exon 1 and polyQ aggregates. *Communications Biology, 4*(1), 1-9.

Gales, L., Cortes, L., Almeida, C., Melo, C. V., do Carmo Costa, M., Maciel, P., . . . Macedo-Ribeiro, S. (2005). Towards a structural understanding of the fibrillization pathway in Machado-Joseph's disease: trapping early oligomers of non-expanded ataxin-3. *Journal of molecular biology, 353*(3), 642-654.

Glabe, C. G. (2006). Common mechanisms of amyloid oligomer pathogenesis in degenerative disease. *Neurobiology of aging, 27*(4), 570-575.

Glabe, C. G., & Kayed, R. (2006). Common structure and toxic function of amyloid oligomers implies a common mechanism of pathogenesis. *Neurology, 66*(1 suppl 1), S74-S78.

Gras, S. L., Waddington, L. J., & Goldie, K. N. (2011). Transmission electron microscopy of amyloid fibrils. In *Protein Folding, Misfolding, and Disease* (pp. 197-214): Springer.

Grunewald, K., Desai, P., Winkler, D. C., Heymann, J. B., Belnap, D. M., Baumeister, W., & Steven, A. C. (2003). Three-dimensional structure of herpes simplex virus from cryo-electron tomography. *Science, 302*(5649), 1396-1398.

Guo, Q., Huang, B., Cheng, J., Seefelder, M., Engler, T., Pfeifer, G., . . . Maurer, M. (2018). The cryo-electron microscopy structure of huntingtin. *Nature, 555*(7694), 117-120.

Hagen, W. J., Wan, W., & Briggs, J. A. (2017). Implementation of a cryo-electron tomography tilt-scheme optimized for high resolution subtomogram averaging. *Journal of Structural Biology, 197*(2), 191-198.

Harding, R. J., Deme, J. C., Hevler, J. F., Tamara, S., Lemak, A., Cantle, J. P., . . . Arrowsmith, C. H. (2021). Huntingtin structure is orchestrated by HAP40 and shows a polyglutamine expansion-specific interaction with exon 1. *Commun Biol, 4*(1), 1374. doi:10.1038/s42003-021-02895-4

Harris, J. R. (2007). Negative staining of thinly spread biological samples. In *Electron Microscopy* (pp. 107-142): Springer.

Herzik, M. A., Wu, M., & Lander, G. C. (2019). High-resolution structure determination of sub-100 kDa complexes using conventional cryo-EM. *Nature communications, 10*(1), 1-9.

Hutchings, J., & Zanetti, G. (2018). Fine details in complex environments: the power of cryo-electron tomography. *Biochemical Society Transactions, 46*(4), 807-816.

Iadanza, M. G., Jackson, M. P., Hewitt, E. W., Ranson, N. A., & Radford, S. E. (2018). A new era for understanding amyloid structures and disease. *Nature Reviews Molecular Cell Biology, 19*(12), 755-773.

Jimenez, J. L., Guijarro, J. I., Orlova, E., Zurdo, J., Dobson, C. M., Sunde, M., & Saibil, H. R. (1999). Cryo-electron microscopy structure of an SH3 amyloid fibril and model of the molecular packing. *The EMBO journal, 18*(4), 815-821.

Kawaguchi, Y., Okamoto, T., Taniwaki, M., Aizawa, M., Inoue, M., Katayama, S., . . . Akiguchi, I. (1994). CAG expansions in a novel gene for Machado-Joseph disease at chromosome 14q32. 1. *Nature genetics, 8*(3), 221-228.

Koning, R. I., Vader, H., van Nugteren, M., Grocutt, P. A., Yang, W., Renault, L. L., . . . Schwertner, M. (2022). Automated vitrification of cryo-EM samples with controllable sample thickness using suction and real-time optical inspection. *Nature communications, 13*(1), 1-10.

Kremer, J. R., Mastronarde, D. N., & McIntosh, J. R. (1996). Computer visualization of three-dimensional image data using IMOD. *Journal of Structural Biology, 116*(1), 71-76.

Kühlbrandt, W. (2014). The resolution revolution. *Science, 343*(6178), 1443-1444.

Lashuel, H. A., Petre, B. M., Wall, J., Simon, M., Nowak, R. J., Walz, T., & Lansbury Jr, P. T. (2002). α-Synuclein, especially the Parkinson's disease-associated mutants, forms pore-like annular and tubular protofibrils. *Journal of molecular biology, 322*(5), 1089-1102.

Li, X., Mooney, P., Zheng, S., Booth, C. R., Braunfeld, M. B., Gubbens, S., . . . Cheng, Y. (2013). Electron counting and beam-induced motion correction enable near-atomic-resolution single-particle cryo-EM. *Nature methods, 10*(6), 584-590.

Li, Y., Zhao, C., Luo, F., Liu, Z., Gui, X., Luo, Z., . . . Li, X. (2018). Amyloid fibril structure of α-synuclein determined by cryo-electron microscopy. *Cell research, 28*(9), 897-903.

Masino, L., Nicastro, G., De Simone, A., Calder, L., Molloy, J., & Pastore, A. (2011). The Josephin domain determines the morphological and mechanical properties of ataxin-3 fibrils. *Biophysical journal, 100*(8), 2033-2042.

Masino, L., Nicastro, G., Menon, R. P., Dal Piaz, F., Calder, L., & Pastore, A. (2004). Characterization of the structure and the amyloidogenic properties of the Josephin domain of the polyglutamine-containing protein ataxin-3. *Journal of molecular biology, 344*(4), 1021-1035.

Mastronarde, D. N. (2005). Automated electron microscope tomography using robust prediction of specimen movements. *Journal of Structural Biology, 152*(1), 36-51.

Mattei, S., Glass, B., Hagen, W. J., Kräusslich, H.-G., & Briggs, J. A. (2016). The structure and flexibility of conical HIV-1 capsids determined within intact virions. *Science, 354*(6318), 1434-1437.

Punjani, A., Rubinstein, J. L., Fleet, D. J., & Brubaker, M. A. (2017). cryoSPARC: algorithms for rapid unsupervised cryo-EM structure determination. *Nature methods, 14*(3), 290-296.

Rames, M., Yu, Y., & Ren, G. (2014). Optimized negative staining: a high-throughput protocol for examining small and asymmetric protein structure by electron microscopy. *JoVE (Journal of Visualized Experiments)*(90), e51087.

Ravelli, R. B., Nijpels, F. J., Henderikx, R. J., Weissenberger, G., Thewessem, S., Gijsbers, A., . . . Peters, P. J. (2020). Cryo-EM structures from sub-nl volumes using pin-printing and jet vitrification. *Nature communications, 11*(1), 1-9.

Sachse, C., Fändrich, M., & Grigorieff, N. (2008). Paired β-sheet structure of an Aβ (1-40) amyloid fibril revealed by electron microscopy. *Proceedings of the National Academy of sciences, 105*(21), 7462-7466.

Scarff, C. A., Almeida, B., Fraga, J., Macedo-Ribeiro, S., Radford, S. E., & Ashcroft, A. E. (2015). Examination of ataxin-3 (atx-3) aggregation by structural mass spectrometry techniques: a rationale for expedited aggregation upon polyglutamine (polyQ) expansion. *Molecular & Cellular Proteomics, 14*(5), 1241-1253.

Scarff, C. A., Fuller, M. J., Thompson, R. F., & Iadanza, M. G. (2018). Variations on negative stain electron microscopy methods: tools for tackling challenging systems. *JoVE (Journal of Visualized Experiments)*(132), e57199.

Scarff, C. A., Sicorello, A., Tomé, R. J., Macedo-Ribeiro, S., Ashcroft, A. E., & Radford, S. E. (2013). A tale of a tail: Structural insights into the conformational properties of the polyglutamine protein ataxin-3. *International Journal of Mass Spectrometry, 345*, 63-70.

Scheres, S. H. (2012). RELION: implementation of a Bayesian approach to cryo-EM structure determination. *Journal of Structural Biology, 180*(3), 519-530.

Schur, F. K., Obr, M., Hagen, W. J., Wan, W., Jakobi, A. J., Kirkpatrick, J. M., . . . Briggs, J. A. (2016). An atomic model of HIV-1 capsid-SP1 reveals structures regulating assembly and maturation. *Science, 353*(6298), 506-508.

Tattum, M. H., Cohen-Krausz, S., Khalili-Shirazi, A., Jackson, G. S., Orlova, E. V., Collinge, J., . . . Saibil, H. R. (2006). Elongated oligomers assemble into mammalian PrP amyloid fibrils. *Journal of molecular biology, 357*(3), 975-985.

Thompson, R. F., Walker, M., Siebert, C. A., Muench, S. P., & Ranson, N. A. (2016). An introduction to sample preparation and imaging by cryo-electron microscopy for structural biology. *Methods, 100*, 3-15.

Turk, M., & Baumeister, W. (2020). The promise and the challenges of cryo-electron tomography. *FEBS letters, 594*(20), 3243-3261.

Wagner, T., Merino, F., Stabrin, M., Moriya, T., Antoni, C., Apelbaum, A., . . . Prumbaum, D. (2019). SPHIRE-crYOLO is a fast and accurate fully automated particle picker for cryo-EM. *Communications Biology, 2*(1), 1-13.

Wan, W., Kolesnikova, L., Clarke, M., Koehler, A., Noda, T., Becker, S., & Briggs, J. A. (2017). Structure and assembly of the Ebola virus nucleocapsid. *Nature, 551*(7680), 394-397.

Winner, B., Jappelli, R., Maji, S. K., Desplats, P. A., Boyer, L., Aigner, S., . . . Campioni, S. (2011). In vivo demonstration that α-synuclein oligomers are toxic. *Proceedings of the National Academy of sciences, 108*(10), 4194-4199.

Chapter 4 - A drug repurposing approach to identify Ataxin-3 aggregation inhibitors

Francisco Figueiredo, Zsuzsa Sárkány, Tiago Silva, Alexandra Silva, Pedro Brites, Pedro Martins, Sandra Macedo Ribeiro

4.1 Introduction

Machado-Joseph disease (MJD), also known as Spinocerebellar Ataxia Type 3 is an inherited autosomal dominant neurodegenerative disorder. MJD is a progressive disorder of late-onset, caused by expansion of an unstable CAG repeat in the coding region of the *ATXN3* gene, which is translated into an expanded polyglutamine (polyQ) tract in the protein ataxin-3 (Atx3). Neuronal inclusions rich in mutated and expanded protein are identified in brain autopsies of MJD patients (Lieberman, Shakkottai, & Albin, 2019). With currently no available treatment options for MJD patients, scientists have been working extensively to develop new therapies for the treatment of MJD.

Currently there are three ongoing clinical trials that include MJD patients. Clinical trial NCT03701399 is testing Troriluzole for treating several neurological disorders, including MJD. Troriluzole is a chemical compound that modulates glutamate, an excitatory neurotransmitter. Recently a statement regarding this clinical trial revealed that patients experienced clinically meaningful improvements in ataxia symptoms on Troriluzole treatment. Clinical trial NCT03378414 proposes to use Umbilical Cord Mesenchymal Stem Cells therapy for SCA patients. These cells are isolated and cultured from umbilical cord and possess several characteristics such as: highly self-renewal, multi-directional differentiation potential and low immunogenicity (Shang, Guan, & Zhou, 2021). However, this clinical trial as not started yet. Lastly, clinical trial NCT05160558 is currently recruiting patients and proposes to use Anti-Sense Oligonucleotide (ASO) that were developed to target *ATXN3* pre-mRNA which in theory, should reduce levels of mutant Atx3 protein. ASO approach is already used for the treatment of spinal muscular atrophy (Chiriboga, 2017) and also tested in clinical trials for Huntington's disease (HD) (NCT03342053 and NCT03761849). Scientists have not reached a consensus about the mechanism of MJD pathogenesis and neither in identifying which are the toxic aggregates present in MJD (L.-B. Li, Yu, Teng, & Bonini, 2008; McGowan et al., 2000; McLoughlin, Moore, & Paulson, 2020; Paulson, Shakkottai, Clark, & Orr, 2017). Because of this extremely complex disease mechanism, it has been difficult to find a successful therapy that treated MJD symptoms without compromising other universal cell functions (Costa, 2020; McLoughlin et al., 2020). At the moment MJD therapies are all symptom-directed and limited (Chen, Hong, Lin, & Harn, 2020; Costa, 2020; Da Silva, Teixeira-Castro, & Maciel, 2019). The type of treatment available for MJD patients depends on the clinical subtype of disease, symptoms and associated comorbidities (D'Abreu, Franca, Paulson, & Lopes-Cendes, 2010; Matos, de Almeida, & Nobrega, 2019). Therefore, it is urgent to develop new therapies that could delay or stop the progression of this fatal disease.

The development of a novel, effective and safe compound that could be suitable for the treatment of diseases is time-consuming and very expensive. Repurposing drugs already approved for the treatment of other conditions/diseases could be an effective way to broaden the available options to treat rare diseases, such as MJD. The advantage of repurposing approved drugs is that they have already been tested for human safety, their modes of action and possible side effects are known (Ashburn & Thor, 2004; Liu et al., 2022). This shortens drug development time and allows to drugs quickly enter in the clinic/market. Several drug repurposing assays to find compounds that could eliminate or inhibit toxic protein aggregates in the context of neurodegenerative diseases have already been made (Hideshima et al., 2022; Liu et al., 2022; Sant'Anna et al., 2016; Socias et al., 2018). Zileuton is a drug used for the treatment of asthma showed that it could reduce amyloid-β deposition and decrease Tau phosphorylation in mice (Giannopoulos, Chiu, & Praticò, 2018). Squalamine is a natural anticancer and antiviral drug that showed that could prevent the production of α-synuclein aggregates (Collier et al., 2017). Thioridazine is used for schizophrenia and was discovered that in cellular and *Drosophila* Amyotrophic Lateral Sclerosis (ALS) models could enhance clearance of TDP-43 aggregates (Cragnaz et al., 2021). Genistein which has antitumor and antibacterial activity showed that it could reduce accumulation of mutant huntingtin aggregates in fibroblasts from HD patients (Pierzynowska, Gaffke, Cyske, & Węgrzyn, 2019). These are just some examples of drug repurposing compounds in the context of neurodegenerative diseases. A review from Socias et al. (2018) explained how many antibiotics that can pass the Blood-Brain Barrier (BBB) could be some excellent candidates to be used as an anti-amyloidogenic effect for several neurodegenerative disorders. Drug repurposing has led to novel treatments for other types of diseases such as stress urinary incontinence, premature ejaculation, breast cancer, myeloma, and fibromyalgia, among other examples (Ashburn & Thor, 2004; Padhy & Gupta, 2011; Sleigh & Barton, 2010).

In this work we evaluated a commercial library of 1280 approved compounds to look for a promising candidate for future drug repositioning. We used our optimized Thioflavin-T (ThT) assay (detailed in Chapter 2) for a high-throughput screening to select four different compounds - Ciclopirox Ethanolamine, Pentetic Acid, Dopamine and Tolcapone. The effectiveness of these four compounds was evaluated by combining Transmission Electron Microscopy (TEM) with Size Exclusion Chromatography (SEC) and Dynamic Light Scattering (DLS). By using different complementary techniques at the same time we increased the robustness of our results.

These *in vitro* results provided a base stone to start our *in vivo* assays using a *Drosophila* model of MJD and primary neuronal cell cultures.

4.2 Materials and methods

4.2.1 Protein expression and purification

Both Atx3 isoforms were expressed and purified as previously described in Chapter 2. Briefly, the pDEST17-ATX3(13Q) plasmid was transformed into *E. coli* BL21(DE3)-SI cells (Life Technologies). Cells were grown at 37 ºC, 180 rpm, in Luria Broth (LB) medium without NaCl supplemented with 100 $\mu g.mL^{-1}$ of ampicillin and 0.4 % (w/v) glucose until OD_{600nm} reached 0.8. The culture was then cooled to 30 ºC and protein expression was induced with 300 mM NaCl. After 3 hours of expression, the cells were harvested by centrifugation and resuspended in buffer A (20 mM sodium phosphate pH 7.5, 600 mM NaCl, 2.5 % (v/v) glycerol, 20 mM imidazole) containing 100 $\mu g.L^{-1}$ lysozyme. Cells were disrupted by stirring 1 hour on ice in the presence of 0.02 $mg.mL^{-1}$ DNase, 0.02 $mg.mL^{-1}$ RNase, 1mM $MgCl_2$ and 1 mM PMSF. After centrifugation supernatant was loaded into a pre-equilibrated Ni^{2+} charged IMAC column (GE Healthcare Life Sciences) and protein was eluted with 250mM of imidazole. Then, loaded into a HiPrep 26/60 Sephacryl S-300 HR column (GE Healthcare Life Sciences) equilibrated with purification buffer (20 mM sodium phosphate pH 7.5, 200 mM NaCl, 5 % (v/v) glycerol, 2 mM EDTA, 1 mM DTT). After SDS-PAGE analysis, fractions corresponding to Atx3 were pooled and concentrated on an Amicon Ultra-15 centrifuge filter (Millipore) to 20-30 $mg.mL^{-1}$, frozen in liquid nitrogen and stored at -80 ºC. Before each aggregation assay, purified Atx3 aliquots were applied to a Superose 12 10/300 GL column (GE Healthcare Life Sciences) pre-equilibrated with aggregation buffer (20 mM HEPES pH 7.5, 150 mM NaCl and 1 mM DTT). Protein elution was monitored at 280 nm and the concentration of the fractions corresponding to monomeric protein was determined by measuring the absorbance at 280 nM and using protein's coefficients, 31650 $M^{-1}.cm^{-1}$.

4.2.2 Thioflavin T aggregation kinetics

Atx3 aggregation was monitored by following the increase in thioflavin T (ThT) fluorescence at 480 nm (440 nm excitation) on the CHAMELEON V plate reader (HIDEX) using a 384-well microplate (low flange, black, flat bottom, polystyrene; Corning, Kennebunk, ME). Briefly, 50 µL samples of Atx3 at 3 µM in aggregation buffer containing

15 µM ThT were incubated at 37 ºC and ThT fluorescence was measured every 30 min for approximately 48h. To prevent evaporation, 20 µL of paraffin oil was put in each reaction well with an automatic multichannel pipette (Eppendorf Xplorer, ref 4861000120).

4.2.3 Compound screening and dose response assay

To identify inhibitors of Atx3 aggregation we used the commercial Prestwick Chemical Library (Illkirch) containing 1280 drug repurposing compounds. Protein was dispensed into a 384-well microplate with an automatic multichannel pipette (Eppendorf). Then an automated liquid handler (JANUS Automated Workstation; PerkinElmer) equipped with pin tool replicators (V&P Scientific) coupled to a Modular Dispense Technology (MDT) head was used to add 0.1 µL of test compounds (from a 1 mM stock) or DMSO (for controls). A total of four 384-well microplates were filled, each plate testing 320 chemical compounds (1 compound per well) and running 32 control reactions in the presence of DMSO. The final reaction mixture contained 3 µM of Atx3 13Q and 2 µM of test compound/DMSO.

Dose response studies were performed using only the compounds that were selected in the screening with both Atx3 isoforms and in the same protein concentration used before (3 µM). Stock solution of each compound was prepared at 40 µM and a series of serial-diluted compound concentrations were made in order to obtain 12 different tested concentrations: 20, 10, 5, 2.5, 1.25, 0.63, 0.31, 0.16, 0.08, 0.04, 0.02 and 0.01 µM. For control it was used the same scheme with a 0.4 % (v/v) stock solution of DMSO. All serial dilutions were prepared using the automatic multichannel pipette - Eppendorf Xplorer, ref 4861000120 (Eppendorf) and three replicas were made per condition.

4.2.4 Transmission electron microscopy

For visualization of protein fibers/aggregates by TEM protein samples collected at different time points of the Atx3 aggregation assay were diluted 5-fold in water and adsorbed onto glow-discharged, carbon-coated films supported on 300-mesh nickel grids and negatively stained with 1 % (w/v) uranyl acetate, using a protocol adapted from (Rames, Yu, & Ren, 2014). Grids were visualized using a JEM-1400 (JEOL) TEM at an accelerating voltage of 80 kV.

4.2.5 Atx3 oligomerization analysis by size exclusion chromatography

Atx3 samples (1 mL at 3 µM) were incubated in aggregation buffer without ThT for 96 hours at 37 ºC without shaking. At different time points (approximately 0, 24, 48 and 72 hours), 100 µL aliquots were collected, filtered and injected in a Superdex 200 Increase 5/150 GL column (GE Healthcare Life Sciences) using a 50 µL loop.

4.2.6 Dynamic light scattering

200 µL samples of 3 µM Atx3 in aggregation buffer were incubated in a UV-Cuvette micro cuvette (Brand) with a cap, maintained at a constant temperature of 37 ºC without shaking. At different time points (0, 24, 48, 72 and 96 hours) samples were taken to Zetasizer Nano ZS DLS system (Malvern Instruments) to make the molecular size measurements. At least three independent measurements were made for each sample at 25 ºC. The intensity size distribution obtained by dynamic light scattering is a plot of the relative intensity of light scattered by particles in different size classes. However, when there is more than one peak in this plot, the intensity size distribution must be converted to a volume size distribution for a more realistic view of the data (Stetefeld, McKenna, & Patel, 2016), as was the case for Atx3 protein samples. All data was analyzed using dynamic light scattering (nano) software (Malvern Instruments) to determine the polydispersity (P_D) and the mean hydrodynamic radius (R_H) values from the volume distributions, used to estimate the molecular weight (assuming globular protein) from a built-in empirical calibration graph.

4.2.7 Thermal shift assay

The melting temperature of Atx3 in the absence and in the presence of the different compounds was determined using the hydrophobic fluorescent dye SYPRO Orange. For each condition, 12.5 µL of SYPRO Orange 5000x (Invitrogen) diluted to 10x in Atx3 purification buffer were mixed with 12.5 µL of ataxin-3 at (0.8 mg mL^{-1}) and loaded in a white 96-well PCR plate, ref 04-082-9056 (NerbePlus). For all the conditions three replicates were prepared. The thermal shift assay was performed in an iCycler iQ5 Multicolor Real Time PCR detection system (Bio-Rad) running the following protocol: heating from 25 °C to 85 °C with a 30s hold time every 0.5 °C, followed by a fluorescence reading using Cy3 dye filter (excitation/emission, 545/585). Melting curves were analysed using the CFX Manager software (Bio-Rad) to calculate melting temperature (Tm) from the maximum value of the first derivative curve of the melting curve.

4.2.8 Primary cell culture protocol

Primary cultures were performed as described by Kaech and Banker (2006). Cortical neurons from seventeen to eighteen old C57BL/6 pups were used. Electroporation of cortical neurons was performed with a 4D-Nucleofector System (Westburg) at a cell density of at least 200.000 cells/condition and left in suspension for 1 hour at 37 ºC in 5 % CO_2. Culture medium was DMEM/F12 (Sigma-Aldrich, D8437) supplemented with 1× B27 (Gibco), 1% penicillin/streptomycin (Gibco), 2 mM L-glutamine (Gibco), and 50 ng/mL NGF (Millipore, 01-125). Subsequently cells were grown on 13 mm coverslips coated with poly-L-lysine (20 $\mu g.mL^{-1}$ - Sigma-Aldrich, P2636) and laminin (0.5 $\mu g.mL^{-1}$, Sigma-Aldrich L2020) for 24 to 96 hours, until fixing or imaging.

4.3 Results

4.3.1 Initial screening

Using the optimized ThT assay described and validated in Chapter 2, we screened the original 1280 compounds to find potential inhibitors of Atx3 13Q aggregation. Since ThT binding progress curves monitor the first step of Atx3 aggregation, common to Atx3 13Q and Atx3 77Q, we used Atx3 13Q for the initial compound screenings. Using this approach, we found 28 compounds that interfered with Atx3 13Q aggregation *in vitro (*Figure 1). Of these 28 compounds, 22 were able to completely suppress protein aggregation (Figure 1A) and 6 compounds delayed Atx3 aggregation (Figure 1B).

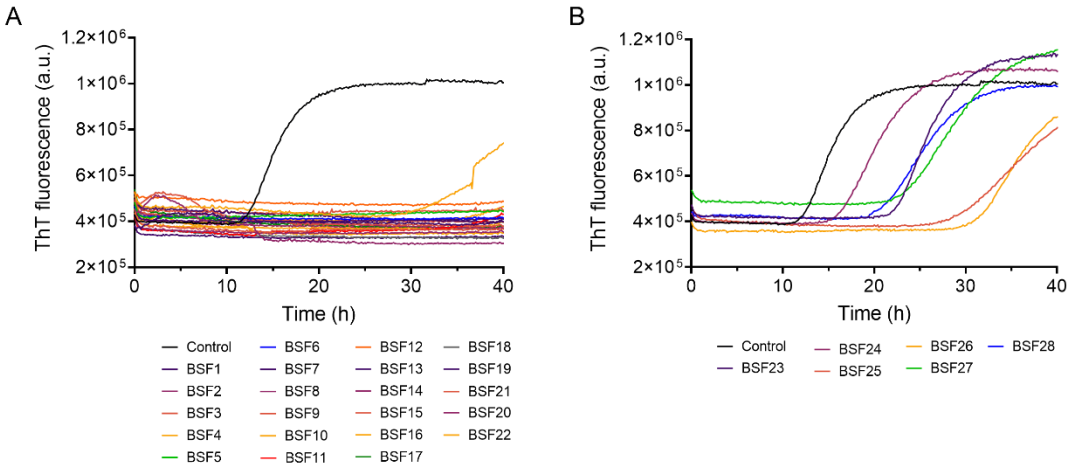

Figure 1 – Modulators of Atx3 13Q aggregation selected from the Prestwick Chemical Library screening. ThT assay to measure the formation of amyloid-like species in Atx3 13Q. **(A)** Compounds that suppress Atx3 13Q aggregation and **(B)** Compounds that delay Atx3 13Q aggregation. Control Atx3 13Q is the black line in both graphics. Curves represent the mean of

eight replicates for control condition and three replicates for each tested compound. Control condition is Atx3 13Q in the presence of 0.04 % (v/v) DMSO.

After the initial screening with Atx3 13Q, we tested if the selected compounds also modified the aggregation of the expanded Atx3 77Q (Figure 2). Using the same conditions in ThT assay we observed that only the BSF9 was able to inhibit Atx3 77Q *in vitro* (Figure 2A). BSF8 and BSF21 that previously inhibited Atx3 13Q aggregation, did not alter Atx3 77Q aggregation, in fact, their presence slightly accelerated aggregation. All other tested compounds delayed Atx3 77Q aggregation.

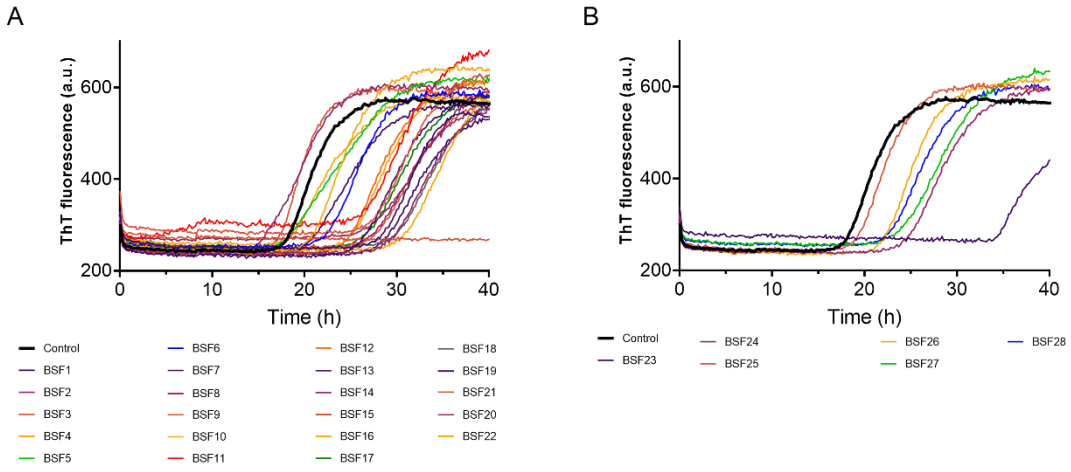

Figure 2 – Modulators of Atx3 77Q aggregation selected from the Prestwick Chemical Library screening. ThT assay to measure the formation of amyloid-like species in Atx3 77Q. **(A)** Compounds that previously suppressed normal Atx3 aggregation. **(B)** Compounds that delayed normal Atx3 aggregation. Control 77Q is the black bold line in both graphics. Curves represent the mean of twelve replicates for control condition and three replicates for each tested condition. Control condition is Atx3 77Q in the presence of 0.04 % (v/v) DMSO.

From the total of 28 compounds, 13 were selected based on different criteria (Table 1). Compounds that already existed in laboratory chemical data base were automatically selected for further studies. Next, since MJD is a neurologic disorder, we investigated which compounds could or could not cross the BBB, although for some of them no information was found. A final parameter taken into consideration was the chemical family to which they belong to. Compounds that had a unique mechanism of action or therapeutic usage were taken in consideration (such as BSF2 or BSF17). Since BSF11 is known to have neurotoxic properties, it was automatically excluded. BSF9 was the only compound from these preliminary tests that inhibited both non-expanded and expanded Atx3 aggregation, therefore, it was also automatically selected. Dose-response studies were then performed for the 13 selected compounds.

Table 1 – List of Atx3 aggregation modulators and their attributes. *From the conjugation of these three factors: availability in the laboratory, BBB permeability and the chemical family, we selected 13 compounds to further investigation.*

Compound	Availability	Can cross BBB	Family	Selected
BSF1	X	Possibly	Emetic	Yes
BSF2		No	Antifungal	Yes
BSF3	X	Probably not	Bronchodilator	Yes
BSF4			Diagnostic agent	No
BSF5		No	Central Nervous System	No
BSF6		Yes	Antihypertensor	Yes
BSF7		No	Central Nervous System	No
BSF8			Bronchodilator	No
BSF9			Diagnostic agent	Yes
BSF10		Yes	Chelating agent	Yes
BSF11		Yes, neurotoxic	Antiseptic	No
BSF12			Vasoconstrictor	No
BSF13			Bronchodilator	No
BSF14		Yes	Expectorant	Yes
BSF15	X	No	Cardiotonic	Yes
BSF16			Bronchodilator	No
BSF17			Dermatology	Yes
BSF18		No	Cardiovascular	No
BSF19	X	Yes	Central Nervous System	Yes
BSF20			Bronchodilator	No
BSF21		Yes	Antihypertensive	Yes
BSF22			Antiseptic	No
BSF23	X	Yes	Alcohol deterrent	Yes
BSF24			Adrenergic (ophthalmic)	No
BSF25		Probably not	Antibacterial	No
BSF26	X	Yes	Central Nervous System	Yes
BSF27			Antineoplastic	No
BSF28			Antipsoriatic	No

4.3.2 Dose-response assays

The inhibitory effect of the selected compounds on Atx3 aggregation was further characterized in dose-response studies using the ThT fluorescence assay and serial-

diluted compound concentrations ranging from 20 to 0.01 µM. The ThT kinetic curves for each tested compound are shown in Figure 2 for Atx3 13Q and Figure 3 for Atx3 77Q.

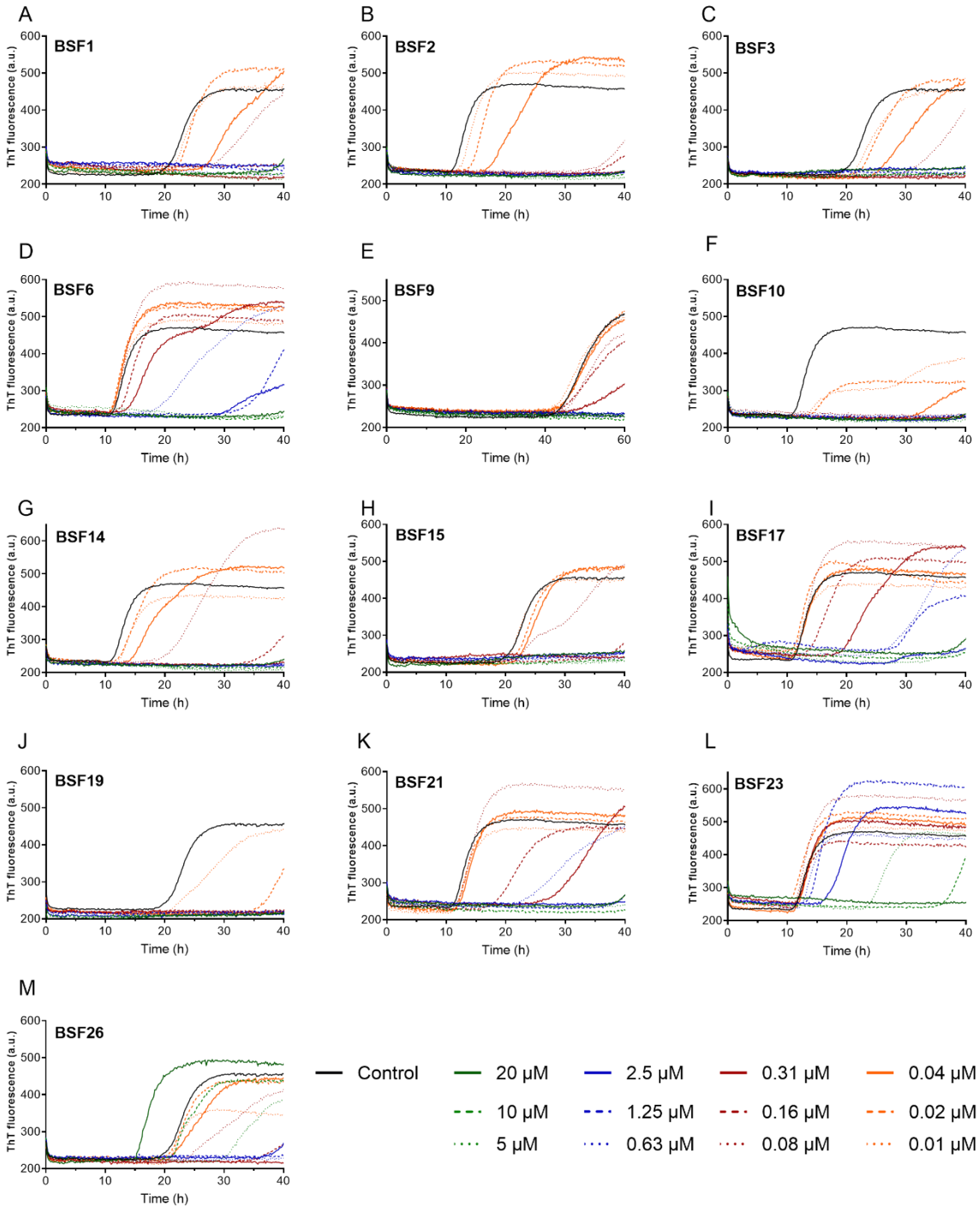

Figure 3 – Dose-response studies of the selected compounds on Atx3 13Q aggregation. ThT assay to measure the formation of amyloid-like species of Atx3 13Q in the presence of different concentrations of **(A)** BSF1, **(B)** BSF2, **(C)** BSF3, **(D)** BSF6, **(E)** BSF9, **(F)** BSF10, **(G)** BSF14, **(H)** BSF15, **(I)** BSF17, **(J)** BSF19, **(K)** BSF21, **(L)** BSF23 and **(M)** BSF26. Each curve represents the mean of three replicates for each tested condition. Control condition is Atx3 13Q in the presence of different DMSO concentrations, from 0.4 to 0.0004 % (v/v).

Overall, lower compound concentrations (0.01, 0.02 and 0.04 µM) had a weaker effect on inhibiting Atx3 13Q aggregation. However, BSF6, BSF17, BSF21, BSF23 and BSF26 (Figure 3D, I, L and M) did not have an effective dose response. The increase in compound concentration was not proportional to the inhibitory effect on Atx3 aggregation. Compounds BSF23 and BSF26 were compounds that only delayed Atx3 13Q aggregation and their efficacy was not increased by increasing concentrations. For these reasons they were not tested any further and removed from the dose response assay for Atx3 77Q (Figure 4).

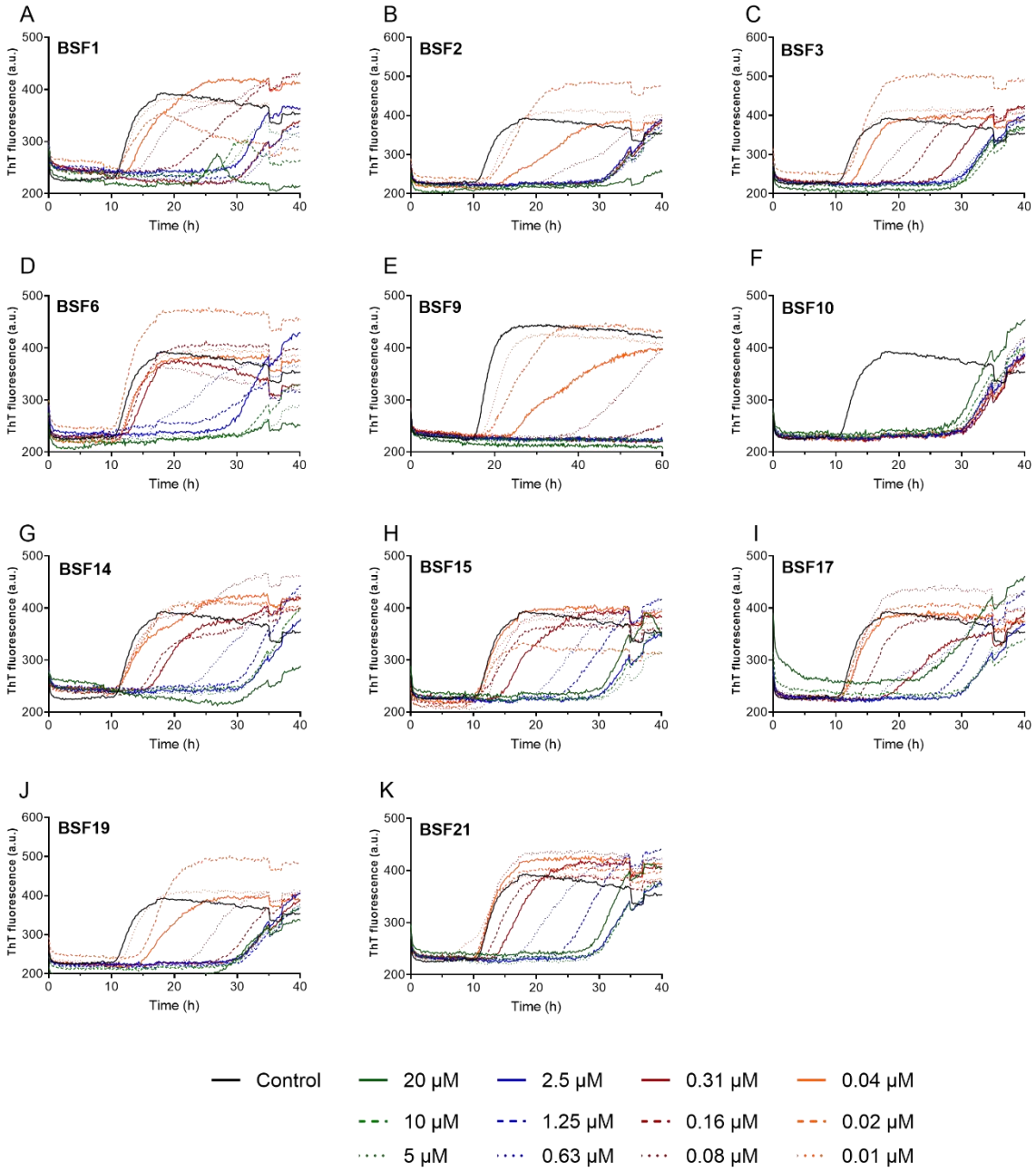

Figure 4 - **Dose-response studies of the selected compounds on Atx3 77Q aggregation.** ThT assay to measure the formation of amyloid-like species of Atx3 13Q in the presence of

different concentrations of **(A)** BSF1, **(B)** BSF2, **(C)** BSF3, **(D)** BSF6, **(E)** BSF9, **(F)** BSF10, **(G)** BSF14, **(H)** BSF15, **(I)** BSF17, **(J)** BSF19 and **(K)** BSF21. Each curve represents the mean of three replicates for each tested condition. Control condition is Atx3 77Q in the presence of different DMSO concentrations, from 0.4 to 0.0004 % (v/v).

As mentioned before, lower compound concentration had a smaller effect on inhibiting Atx3 aggregation and this was common to both non-expanded and expanded Atx3. However, it is important to note that some compounds have a better inhibitory result for Atx3 13Q than for Atx3 77Q. This is evident for BSF1, BSF3, BSF14 and BSF15. In the presence of these four compounds, Atx3 13Q only aggregated in low compound concentrations (< 0.31 µM), while in Atx3 77Q, aggregation could still be observable at higher concentrations, 10 µM. This result further supports the hypothesis that the polyQ region influences the self-assembly multistep mechanism of Atx3.

From all gathered data obtained so far, we decided to proceed our studies only with four different compounds whose structures are in depicted in Figure 5.

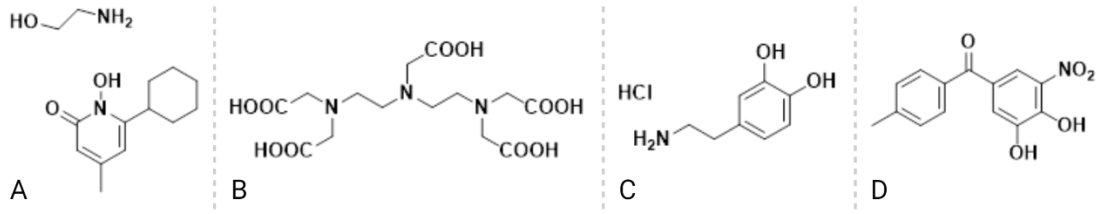

Figure 5 – The structure of the final four selected compounds from the Prestwick Chemical Library. (A) BSF2 – Ciclopirox Ethanolamine, **(B)** BSF9 – Pentetic Acid, **(C)** BSF15 – Dopamine Hydrochloride and **(D)** BSF19 – Tolcapone.

Because studying 13 distinct compounds with different techniques would require a lot of resources and time, we reduced the list to the final four: BF2 – Ciclopirox Ethanolamine, BSF9 – Pentetic Acid, BSF15 – Dopamine Hydrochloride and BSF19 – Tolcapone. Ciclopirox ethanolamine was selected because of its good *in vitro* inhibitory results on Atx3 aggregation and because its mechanism of action was different from the others. Pentetic Acid was an obvious choice, since it was the compound with best *in vitro* results for both Atx3 isoforms. Dopamine is an important neurotransmitter whose effect on protein aggregation is already studied in the context of other neurological disorders and Tolcapone is a compound already used for the treatment of other neurodegenerative diseases.

All tested compounds in the Prestwick Chemical Library are dissolved in DMSO and all controls presented in this work are of Atx3 protein with the same concentration of compound solvent. However, when performing dose response assay with Pentetic Acid, a change of solvent had to be made because of its chemical properties. Instead of dissolved in DMSO, stock solution of 10 mM was prepared in 0.05 M NaOH. As observed in Figure 6, both used concentrations of NaOH and DMSO did not alter aggregation. These conclusions were also validated in all used techniques, ThT, Transmission Electron Microscopy (TEM), Size Exclusion Chromatography (SEC) and Dynamic Light Scattering (DLS). Therefore, from here on we only present control data of Atx3 alone with DMSO or NaOH.

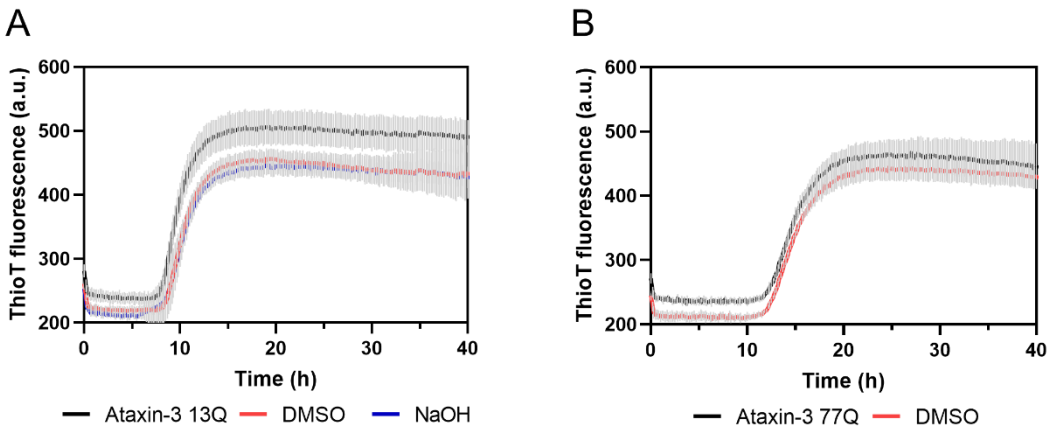

Figure 6 – Effect of solvents used to dissolve the compounds tested on Atx3 aggregation. ThT assay to measure the formation of amyloid-like species in **(A)** Atx3 13Q and **(B)** in the presence 0.04 % (v/v) DMSO and 25 µM of NaOH solvents. Curves represent the mean and standard deviation of eight replicas for each condition.

We were interested in studying how Atx3 aggregation is modulated by the presence of these four selected compounds. Because ThT assays are limiting, since they only display data for the first step of Atx3 aggregation (detailed discussion in Chapter 2) we must use other biophysical techniques to complement these findings. Therefore, we combined ThT fluorescence with TEM, SEC, DLS to do an in-depth evaluation.

By performing a time-course aggregation analysis using SEC and DLS we can evaluate how the size of Atx3 aggregates are changing over time. These two techniques are very distinct and provide different data. The principle for SEC experiments is that samples are injected into a SEC column that will separate particles by size, as detailed in Figure 7. Briefly, sample is filtered to remove all insoluble aggregates and then is

injected into a SEC column. After loading into a SEC column, sample passes through the column matrix which is made from a specific gel with spherical beads. Smaller-sized molecules elute last because the can access more pores that are created from the spherical beads. Since larger-sized molecules do not access so many pores, they elute faster as they spend less time in the column (Figure 7).

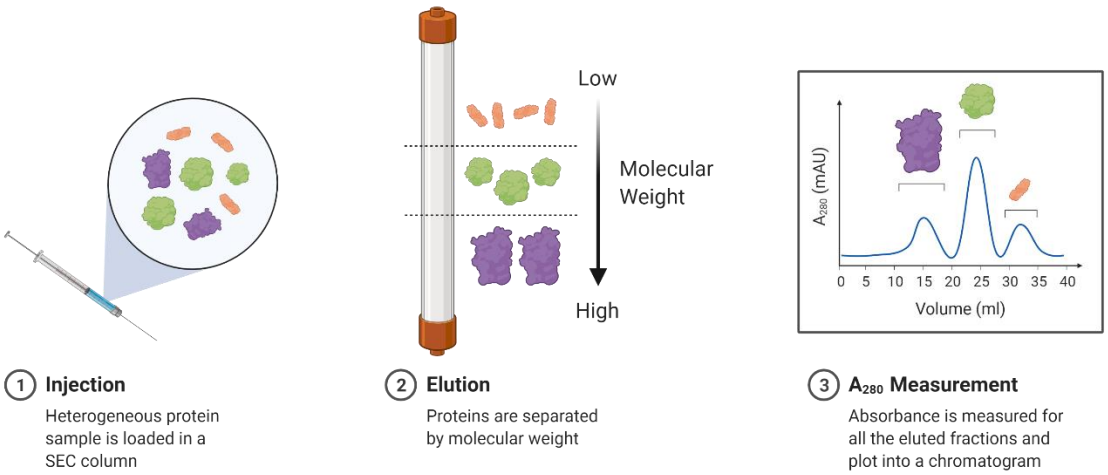

Figure 7 – Scheme of the Size Exclusion Chromatography principle. Protein is injected into a SEC column which separates samples by molecular weight. Larger samples elute first than smaller ones. Protein elution is monitored by absorbance at 280 nm.

DLS also provides insights on Atx3 aggregation since it can estimate particle size in solution. The principle behind this technique is that particles in solution are dispersed and move randomly in all directions. DLS equipment applies light source into the sample solution and then detects the scattering light from the sample (Stetefeld et al., 2016). From this scattering, the particle size can be estimate using following equation. Hydrodynamic radius (R_H) is calculated from the diffusion coefficient (D) using the Stokes-Einstein Equation 1, where *k* is the Boltzmann constant; *T* is the temperature, and η is the medium viscosity (Berne & Pecora, 2000):

$$R_H = k\,T / 6\,\pi\,\eta\,D$$

There are several methodologies to evaluate sample aggregation and in this work we use Size Distribution by Intensity and Size Distribution by Volume. We always present these two analysis because they are different and complement each other. Size Distribution by Intensity gives the amount of light that is scattered by each particle fraction while Size Distribution by Volume gives the total volume of particles in various particle fractions. If both Size Distributions are not presented, conclusions could be misleading, since scattering intensity depends on size macromolecules (on the 6th

power). Very few but large aggregates, will affect measurements (Stetefeld et al., 2016). By combining four different techniques we are increasing the robustness of our conclusions.

4.3.3 Ciclopirox Ethanolamine

Ciclopirox Ethanolamine is a broad-spectrum antifungal that can be used to treat superficial fungal and yeast infections, vaginal candidiasis, seborrheic dermatitis and onychomycosis (Gupta & Plott, 2004).

To monitor Atx3 aggregation, a ThT assay was made with at least 8 independent replicates (Figure 8). In the selected concentrations, Ciclopirox Ethanolamine was able to delay Atx3 aggregation in both expanded and non-expanded Atx3.

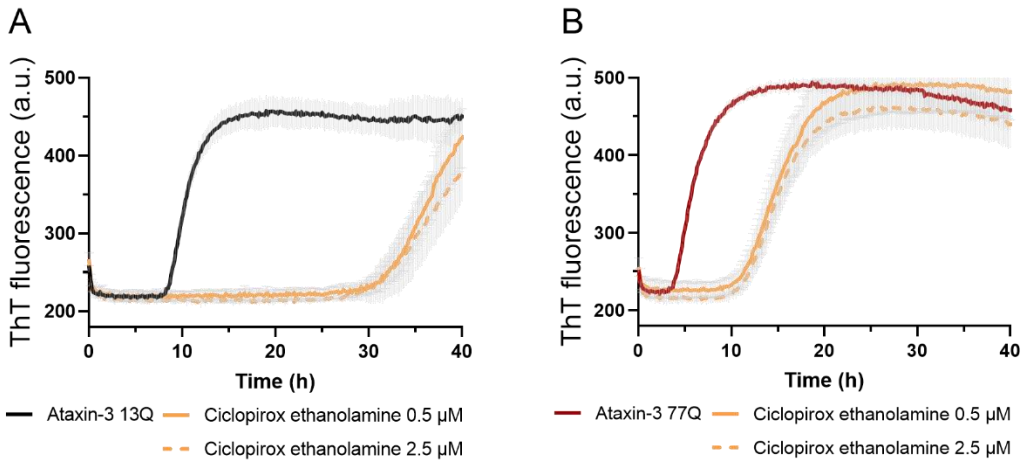

Figure 8 – Effect of Ciclopirox Ethanolamine on Atx3 aggregation kinetics. ThT assay to measure the formation of amyloid-like species in **(A)** Atx3 13Q and **(B)** Atx3 77Q aggregation in the presence of 0.5 and 2.5 µM Ciclopirox Ethanolamine. Curves represent the mean and standard deviation of eight replicates for each condition. Control condition are Atx3 isoforms in the presence of 0.04 % (v/v) DMSO.

Evaluation of the effect of Ciclopirox Ethanolamine by SEC (Figure 9 and 10) was performed at the same time as the ThT assay. SEC chromatograms are presented in Figure 9. For both Atx3 isoforms, Ciclopirox Ethanolamine was able to delay Atx3 aggregation. Control Atx3 13Q and Atx3 77Q aggregated in less than 20 hours as confirmed by SEC (Figure 9A, B). This is visible in Figure 10, where the areas of the peaks are presented, showing that the addition of Ciclopirox Ethanolamine stabilizes Atx3 monomers. High Molecular Weight (HMW) oligomers are the majority of observable species at 24h in both Atx3 controls (Figure 10A, B). In both tested concentrations,

Ciclopirox Ethanolamine was able to stabilize monomeric Atx3 for at least 20 hours (Figure 9C, D, E, F and Figure 10C, D, E, F), and only after 44 hours the peak corresponding to the monomeric Atx3 is shifted to the left, suggesting that all monomers are converted to HMW soluble aggregates (Figure 9C, D, E, F).

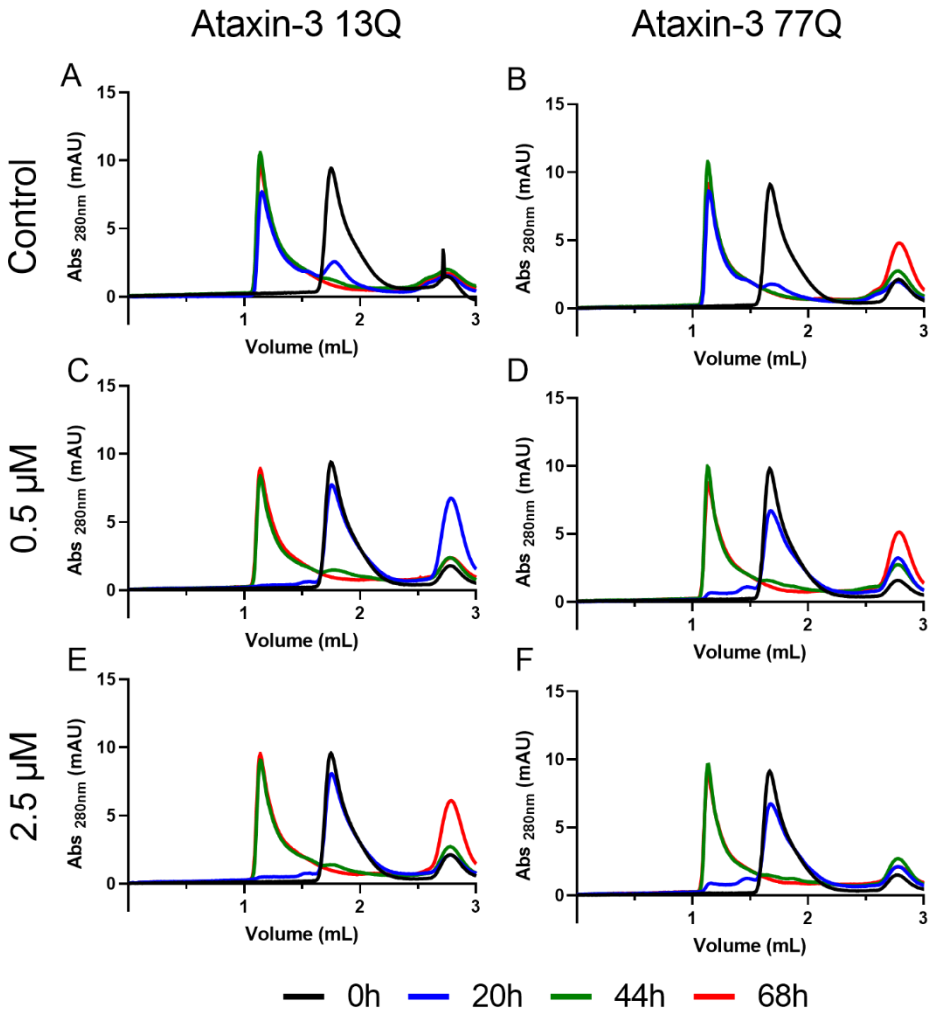

Figure 9 – Effect of Ciclopirox Ethanolamine on Atx3 aggregation. Size Exclusion Chromatography (SEC) assay to measure the aggregation of Atx3 13Q (**A, C, E**) and Atx3 77Q (**B, D, F**) in the presence of 0.5 and 2.5 µM Ciclopirox Ethanolamine. Samples were injected over time (at 0, 20, 44 and 68 hours) in a SEC column. Control condition are Atx3 isoforms in the presence of 0.04 % (v/v) DMSO.

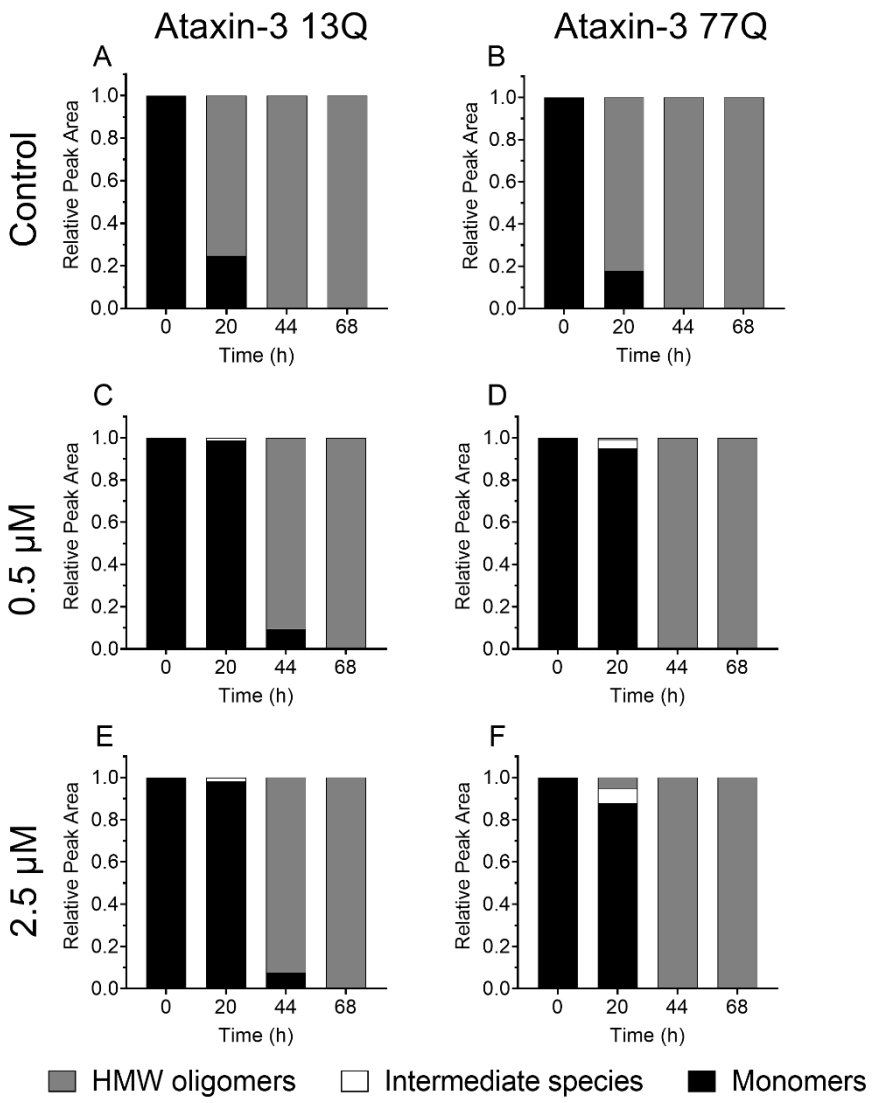

Figure 10 – Effect of Ciclopirox Ethanolamine on Atx3 aggregation measured by SEC. Peak areas from chromatograms presented in Figure 9.

TEM assay that performed at the same time (Figure 11) showed that after 24 hours both non-expanded and expanded Atx3 present fibrillar structures. This was not observed when in the presence of Ciclopirox Ethanolamine, where most of observed structures were oligomeric and not of fibrillar type. Fibrillar structures only appear visible at 48 and 96 hours, confirming a delay in the fibrillization pathway in the presence of Ciclopirox Ethanolamine. Mature Atx3 77Q fibrils are present after only after 96 hours.

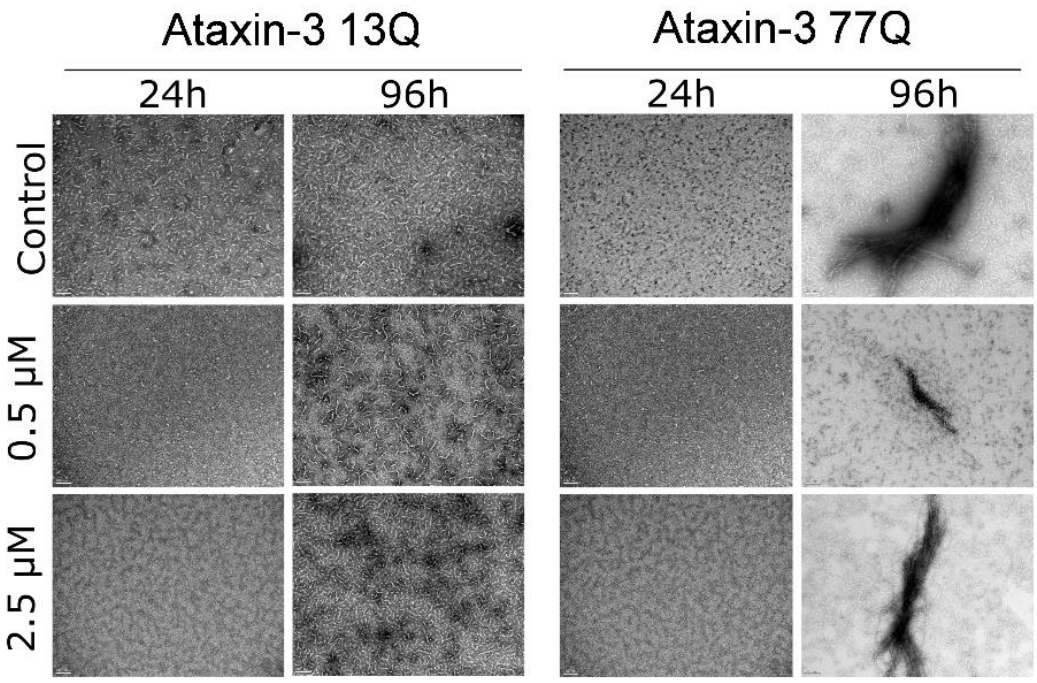

Figure 118 – Effect of Ciclopirox Ethanolamine on the morphologies of Atx3 fibrils. TEM images after negative staining of several time points (24, 48 and 96 h) of Atx3 13Q and Atx3 77Q in the presence of 0.5 and 2.5 µM of Ciclopirox Ethanolamine. Scale bars correspond to 100 nm. Control condition are Atx3 isoforms in the presence of 0.04 % (v/v) DMSO.

To further evaluate the distribution of Atx3 aggregates during the aggregation assay we used DLS. Atx3 samples were incubated at 37 ºC in the absence and in the presence of Ciclopirox Ethanolamine and at specific time points they were analysed by DLS (Figure 12). Atx3 13Q samples showed an average size of 10 nm in radius at the start of the aggregation assay (t=0h, Figure 12A). A shift in the peak occurred overtime and the average particle size increased to 24 nm after 48 hours at 37 °C (Figure 12A) and no observable alteration occurs at 72 and 96 hours of aggregation.

To better understand the effect of Ciclopirox Ethanolamine by DLS, it is necessary to observe both size distribution by intensity and by volume (Figure 12C, D). In the presence of Ciclopirox Ethanolamine larger species of 142 nm start to be observed after 24 hours (Figure 12C), but the quantity of aggregated protein is residual (Figure 12D). The majority of protein remained monomeric until 72 hours of incubation in the presence of Ciclopirox Ethanolamine.

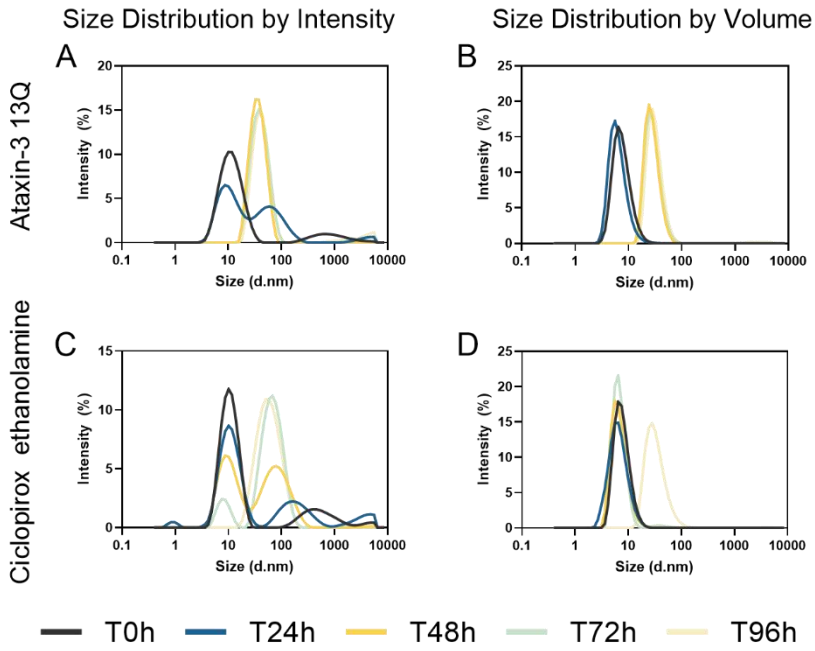

Figure 12 - Evaluation of Atx3 13Q aggregation with Ciclopirox Ethanolamine by DLS. Atx3 13Q aggregation in the presence of 5 µM Ciclopirox Ethanolamine by DLS, Atx3 13Q **(A, B)** and Ciclopirox ethanolamine **(C, D)**. Curves represent the mean of three independent replicates for each tested condition. In the left column is the Size Distribution by Intensity and on the right column, the Size Distribution by Volume. Control condition is Atx3 13Q in the presence of 0.04 % (v/v) DMSO.

4.3.4 Pentetic Acid

Pentetic Acid is a contrast agent used for diagnostic imaging, such as magnetic resonance imaging (Gi et al., 2014), and it was the only compound that inhibited the aggregation of both expanded and non-expanded Atx3 in the initial screening. To confirm this data, we performed another ThT aggregation assay with Pentetic Acid at 0.5 and 2.5 µM (Figure 13). The tested concentrations were able to inhibit Atx3 13Q aggregation (Figure 13A) but on this experiment Atx3 77Q aggregation was only inhibited with the higher concentration of Pentetic Acid used in this assay (Figure 13B).

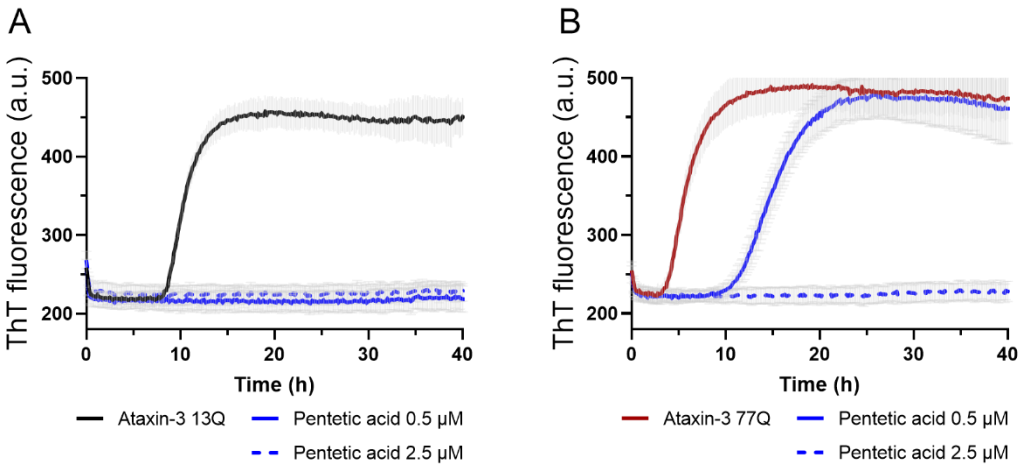

Figure 13 - Effect of Pentetic Acid on Atx3 aggregation kinetics. ThT assay to measure the formation of amyloid-like species in **(A)** Atx3 13Q and **(B)** Atx3 77Q aggregation in the presence of 0.5 and 2.5 µM Pentetic Acid. Curves represent the mean and standard deviation of eight replicates for each condition. Control condition are Atx3 isoforms in the presence of 25 µM of NaOH.

SEC data showed that both Atx3 13Q and 77Q aggregated in less than 20 hours (Figure 14A, B and Figure 15A, B) and that the presence of 0.5 µM Pentetic Acid delayed the aggregation for 24 hours (Figure 14C, D and Figure 15C, D). However, 2.5 µM Pentetic Acid inhibit both Atx3 isoforms (Figure 14E, F), and the protein remained mostly monomeric throughout the 68 hours of the assay (Figure 15E, F).

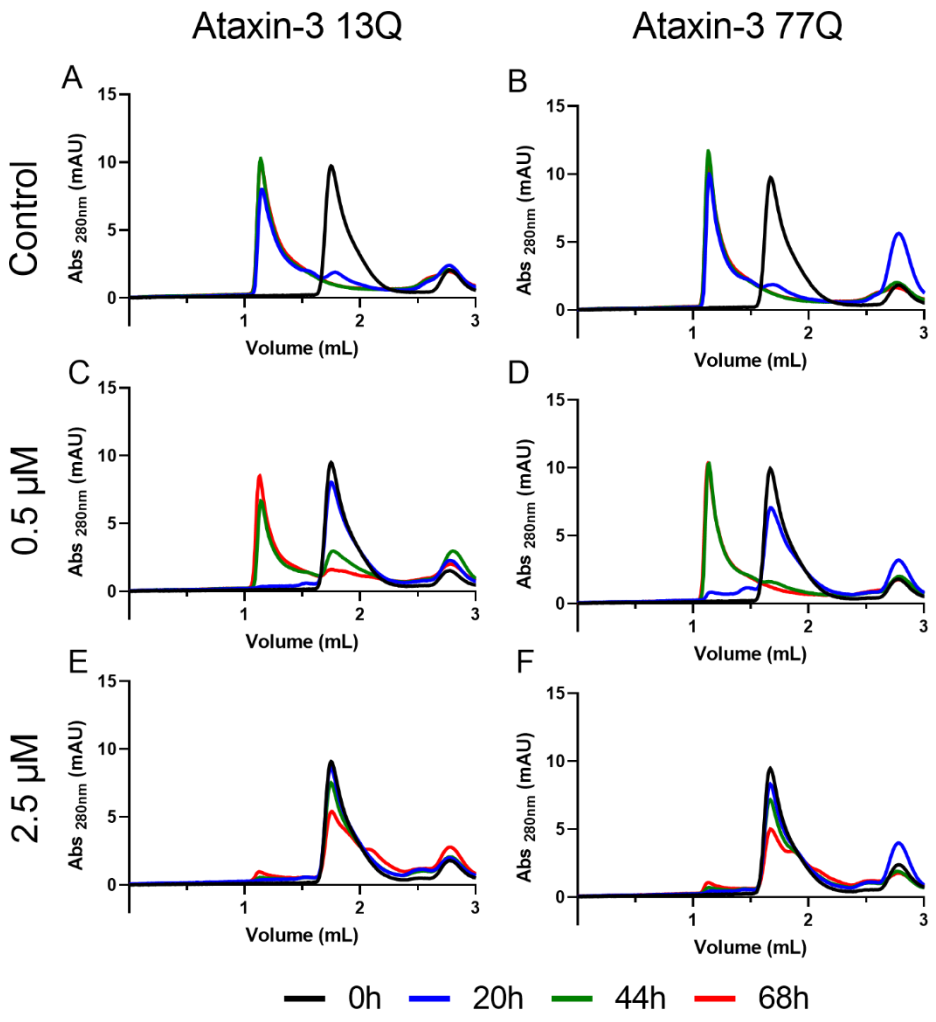

Figure 14 - Effect of Pentetic Acid on Atx3 aggregation. Size Exclusion Chromatography (SEC) assay to monitor the aggregation of Atx3 13Q **(A, C, E)** and Atx3 77Q **(B, D, F)** in the presence of 0.5 and 2.5 µM Pentetic Acid. Samples were injected over time (at 0, 20, 44 and 68 hours) in a SEC column. Control condition are Atx3 isoforms in the presence of 25 µM of NaOH.

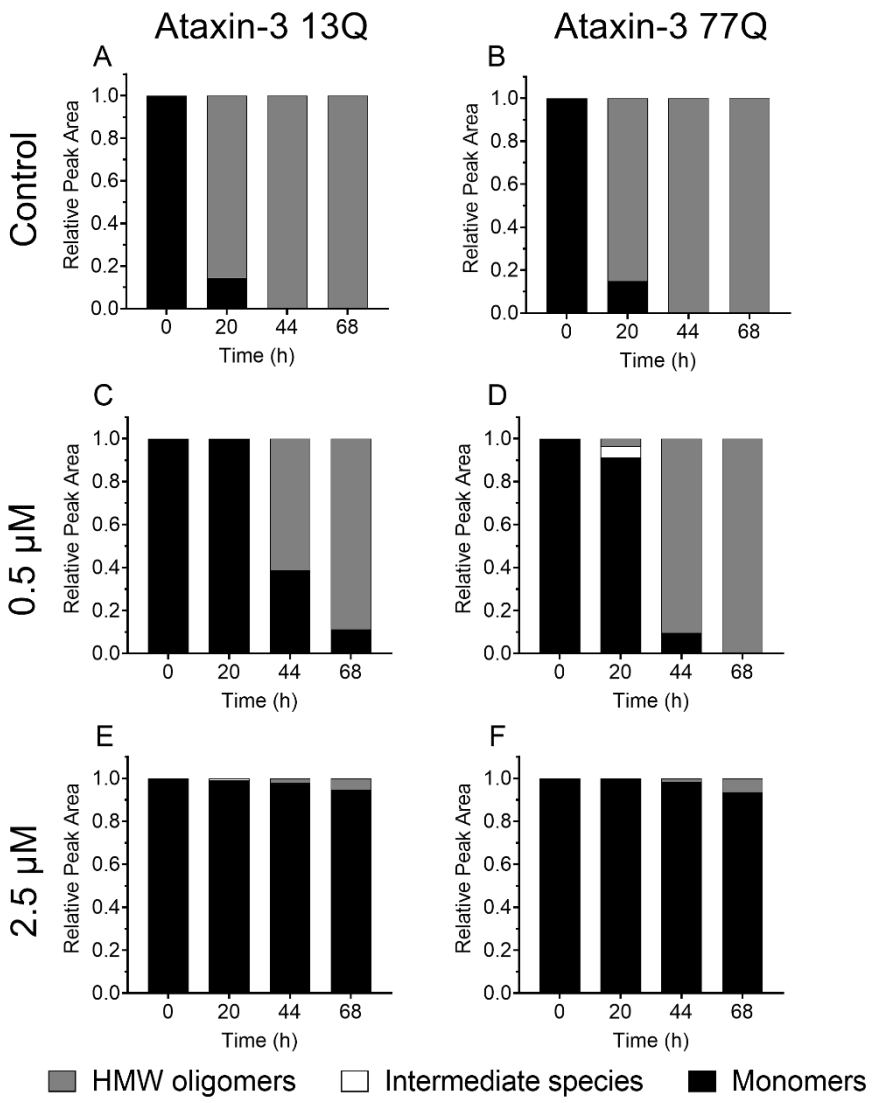

Figure 15 - Effect of Pentetic Acid on Atx3 aggregation measured by SEC. Peak areas from chromatograms presented in Figure 14.

At the same time that SEC analysis was performed, samples were collected for TEM and results are shown in Figure 16. At 24 hours of aggregation it was possible to visualize Atx3 protofibers in both expanded and non-expanded Atx3 (Figure 16). At this time point and in the presence of Pentetic Acid, some oligomeric from Atx3 77Q structures could be observed. The presence of 0.5 µM of Pentetic Acid delayed Atx3 fibrillization, as the number of Atx3 13Q protofibrils present were lower and no mature Atx3 77Q fibrils were seen. However, these differences were not observed at 96 hours of aggregation (Figure 16). The presence of 2.5 µM of Pentetic Acid completely compromised protein aggregation as very few fibrillar structures are observed in both Atx3 isoforms at all collected time points.

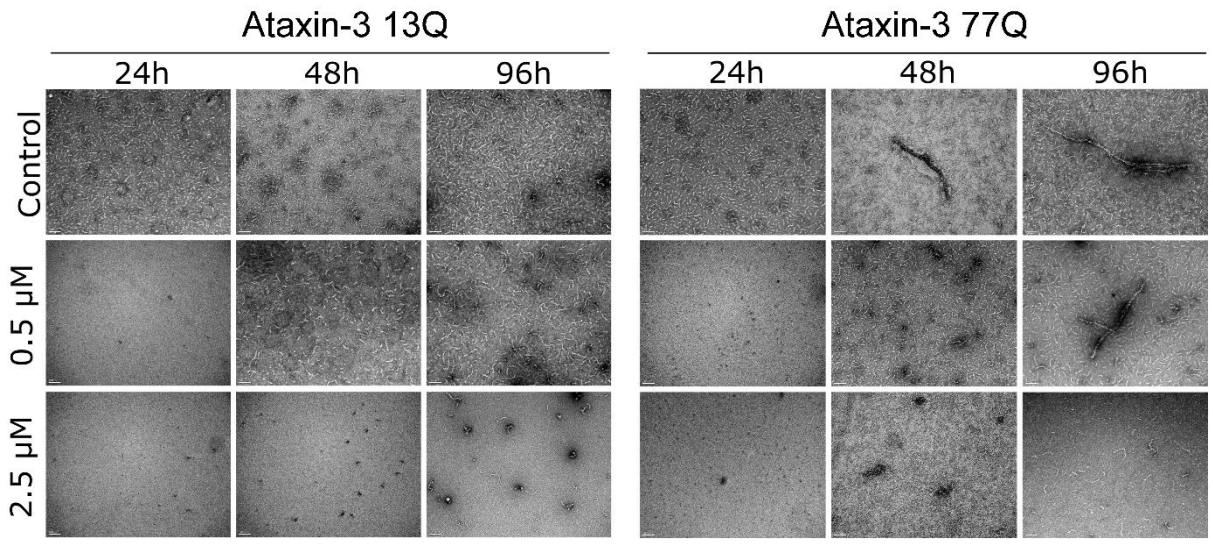

Figure 16 - Effect of Pentetic Acid in Atx3 aggregation by TEM. TEM images after negative staining of several time points (24, 48 and 96 h) of Atx3 13Q and Atx3 77Q in the presence of 0.5 and 2.5 µM of Pentetic Acid. Scale bars correspond to 100 nm. Control condition are Atx3 isoforms in the presence of 25 µM of NaOH.

DLS showed that in the presence of Pentetic Acid, Atx3 13Q aggregation was greatly compromised (Figure 17). Atx3 13Q aggregation observed by size distribution by volume generates species of an average size of 24 nm (Figure 17B) and the presence of Pentetic Acid maintained most protein monomeric, with an average size of 8 nm, even after 96 hours of aggregation (Figure 17D). However, some residual but very large aggregates (~100 nm) can be observed at 24 hours of aggregation and onwards (Figure 17C). These results are in accordance to what have been obtained so far, Pentetic Acid can impair the Atx3 fibrillization assembly by monomer stabilization.

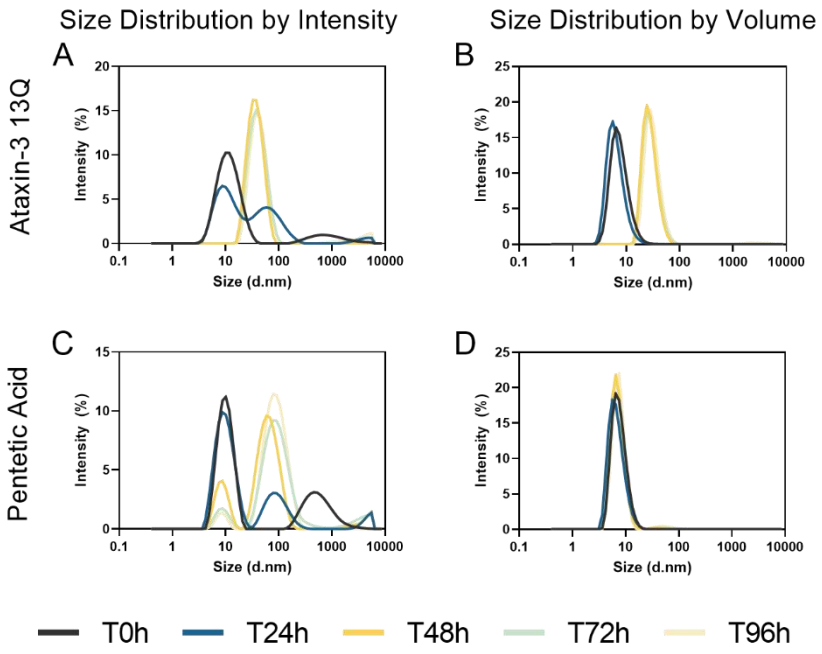

Figure 17 - Evaluation of Atx3 13Q aggregation with Pentetic Acid by DLS. Atx3 13Q aggregation in the presence of 5 µM Pentetic Acid by DLS, Atx3 13Q **(A, B)** and Pentetic Acid **(C, D)**. Curves represent the mean of three independent replicates for each tested condition. In the left column is the Size Distribution by intensity and on the right column, the Size Distribution by volume. Control condition are Atx3 isoforms in the presence of 25 µM of NaOH.

4.3.5 Dopamine

Dopamine is a very important neurotransmitter needed for normal brain function (J. Li, Zhu, Manning-Bog, Di Monte, & Fink, 2004) and at concentrations of 1 and 5 µM was it able to inhibit the aggregation of both Atx3 isoforms *in vitro* (Figure 18).

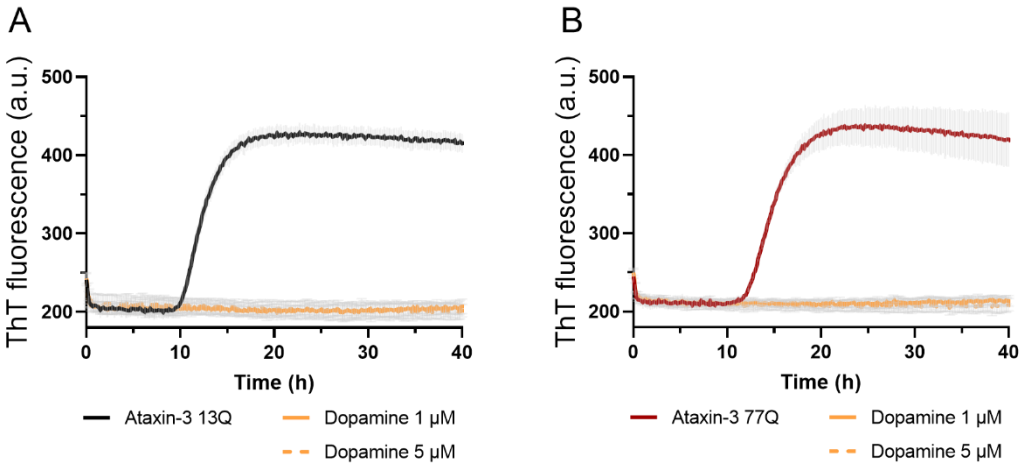

Figure 18 - Effect of Dopamine on Atx3 aggregation kinetics. ThT assay to measure the formation of amyloid-like species in **(A)** Atx3 13Q and **(B)** Atx3 77Q aggregation in the presence of 1 and 5 µM Dopamine. Curves represent the mean and standard deviation of eight replicates for each condition. Control condition are Atx3 isoforms in the presence of 0.04 % (v/v) DMSO.

SEC aggregation assay with 1 and 5 µM Dopamine is shown below, in Figure 19 and Figure 20. Both control non-expanded and expanded Atx3 aggregated in 44 hours (Figure 19A, B). However, in the presence of the tested concentrations of Dopamine, for both Atx3 isoforms, this did not occur (Figure 19C, D, E, F). Analysis of peak areas (Figure 20) show that Atx3 13Q stayed monomeric throughout the assay while Atx3 77Q had some HMW species being present at 68 hours of aggregation, even though it remained mostly monomeric.

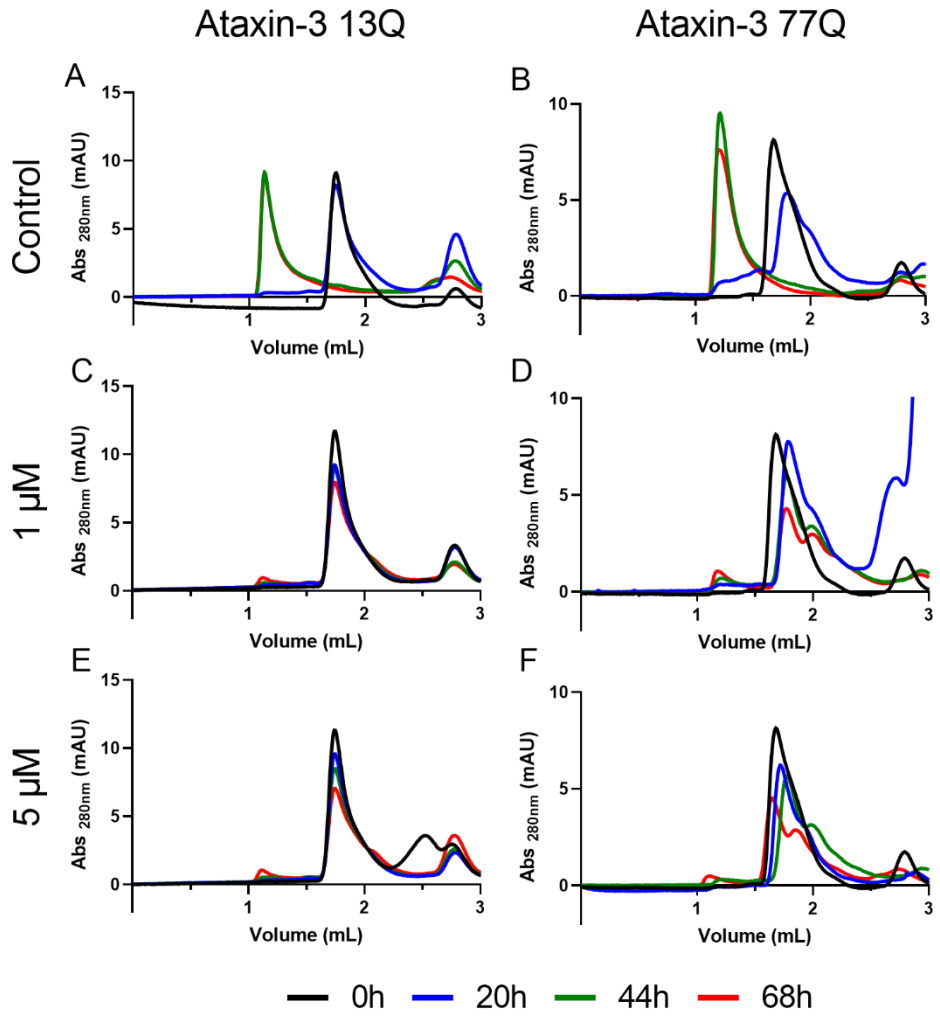

Figure 19 - Effect of Dopamine on Atx3 aggregation. Size Exclusion Chromatography (SEC) assay to measure the aggregation of Atx3 13Q **(A, C, E)** and Atx3 77Q **(B, D, F)** in the presence of 1 and 5 µM Dopamine. Samples were injected over time (at 0, 20, 44 and 68 hours) in a SEC column. Control condition are Atx3 isoforms in the presence of 0.04 % (v/v) DMSO.

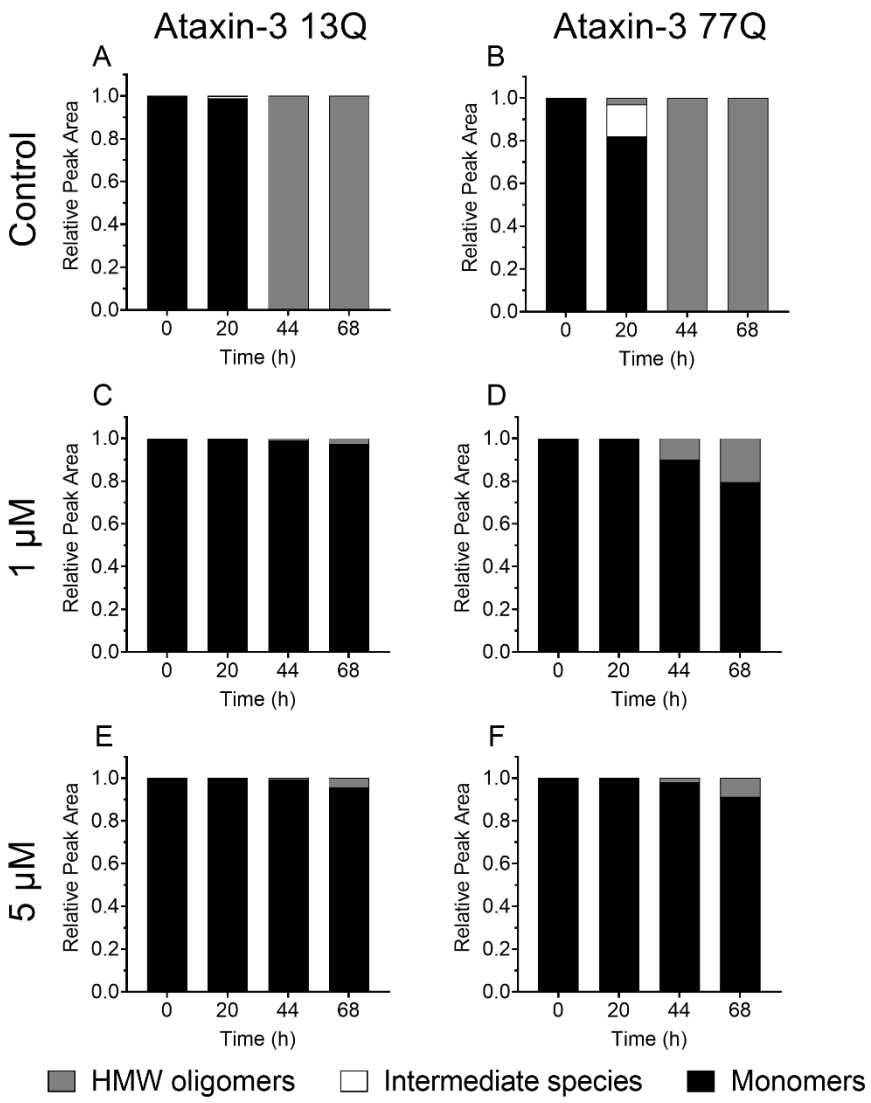

Figure 20 - Effect of Dopamine on Atx3 aggregation measured by SEC. Peak areas from chromatograms presented in Figure 19.

TEM analysis was performed at the same time and results are exposed in Figure 21. At 96 hours of aggregation Atx3 13Q formed mostly fibrillar structures, while Atx3 77Q assembled into fibrillar structures as well as mature fibrils (Figure 21). The presence of Dopamine in both concentrations used compromised fibrillization of both non-expanded and expanded Atx3. At 96 hours of incubation with Dopamine some fibrillar structures were present but not in the same quantities as the control group. It is important to note that Dopamine did not completely stop Atx3 aggregation, since mature Atx3 77Q fibrils are present at 96 hours of aggregation with 5 µM of Dopamine (Figure 21).

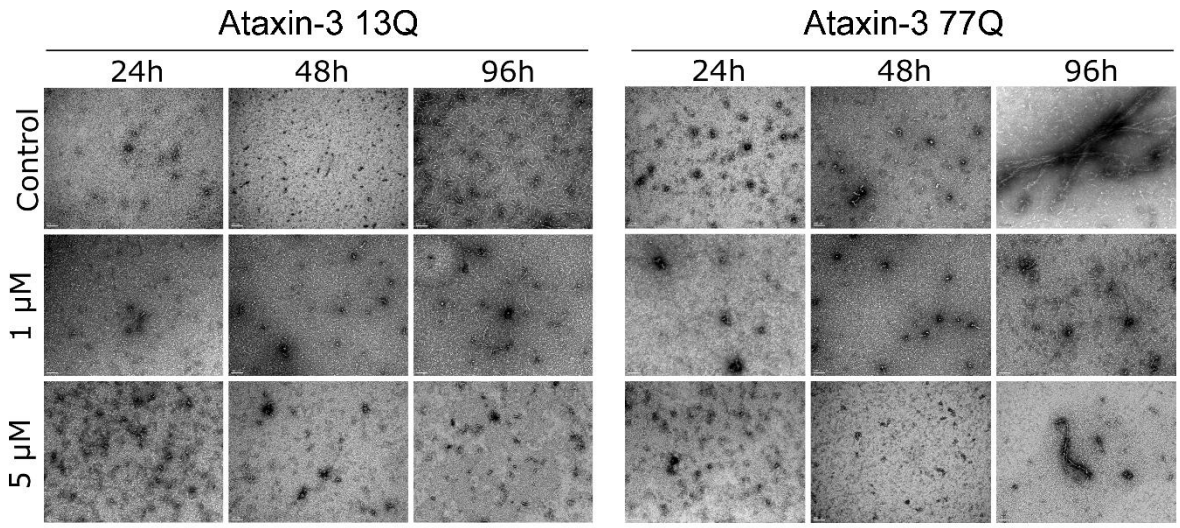

Figure 21 - Effect of Dopamine in Atx3 aggregation by TEM. TEM images after negative staining of several time points (24, 48 and 96 h) of Atx3 13Q and Atx3 77Q in the presence of 1 and 5 µM of Dopamine. Scale bars correspond to 100 nm. Control condition are Atx3 isoforms in the presence of 0.04 % (v/v) DMSO.

DLS was also performed with Atx3 13Q with and without Dopamine (Figure 22). Data shows that the rates of Atx3 13Q aggregation were considerably slower in the presence of Dopamine. Atx3 13Q aggregated in 48 hours (Figure 22A, B). Upon addition of Dopamine, some protein appeared to be aggregated after 48 hours (Figure 22C), but these larger particles exist only in minute amounts, as shown on the size distribution by volume (Figure 22D) where particles of ~10nm are predominant suggesting that Atx3 remained mostly monomeric. Only after 96 hours of aggregation assay Atx3 was mostly aggregated and self-assembled into particles with an average size of ~50 nm.

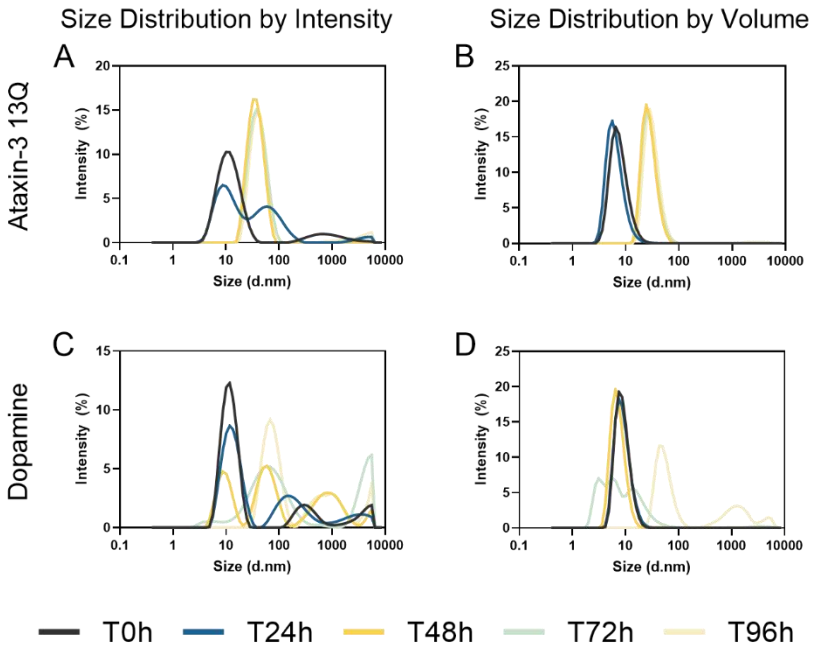

Figure 22 - Evaluation of Atx3 13Q aggregation with Dopamine by DLS. Atx3 13Q aggregation in the presence of 5 µM Dopamine by DLS, Atx3 13Q **(A, B)** and Dopamine **(C, D)**. Curves represent the mean of three independent replicates for each tested condition. In the left column is the Size Distribution by Intensity and on the right column, the Size Distribution by Volume. Control condition is Atx3 13Q in the presence of 0.04 % (v/v) DMSO.

4.3.6 Tolcapone

Tolcapone is a compound from the Catechol *O*-methyltransferase (COMT) inhibitor family, which is already used for the treatment of Parkinson's disease (Calne, 1993). Our ThT assay demonstrated that Tolcapone is also capable of inhibiting Atx3 aggregation *in vitro* (Figure 23). For both non-expanded and expanded Atx3, no increase in fluorescence signal is observed in the tested concentrations (Figure 23A, B).

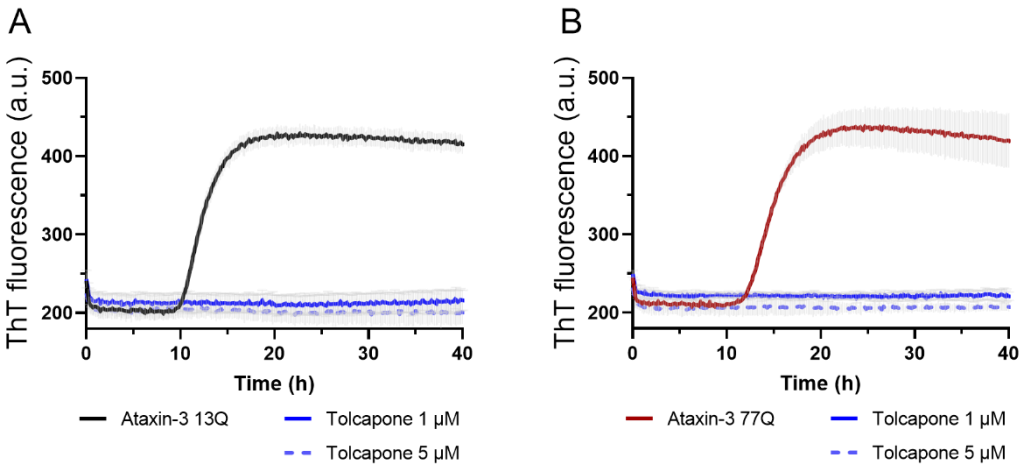

Figure 23 - Effect of Tolcapone on Atx3 aggregation kinetics. ThT assay to measure the formation of amyloid-like species in **(A)** Atx3 13Q and **(B)** Atx3 77Q aggregation in the presence of 1 and 5 µM Dopamine. Curves represent the mean and standard deviation of eight replicates for each condition. Control condition are Atx3 isoforms in the presence of 0.04 % (v/v) DMSO.

SEC analysis were also performed with Tolcapone at 1 and 5 µM and results are shown in Figure 24 and Figure 25. Both Atx3 isoforms were monomeric at the starting point of the aggregation assay (0 hours – Figure 24 A, B and Figure 25A, B) but after 44 hours of aggregation their SEC profiles shifted into a HMW oligomeric species (Figure 24A, B and Figure 25A, B). In the presence of both tested Tolcapone concentrations, conversion of non-expanded and expanded Atx3 to HMW oligomers was abolished (Figure 24C, D, E, F and Figure 25C, D, E, F).

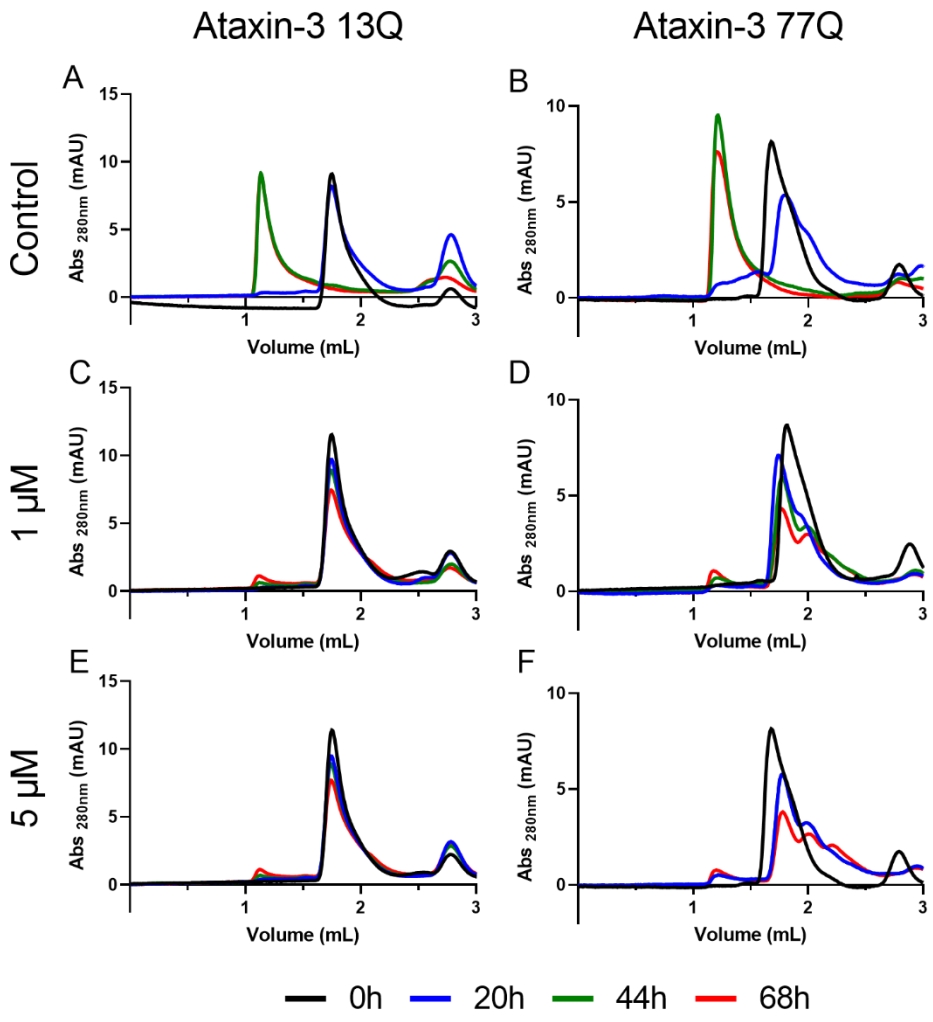

Figure 24 - Effect of Tolcapone on Atx3 aggregation. Size Exclusion Chromatography (SEC) assay to measure the aggregation of Atx3 13Q **(A, C, E)** and Atx3 77Q **(B, D, F)** in the presence of 1 and 5 µM Tolcapone. Samples were injected over time (at 0, 20, 44 and 68 hours) in a SEC column. Control condition are Atx3 isoforms in the presence of 0.04 % (v/v) DMSO.

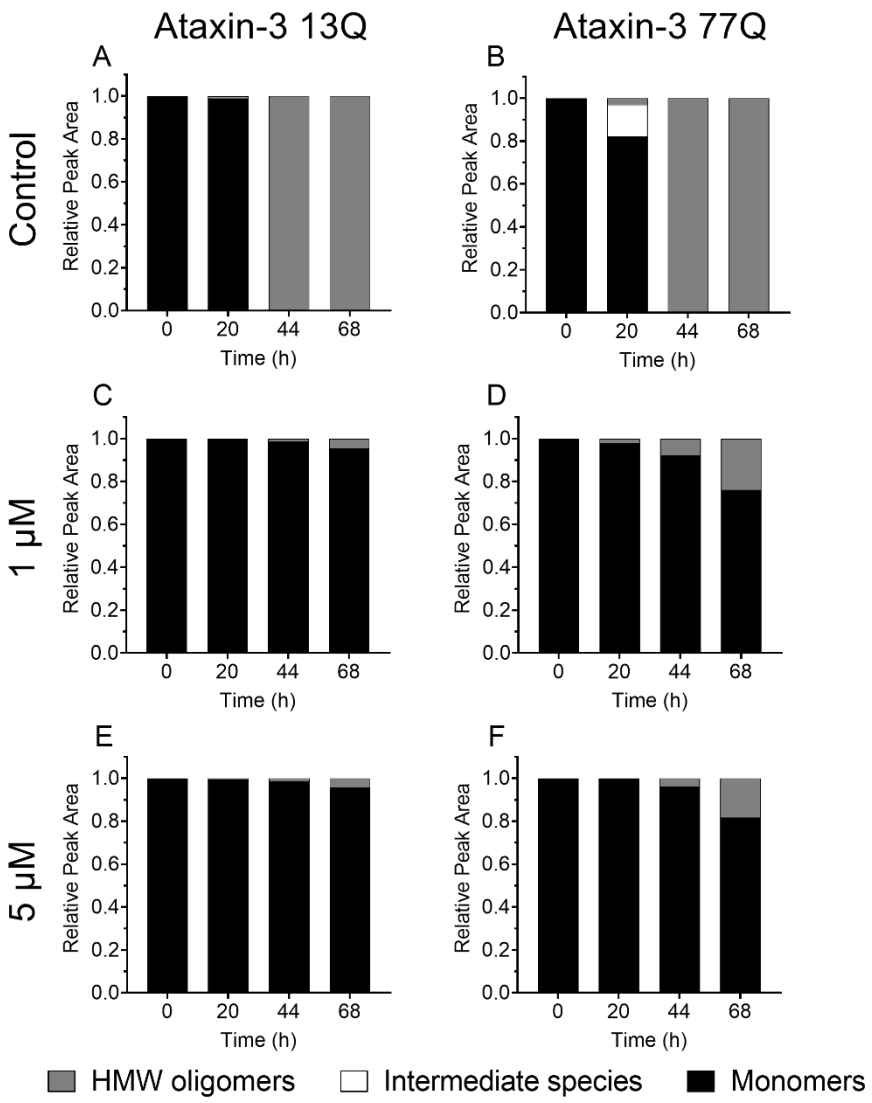

Figure 25 - Effect of Tolcapone on Atx3 aggregation measured by SEC. Peak areas from chromatograms presented in Figure 20.

Further analysis was carried out by TEM and results are detailed in Figure 26. These TEM results showed that after 96 hours of aggregation *in vitro*, the amount of Atx3 13Q protofibers formed is greatly reduced when compared with Atx3 13Q that was not incubated with Tolcapone (Figure 26). For expanded Atx3 77Q, although one mature fibril is observed at 96 hours of aggregation in the presence of 5 µM Tolcapone, we can assume that this chemical compound can greatly compromise Atx3 fibril maturation.

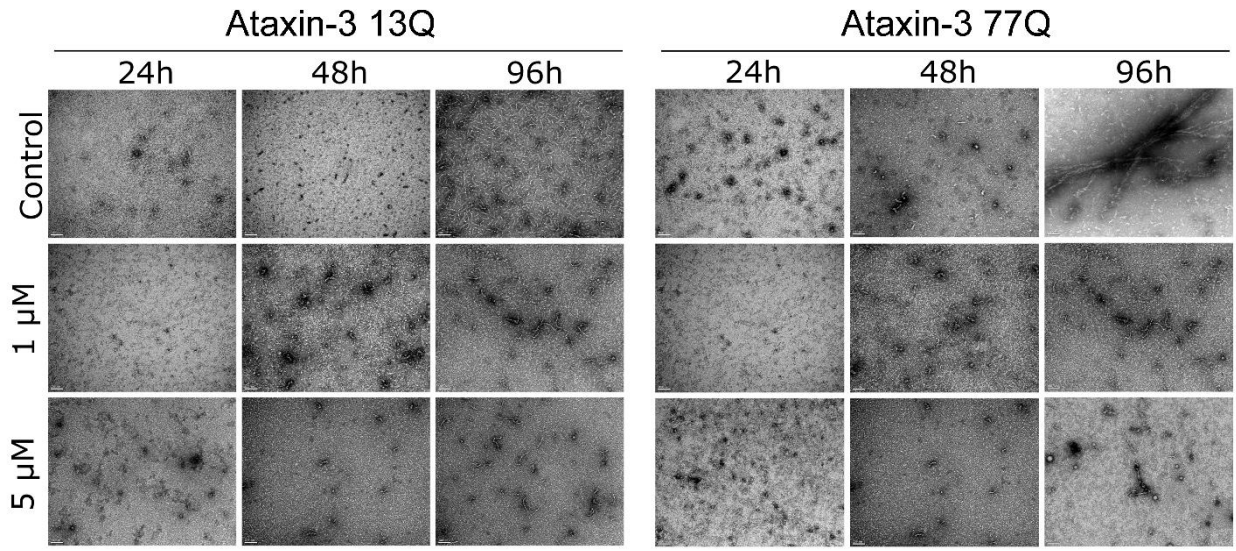

Figure 26 - Effect of Tolcapone in Atx3 aggregation by TEM. TEM images after negative staining at several time points (24, 48 and 96 h) throughout Atx3 13Q and Atx3 77Q aggregation assay in the presence of 1 and 5 µM of Tolcapone. Scale bars correspond to 100 nm. Control condition are Atx3 isoforms in the presence of 0.04 % (v/v) DMSO.

DLS data for Atx3 aggregation in the presence of Tolcapone shows a similar effect as the one observed for Dopamine (Figure 27). Normal Atx3 13Q aggregated at 48 hours (Figure 27A, B). Although at that time point the samples with 5 µM Tolcapone showed some large species of average size 58.8 nm (Figure 27C), it corresponds to a residual amount since no peak with those larger particles was visible in the size distribution by volume (Figure 27D). Large aggregated species only appeared after 96 hours of Atx3 aggregation assay in the presence of Tolcapone, which corresponds to twice the time required for the appearance of these aggregates of Atx3 in the absence of Tolcapone.

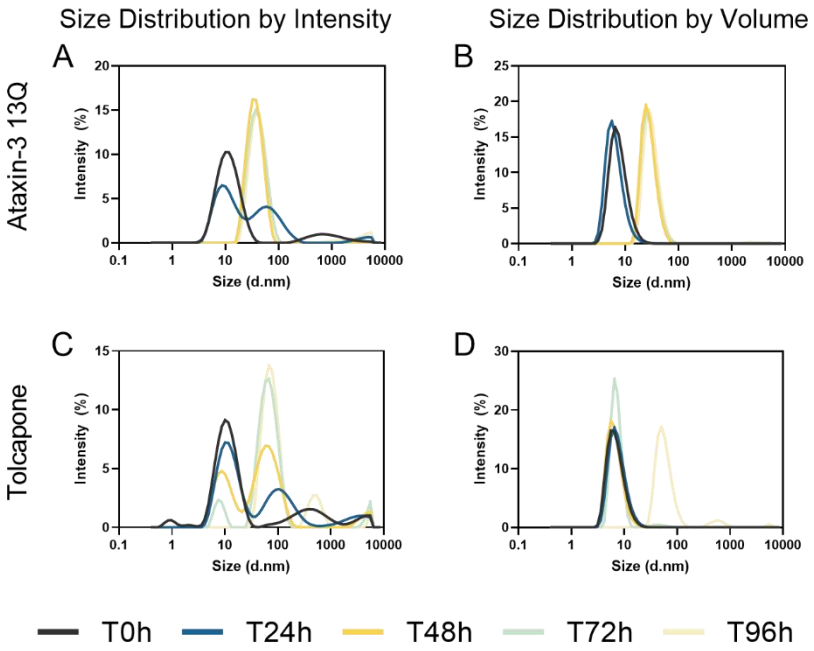

Figure 27 - Evaluation of Atx3 13Q aggregation with Tolcapone by DLS. Atx3 13Q aggregation in the presence of 5 µM Tolcapone by DLS, Atx3 13Q **(A, B)** and Tolcapone (C, D). Curves represent the mean of three independent replicates for each tested condition. In the left column is the Size Distribution by Intensity and on the right column, the Size Distribution by Volume. Control condition is Atx3 13Q in the presence of 0.04 % (v/v) DMSO.

4.3.7 Thermal shift assay

A Thermal Shift Assay is a high-throughput simple and inexpensive experiment that allow us to quickly test if our compounds of interest in the selected ratios could significantly bind to Atx3 13Q and enhancing its stability. Normally, a protein stabilization is also followed with an increase in melting temperature (Huynh & Partch, 2015; Scott, 2017). This evaluation was made by incubating Atx3 with selected compounds on a buffer containing SYPRO Orange dye. Then, the mixture was gradually heated until protein chain quickly unfolds exposing hydrophobic regions, which allow the dye to bind and increase fluorescence signal (Scott, 2017).

When incubated in the same ratios as other experiments, the compounds did not change the melting point of both Atx3 isoforms (Figure 28). This means that although compounds had the ability to compromise Atx3 aggregation they did not interact with Atx3 with high affinity.

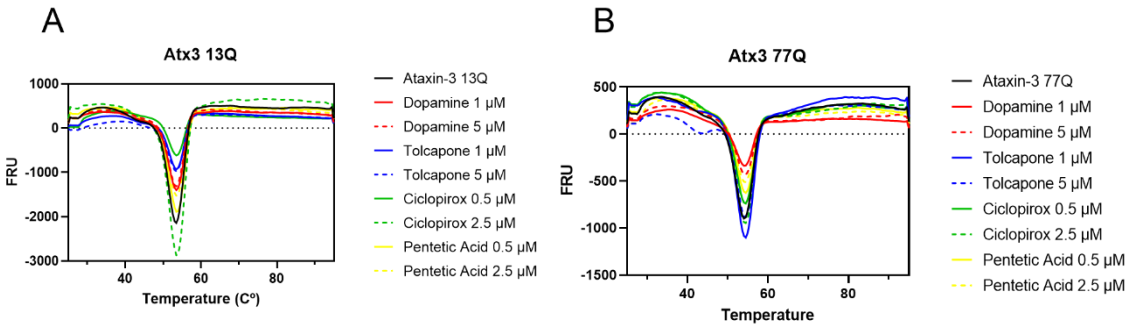

Figure 28 – Thermal Shift Assay of both Atx3 isoforms with the selected compounds. No thermal shift was observed in both (A) Atx3 13Q and (B) Atx3 77Q in the presence of selected compounds in different concentrations. Control conditions are Atx3 isoforms in the presence of 0.04 % (v/v) DMSO.

4.3.8 *In cell* experiments

After *in vitro* characterization of Atx3 aggregation in the presence of the selected compounds, we stablished a new collaboration with Pedro Brites's Neurolipid Biology laboratory at i3S to pursuit the next step of this work, the *in cell* experiments using mouse primary cortical neurons overexpressing expanded and non-expanded GFP-Atx3. I received extensive training in cell isolation, grown and transfection; obtained FELASA certification A, B and D to be able to work with animals; acquire experience on operating different confocal microscopes. Unfortunately, protocol optimization for the transfection neuronal cultures was the achieved result so far, which is what is observed in Figure 29: electroporated primary cortical neurons dissociated from E17.5 mice, expressing GFP-Atx3 13Q for 72 hours. It is also possible to observe that these cells form some type of granules, possible GFP-Atx3 13Q aggregates.

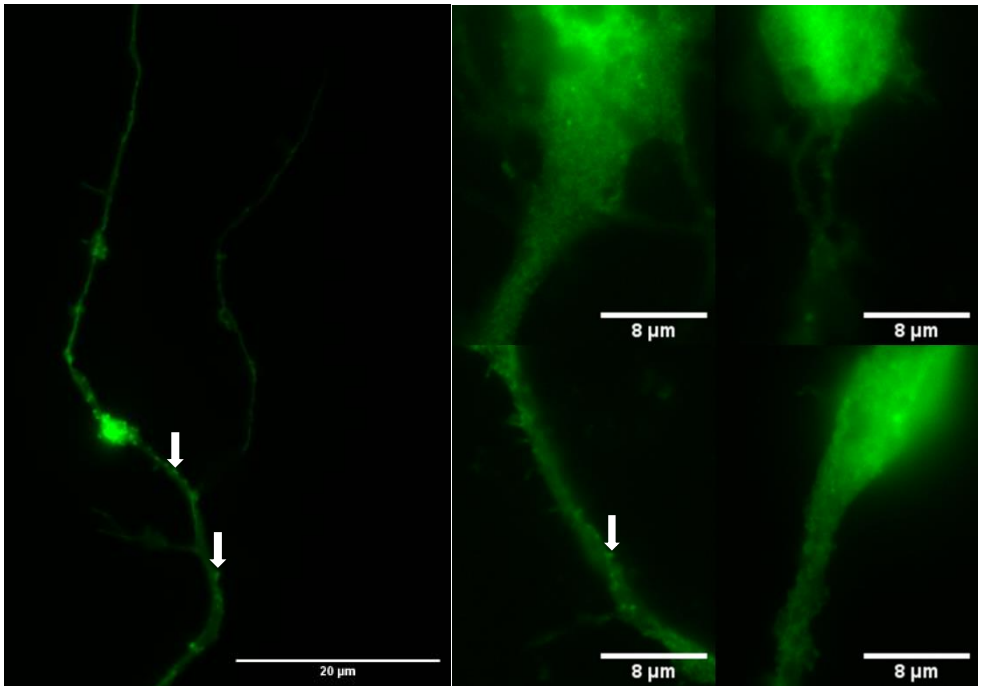

Figure 29 – Primary cortical neurons expressing GFP-Atx3 13Q for 72 hours. Cells were electroporated at E17.5 and after hours of GFP-Atx3 13Q expression several type of protein aggregates (white arrow) appear over the axon.

4.4 Discussion

The main objective of this study was to screen a commercial chemical library of compounds, to identify possible candidates of Atx3 aggregation inhibitors/modulators. To achieve this, we used our previously validated ThT aggregation assay to monitor aggregation of non-expanded Atx3. This allowed us to quickly and efficiently screen 1280 different compounds, from which 28 could interfere with Atx3 aggregation *in vitro*. From this 28 possible candidates, four were selected – Ciclopirox Ethanolamine, Pentetic Acid, Dopamine and Tolcapone – for further evaluation on how these compounds can modulate non-expanded and expanded Atx3 aggregation. This evaluation was performed by combining ThT aggregation assay with TEM, SEC and DLS analysis, as illustrated in Figure 30.

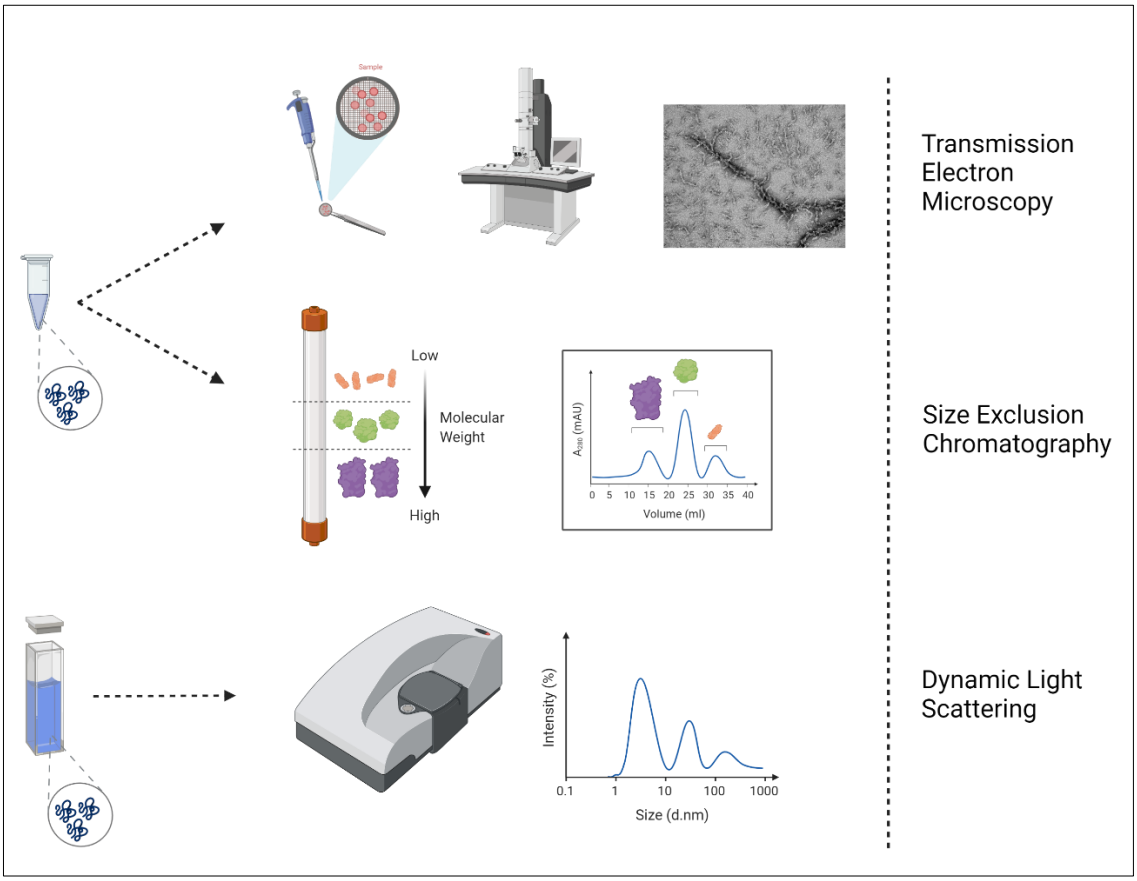

Figure 30 – Scheme of different techniques used to evaluate how select compounds could interfere with Atx3 aggregation. Protein aggregation was performed by combining Transmission Electron Microscopy, Size Exclusion Chromatography, Dynamic Light Scattering and Thioflavin-T assays.

Time-course aggregation analysis by TEM allow us to detect and characterize the oligomeric and fibrillar species formed. It is known that non-expanded and expanded Atx3 can form fibrillar structures. In the presence of the selected compounds we could

observe that protein fibrillization was greatly impaired. Although some fibrillar structures could be observed in the experimental time points, the amount of aggregates was greatly reduced. Suggesting that these compounds do not completely stop protein aggregation but significantly reduce it. Evaluating TEM data we observe that Ciclopirox Ethanolamine was the compound that was least effective in modulating protein aggregation, as protofibrils could be observed after 48 hours of aggregation. At the same time, TEM analysis showed that 2.5 µM Pentetic Acid showed the most promising results.

SEC analysis was performed simultaneously with TEM and this technique provides information about the overall population of Atx3 aggregates. SEC analysis reports only on the soluble fraction since all samples that are studied by SEC are filtered. Therefore, insoluble aggregates such as mature fibrils and/or protofibers are removed. By looking at the resulting chromatograms and their areas we can observe that both Atx3 isoforms in the presence of Ciclopirox Ethanolamine and 0.5 µM Pentetic Acid had their aggregation times delayed by 24 hours when compared to control samples. At the same time, Dopamine, Tolcapone and 2.5 µM Pentetic Acid could successfully stabilize lower molecular weight species, likely Atx3 monomers, thereby reducing its aggregation.

For technical reasons, DLS analysis could not be performed simultaneously with TEM and SEC analysis. And due to sampling and time limitations, analysis was done only in non-expanded Atx3 and with one compound concentration. DLS analysis allowed us to determine the size distribution profiles of Atx3 aggregates in suspension. DLS has also high sensibility to large aggregates, that is why in our results of Atx3 13Q in the presence of the selected compounds it was possible to observe several aggregated species even though the majority of the protein had a monomeric profile. DLS results showed that Atx3 13Q aggregated in 48 hours, but in the presence of Pentetic Acid, this aggregation did not occur after 96 hours. All other three compounds delayed Atx3 aggregation for at least 72 hours.

4.4.2 Ciclopirox Ethanolamine

Ciclopirox Ethanolamine is an off-patent potent antimycotic chemical and iron chelator (Gupta & Plott, 2004). In our *in vitro* experiments, Ciclopirox Ethanolamine was able to delay both non-expanded and expanded Atx3 aggregation. Unfortunately, our results also showed that this compound had the weaker effect as a modulator of Atx3 aggregation. Atx3 fibril maturation was delayed, but still observable by TEM and SEC analysis, which showed that soluble oligomeric species were still formed for both tested concentrations. Dose response ThT analysis showed that both expanded and non-expanded Atx3 aggregation in the presence of 20 µM Ciclopirox Ethanolamine was

severely compromised. These weak inhibitory effects could be consequence of the low (0.5 and 2.5 µM) compound concentrations tested.

Ciclopirox Ethanolamine is also being studied in the treatment of other diseases such as cancer, diabetes and HIV infection (Feng et al., 2020; Huang & Huang, 2021). This compound also showed promising results in modifying human hematopoietic stem cell *ex vivo* (Talkhoncheh et al., 2015). Ciclopirox Ethanolamine can pass the BBB and it is currently being studied as a promising anti-ischemic stroke agent (Feng et al., 2020; Hu et al., 2020). To our knowledge, Ciclopirox Ethanolamine was never studied for the treatment of any other neurodegenerative disease.

4.4.3 Pentetic Acid

Pentetic Acid is a chemical compound from the EDTA family. It is used as a quelant due to its ability to form complexes with many metallic cations (al Sadat Shafiof & Nezamzadeh-Ejhieh, 2020) although it can be used as a magnetic resonance imaging contrast agent when combined with gadolinium (Capra, Marcianò, Vignolo, Chiesa, & Gasparotti, 1992). Pentetic Acid is also used in the cosmetic industry, mostly in hair dyes and colours (Benes & Burnett, 2008). This compound does not pass the normal BBB and because of that, it can be used as a biomarker for BBB dysfunction (Löscher & Friedman, 2020). Even though Pentetic Acid it is not able to cross the BBB, it was selected mainly because it is from a distinct chemical family and was the only compound in the initial screening that inhibit both expanded and non-expanded Atx3 aggregation *in vitro*. Our results showed that the presence of 2.5 µM Pentatic Acid completely compromised the aggregation for both non-expanded and expanded Atx3. This result was confirmed in all techniques used in this study. No mature fibrils were observed by TEM and no HMW oligomers were observed by SEC. DLS showed that after 96 hours of aggregation protein still had a monomeric profile even though some aggregates were detected.

In other drug repositioning screenings, Pentetic Acid showed a potential therapeutic effect against Gram-negative *Pseudomonas aeruginosa* airway infection (Gi et al., 2014) and also extended lifespan and ameliorated symptoms in Limb-Girdle Muscular Dystrophy 21 zebrafish model (Serafini et al., 2018). No data on the use of Pentetic Acid for the treatment of any neurologic disease was found, but its strong effect reducing the maturation of polyQ-expanded Atx3 fibrils hints that it might be also have beneficial effects in other polyQ-expansion disorders.

4.4.4 Dopamine

Dopamine is a neuromodulatory molecule, that is very important for normal brain function and it cannot pass through the BBB (Lopalco et al., 2018). Our data demonstrates that Dopamine can delay Atx3 aggregation, for both non-expanded and expanded Atx3 and greatly decreased the number of fibrils formed *in vitro*. Our SEC analysis showed that the amount of soluble HMW oligomers was very residual and that protein maintained a monomeric profile throughout the assay, despite the fact that fibrillar structures could be detected by TEM and DLS analysis showed the presence of large aggregates.

The loss of dopaminergic neurons is associated with Parkinson's disease (Leong, Cappai, Barnham, & Pham, 2009), therefore the influence of Dopamine in the modulation of α-synuclein aggregation is a subject of study (Cappai et al., 2005; Y. Li, Nara, & Nakamura, 2004) and reviewed by Leong et al. (2009). Dopamine can disaggregate α-synuclein insoluble fibrils into small soluble oligomeric species (J. Li et al., 2004) and it can also promote α-synuclein to form SDS-resistant soluble oligomers that are off-pathway intermediates of amyloid fibrils (Leong et al., 2009). The strong effect of Dopamine in reducing the maturation of polyQ-expanded Atx3 fibrils hints that it might be also have beneficial effects in other polyQ-expansion disorders.

4.4.5 Tolcapone

Tolcapone is a compound from the COMT inhibitors family and can cross the BBB (Silva et al., 2016). COMT are very important for the nervous system because they metabolize catecholamine neurotransmitters such as dopamine (Vidgren, Svensson, & Liljas, 1994). Tolcapone is currently used for the treatment of Parkinson's disease symptoms when combined with levodopa/carabidopa therapy because it improves symptom fluctuations and also decreases the amount of levodopa requirements (Keating & Lyseng-Williamson, 2005). Levodopa can cross BBB and is metabolized to dopamine, and COMT metabolizes dopamine into 3-*O*-methyldopa. The role of Tolcapone is to reduce the degradation of levodopa into 3-*O*-methyldopa and therefore, improve levodopa bioavailability and provide a constant dopaminergic stimulation (Keating & Lyseng-Williamson, 2005). However, Tolcapone is also associated with hepatoxicity (Silva et al., 2016). Our study shows very promising data, showing that Tolcapone can severely reduce Atx3 aggregation *in vitro* of both non-expanded and expanded isoforms. It is already described in the literature that Tolcapone could block fibril formation and protect against amyloid-induced toxicity for α-synuclein and β-amyloid (Di Giovanni et al., 2010). Tolcapone did compromise the formation of mature Atx3 77Q fibrils and at the

same time also inhibited the formation of soluble HMW Atx3 oligomers. Tolcapone also showed very promising results for inhibiting transthyretin amyloidogenesis (Sant'Anna et al., 2016).

Buhmann and colegues reported a patient that later was diagnosed with MJD but presented signs indistinguishable from Parkinson's disease. After ten years of treatment with levodopa and other dopamine agonists the patient developed the classical MJD symptonts, cerebellar ataxia and pyramidal signs (Buhmann, Bussopulos, & Oechsner, 2003). Although this is only one example, it is a promising report on a positive response to dopamine agonists in MJD. Tolcapone strong effects in reducing the maturation of polyQ-expanded Atx3 fibrils hints that it might be also have beneficial effects in other polyQ-expansion disorders.

4.4.6 Conclusion and future studies

As discussed in Chapter 1, MJD is oncluded in the group of polyQ expansion diseases, which are characterized by the presence of nuclear inclusions in certain regions of the brain (Lieberman et al., 2019). This is also a feature shared with other proteins that are associated with distinct neurodegenerative disorders such as AD, PD and ALS (Benilova, Karran, & De Strooper, 2012; Sangwan et al., 2017; Winner et al., 2011). The discovery of a novel compound that impairs Atx3 aggregation has the potential to be tested in other neuropathological proteins. Tolcapone is a great example, since is a potent Atx3 aggregator inhibitor (this study) and showed also very good results in inhibiting transthyretin aggregation (Sant'Anna et al., 2016).

These *in vitro* results paved the way for us to start new *in cell* and *in vivo* studies. We have already implemented in our laboratory – with our collaborators - a mice primary neuronal cell culture model to evaluate how these compounds modulate Atx3 aggregation *in vivo*. At the same time, we also have access to a MJD *Drosophila* model that we are already using in parallel. We will combine the findings of both *in vivo* models in the expectation of creating a more robust data set.

Furthermore, we describe for the first time the usage of Ciclopirox Ethanolamine, Pentetic Acid, Dopamine and Tolcapone in Atx3 aggregation. By combining different biophysical techniques, we showed the potential inhibitory effect of these compounds *in vitro*. None of these compounds were ever used in this context.

4.5 References

al Sadat Shafiof, M., & Nezamzadeh-Ejhieh, A. (2020). A comprehensive study on the removal of Cd (II) from aqueous solution on a novel pentetic acid-clinoptilolite nanoparticles adsorbent: Experimental design, kinetic and thermodynamic aspects. *Solid State Sciences, 99*, 106071.

Ashburn, T., & Thor, K. (2004). Drug repositioning: identifying and developing new uses for existing drugs. *Nature Reviews Drug Discovery, 3*(8), 673-683. doi:10.1038/nrd1468

Benes, D., & Burnett, C. (2008). Final report on the safety assessment of pentasodium pentetate and pentetic acid as used in cosmetics. *International Journal of Toxicology, 27*, 71-92.

Benilova, I., Karran, E., & De Strooper, B. (2012). The toxic Aβ oligomer and Alzheimer's disease: an emperor in need of clothes. *Nature neuroscience, 15*(3), 349-357.

Berne, B., & Pecora, R. (2000). *Dynamic light scattering: with applications to chemistry, biology, and physics*: Courier Corporation.

Buhmann, C., Bussopulos, A., & Oechsner, M. (2003). Dopaminergic response in Parkinsonian phenotype of Machado-Joseph disease. *Movement Disorders, 18*(2), 219-221.

Calne, D. B. (1993). Treatment of Parkinson's disease. *New England Journal of Medicine, 329*(14), 1021-1027.

Cappai, R., Leck, S. L., Tew, D., Williamson, N., Smith, D., Galatis, D., . . . Cherny, R. (2005). Dopamine promotes α-synuclein aggregation into SDS-resistant soluble oligomers via a distinct folding pathway. *The FASEB journal, 19*(10), 1377-1379.

Capra, R., Marcianò, N., Vignolo, L. A., Chiesa, A., & Gasparotti, R. (1992). Gadolinium—Pentetic Acid Magnetic Resonance Imaging in Patients With Relapsing Remitting Multiple Sclerosis. *Archives of neurology, 49*(7), 687-689.

Chen, Y.-S., Hong, Z.-X., Lin, S.-Z., & Harn, H.-J. (2020). Identifying Therapeutic Targets for Spinocerebellar Ataxia Type 3/Machado–Joseph Disease through Integration of Pathological Biomarkers and Therapeutic Strategies. *International Journal of Molecular Sciences, 21*(9), 3063.

Chiriboga, C. (2017). Nusinersen for the treatment of spinal muscular atrophy. *Expert review of neurotherapeutics, 17*(10), 955-962.

Collier, T., Srivastava, K., Justman, C., Grammatopoulous, T., Hutter-Paier, B., Prokesch, M., . . . Jock, K. (2017). Nortriptyline inhibits aggregation and neurotoxicity of alpha-synuclein by enhancing reconfiguration of the monomeric form. *Neurobiology of disease, 106*, 191-204.

Costa, M. d. C. (2020). Recent therapeutic prospects for Machado-Joseph disease. *Current Opinion in Neurology, 33*(4), 519-526. doi:10.1097/WCO.0000000000000832

Cragnaz, L., Spinelli, G., De Conti, L., Bureau, E. A., Brownlees, J., Feiguin, F., . . . Kettleborough, C. A. (2021). Thioridazine reverts the phenotype in cellular and Drosophila models of amyotrophic lateral sclerosis by enhancing TDP-43 aggregate clearance. *Neurobiology of disease, 160*, 105515.

D'Abreu, A., Franca, M. C., Jr., Paulson, H. L., & Lopes-Cendes, I. (2010). Caring for Machado-Joseph disease: current understanding and how to help patients. *Parkinsonism & Related Disorders 16*(1), 2-7. doi:10.1016/j.parkreldis.2009.08.012

Da Silva, J. D., Teixeira-Castro, A., & Maciel, P. (2019). From Pathogenesis to Novel Therapeutics for Spinocerebellar Ataxia Type 3: Evading Potholes on the Way to Translation. *Neurotherapeutics, 16*(4), 1009-1031. doi:10.1007/s13311-019-00798-1

Di Giovanni, S., Eleuteri, S., Paleologou, K. E., Yin, G., Zweckstetter, M., Carrupt, P.-A., & Lashuel, H. A. (2010). Entacapone and tolcapone, two catechol O-methyltransferase inhibitors, block fibril formation of α-synuclein and β-amyloid and protect against amyloid-induced toxicity. *Journal of Biological Chemistry, 285*(20), 14941-14954.

Feng, H., Hu, L., Zhu, H., Tao, L., Wu, L., Zhao, Q., . . . Li, X. (2020). Repurposing antimycotic ciclopirox olamine as a promising anti-ischemic stroke agent. *Acta Pharmaceutica Sinica B, 10*(3), 434-446.

Gi, M., Jeong, J., Lee, K., Lee, K.-M., Toyofuku, M., Yong, D. E., . . . Choi, J. Y. (2014). A drug-repositioning screening identifies pentetic acid as a potential therapeutic agent for suppressing the elastase-mediated virulence of Pseudomonas aeruginosa. *Antimicrobial agents and chemotherapy, 58*(12), 7205-7214.

Giannopoulos, P. F., Chiu, J., & Praticò, D. (2018). Antileukotriene therapy by reducing tau phosphorylation improves synaptic integrity and cognition of P301S transgenic mice. *Aging Cell, 17*(3), e12759.

Gupta, A. K., & Plott, T. (2004). Ciclopirox: a broad-spectrum antifungal with antibacterial and anti-inflammatory properties. *International journal of dermatology, 43*(S1), 3-8.

Hideshima, M., Kimura, Y., Aguirre, C., Kakuda, K., Takeuchi, T., Choong, C.-J., . . . Baba, K. (2022). Two-step screening method to identify α-synuclein aggregation inhibitors for Parkinson's disease. *Scientific reports, 12*(1), 1-11.

Hu, L., Feng, H., Zhang, H., Yu, S., Zhao, Q., Wang, W., . . . Wang, M. (2020). Development of novel N-hydroxypyridone derivatives as potential anti-ischemic stroke agents. *Journal of Medicinal Chemistry, 63*(3), 1051-1067.

Huang, Z., & Huang, S. (2021). Reposition of the fungicide ciclopirox for cancer treatment. *Recent Patents on Anti-Cancer Drug Discovery, 16*(2), 122-135.

Huynh, K., & Partch, C. L. (2015). Analysis of protein stability and ligand interactions by thermal shift assay. *Current protocols in protein science, 79*(1), 28.29. 21-28.29. 14.

Kaech, S., & Banker, G. (2006). Culturing hippocampal neurons. *Nature protocols, 1*(5), 2406-2415.

Keating, G. M., & Lyseng-Williamson, K. A. (2005). Tolcapone. *CNS drugs, 19*(2), 165-184.

Leong, S. L., Cappai, R., Barnham, K. J., & Pham, C. L. L. (2009). Modulation of α-synuclein aggregation by dopamine: a review. *Neurochemical research, 34*(10), 1838-1846.

Li, J., Zhu, M., Manning-Bog, A. B., Di Monte, D. A., & Fink, A. L. (2004). Dopamine and L-dopa disaggregate amyloid fibrils: implications for Parkinson's and Alzheimer's disease. *The FASEB journal, 18*(9), 962-964.

Li, L.-B., Yu, Z., Teng, X., & Bonini, N. M. (2008). RNA toxicity is a component of ataxin-3 degeneration in Drosophila. *Nature, 453*(7198), 1107-1111.

Li, Y., Nara, T., & Nakamura, M. (2004). *Regulation of highly unsaturated fatty acids (HUFA) synthesis: a new physiological role of peroxisome proliferator-activated receptor alpha (PPAR alpha).* Paper presented at the The FASEB journal.

Lieberman, A., Shakkottai, V., & Albin, R. (2019). Polyglutamine Repeats in Neurodegenerative Diseases. *Annual Review of Pathology: Mechanisms of Disease, 14*, 1-27. doi:10.1146/annurev-pathmechdis-012418-012857

Liu, W., Wang, G., Wang, Z., Wang, G., Huang, J., & Liu, B. (2022). Repurposing small-molecule drugs for modulating toxic protein aggregates in neurodegenerative diseases. *Drug Discovery Today*.

Lopalco, A., Cutrignelli, A., Denora, N., Lopedota, A., Franco, M., & Laquintana, V. (2018). Transferrin functionalized liposomes loading dopamine HCl: development and permeability studies across an in vitro model of human blood–brain barrier. *Nanomaterials, 8*(3), 178.

Löscher, W., & Friedman, A. (2020). Structural, molecular, and functional alterations of the blood-brain barrier during epileptogenesis and epilepsy: a cause, consequence, or both? *International Journal of Molecular Sciences, 21*(2), 591.

Matos, C. A., de Almeida, L., & Nobrega, C. (2019). Machado-Joseph disease/spinocerebellar ataxia type 3: lessons from disease pathogenesis and clues into therapy. *Journal of Neurochemistry, 148*(1), 8-28. doi:10.1111/jnc.14541

McGowan, D., van Roon-Mom, W., Holloway, H., Bates, G., Mangiarini, L., Cooper, G., . . . Snell, R. (2000). Amyloid-like inclusions in Huntington's disease. *Neuroscience, 100*(4), 677-680.

McLoughlin, H. S., Moore, L. R., & Paulson, H. L. (2020). Pathogenesis of SCA3 and implications for other polyglutamine diseases. *Neurobiology of disease, 134*, 104635.

Padhy, B., & Gupta, Y. (2011). Drug repositioning: re-investigating existing drugs for new therapeutic indications. *Journal of Postgraduate Medicine 57*(2), 153-160. doi:10.4103/0022-3859.81870

Paulson, H. L., Shakkottai, V. G., Clark, H. B., & Orr, H. T. (2017). Polyglutamine spinocerebellar ataxias—from genes to potential treatments. *Nature Reviews Neuroscience, 18*(10), 613-626.

Pierzynowska, K., Gaffke, L., Cyske, Z., & Węgrzyn, G. (2019). Genistein induces degradation of mutant huntingtin in fibroblasts from Huntington's disease patients. *Metabolic brain disease, 34*(3), 715-720.

Rames, M., Yu, Y., & Ren, G. (2014). Optimized negative staining: a high-throughput protocol for examining small and asymmetric protein structure by electron microscopy. *JoVE (Journal of Visualized Experiments)*(90), e51087.

Sangwan, S., Zhao, A., Adams, K. L., Jayson, C. K., Sawaya, M. R., Guenther, E. L., . . . Soriaga, A. B. (2017). Atomic structure of a toxic, oligomeric segment of SOD1 linked to amyotrophic lateral sclerosis (ALS). *Proceedings of the National Academy of sciences, 114*(33), 8770-8775.

Sant'Anna, R., Gallego, P., Robinson, L. Z., Pereira-Henriques, A., Ferreira, N., Pinheiro, F., . . . Rosario Almeida, M. (2016). Repositioning tolcapone as a potent inhibitor of transthyretin amyloidogenesis and associated cellular toxicity. *Nature communications, 7*(1), 1-13.

Scott, A. D. (2017). Fluorescent Thermal Shift Assays for Identifying Small Molecule Ligands. *Biophysical Techniques in Drug Discovery, 61*, 208.

Serafini, P. R., Feyder, M. J., Hightower, R. M., Garcia-Perez, D., Vieira, N. M., Lek, A., . . . Kawahara, G. (2018). A limb-girdle muscular dystrophy 2I model of muscular dystrophy identifies corrective drug compounds for dystroglycanopathies. *JCI insight, 3*(18).

Shang, Y., Guan, H., & Zhou, F. (2021). Biological Characteristics of Umbilical Cord Mesenchymal Stem Cells and Its Therapeutic Potential for Hematological Disorders. *Frontiers in Cell and Developmental Biology, 9*, 1096.

Silva, T., Mohamed, T., Shakeri, A., Rao, P. P., Martinez-Gonzalez, L., Pérez, D. I., . . . Uriarte, E. (2016). Development of blood–brain barrier permeable nitrocatechol-based catechol O-methyltransferase inhibitors with reduced potential for hepatotoxicity. *Journal of Medicinal Chemistry, 59*(16), 7584-7597.

Sleigh, S. H., & Barton, C. L. (2010). Repurposing strategies for therapeutics. *Pharmaceutical Medicine, 24*(3), 151-159.

Socias, S. B., Gonzalez-Lizarraga, F., Avila, C. L., Vera, C., Acuña, L., Sepulveda-Diaz, J. E., . . . Chehin, R. N. (2018). Exploiting the therapeutic potential of ready-to-use drugs: Repurposing antibiotics against amyloid aggregation in neurodegenerative diseases. *Progress in neurobiology, 162*, 17-36.

Stetefeld, J., McKenna, S., & Patel, T. (2016). Dynamic light scattering: a practical guide and applications in biomedical sciences. *Biophysical reviews, 8*(4), 409-427. doi:10.1007/s12551-016-0218-6

Talkhoncheh, M. S., Ek, F., Baudet, A., Karlsson, C., Olsson, R., & Larsson, J. (2015). Ciclopirox Ethanolamine Is a Novel Modifier of Human Hematopoietic Stem Cell Ex Vivo Expansion. *Blood, 126*(23), 36.

Vidgren, J., Svensson, L. A., & Liljas, A. (1994). Crystal structure of catechol O-methyltransferase. *Nature, 368*(6469), 354-358.

Winner, B., Jappelli, R., Maji, S. K., Desplats, P. A., Boyer, L., Aigner, S., . . . Campioni, S. (2011). In vivo demonstration that α-synuclein oligomers are toxic. *Proceedings of the National Academy of sciences, 108*(10), 4194-4199.

Chapter 5 - General Discussion

5.1 General discussion

Machado-Joseph Disease (MJD) is an inherited autosomal neurodegenerative disorder of late onset that is caused by the expansion of the polyglutamine (polyQ) tract of the Ataxin-3 (Atx3) protein. Atx3 aggregation is the major factor that leads to neurodegeneration, however, the link between protein aggregation and its neurotoxicity is not clear and is the subject of debate. This work had four distinct objectives with the ultimate goal of studying the Atx3 aggregation to unveil new insights into the structures that are formed during the fibrillization and how different molecules could affect it. Over the next topics, we will discuss each objective that is detailed in Chapter 1.

5.1.1 Establishment of a standardized and reproducible protocol for studying the Atx3 aggregation *in vitro*

Over the literature, we can find within the same family of affected individuals with different polyQ repeat sizes. Furthermore, several independent studies have shown individuals with the same number of glutamine repeats showing different ages of onset of the disease with often non-overlapping symptoms (Gu et al., 2004; Hsieh et al., 1997; Kawaguchi et al., 1994; Padiath, Srivastava, Roy, Jain, & Brahmachari, 2005; Takiyama, Sakoe, Nakano, & Nishizawa, 1997; Van Alfen et al., 2001). These studies highlight that polyQ expansion is not the only factor underlying the development of MJD and that other genetic, physiological and external factors can have a role in the manifestation of the disease. Our first goal for this work was to develop a methodology that allowed us to routinely study Atx3 aggregation *in vitro*, in order to further explore the effect of exogenous factors on its self-assembly mechanisms. We evaluated how different parameters could influence Atx3 aggregation *in vitro*: different Atx3 variants, ionic strength, buffer additives, detergents, molecular crowders and Atx3 interactors.

Single genetic variations have demonstrated their influence on protein function in other rare disorders, for example, Brugada Syndrome and Ornithine transcarbamylase deficiency (Lopes-Marques et al., 2021; Marangoni et al., 2011; Poelzing et al., 2006). In this context, we found that rs12895357 is an important variant in the *ATXN3* gene. The replacement of glycine for an arginine immediately after the polyQ tract is frequent in the general population and its polymorphic position is used to study MJD haplotype and origins (Gaspar et al., 2001; Li et al., 2018; Sharony et al., 2019). Our results showed that the presence of an arginine or a glycine at this position does not influence the dynamics of Atx3 aggregation *in vitro*. This is not surprising if we take into consideration the data available in the 1000 Genome project phase 3 (Genomes Project et al., 2015)

which gathered genomic information from 4973 healthy individuals. These data showed that homozygotes individuals for p.Gly306Arg are found in all populations, being more prevalent in the East Asian population.

We also evaluated how ionic strength, through different NaCl concentrations and different buffer pH, could influence Atx3 aggregation. It is already described in the literature that different ionic strengths can modulate the aggregation of several amyloid proteins, such as α-synuclein (Flynn, McGlinchey, Walker, & Lee, 2018; Moller et al., 2012; Munishkina, Henriques, Uversky, & Fink, 2004; Ziaunys, Sakalauskas, Mikalauskaite, & Smirnovas, 2021), amyloid beta-peptide (Abelein, Jarvet, Barth, Graslund, & Danielsson, 2016; Campos-Ramirez, Marquez, Quintanar, & Rojas-Ochoa, 2017) and amylin (Marek, Patsalo, Green, & Raleigh, 2012). Both Munishkina et al. (2004) and Ziaunys et al. (2021) reported that by increasing the NaCl concentration in α-synuclein buffer, fibrillation accelerates. Our ThT results showed that alone, changing the NaCl concentration does not change Atx3 aggregation dynamics. Although maximum fluorescence values could be different, aggregation kinetics is equal for all tested NaCl concentrations in both expanded and non-expanded isoforms. Salt-binding effects are strongly pH-dependent since pH influences the type and total charge of the protein, therefore affecting electrostatic interactions (Chi, Krishnan, Randolph, & Carpenter, 2003). Because pH is continuously maintained at 7.5 in all buffers, we could be limiting NaCl-Atx3 interactions. Our results on pH influence were similar to ones obtained by varying NaCl concentrations. The aggregation rates and maximum fluorescence were not greatly affected by pH alone in the ThT assay, a result confirmed by the observation of no alterations in fibril morphology as visualized by Transmission Electron Microscopy (TEM). This Atx3 behaviour is different than what is reported for other amyloid proteins such as amyloid beta-peptide (Fraser, Nguyen, Surewicz, & Kirschner, 1991; Su & Chang, 2001), amylin (Jha et al., 2014) and α-synuclein (Uversky, Yamin, et al., 2002) where authors demonstrate that decreasing pH resulted in an acceleration of the aggregation kinetics.

Of all buffer additives tested, only glycerol had an impact on Atx3 aggregation. Glycerol can be used to stabilize proteins since it can induce protein compaction, reduce protein flexibility, stabilize specific partially unfolded intermediates and affect both native and non-native protein aggregation (Vagenende, Yap, & Trout, 2009). Our results are in concordance, since Atx3 aggregation in the presence of glycerol was greatly impaired. Therefore, the presence of glycerol is an important parameter to define when designing the aggregation protocol.

The influence of different lipid membranes is often explored in the aggregation of amyloid proteins such as amyloid β-peptide (Terzi, Hölzemann, & Seelig, 1997; Warmlander et al., 2013), α-synuclein (Zhu & Fink, 2003) and prion protein (Kazlauskaite, Sanghera, Sylvester, Vénien-Bryan, & Pinheiro, 2003). Authors also use detergents such as SDS, Triton X-100 and Tween 20 to mimic cell membranes, since they can form micelles in solution. Saunders, Hughes, Cappai, and Bottomley (2013) studied the effect of SDS in Atx3 aggregation and observed that the presence of 1 mM of SDS leads to the disappearance of the lag-phase and a rapid Atx3 aggregation at concentrations above the critical micelle concentration (CMC) which is the concentration in which compounds form micelles in solution. In this study CMC of SDS is 1.2 mM and SDS concentrations above this value showed no increase in ThT signal. In our results, 1 mM of SDS was sufficient to prevent Atx3 aggregation and 5 mM completely inhibited Atx3 fibrillization since no aggregates were observed by TEM. Those previous results were different from what we obtained, a difference that could be explained by the different Atx3:SDS ratios used in the different experiments. In all our experiments, Atx3 concentration was 5 μM while Saunders and colleagues used six times more protein, 30 μM. Although SDS concentration is similar, the overall ratio is quite different and could explain the observed differences.

It is also important to note that the presence of detergents in solution can have a profound impact in the ThT signal (Kumar, Singh, Krishnamoorthy, & Swaminathan, 2008). ThT signal in the presence of detergents should be interpreted with caution. Our results displayed an apparent Atx3 aggregation inhibition with 5 mM of Triton X-100 and Tween 20, but analysis by TEM showed the presence of both protofibrils and mature fibers. Although SDS inhibit Atx3 aggregation, the effect was not the same in the presence of Triton X-100 and Tween 20. Siposova, Sedlak, Kozar, Nemergut, and Musatov (2019) studied the effect of Triton X-100 in the aggregation of insulin and the effect was very distinct depending on the concentration used. At higher concentrations, namely at 0.5 mM of Triton-X 100, no fluorescence was observable by ThT and the number of amyloid fibrils was very low. Concentrations of 0.05 mM of Triton X-100 caused a two-fold extension of the insulin lag-phase and increased ThT fluorescence (Siposova et al., 2019). In our experiments, 0.08 mM Triton X-100 and Tween 20 promoted faster Atx3 nucleation, since no lag-phase of ThT fluorescence was observed. At higher concentrations of Triton X-100 or Tween 20, such as 5 mM, Atx3 had a low ThT fluorescence, suggesting that amyloid-like formation was compromised, but TEM analysis showed the presence of protofibrils and mature SDS-resistant fibrils, although with smaller bundles of mature SDS-resistant fibrils.

The intracellular environment is very complex and to mimic its complexity and study how this factor could impact Atx3 aggregation we used different crowding agents. It is known that the effect of crowders on amyloid proteins varies with the concentration and type of crowder used (Fang, Yousaf, Huang, Yang, & Wang, 2018; Groover et al., 2021; Seeliger, Werkmuller, & Winter, 2013; Uversky, Cooper, Bower, Li, & Fink, 2002). In general, α-synuclein aggregation is accelerated by PEG, dextran and other crowders (Uversky, Cooper, et al., 2002). Groover et al. (2021) reported that huntingtin aggregation is affected by the presence of dextran, ficoll and PEG 20000, enhancing the heterogeneity of huntingtin non-fibrillar aggregate species formed (Groover et al., 2021). Human Islet Amyloid Polypeptide (hIAPP) aggregation is also affected by the presence of crowders (Fang et al., 2018; Seeliger et al., 2013), namely of dextran, which its presence on hIAPP aggregation induces an effect similar to the one observed on our Atx3 ThT assays. At increasing concentrations of dextran ThT fluorescence intensity decreases, in both hIAPP (Seeliger et al., 2013) and Atx3. This was further validated by TEM where we observed that not only dextran but also PEG 5000 and PEG 10000 could inhibit fibrillization of both expanded and non-expanded Atx3.

Atx3 is deubiquitinase, which preferentially cleaves K63-linkages (Burnett, Li, & Pittman, 2003; Winborn et al., 2008) in chains of four or more ubiquitin moieties. Our results showed that in our conditions and ratios, the *Homo sapiens* linear triubiquitin chain (HsUBB) does not interfere with Atx3 aggregation. Although on the expanded Atx3, some decrease in the ThT fluorescence at the highest molar ratio (1:10) was noted, and the filter retardation assay showed less mature SDS-resistant fibrils. This effect could be explained by a possible crowding effect from HsUBB. Alternatively, HsUBB, which interacts weakly with Atx3, could hinder the exposure of aggregation-prone sites on polyQ-expanded Atx3.

PolyQ Binding Peptide 1 (QBP1) is an 11-residue sequence that can inhibit polyQ aggregation both *in vitro* and *in vivo* (Armen, Bernard, Day, Alonso, & Daggett, 2005; Knight, Karamanos, Radford, & Ashcroft, 2018; Nagai et al., 2000; Tomita et al., 2009). Knight et al. (2018) showed that QBP1 does not bind to the polyQ region, but it interacts with a 39-residue sequence immediately C-terminal to the Josephin Domain. Although binding to Atx3 does not occur in the polyQ region, QBP1is very efficient in inhibiting the formation of mature SDS-resistant fibrils without, interfering with the first step of Atx3 aggregation. Our studies corroborated this and allowed us to verify that ThT is a great tool to evaluate Atx3 aggregation, but only the polyQ-independent aggregation step. As presented in our results, all ThT aggregation curves with and without the presence of

QBP1 are very similar, even though when sample is collected and analysed by TEM, it is clear that no mature SDS-resistant fibrils are formed.

Overall, we successfully optimized a protocol to study Atx3 aggregation *in vitro* that can be used for the screening of compounds or conditions that can help prevent, or reverse, aggregation. We also highlight the factors that should be considered when studying the aggregation process of Atx3, as well as the need for more than one method to monitor the aggregation kinetics of a protein.

5.1.2 Investigation of the structural and morphological characteristics of Atx3 oligomers and fibrils along the aggregation pathway using an optimized Transmission Electron Microscopy-based method complemented with the cryo-Electron Microscopy technique

In this second objective, we proposed to evaluate the structural and morphological characteristics of Atx3 oligomers and fibrils that are formed in the aggregation pathway using conventional and cryogenic Electron Microscopy (EM) techniques.

Using endpoint experiment samples, we firstly optimized our negative staining protocol, which allowed us to obtain consistently a better and homogeneous staining in the grid. The negative staining technique was developed in the late 1950s, and its mainly consists in using a water-soluble heavy metal salt to surround and permeate the biological sample (Harris, 2007). We tested a 1% (w/v) solution of uranyl acetate, which is one of the most common solutions used for negative staining by applying an adapted version of the protocol published by Rames, Yu, and Ren (2014). By glow discharging the grid prior to usage, perform several washing steps with water and staining agent and carry out all these steps over ice we created a protocol that delivered consistently good quality negative staining images. We can successfully observe and evaluate sample quality for both non-expanded and expanded Atx3. Since negative staining is limited to ~20 Å resolution (Scarff, Fuller, Thompson, & Iadanza, 2018), we proposed to apply cryo-EM to our Atx3 samples to obtain high resolution information about the oligomers and fibrils formed during Atx3 aggregation.

The amount of information about polyQ expanded protein aggregates is very scarce. Recently Galaz-Montoya, Shahmoradian, Shen, Frydman, and Chiu (2021) published novel insights about mutant huntingtin exon1 and polyQ aggregates using cryo-Electron Tomography (cryo-ET). By combining cryo-ET with subtomogram averaging, they were able to show that mutant huntingtin exon1 and polyQ-only

aggregates *in vitro* are structurally heterogeneous and filamentous. Our preliminary results show that both non-expanded and expanded Atx3 protofibers appear to be shorter than the filaments from huntingtin exon-1 and the polyQ region. Galaz-Montoya et al. (2021) show that both this constructs formed an aggregated group of filaments, while both Atx3 isoforms do not. Mature expanded Atx3 fibrils are much more longer compared to huntingtin obtained structures. Unfortunately, our lack of tomographic reconstruction does not allow us to compare the structure topology, yet.

Nazarov, Chiki, Boudeffa, and Lashuel (2021) recently published in bioarchives their work where they show that the core of *in vitro* fibrils of huntingtin exon1 are composed of β-hairpins with long planar β-sheets with variable stacking angle, a feature that is not observed in any other amyloid structure.

More studies on the structures that are formed in Atx3 aggregation, and other polyQ proteins, are still needed to ensure powerful insights into their mechanism of formation and exactly which structures are formed. By ensuring this, we will have a greater knowledge of how to overcome or tackle polyQ aggregation and design advanced therapies for MJD and other polyQ diseases.

5.1.3 Characterization of morphological changes in Atx3 oligomers/fibrils induced by Atx3-interacting nanobodies

Our host lab is currently studying nanobodies as a novel therapy against Atx3 aggregation. As mentioned before, nanobodies are very small and highly specific, making them great candidates for inhibitors of Atx3 aggregation. Nanobodies display great results for the treatment of distinct types of pathologies and currently, there are more than fifteen different nanobodies that are (or will be) in clinical testing (Muyldermans, 2021). NbBI.1031020 is one of these fifteen nanobodies which is being explored as a potential treatment for Alzheimer's disease (AD). Currently it is in phase 1 clinical trial (Marino & Holt, 2022; Muyldermans, 2021).

In this project, we selected five different nanobodies with the best preliminary results obtained by Thioflavin-T (ThT) aggregation assay and TEM, among other techniques. These nanobodies could compromise Atx3 aggregation, for both non-expanded and expanded isoforms. The objective was to collect several cryo-EM data sets of the complexes Atx3:Nanobody and to obtain a structure of the formed complex. Although cryo-EM has several advantages over X-ray crystallography and solid-state or solution Nuclear Magnetic Resonance, it also has some limitations. Despite the fact that there are some examples, it is difficult to determine 3D structures of proteins like Atx3

which have a small size, <100 kDa. Smaller proteins have low signal-to-noise ratio (Zhang, Tammaro, Peters, & Ravelli, 2020), they likely overlap on the ice layer, can preferentially orientate and/or denaturate when attaching to the air-water interface (D'Imprima et al., 2019). At the same time, Atx3 is an unusually-shape protein. Small, non-globular and asymmetric proteins are challenging to solve their 3D structures (Bepler et al., 2019). By combining Atx3 with other interacting nanobody, we likely increase its monodispersity, structural stability and conformational homogeneity (Harding et al., 2021). This type of approach was used by Guo et al. (2018), Huang et al. (2021) and Harding et al. (2021), who determined the structure of huntingtin in complex with HAP40 which is a known huntingtin interactor - by cryo-EM.

However, due to time and cost limitations, only one data set for the nanobody five (NB05) with both Atx3 isoforms was collected. Preliminary analysis of this data set showed that no fibrillar structures were formed compared to Atx3 samples without NB05 and for future work we will continue to analyse this data to obtain a structure of the Atx3:NB05 complex.

5.1.4 Screening of novel compounds with an inhibitory effect on Atx3 aggregation complemented with *in vitro* characterization

The last objective of our proposed work was to screen a chemical library of 1280 compounds to find a possible novel inhibitory compound of Atx3 aggregation, that may ultimately be used in MJD therapy. Using our robust assay to monitor Atx3 fibrillization (Objective 1 - described in Chapter 2) we quickly screened all compounds that could interfere in the first step of Atx3 aggregation. We continued to study these positive hits until we reduced the list to 4 different compounds. Chapter 4 describes how the non-expanded and expanded Atx3 aggregation is affected in the presence of these 4 compounds used in two different concentrations.

Repurposing drugs for the treatment of other pathologies different than the ones that were originally developed is a reality already applied by the pharmaceutical industry. There are several different examples of a new use for several drugs, such as celecoxib (before used in osteoarthritis and then for colon and breast cancer), finasteride (before used in benign prostatic hyperplasia and then for hair loss), mifepristone (before used in pregnancy termination and then for psychotic major depression) and topiramate (before used in epilepsy and then for obesity), with more examples extensively reviewed by Ashburn and Thor (2004). Drug repurposing is a fast way to broaden the range of available treatments or even develop a brand new therapy for another disease (Foerster

et al., 2020). The Prestwich Chemical Library was successfully explored for new treatment options against tuberculosis (Goldman, 2013) and *Staphylococcus aureus* infections (Torres et al., 2016). Bexarotene is an anti-cancer FDA approved drug and shown to eliminate amyloid-β aggregates in AD mouse models (Cramer et al., 2012). This allowed to rapidly be used in a Phase 2 clinical trial (NCT01782742).

There are also several examples of high-throughput screens for compounds that can inhibit the aggregation of different proteins associated with neurodegenerative disorders such as α-synuclein (Hideshima et al., 2022; Pujols et al., 2017), amyloid-β (Cox et al., 2020; McKoy, Chen, Schupbach, & Hecht, 2012), transthyretin (Dolado et al., 2005) and huntingtin (Lo et al., 2020). Pujols et al. (2017) used an optimized ThT aggregation assay which identified 11 different compounds in a library of 14000 that could modulate α-synuclein aggregation. A similar approach was performed by Hideshima et al. (2022) which used a double assay (ThT + Cell-based assay) to screen a library of more than 1200 compounds to identify α-synuclein aggregation inhibitors. They successfully found 30 different molecules. Interestingly, from these 30 different compounds, 5 were also found to inhibit Atx3 aggregation in our initial screening.

This work was the first to successfully identify different compounds that until now were never associated with the treatment of MJD or Atx3 aggregation. For future work, we will continue to explore their effect *in vivo* by using our in house *Drosophila* MJD (Sutton et al., 2017) model and mouse neuronal primary cell cultures expressing Atx3.

5.2 References

Abelein, A., Jarvet, J., Barth, A., Graslund, A., & Danielsson, J. (2016). Ionic Strength Modulation of the Free Energy Landscape of Abeta40 Peptide Fibril Formation. *Journal of the American Chemical Society, 138*(21), 6893-6902. doi:10.1021/jacs.6b04511

Armen, R., Bernard, B., Day, R., Alonso, D., & Daggett, V. (2005). Characterization of a possible amyloidogenic precursor in glutamine-repeat neurodegenerative diseases. *Proceedings of the National Academy of sciences, 102*(38), 13433-13438.

Ashburn, T., & Thor, K. (2004). Drug repositioning: identifying and developing new uses for existing drugs. *Nature Reviews Drug Discovery, 3*(8), 673-683. doi:10.1038/nrd1468

Bepler, T., Morin, A., Rapp, M., Brasch, J., Shapiro, L., Noble, A., & Berger, B. (2019). Positive-unlabeled convolutional neural networks for particle picking in cryo-electron micrographs. *Nature methods, 16*(11), 1153-1160.

Burnett, B., Li, F., & Pittman, R. (2003). The polyglutamine neurodegenerative protein ataxin-3 binds polyubiquitylated proteins and has ubiquitin protease activity. *Human molecular genetics, 12*(23), 3195-3205. doi:10.1093/hmg/ddg344

Campos-Ramirez, A., Marquez, M., Quintanar, L., & Rojas-Ochoa, L. (2017). Effect of ionic strength on the aggregation kinetics of the amidated amyloid beta peptide Abeta (1-40) in aqueous solutions. *Biophysical Chemistry, 228*, 98-107. doi:10.1016/j.bpc.2017.05.004

Chi, E., Krishnan, S., Randolph, T., & Carpenter, J. (2003). Physical stability of proteins in aqueous solution: mechanism and driving forces in nonnative protein aggregation. *Pharmaceutical research, 20*(9), 1325-1336.

Cox, S. J., Lam, B., Prasad, A., Marietta, H. A., Stander, N. V., Joel, J. G., . . . Ivanova, M. I. (2020). High-throughput screening at the membrane interface reveals inhibitors of Amyloid-β. *Biochemistry, 59*(24), 2249-2258.

Cramer, P. E., Cirrito, J. R., Wesson, D. W., Lee, C. D., Karlo, J. C., Zinn, A. E., . . . James, M. J. (2012). ApoE-directed therapeutics rapidly clear β-amyloid and reverse deficits in AD mouse models. *Science, 335*(6075), 1503-1506.

D'Imprima, E., Floris, D., Joppe, M., Sánchez, R., Grininger, M., & Kühlbrandt, W. (2019). Protein denaturation at the air-water interface and how to prevent it. *Elife, 8*, e42747.

Dolado, I., Nieto, J., Saraiva, M. J. M., Arsequell, G., Valencia, G., & Planas, A. (2005). Kinetic assay for high-throughput screening of in vitro transthyretin amyloid fibrillogenesis inhibitors. *Journal of Combinatorial Chemistry, 7*(2), 246-252.

Fang, X., Yousaf, M., Huang, Q., Yang, Y., & Wang, C. (2018). Dual effect of PEG-PE micelle over the oligomerization and fibrillation of human islet amyloid polypeptide. *Scientific reports, 8*(1), 4463. doi:10.1038/s41598-018-22820-w

Flynn, J., McGlinchey, R., Walker, R., & Lee, J. (2018). Structural features of alpha-synuclein amyloid fibrils revealed by Raman spectroscopy. *Journal of Biological Chemistry, 293*(3), 767-776. doi:10.1074/jbc.M117.812388

Foerster, S., Gustafsson, T., Brochado, A. R., Desilvestro, V., Typas, A., & Unemo, M. (2020). The first wide-scale drug repurposing screen using the Prestwick Chemical Library (1200 bioactive molecules) against Neisseria gonorrhoeae identifies high in vitro activity of auranofin and many additional drugs. *APMIS, 128*(3), 242-250. doi:10.1111/apm.13014

Fraser, P., Nguyen, J., Surewicz, W., & Kirschner, D. (1991). pH-dependent structural transitions of Alzheimer amyloid peptides. *Biophysical journal, 60*(5), 1190-1201.

Galaz-Montoya, J. G., Shahmoradian, S. H., Shen, K., Frydman, J., & Chiu, W. (2021). Cryo-electron tomography provides topological insights into mutant huntingtin exon 1 and polyQ aggregates. *Communications Biology, 4*(1), 1-9.

Gaspar, C., Lopes-Cendes, I., Hayes, S., Goto, J., Arvidsson, K., Dias, A., . . . Lima, M. (2001). Ancestral origins of the Machado-Joseph disease mutation: a worldwide haplotype study. *The American Journal of Human Genetics, 68*(2), 523-528.

Genomes Project, C., Auton, A., Brooks, L. D., Durbin, R. M., Garrison, E. P., Kang, H. M., . . . Abecasis, G. R. (2015). A global reference for human genetic variation. *Nature, 526*(7571), 68-74. doi:10.1038/nature15393

Goldman, R. C. (2013). Why are membrane targets discovered by phenotypic screens and genome sequencing in Mycobacterium tuberculosis? *Tuberculosis, 93*(6), 569-588.

Groover, S., Adegbuyiro, A., Fan, C., Hodges, B., Beasley, M., Taylor, K., . . . Legleiter, J. (2021). Macromolecular crowding in solution alters huntingtin interaction and aggregation at interfaces. *Colloids and Surfaces B: Biointerfaces, 206*, 111969. doi:10.1016/j.colsurfb.2021.111969

Gu, W., Ma, H., Wang, K., Jin, M., Zhou, Y., Liu, X., . . . Shen, Y. (2004). The shortest expanded allele of the MJD1 gene in a Chinese MJD kindred with autonomic dysfunction. *European Neurology, 52*(2), 107-111. doi:10.1159/000080221

Guo, Q., Huang, B., Cheng, J., Seefelder, M., Engler, T., Pfeifer, G., . . . Maurer, M. (2018). The cryo-electron microscopy structure of huntingtin. *Nature, 555*(7694), 117-120.

Harding, R., Deme, J., Hevler, J., Tamara, S., Lemak, A., Cantle, J., . . . Arrowsmith, C. (2021). Huntingtin structure is orchestrated by HAP40 and shows a polyglutamine expansion-specific interaction with exon 1. *Communications Biology, 4*(1), 1374. doi:10.1038/s42003-021-02895-4

Harris, J. R. (2007). Negative staining of thinly spread biological samples. In *Electron Microscopy* (pp. 107-142): Springer.

Hideshima, M., Kimura, Y., Aguirre, C., Kakuda, K., Takeuchi, T., Choong, C.-J., . . . Baba, K. (2022). Two-step screening method to identify α-synuclein aggregation inhibitors for Parkinson's disease. *Scientific reports, 12*(1), 1-11.

Hsieh, M., Tsai, H.-F., Lu, T.-M., Yang, C.-Y., Wu, H.-M., & Li, S.-Y. (1997). Studies of the CAG repeat in the Machado-Joseph disease gene in Taiwan. *Human genetics, 100*(2), 155-162.

Huang, B., Guo, Q., Niedermeier, M. L., Cheng, J., Engler, T., Maurer, M., . . . Kochanek, S. (2021). Pathological polyQ expansion does not alter the conformation of the Huntingtin-HAP40 complex. *Structure, 29*(8), 804-809. e805.

Jha, S., Snell, J., Sheftic, S., Patil, S., Daniels, S., Kolling, F., & Alexandrescu, A. (2014). pH dependence of amylin fibrillization. *Biochemistry, 53*(2), 300-310. doi:10.1021/bi401164k

Kawaguchi, Y., Okamoto, T., Taniwaki, M., Aizawa, M., Inoue, M., Katayama, S., . . . Akiguchi, I. (1994). CAG expansions in a novel gene for Machado-Joseph disease at chromosome 14q32. 1. *Nature genetics, 8*(3), 221-228.

Kazlauskaite, J., Sanghera, N., Sylvester, I., Vénien-Bryan, C., & Pinheiro, T. J. (2003). Structural changes of the prion protein in lipid membranes leading to aggregation and fibrillization. *Biochemistry, 42*(11), 3295-3304.

Knight, P., Karamanos, T. K., Radford, S. E., & Ashcroft, A. E. (2018). Identification of a novel site of interaction between ataxin-3 and the amyloid aggregation inhibitor polyglutamine binding peptide 1. *European Journal of Mass Spectrometry, 24*(1), 129-140. doi:10.1177/1469066717729298

Kumar, S., Singh, A. K., Krishnamoorthy, G., & Swaminathan, R. (2008). Thioflavin T displays enhanced fluorescence selectively inside anionic micelles and mammalian cells. *Journal of Fluorescence, 18*(6), 1199-1205.

Li, T., Martins, S., Peng, Y., Wang, P., Hou, X., Chen, Z., . . . Jiang, H. (2018). Is the High Frequency of Machado-Joseph Disease in China Due to New Mutational Origins? *Frontiers in Genetics, 9*, 740. doi:10.3389/fgene.2018.00740

Lo, C. H., Pandey, N. K., Lim, C. K.-W., Ding, Z., Tao, M., Thomas, D. D., . . . Sachs, J. N. (2020). Discovery of small molecule inhibitors of huntingtin exon 1 aggregation by FRET-Based high-throughput screening in living cells. *ACS Chemical Neuroscience, 11*(15), 2286-2295.

Lopes-Marques, M., Pacheco, A. R., Peixoto, M. J., Cardoso, A. R., Serrano, C., Amorim, A., . . . Azevedo, L. (2021). Common polymorphic OTC variants can act as genetic modifiers of enzymatic activity. *Human Mutation, 42*(8), 978-989. doi:10.1002/humu.24221

Marangoni, S., Di Resta, C., Rocchetti, M., Barile, L., Rizzetto, R., Summa, A., . . . Zaza, A. (2011). A Brugada syndrome mutation (p.S216L) and its modulation by p.H558R polymorphism: standard and dynamic characterization. *Cardiovascular Research, 91*(4), 606-616. doi:10.1093/cvr/cvr142

Marek, P., Patsalo, V., Green, D., & Raleigh, D. (2012). Ionic strength effects on amyloid formation by amylin are a complicated interplay among Debye screening, ion selectivity, and Hofmeister effects. *Biochemistry, 51*(43), 8478-8490. doi:10.1021/bi300574r

Marino, M., & Holt, M. G. (2022). AAV Vector-Mediated Antibody Delivery (A-MAD) in the Central Nervous System. *Frontiers in neurology, 13*, 870799.

McKoy, A. F., Chen, J., Schupbach, T., & Hecht, M. H. (2012). A novel inhibitor of amyloid β (Aβ) peptide aggregation: from high throughput screening to efficacy in an animal model of Alzheimer disease. *Journal of Biological Chemistry, 287*(46), 38992-39000.

Moller, J., Schroer, M., Erlkamp, M., Grobelny, S., Paulus, M., Tiemeyer, S., . . . Winter, R. (2012). The effect of ionic strength, temperature, and pressure on the interaction potential of dense protein solutions: from nonlinear pressure response to protein crystallization. *Biophysical journal, 102*(11), 2641-2648. doi:10.1016/j.bpj.2012.04.043

Munishkina, L. A., Henriques, J., Uversky, V. N., & Fink, A. L. (2004). Role of protein− water interactions and electrostatics in α-synuclein fibril formation. *Biochemistry, 43*(11), 3289-3300.

Muyldermans, S. (2021). Applications of nanobodies. *Annual review of animal biosciences, 9*, 401-421.

Nagai, Y., Tucker, T., Ren, H., Kenan, D. J., Henderson, B. S., Keene, J. D., . . . Burke, J. R. (2000). Inhibition of polyglutamine protein aggregation and cell death by novel peptides identified by phage display screening. *Journal of Biological Chemistry, 275*(14), 10437-10442. doi:10.1074/jbc.275.14.10437

Nazarov, S., Chiki, A., Boudeffa, D., & Lashuel, H. (2021). The structural basis of huntingtin (Htt) fibril polymorphism, revealed by cryo-EM of exon 1 Htt fibrils. *bioRxiv*.

Padiath, Q., Srivastava, A., Roy, S., Jain, S., & Brahmachari, S. K. (2005). Identification of a novel 45 repeat unstable allele associated with a disease phenotype at the MJD1/SCA3 locus. *American Journal of Medical Genetics Part B, 133B*(1), 124-126. doi:10.1002/ajmg.b.30088

Poelzing, S., Forleo, C., Samodell, M., Dudash, L., Sorrentino, S., Anaclerio, M., . . . Deschenes, I. (2006). SCN5A polymorphism restores trafficking of a Brugada syndrome mutation on a separate gene. *Circulation, 114*(5), 368-376. doi:10.1161/CIRCULATIONAHA.105.601294

Pujols, J., Peña-Díaz, S., Conde-Giménez, M., Pinheiro, F., Navarro, S., Sancho, J., & Ventura, S. (2017). High-throughput screening methodology to identify alpha-synuclein aggregation inhibitors. *International Journal of Molecular Sciences, 18*(3), 478.

Rames, M., Yu, Y., & Ren, G. (2014). Optimized negative staining: a high-throughput protocol for examining small and asymmetric protein structure by electron microscopy. *JoVE (Journal of Visualized Experiments)*(90), e51087.

Saunders, H. M., Hughes, V. A., Cappai, R., & Bottomley, S. P. (2013). Conformational behavior and aggregation of ataxin-3 in SDS. *PLoS One, 8*(7), e69416. doi:10.1371/journal.pone.0069416

Scarff, C. A., Fuller, M. J., Thompson, R. F., & Iadanza, M. G. (2018). Variations on negative stain electron microscopy methods: tools for tackling challenging systems. *JoVE (Journal of Visualized Experiments)*(132), e57199.

Seeliger, J., Werkmuller, A., & Winter, R. (2013). Macromolecular crowding as a suppressor of human IAPP fibril formation and cytotoxicity. *PLoS One, 8*(7), e69652. doi:10.1371/journal.pone.0069652

Sharony, R., Martins, S., Costa, I., Zaltzman, R., Amorim, A., Sequeiros, J., & Gordon, C. (2019). Yemenite-Jewish families with Machado-Joseph disease (MJD/SCA3) share a recent common ancestor. *European Journal of Human Genetics, 27*(11), 1731-1737. doi:10.1038/s41431-019-0449-7

Siposova, K., Sedlak, E., Kozar, T., Nemergut, M., & Musatov, A. (2019). Dual effect of non-ionic detergent Triton X-100 on insulin amyloid formation. *Colloids Surf B Biointerfaces, 173*, 709-718. doi:10.1016/j.colsurfb.2018.10.039

Su, Y., & Chang, P.-T. (2001). Acidic pH promotes the formation of toxic fibrils from β-amyloid peptide. *Brain research, 893*(1-2), 287-291.

Sutton, J. R., Blount, J. R., Libohova, K., Tsou, W.-L., Joshi, G. S., Paulson, H. L., . . . Todi, S. V. (2017). Interaction of the polyglutamine protein ataxin-3 with Rad23 regulates toxicity in Drosophila models of Spinocerebellar Ataxia Type 3. *Human molecular genetics, 26*(8), 1419-1431.

Takiyama, Y., Sakoe, K., Nakano, I., & Nishizawa, M. (1997). Machado-Joseph disease: cerebellar ataxia and autonomic dysfunction in a patient with the shortest known expanded allele (56 CAG repeat units) of the MJD1 gene. *Neurology, 49*(2), 604-606. doi:10.1212/wnl.49.2.604

Terzi, E., Hölzemann, G., & Seelig, J. (1997). Interaction of Alzheimer β-amyloid peptide (1− 40) with lipid membranes. *Biochemistry, 36*(48), 14845-14852.

Tomita, K., Popiel, A., Nagai, Y., Toda, T., Yoshimitsu, Y., Ohno, H., . . . Fujii, N. (2009). Structure-activity relationship study on polyglutamine binding peptide QBP1. *Bioorg Med Chem, 17*(3), 1259-1263. doi:10.1016/j.bmc.2008.12.018

Torres, N. S., Abercrombie, J. J., Srinivasan, A., Lopez-Ribot, J. L., Ramasubramanian, A. K., & Leung, K. P. (2016). Screening a commercial library of pharmacologically active small molecules against Staphylococcus aureus biofilms. *Antimicrobial agents and chemotherapy, 60*(10), 5663-5672.

Uversky, V. N., Cooper, E. M., Bower, K. S., Li, J., & Fink, A. L. (2002). Accelerated α-synuclein fibrillation in crowded milieu. *FEBS letters, 515*(1-3), 99-103.

Uversky, V. N., Yamin, G., Souillac, P. O., Goers, J., Glaser, C. B., & Fink, A. L. (2002). Methionine oxidation inhibits fibrillation of human α-synuclein in vitro. *FEBS letters, 517*(1-3), 239-244.

Vagenende, V., Yap, M., & Trout, B. (2009). Mechanisms of protein stabilization and prevention of protein aggregation by glycerol. *Biochemistry, 48*(46), 11084-11096. doi:10.1021/bi900649t

Van Alfen, N., Sinke, R. J., Zwarts, M. J., Gabreëls-Festen, A., Praamstra, P., Kremer, B. P., & Horstink, M. W. (2001). Intermediate CAG repeat lengths (53, 54) for MJD/SCA3 are associated with an abnormal phenotype. *Annals of Neurology, 49*(6), 805-808.

Warmlander, S., Tiiman, A. T., Abelein, A., Luo, J., Jarvet, J. J., Soderberg, K., . . . Graslund, A. (2013). Biophysical studies of the amyloid beta-peptide: interactions with metal ions and small molecules. *Chembiochem, 14*(14), 1692-1704. doi:10.1002/cbic.201300262

Winborn, B., Travis, S., Todi, S. V., Scaglione, M., Xu, P., Williams, A., . . . Paulson, H. L. (2008). The deubiquitinating enzyme ataxin-3, a polyglutamine disease protein, edits Lys63 linkages in mixed linkage ubiquitin chains. *Journal of Biological Chemistry, 283*(39), 26436-26443. doi:10.1074/jbc.M803692200

Zhang, Y., Tammaro, R., Peters, P. J., & Ravelli, R. (2020). Could Egg white lysozyme be solved by single particle cryo-EM? *Journal of chemical information and modeling, 60*(5), 2605-2613.

Zhu, M., & Fink, A. L. (2003). Lipid binding inhibits alpha-synuclein fibril formation. *Journal of Biological Chemistry, 278*(19), 16873-16877. doi:10.1074/jbc.M210136200

Ziaunys, M., Sakalauskas, A., Mikalauskaite, K., & Smirnovas, V. (2021). Polymorphism of Alpha-Synuclein Amyloid Fibrils Depends on Ionic Strength and Protein Concentration. *International Journal of Molecular Sciences, 22*(22). doi:10.3390/ijms222212382